UNIVERSITY OF SOUTHAMPTON

FACULTY OF ENGINEERING AND THE ENVIRONMENT

Fluid Structure Interaction Research Group

Modelling the propelled resistance of a freestyle swimmer using Computational Fluid Dynamics

by

Joseph Banks

Thesis for the degree of Doctor of Philosophy

June 2013

UNIVERSITY OF SOUTHAMPTON

ABSTRACT

FACULTY OF ENGINEERING AND THE ENVIRONMENT

Fluid Structure Interactions

Thesis for the degree of Doctor of Philosophy

MODELLING THE PROPELLED RESISTANCE OF A FREESTYLE SWIMMER USING COMPUTATIONAL FLUID DYNAMICS

Joseph Banks

Competitive swimming has always been a traditional sport, with performance being governed by athlete instinct and feel, the coaches' experience and time spent in the water. However in recent years the introduction and subsequent banning of the 'super' suits has opened the eyes of the sport to what science and engineering can achieve.

The focus of improvement is often on generating more propulsive force; however increases in swimming speed can be achieved for the same propulsive power if the resistance is reduced. The resistance acting on a freestyle swimmer is governed by the complex unsteady flow regime, featuring significant body and arm motions, large separated regions and interactions with the free surface. Physically simulating all these aspects within a CFD methodology is computationally very expensive. However it is unclear which unsteady flow features need to be included to accurately represent the active resistance of a freestyle swimmer.

The unsteady fluid flow around a freestyle swimmer has be investigated numerically through the use of a combine free surface RANS methodology with the impact of the arms represented using a generic body force model.

A detailed analysis of a passive swimmer on the surface has been conducted identifying that free surface interactions have a significant effect on the resistance components of a freestyle swimmer and should be included within future research aimed at reducing resistance.

The impact of the arms in the propelled simulations produced a significant variation in total resistance due to free surface interactions, highlighting the importance of the arm entry phase of the stroke. However the arms caused no significant change in the mean resistance and the impact of the arm induced velocities on the resistance is very small. Therefore it is concluded that the effect of the arms are not required in an assessment of mean propelled resistance in freestyle swimming.

Contents

List of tables

List of figures

DECLARATION OF AUTHORSHIP

I, Joseph Banks

declare that the thesis entitled

Modelling the propelled resistance of a freestyle swimmer using Computational Fluid Dynamics

and the work presented in the thesis are both my own, and have been generated by me as the result of my own original research. I confirm that:

this work was done wholly or mainly while in candidature for a research degree at this University;

where any part of this thesis has previously been submitted for a degree or any other qualification at this University or any other institution, this has been clearly stated;

where I have consulted the published work of others, this is always clearly attributed;

where I have quoted from the work of others, the source is always given. With the exception of such quotations, this thesis is entirely my own work;

I have acknowledged all main sources of help;

where the thesis is based on work done by myself jointly with others, I have made clear exactly what was done by others and what I have contributed myself;

parts of this work have been published as:(Banks, Phillips, Bull, & Turnock, 2010; Banks, Phillips, Turnock, & Hudson, 2011; Banks, Phillips, Turnock, Hudson, & Taunton, 2013; Webb et al., 2011)

Signed: …………………………………………………………………………..

Date:…………………………………………………………………………….

Acknowledgements

I would like to thank all the people that have helped me over the last three years. In particular I would like to thank my supervisors Prof. Stephen Turnock and Dr. Dominic Hudson for their supervision and assistance. I would especially like to thank Dr Alex Phillips who has provided expert CFD assistance and supervision throughout the entire project.

I would like to thank my co-workers on the UK Sport project Angus Webb and Christopher Phillips for all the enjoyable times we have spent working together. I would like to thank other supervising academics such as Dr. Dominic Taunton and Dr. Alex Forrester for their assistance and support.

I would particularly like to thank Sue, Bryan and Dan for their production line efforts in proof reading and general support and encouragement.

I would like to thank both UK Sport and EPSRC for the funding of this project and British Swimming for supporting this work.

Nomenclature

2D	Two Dimensional
3D	Three dimensional
CFD	Computational Fluid Dynamics
DES	Detatched Eddy Simulation
GUI	Graphical User Interface
ITTC'57	International Towing Tank Conference Skin friction correlation line
RANS	Reynolds Averaged Navier-Stokes
STL	Stereolithography file format
SPH	Smooth particle hydrodynamics
VOF	Volume of Fluid
N003	Passive tow case with head in-line with torso
DA003	Passive tow case with head up
C009	Propelled or active tow case of arms only freestyle
C012	Passive tow case for comparison with C009

A,B	Coordinates of each end of the arm section
$\widehat{AB}$	Unit vector along the blades span
Cr	Courant Number
C_l	Lift coefficient
C_d	Drag coefficient
C_f	Coefficient of frictional resistance
C_{f_x}	Local coefficient of skin friction resistance
C_{p_rgh}	Local coefficient of pressure

C_{px_rgh}	Local coefficient of pressure resistance
c	Blade chord
f_i	Momentum source term
F_L	Lift force
F_D	Drag force
Fn	Froude Number
F_n	Force normal to the blade
k	Turbulent kinetic energy
L	Reference length/ Swimmer length
l	Blade or arm length
$\hat{n}$	Unit vector normal to the blade
p	Pressure
r	Paddle radius
R	Resistance
R_e	Reynolds Number
R_f	Frictional resistance
S_w	Wetted surface area
S_p	projected frontal area
S_n	Surface normal
t	Time
T	Thrust
T_{stroke}	Stroke period
u^+	Non-dimensional velocity within the boundary layer
u_τ	Friction velocity

u’	Fluctuation of instantaneous velocity about the mean
u_i	Velocity components (ux, uy, uz)
U	Velocity
U_0	Free stream velocity / Swimmer velocity
V_A,V_B	Velocity vectors of each end of the arm section
V_{armRel},	Velocity of arm relative to the swimmer.
$V_{\_arm}$	Velocity of arm relative to the fluid
V_n	Normal velocity
V_s	Sector volume
x_i	coordinates (x, y, z)
y^+	Non-dimensional distance throughout the boundary layer

α	Angle of attack of fluid to blade / hand
α_0	Unit vector defining hand orentation
ν	Kinematic viscosity
μ	Dynamic viscosity
ρ	Fluid density
ε	Turbulent dissipation
ω	Turbulent frequency
μ_T	Eddy viscosity
τ_w	Wall shear stress
φ	Volume fraction
θ	Rotation angle
$\dot{\theta}$	Angular velocity

$\hat{\dot{\theta}}$	Angular velocity unit vector
η	Hydrodynamic propulsive efficiency

1. Introduction

Competitive swimming has always been a traditional sport, with performance being governed by instinctive athlete optimisation based on feel, the coaches' experience and time spent in the water. However in recent years the introduction and subsequent banning of the 'super' suits has opened the eyes of the sport to what science and engineering can achieve. On average the full body swimsuits provided a two percent improvement in performance through improving the shape of the body in the water. This led to a string of new world records in 2008 and 2009 before the suits were banned. Since then there has been a real drive within the sport to regain those performance gains.

This project is part of a UK Sport funded research program which sponsored three PhD students, in collaboration with other innovation partners, to improve the performance of the British Swimming team at the London 2012 Olympics. The overall aim of this wider project was to provide a scientific and controlled environment in which an athlete's technique, body posture or equipment could be analysed to provide greater insight and understanding to coaches and athletes on how the fluid dynamic forces affect performance. This project included an extensive experimental testing program resulting in 90% of the Olympic squad having their technique analysed before London. Alongside this experimental program individual research projects have been conducted by the other two PhD students focused on race simulation, providing the impact of hydrodynamic changes on the race time (Webb, 2013), and musculoskeletal modelling, investigating overall stroke efficiency (C. Phillips, 2013). This thesis presents the third research project into numerical modelling the resistance of a freestyle swimmer.

In order to improve a swimmer's performance, which in this context means to increase their speed, requires either an increase in the propulsive force generated or a reduction in the resistance, or more likely a combination of both. Traditionally competitive swimming programs have invested in maximising the propulsive power of their athletes, employing strength and conditioning coaches alongside technical swimming coaches. However performance gains can also be made through minimising the swimmer's resistance.

The resistance acting on a freestyle swimmer is governed by the complex unsteady flow regime that develops around the body. Many different flow features can be observed due to the complex moving geometry and interactions with the free surface, all of which contribute to the resistance in a different way. The high curvature associated with a human body creates large regions of flow separation which add to the pressure resistance and make regions of the flow inherently unstable. The interaction of the air water interface over this complex geometry causes changes in the pressure field, generating large amplitude waves that are often unsteady and breaking. The body motion and the impact of the arms and legs result in unsteady variation in resistance and thrust. This provides an incredibly complicated flow regime which needs to be understood if reductions in resistance are going to be found.

Analysing the hydrodynamic forces on a freestyle swimmer presents a difficult problem. The complex interaction between propulsive and resistive forces makes it difficult to accurately measure what is happening in the fluid flow around the body. It is also impossible to experimentally measure the forces on the body without altering the stroke in some way. Therefore, if it were possible to simulate the fluid regime around the swimmer, greater insight into this complex problem could be gained.

Computational fluid dynamics (CFD) is commonly used in naval architecture to provide simulated solutions to complex fluid dynamic problems which are difficult or expensive to analyse experimentally (Molland, A. F., Turnock, S. R., & Hudson, 2011). CFD has also played a significant role in well funded sports which have a strong engineering design element to them, such as F1 racing and the America’s Cup in sailing. However, CFD is starting to be used more widely within the sports engineering community with applications varying from cycling (Defraeye, Blocken, Koninckx, Hespel, & Carmeliet, 2010) to football aerodynamics (Barber, Chin, & Carré, 2009).

The advantage of using a CFD methodology to analyse swimming is that both the resistance and the propulsion forces can be assessed over the body. The simulation results also allow the flow features behind the hydrodynamic forces to be assessed, providing far more detail and insight to the flow than can be achieved experimentally.

The application of CFD to swimming has advanced significantly in recent years with simulated solutions ranging from unsteady forces on a swimmer's hand (Sato & Hino, 2003) and passive resistance of deeply submerged swimmers. More recently this has included swimmers on the surface (Bixler, Pease, & Fairhurst, 2007; Sato & Hino, 2010), active swimming simulations of underwater fly-kick (Von Loebbecke, Mittal, Mark, & Hahn, 2009) and even full freestyle simulations on the surface (Keys,M., Lyttle, Blanksby, & Cheng, 2010). These works have all contributed to the understanding of fluid dynamics in swimming, however there has generally been a lack of detailed analysis of the fluid flow structures in favour of presenting the total forces acting on the body. There has also been a lack of presented validation data for the more complex cases simulated. This is especially the case regarding simulations including the free surface. However to have confidence in the solutions provided by CFD it is important that they are validated against experimental data. This highlights the benefits of this CFD research project being embedded within the larger experimental project with UK Sport, allowing specific experimental test cases to be designed and conducted.

Using CFD to simulate the flow around a freestyle swimmer presents significant challenges. The fluid domain has to be discretised into small cells for which a numerical solution to the flow can be obtained. The complex geometry of a human body requires a very small cell size to capture the flow physics correctly. This is primarily due to the need to resolve the boundary layer growth over the body, requiring a significant computational resource. This is increased further by the inclusion of a free surface within the simulation due to the small cell sizes required to capture the interface between air and water. Based on observations of the British Olympic swimming squad it is clear that the influence of the free surface will play a significant role in the resistance. A range of experimentally determined wave resistance values have been published (Toussaint & Truijens, 2005; Vennell, Pease, & Wilson, 2006); however very little attention has been paid to understanding the local free surface flow features and how they impact on resistance. If reductions in resistance are to be found for freestyle swimmers this free surface interaction needs to be more fully understood.

If the full kinematic motion of the arms is included in the meshed geometry, the computational costs can become prohibitive. This is mainly due to the small cell size and reduced time step required to resolve the unsteady flow over an arm moving significantly faster than the body. Additional complexity and cost is associated with incorporating the arm's extensive range of motion throughout the domain, due to simple mesh deformation being inadequate. However to investigate the resistance components acting on a freestyle swimmer the full complexity of the problem does not necessarily need to be solved. It would seem logical that the majority of the resistance force comes from the head and torso, whilst the arms and legs produce mainly thrust. This appears to be confirmed by the full body simulations of freestyle (Keys,M. et al., 2010). However it is unclear what effect the arms have on the resistance of the head and body through modifying the local flow, both ahead and around the body. This poses the question as to which aspects of the unsteady flow around a freestyle swimmer need to be included to assess potential reductions in resistance due to body shape, body attitude and equipment design.

Investigating the interaction between the arms and the body requires only the effect the arms have on the fluid to be simulated, not the detailed resolution of the forces on the arms themselves. This presents the possibility of adopting a naval architecture approach to self-propelled simulations, where the head and body of the swimmer are thought of as the hull generating resistance and the impact of the arms is simulated through the use of a body force model.

1.1 Aims and objectives

The aim of this research is to investigate numerically the unsteady fluid flow around a freestyle swimmer. In order to determine the importance of free surface interactions and the impact of the arms on the propelled resistance.

In order to achieve this aim the completion of the following objectives is necessary:

1. development of a free-surface CFD methodology, appropriate for a human geometry, that allows the passive resistance components of a freestyle swimmer to be determined;
2. development of a body-force model capable of representing a freestyle swimmer's arm, as a series of momentum source terms, based on generic kinematic input data;

3. combine the previous two methodologies to perform propelled swimming simulations that allow the impact of a freestyle swimmer's arm on the resistance to be assessed;
4. provide recommendation on which aspects of the unsteady freestyle stroke are required to assess potential reductions in resistance

This work should also provide insight and recommendations on appropriate CFD modelling techniques and their validation when applied to the field of swimming.

1.2 Adopting a naval architecture approach to freestyle swimming

To increase a swimmer's speed for the same energy expenditure, they either have to increase their propulsive force (thrust) or reduce their resistance (drag). The same fluid dynamic principles apply to designing a ship and can provide insight into the complex problem of understanding the forces acting on a swimmer. Typically naval architects split the problem into three components. The passive (or naked hull) resistance of the hull-form moving through the water, at a constant velocity; the thrust generated by the propeller and finally the interaction between the two, providing the self-propelled velocity where the average resistance equals the average thrust. This approach is very effective as the hull can be viewed as a rigid body, independent of the propulsion system. This typically provides three distinct phases of analysis to build up a self-propelled assessment of a ship design:

- Passive resistance tests, where the naked hull is assessed at a constant speed to determine the total resistance and provide a component breakdown. This has traditionally been conducted experimentally, however it is increasingly being undertaken using CFD, providing a solid knowledge base to free-surface resistance simulations (Larsson, Stern, & Visonneau, 2010; Larsson, L., Stern, F., & Bertram, 2003; Molland, A. F., Turnock, S. R., & Hudson, 2011);
- Open water propeller analysis, where the thrust produced by the propeller is assessed independently from the hull. Again this can be conducted experimentally or numerically at varying levels of complexity

and hydrodynamic fidelity (Molland, A. F., Turnock, S. R., & Hudson, 2011);

- Self-propelled analysis, where the interaction between the propeller and the hull is assessed. Traditionally this was conducted experimentally at model scale however several different CFD methodologies can also be applied. The physical propeller can be simulated through the use of sliding, or overlapping, mesh interfaces, however the computational cost of such approaches is often prohibitive. Nevertheless, the effect the propeller has on the flow can be simulated through the use of body-force models, which induce the correct propeller velocities into the fluid through the use of momentum sources (more detail on these methods is provided in chapter 4.4.1).

To understand how this established methodology can be applied to a free style swimmer it is important to understand the different forces acting on the body and how they differ from those found on a ship.

1.2.1 Forces acting on a freestyle swimmer

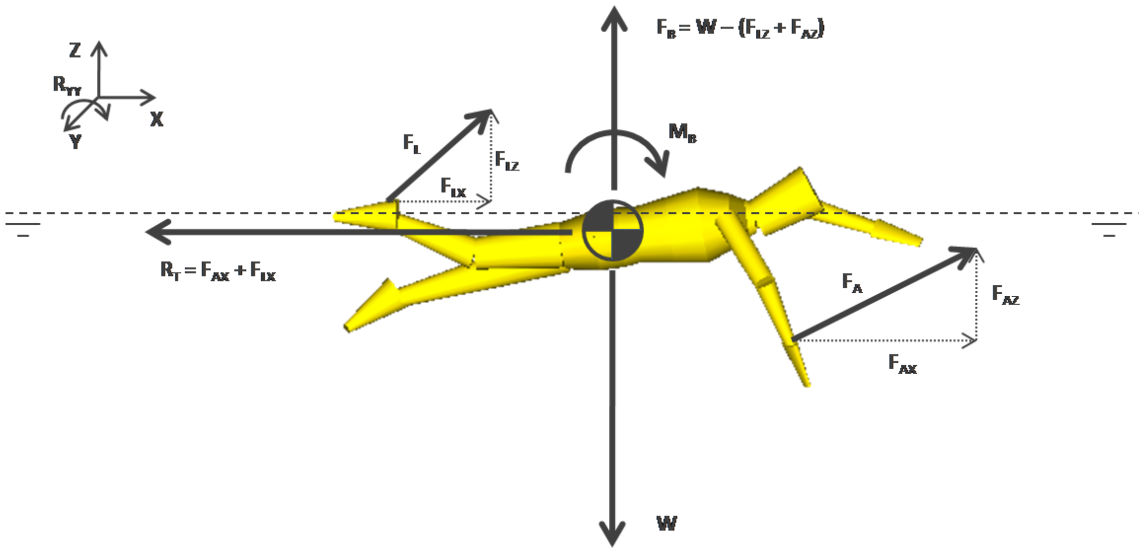

Figure 1-1 – Schematic of forces acting on a freestyle swimmer (Body representation generated using SWUM (Nakashima, Satou, & Miura, 2007))

When a swimmer is moving through the water their motion is determined by the forces acting on their body. Their forward velocity is determined by balancing the generated resistance (drag) with propulsion (thrust). Their attitude and depth in the water is mainly determined by balancing the vertical forces of weight and buoyancy, although other forces contribute such as the vertical component of the leg kick.

1.2.2 Components of resistance

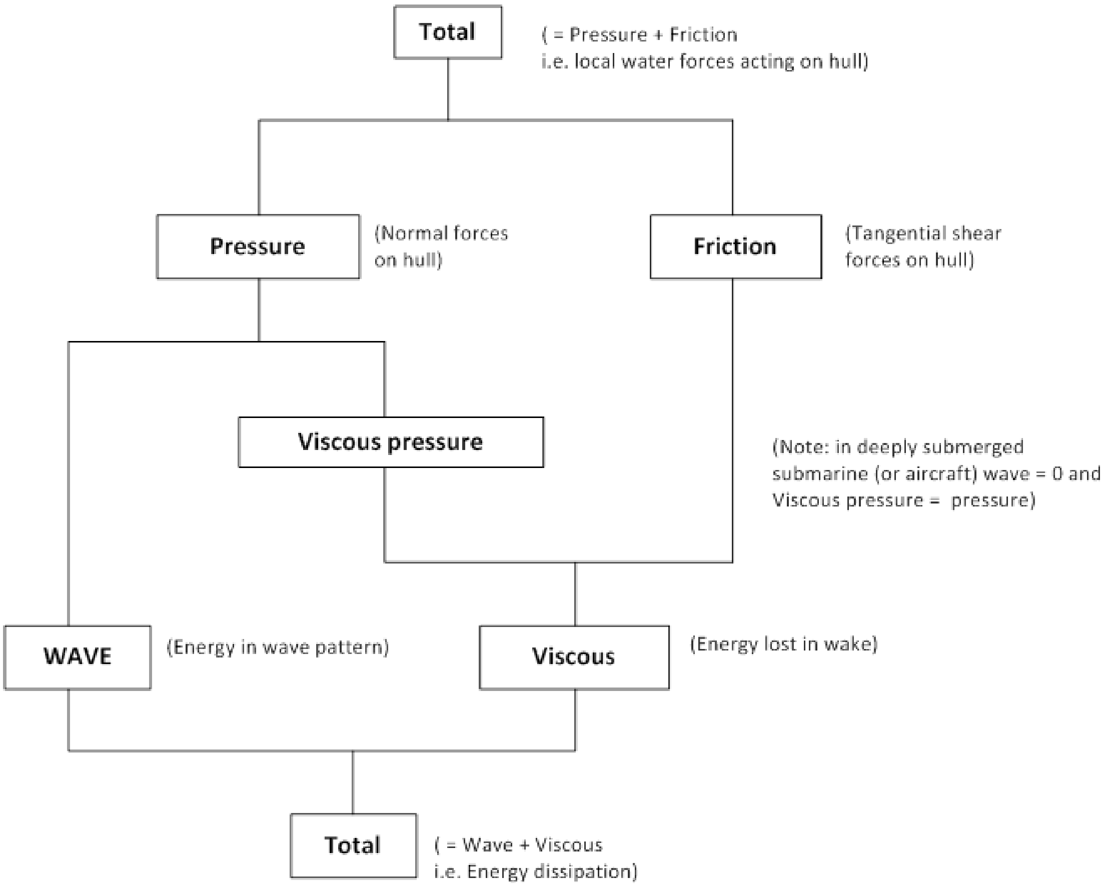

Figure 1-2 - Breakdown of the total resistance of a ship into different components, based on forces on the hull (top) and energy lost to the fluid (bottom). Image taken from (Molland, A. F., Turnock, S. R., & Hudson, 2011) with the permission of the authors.

The total resistance force acting on the swimmers body can be broken down in two different components:

- **Skin Friction**, due to the tangential shear force acting on the body and;
- **Pressure resistance**, due to the normal forces acting on the body.

The frictional resistance is caused by the development of a viscous boundary layer over the surface of the body. The pressure resistance can again be split into two further components:

- **Wave resistance**, due to the difference in pressure over the body as a result of the free-surface deformations resulting in energy being lost to the wave pattern and;
- **Viscous Pressure Resistance**, due to the loss in pressure associated with viscous effects. This includes separation drag and is also known as form drag.

The exact same breakdown of forces is applied to a ship hull, presented in figure 1-2. The total resistance can also be thought of as the energy lost to the viscous wake and energy lost to the wave pattern that is developed. Within this definition there is a degree of crossover regarding breaking waves. Wave breaking and spray contribute to the wave resistance but result in viscous losses represented in the wake, not the wave pattern. This viscous component of wave resistance could be significant in swimming due to the large amplitude breaking waves that are generated. When the swimmer is deeply submerged the wave resistance disappears and entire resistance is represented by the viscous wake.

1.2.3 Propulsion force (Thrust)

The propulsive forces generated in freestyle come from the arms and legs, however previous research concluded that as much as 85-90 % of the total thrust is generated by the arms (Marinho, Barbosa, Kjendlie, et al., 2012). The vertical forces generated by the legs do play a significant part in defining the body's depth and attitude in the water, which in turn affects the resistance acting on the body. The thrust generated by the arms is comprised of both lift and drag forces due to the significant lateral motion of the arm throughout a stroke, creating an angle of attack for the flow over the hand.

1.2.4 Self-propelled resistance (or Active Drag)

The self-propelled resistance, often referred to as active drag in swimming, refers to the resistance force acting on the swimmer's body whilst swimming. This includes the unsteady effects of the body's motion and the interaction between generating thrust and the fluid forces on the rest of the body.

If we consider a self-propelled ship, the impact of the propeller at the stern of the hull is to accelerate the flow in this region. This increases the viscous shear and reduces the pressure in this location resulting in an increase in the resistance of the ship. This process is well understood and is accounted for as a thrust deduction in the powering calculation of ships (Molland, A. F., Turnock, S. R., & Hudson, 2011). However it is currently unclear to what extent the thrust produced by the arms and legs affect the resistance on the rest of the swimmer's body.

1.2.5 Simplifications and assumptions

The resistance and propulsion of a freestyle swimmer is a more complex problem to break down than a propelled ship, due to the fact that the majority of the body is in motion associated with generating propulsion. However a couple of key assumptions allow the problem to be significantly simplified. Firstly the forward velocity of the swimmer will be assumed to be constant. In the extreme case of an Olympic sprint freestyler the velocity variation throughout a stroke was measured as 19% (Keys,M. et al., 2010), however this is likely to be significantly less for longer distance events. Secondly the contribution of the legs to propulsion will be neglected based on the previous research concluding that 85-90 % of propulsion is generated from the arms (Marinho, Barbosa, Kjendlie, et al., 2012). Due to the position of the legs downstream from the head and body they are also unlikely to significantly alter the flow upstream around the torso. Thirdly the motion of the swimmer's body will be neglected in all directions except the forward motion. Assessment of experimental video footage (see chapter 3.3) of freestyle swimmers indicates that this is a valid assumption, except for the roll motion which can vary up to ± 50 degrees throughout a stroke cycle (approximately 1.2 seconds long).

If we ignore the swimmer's roll motion then the legs, torso and head can be thought of as a rigid body moving through the water at a constant speed. This is then equivalent to a ship's hull. The propulsion generated from the arms can then be assessed separately. This allows methodologies for investigating the different aspects of resistance and propulsion to be developed and validated in isolation before conducting propelled freestyle analysis. This greatly simplifies the problem.

It is acknowledged that the body roll is likely to have a significant impact on the resistance of a free style swimmer; however this is not included within the scope of this research. It would be possible to include roll motion into the developed methodology at a later stage as further work to this project.

1.2.6 Computational cost implications

The key issue with modelling the full body freestyle kinematics using CFD is predominantly in the capturing of the arm and leg motions. This causes increased levels of complexity regarding the methodologies required and the additional computational cost associated with them.

Firstly, due to the arm's extensive range of motion, simple mesh deformation cannot be used to simulate its kinematics alongside the body. Therefore techniques such as adaptive re-meshing, overset grids or immersed boundary methods are required (see section 4.4.1 for more detail). Each of these have their own drawbacks, such as the additional computational cost of repeatedly re-meshing and transferring data from one mesh to another, or the reduced boundary layer detail associated with immersed boundary methods.

Secondly, fully resolving the flow over a hand will have a large impact on the time step required for the simulation. It has been estimated in chapter 4.4.1 that a full arm simulation would require a minimum cell size at least 2-3 times smaller than that required for the body. To maintain numerical stability the time step would need to be reduced by the same amount. When you include the increased mesh size needed to resolve the arm, it is easy to see how computationally expensive full body simulations are likely to be compared to passive simulations.

The additional computational cost and complexity associated with full body freestyle simulations is perfectly justified to fully assess both the resistance and the propulsive forces acting on a freestyle swimmer. Indeed, the insight that this type of analysis can provide will be invaluable although the computational cost is likely to limit its use to a very small number of applications. However for the purpose of providing insight into how the resistance varies during freestyle, it is not the flow detail around the arms that is required so much as the impact the arms have on the flow over the rest of the body. Therefore if the impact the swimmer's arms have on the fluid flow could be simulated through the use of a body-force model, without fully resolving the arm geometry, a significant computational saving could be made. This would still enable the aims of the research to be met. Such a methodology could then be used to provide active freestyle analysis for a greater range of applications focussing on minimising a swimmer's resistance, such as swimsuit design and body shape investigations.

The application of a naval architecture base methodology for breaking down and analysing the self-propelled resistance has clear benefits. It also allows some of the experience in CFD simulations of this type to be utilised in this work. With this in mind an initial study was conducted at the beginning of this research project applying a similar methodology to a container ship hull. This resulted in a combined submission, with the industrial partner QinetiQ, to *Gothenburg 2010: A workshop on numerical ship hydrodynamics* (Banks et al., 2010). This work provided experience in free surface simulations and the application of propeller body-force models. It also highlighted the benefit of detailed validation cases with which to compare simulated results. The submitted paper outlining the work conducted is provided in Appendix 1.

1.3 Thesis structure

Chapter 2 provides a review of the previous CFD research conducted on swimming. This establishes what has already been achieved in this area and provides a critical review of the methods used and the analysis conducted. This identifies several key areas that need further research in the field of freestyle resistance and highlights the need for methods to be validated against experimental data.

A brief overview of the experimental testing program conducted with British Swimming is provided at the beginning of Chapter 3. This details the experimental systems and their capabilities, before providing detailed descriptions of the passive and propelled experimental test cases that are later replicated using CFD. The experimental data along with video screen shots of these cases are presented, allowing key flow features to be identified and discussed to illustrate the complexity of the flow.

Based on the experimental test cases Chapter 4 provides a summary of the challenges faced when attempting to accurately capture the identified flow features using CFD. A background of the implemented Reynolds averaged Navier-Stokes (RANS) methodology is provided which presents justifications for some of the decisions made, whilst highlighting some of the known limitations of these methods.

Chapter 5 describes the development of the free surface RANS methodology, presenting studies investigating boundary layer modelling techniques, free surface mesh requirements and a global mesh sensitivity study that establishes the magnitude of the grid based errors. This chapter concludes with a final mesh structure that can then be applied to the different experimental cases.

Chapter 6 presents the analysis of the passive resistance components for a swimmer on the free-surface for two separate test cases. In both cases comparisons are made to the experimental test cases to provide validation of the simulated results. A detailed assessment of the free surface interaction with the other resistance components is provided.

Chapter 7 describes the separate development of a generic body-force model capable of simulating the impact a swimmer’s arm has on the fluid flow. The forces on the arm are estimated using a blade element approach and applied as momentum sources within the solution domain. A validation case is presented which replicates experimental data for a rotating kayak paddle. A detailed analysis is then provided of the forces generated by the body-force model based on experimental arm kinematics.

Chapter 8 describes a propelled freestyle analysis of the impact the swimmer’s arms have on the fluid flow and resistance components. This was achieved by combining the free surface RANS methodology used in chapter 6 with the body-force representation of the arm. An assessment is made of the fluid flow features and the resulting resistance force at key times within the stroke, with comparisons made to experimental data.

Chapter 9 summarises the thesis conclusions and contributions. The outcomes are compared to the research objectives and future work in this field is discussed.

1.4 Novel Contributions

New contributions have been made in the following areas:

- A detailed breakdown of the passive free surface resistance components for swimmers is provided. This includes independent measurements of the wave resistance.
- A detailed analysis of how the free surface interacts with the flow around a swimmer is provided. This has highlighted the significant changes to the flow regime observed on the body due to the free surface.
- A generic body-force model has been developed capable of simulating any freestyle stroke path based on arm kinematic data. This implements a propulsive domain than can move anywhere within a static mesh allowing complex propulsive mechanisms to be simulated efficiently.
- The impact the arm has on the active resistance of a freestyle swimmer has been quantified.

Publications that have been made based on this and relevant previous research include:

a) Banks, J., Phillips, A. B., Turnock, S. R., Hudson, D. A., & Taunton, D. J. (2013). **Kayak blade-hull interactions: A Body-Force approach for self-propelled simulations.** Proceedings of the Institution of Mechanical Engineers, Part P, Journal of Sports Engineering and Technology. (Accepted for publication on 14/05/13)

b) Banks, J, Phillips, A. B., Turnock, S. R., & Hudson, D. A. (2011). **Performing self propelled simulations of a kayak , using a Body-**

force paddle model. In D. A. Turnock, S.R., Bertram, V., Hudson (Ed.), Proceedings of the 14th Numerical Towing Tank Symposium (pp. 71–76). Poole, UK.

c) Banks, J., Phillips, A. B., Bull, P.W., Turnock, S. R. (2010) **RANS simulations of the multiphase flow around the KCS hullform**, Proceedings of Gothenburg 2010 – A Workshop on CFD in Ship Hydrodynamics, Gothenberg.

d) Banks, J., Phillips, A. B., Turnock, S. R. (2010) **Free-surface CFD Prediction of Components of Ship Resistance for KCS**, 13th Numerical Towing Tank Symposium, Duisburg, Germany.

e) Turnock, S.R., Lewis, S.G., Phillips, A.B., Banks, J., Winden, B., Hudson, D.A. and Molland, A.F. (2010) **Evaluating the self propulsion of a container ship in a seastate using Computational Fluid Dynamics**, William Froude Conference: Advances in Theoretical and Applied Hydrodynamics - Past And Future, Portsmouth, UK.

f) Turnock, S.R., Phillips, A.B., Banks, J., Nicholls-Lee, R., (2011) **Modelling tidal current turbine wakes using a coupled RANS-BEMT approach as a tool for analysing power capture of arrays of turbines**, Ocean Engineering, V38 11-12, p1300-1307.

g) Webb, A.P., Banks, J., Phillips, C., Hudson, D.A. Taunton and Turnock, S.R. (2011) **Prediction of passive and active drag in swimming.** 5th APCST. Melborne.

2. Literature Review

Before describing the numerical methods and test cases used to complete the aims and objectives it is important to review the relevant research that has preceded this work. A brief review is provided of some of the experimental methods which have been used to investigate resistance and propulsion. These highlight some of the advantages of performing CFD analysis. A thorough assessment of the previous CFD research conducted in swimming is then presented, providing critical analysis and identifying areas where more research is required.

2.1 Computational Vs Experimental fluid dynamics

Traditionally, academic research in swimming has focused on experimental and theoretical studies that endeavour to understand how the propulsive forces are generated from the arms, and the components of drag that make up the resistance (Toussaint & Truijens, 2005).

An over view of how the arms generate propulsion in free style swimming is provided by Toussaint et al (Toussaint & Truijens, 2005). Some of the key points presented in this paper will be summarised here. The thrust generated by the arm used to be thought of as purely drag based, however the dominant view now is that the hand acts as a hydrofoil generating both lift and drag. This view is backed up by previous experimental studies of model hands at varying angles of attack and quasi-steady analysis of stroke paths. The relative magnitudes of the lift and drag forces generated depend on the orientation of the hand in the flow and the shape it forms. Therefore changes in hand curvature and finger spacing can change the thrust produced. It is acknowledged, however, that the flow field around a freestyle swimmers arm is far from steady. The complex stroke paths adopted by modern freestyle swimmers involve significant lateral motion of the hand as it moves backwards through the water. This causes the velocity and angle of attack to vary significantly throughout the stroke. Complex three dimensional (3D) flows develop due to the arm rotation inducing a radial flow from the shoulder to fingers. This has been observed experimentally though local pressure readings and flow visualisation using tufts. This radial flow is thought to enhance the pressure difference over the hand increasing the thrust generated. These complex flow features will all influence the propulsion generated by the arms however it is difficult to know to what extent due to the inability to measure the forces acting on a swimmers arm.

Measuring the passive drag of a swimmer (the resistance caused by a static swimmer moving through the water) can easily be measured using a tow system or a flume (Vennell et al., 2006). However the active drag, or propelled resistance (the resistance experienced by a swimmer whilst swimming) and the propulsive forces are difficult to measure without affecting the swimmers stroke (Webb et al., 2011). Unfortunately it is precisely these active swimming forces that need to be understood to allow performance gains to be made. The two principal methods for measuring active drag are the MAD system and the velocity perturbation method (Toussaint & Truijens, 2005). The MAD system measures the propulsive force from the arms through the use of instrumented paddles, fixed underwater. The swimmer places their hand against a paddle during their arm stroke, allowing them to push against these rather than the water. The active drag is then assumed to be equal to the mean propulsive force measured over all the paddles. The velocity perturbation method uses the difference between a swimmer’s free swimming speed and the speed achieved when towing an object of a known resistance, to determine the active drag based on the assumption that the delivered power of the swimmer remains the same. Both these methods are described in more detail in (Toussaint & Truijens, 2005). The problem with both systems is that to enable forces to be measured the stroke technique has to be altered, which will ultimately change the forces produced.

Computational Fluid Dynamics (CFD) can recreate the flow conditions in a numerical model rather than trying to experimentally measure the complex flow features around a swimmer. The simulation domain around the swimmer is split up into small cells creating a mesh. The Reynolds Averaged Navier-Stokes (RANS) equations are then iteratively solved for each cell, providing a numerical solution to the fluid flow around a moving swimmer. More detailed information regarding CFD is provided later in Chapter 4.

The advantage of numerical techniques such as CFD is that once the local flow is correctly simulated it is possible to obtain detailed information about a complicated flow without impacting on it. This information about the local flow cannot be obtained experimentally. For instance, if you can perform a simulation of active swimming it is then easy to determine where the propulsive and resistive forces are coming from. This provides much greater insight to where performance increases might be made. This allows you to make alterations to the stroke technique and accurately identify what impact it has on the different components of force.

2.2 Previous CFD research in swimming

A critical review of the previous CFD research in swimming is presented in three sections. The first concerns the simulations investigating arm propulsion alone; the second the passive resistance simulations and the third active simulations of swimming. A summary of the implications of this previous work for this current research is then provided.

2.2.1 Arm propulsion

The first example of CFD being used to investigate swimming was (Bixler & Schloder, 1996) who used simulations of a hand sized disk accelerating within water to predict the thrust from the hand. A more realistic simulation was conducted by the same authors (Bixler & Riewald, 2002) when they performed 3D steady-state RANS simulations of a hand and forearm at varying flow speeds and angles of attack. These simulations were validated against several different sets of experimental data showing good correlation. However, due to the steady state methodology, this study failed to establish the impact of the unsteady flow regime actually found around a swimmer's hand as it accelerates through a stroke path.

The potential impact of an unsteady flow was revealed by two dimensional (2D) simulations of an accelerating hand and forearm by (Rouboa, Silva, Leal, Rocha, & Alves, 2006). They found that the drag force while accelerating was increased by as much as 24% compared to the same steady-state velocity.

A more complete analysis of the propulsive forces generated by a hand was provided by (Sato & Hino, 2003). Initially steady state and constant acceleration drag coefficients for a hand and forearm were validated using experimental data. They also confirmed the importance of unsteady simulations by plotting drag coefficients for varying constant accelerations. Then, by rotating and translating a rigid mesh containing a single hand, they were able to simulate an actual stroke path of a freestyle swimmer taken from video footage analysis. This simple methodology allowed the unsteady direction and velocity of a real stroke to be analysed without the need for computationally expensive mesh deformation or re-meshing. However this technique is limited to analysis of just a single hand due to the rigid nature of the grid.

Other three dimensional (3D) studies looking at the hand and arm have used steady-state CFD methods to optimise finger spacing for maximum propulsive force (Marinho et al., 2010; Minetti, Machtsiras, & Masters, 2009). Both studies found moderate finger spacing produced the largest drag force on the hand, resulting in increased thrust. This is due to the boundary layer growth preventing flow between the fingers for small or moderate spacing, increasing the effective projected area.

These hand and arm simulations indicate the potential value of CFD methods to allow greater understanding of a swimmer's arm technique. They also provide an insight to the complexity and computational cost of simulating just the hand or arm by itself. This is helpful when considering the advantages and disadvantages of including the arms in propelled freestyle simulations.

2.2.2 Passive resistance

Alongside studies seeking to understand the propulsive power of the arms, CFD methodologies have also been applied to modelling the resistance of a swimmer. Most notably (Bixler et al., 2007) simulated the passive drag of a fully submerged swimmer in a streamlined glide position. The athlete geometry was obtained by laser scanning and both the athlete and a mannequin, made from the scan, were tested in a water flume to provide validation data. The CFD results and the mannequin data were within 4% of each other; this establishes the ability of CFD to accurately simulate the flow around a swimmer's geometry. However the resistance of the athlete within the flume was significantly higher than the mannequin, which was attributed to an inability to hold a consistent body position, differences in hand position due to the athlete holding a handle whilst in the flume, and potential differences in surface roughness.

A comparison of the two fully submerged glide positions adopted by breaststrokers in their underwater phase was conducted by (Marinho et al., 2009). This compared CFD simulations of the typical prone (or streamlined) glide position (arms out stretched ahead of the swimmer) with the arms by the swimmer's side (such as adopted after a breaststroke pull-down). The breakdown of resistance into frictional and pressure drag is provided for two body positions over a range of velocities. A significant increase in drag coefficient was demonstrated when the arms were placed by the athlete's side, however no experimental comparison is provided with which to compare.

Lower fidelity 2D passive drag simulations have included studies looking at the influence of head position on resistance (Zaïdi, Taïar, Fohanno, & Polidori, 2008) and the potential drag reduction due to drafting behind another swimmer (Silva, Rouboa, Moreira, Reis, & Alves, 2008). These studies provide a useful insight into how the use of CFD might benefit the sport, however the lack of 3D effects, or in the case of the drafting study a free surface or adequate mesh refinement, means that the results should be considered with caution.

A more recent study of passive drag looked at the effect of water depth during the glide phase of a race (Novais et al., 2012). Using a simulated swimming pool of 2m depth the impact of the free-surface on passive drag was assessed for a variety of different depths. The presence of wave resistance is seen as an increase in drag as the swimmer approaches the surface of the water, however nothing more than total resistance is provided to give insight into how the free surface is affecting the resistance components. There is also a lack of detail about the mesh structure and free surface methodology adopted. The author does claim a total mesh size of 900 million cells although this seems improbable. Therefore with no free surface visualisations or comparison to experimental data it is difficult to judge the quality of these simulations.

The most comprehensive CFD study into passive resistance near the free surface was conducted on a swimmer's geometry in a prone glide position at several depths near the surface (Sato & Hino, 2010). A detailed description of the implemented numerical methodology and mesh structure is provided. A comprehensive assessment of the flow characteristics around the swimmer's geometry, both deeply submerged and near the surface, provides much greater insight into the complex flow field than in any other presented research. An estimate of the coefficient of wave resistance is calculated as the difference in total resistance between the surface and deeply submerged cases. A clear interaction between the free-surface and the flow features observed on the surface of the body is identified. This appears to indicate that understanding the interaction of the free surface with resistance will be more complicated than simply adding a wave resistance component to that of a deeply submerged case. Unfortunately no experimental data for the simulated conditions is presented as a comparison. Further analysis and validation of free-surface interactions was identified as a key area of research for the future.

The majority of passive resistance analysis conducted to date focuses entirely on mean force without looking into the details of the flow characteristics. The analysis by (Sato & Hino, 2010) provides much greater depth and insight, however the free-surface analysis is conducted for a streamlined glide position. This is very different to the position adopted by swimmers during surface swimming. The general lack of CFD studies into how the free surface affects the passive resistance is noted in a review of previous research in this area (Marinho, Barbosa, Kjendlie, et al., 2012). It is clear that the flow around a swimmer's body is extremely complex with the free-surface likely to interact with all the resistance components. This makes the commonly adopted assumption that wave resistance can be determined from comparing surface and deeply submerged total resistances appear overly simplistic.

2.2.3 Full body or active swimming simulations

The independent study of passive drag and thrust has the potential to provide significant benefits to swimming performance. However the most notable impact that CFD could provide is enabling all the forces in active swimming to be investigated. This is impossible to do experimentally without impacting on the stroke itself.

The first example of an active swimming simulation was an underwater fly kick model that replicated a swimmer's geometry and motion through use of a laser scanner and manually digitized video footage, obtained at the Australian Institute of Sport (AIS) (Lyttle, A. & Keys, 2006). The body motion was split into discrete time steps and the flow resolved at each stage before moving on to the next. The body movement was captured by user defined functions and domain re-meshing with the result from the previous time step used as an initial condition for the next (Lyttle & Keys, 2004). The terminology used by the authors suggests a quasi-steady analysis of the motion which would be unable to capture the unsteady flow field that develops during underwater fly kick. However the results presented show propulsion generated from the motion which would not occur within a truly quasi-steady simulation, therefore it is assumed that an unsteady time accurate methodology is used, although this is not explicitly stated. To what extent the velocity of the boundaries is included is also not clear. Steady state validation of the CFD methodology was quoted as being within two SD of experimental passive data in a static glide position, however no active swimming comparison is given. This methodology was then used to compare two different styles of fly kick performed by an athlete, varying amplitude and frequency along with a study looking at the effects of ankle flexibility. This work highlights the potential benefits of CFD analysis being used to investigate both the resistance and the propulsion acting on a swimmer, however there is very little detail provided for the adopted numerical methods. For instance there is the obvious drawback of the constant re-meshing required to simulate the body motion but the computational cost of this is not provided.

More recently a fully unsteady underwater fly kick simulation was performed using an immersed boundary method (Von Loebbecke et al., 2009). A similar process of body scanning and video digitisation was used to obtain the geometry and motion, while interpolation was used to provide simulation geometries for the 1000 time steps used to simulate a single fly kick cycle. The immersed boundary method takes account of the geometry's velocity and acceleration within the surface boundary condition making the simulation fully unsteady. This method has the advantage of requiring no mesh movement or adaptations; however it does prevent the increase in mesh density near the geometry's surface. It is likely that this will impede the accurate modelling of the boundary layer growth although as no near wall mesh data is provided it is difficult to assess its impact. The results obtained are validated to some degree by the development of a vortex ring during the down kick which was experimentally measured by (Miwa, Matsuuchi, Shintani, Kamata, & Nomura,

2006) and, to a lesser extent, through comparison with flow visualisation from entrained bubbles in video footage. The study then goes on to provide a detailed analysis of the developed flow field produced by both a male and female swimmer's stroke kinematics.

A more comprehensive study of the effect of varying velocity and stroke frequency on underwater fly-kick was conducted by (Cohen, Cleary, & Mason, 2012). In this work a smooth particle hydrodynamics (SPH) methodology was used, removing the need for a computational mesh. This makes implementing complex body motions simpler. These methods are in their infancy compared to finite volume methods but have been shown to have advantages for simulating inertial and free surface flows. Unfortunately their ability to simulate complex viscous boundary layers is limited due to their inability to resolve the flow down the scales required in this region. This means that caution over the resistance values reported using these methods should be applied. This being said, interesting insight is provided into the key parameters that govern the propulsive forces generated by this swimming technique. A reasonable agreement is also claimed to previous studies in this area.

To date only one group has published simulations for the full body stroke of an athlete swimming on the water's surface (Honda et al., 2012; Keys,M. et al., 2010). In these two conference papers the results are presented for CFD analysis of stroke kinematics of a sprint freestyle world record holder. Very little detail is provided about the numerical method used but it is assumed that similar techniques as the author's previous work (Lyttle, A. & Keys, 2006) were adopted. This would suggest that re-meshing was used to provide movement of the geometry. It is unclear, however, to what extent the potentially quasi-static approach previously alluded to was used. The first study provides a net force trace throughout a single stroke cycle and a breakdown of the average forces acting on different body parts over a stroke cycle (Keys,M. et al., 2010). More recently an assessment of the potential impact of this work is provided along with a more detailed breakdown of the net force trace into phases of the stroke. This type of analysis allows the unsteady forces acting on the body to be assessed for the first time. The outcomes of this research were clearly stated as an increased technical understanding of net thrust production in freestyle technique, however the analysis presented in these conference papers is extremely limited considering the complexity of the simulations conducted. Unfortunately no detail is provided about the free-surface interactions or flow features that develop around a free-style swimmer and no comparisons are made to any experimental data. This lack of any attempt to validate the freestyle methodology is disappointing and should lead to a degree of caution regarding the presented data.

2.3 Conclusion

It would be reasonable to make a general criticism about many of the swimming CFD publications; that there is a lack of adequate description of applied numerical methods and, in particular, details of mesh structure and quality are not provided. This can make it difficult to assess the quality of the work, particularly if no experimental comparison is provided.

Regarding the passive resistance simulations, free-surface interaction has been identified as an area requiring greater investigation. In particular there is a complete lack of validation between simulated and experimental free-surface flow features, or generated wave patterns. The current analysis of passive resistance components on the free-surface would benefit from a greater understanding of the wave resistance and its interaction with the skin friction and form drag. In general, a greater understanding of the complex flow features observed around a swimmer on the free-surface is needed to understand what influences the resistance acting on a freestyle swimmer.

A general failing of the full-body swimming simulations appears to be that no direct comparisons are made to experimental data to provide validation of the different methods used. However it is clear that the capability of swimming CFD has developed dramatically in recent years, allowing the first simulations of active drag to be performed for an entire swimmer. This will have significant implications for the sport as it allows swimsuit designs, body position and stroke technique to be optimised for the unsteady free surface flow usually found around a swimmer. However, to be able to utilise this capability tools will be required to be computationally efficient, otherwise they become impractical to use. Indeed (Honda et al., 2012) stated that the main difficulty associated with these type of simulations is the labour and computational cost.

However, as many of the published studies fail to detail the computational cost associated with the simulations, the extent of the problem is difficult to assess.

To understand how to reduce the resistance of a free style swimmer more detail is required to identify which aspects of the complex unsteady problem need to be included. For example it needs to be determined whether the impact the arms have on the fluid flow need to be included in the assessment of potential resistance gains or whether passive simulations should be used. The full body freestyle simulation methods have the capability to assess these questions, albeit at a significant computational cost, yet this type of detailed analysis has not yet been presented. Indeed there is a distinct lack of detailed analysis presented on the full freestyle simulation, indicating that the wider swimming community has yet to benefit from these developments.

This review of the previous research conducted using CFD in swimming has highlighted the need to understand the free surface interactions and the impact the arms have on the resistance forces acting on a swimmer. This has helped form the aims and objectives of this research. It is important to stress once again, however, that CFD analysis of these complex flows can only provide reliable insight if an effort is made to validate the numerical methods against experimental data. Therefore before presenting the numerical methods adopted to achieve the aims and objectives of this research an overview of the experimental test cases used in this work will be presented.

3. Experimental test cases

The importance of providing a comparison between simulated and experimental results has already been discussed. The involvement in a wider experimental research program (SwimSIM) provided the opportunity to obtain experimental validation cases in two different ways. Firstly the testing program conducted with British swimming provided a large number of experimental conditions with different elite athletes. However all of these tests were conducted with a specific objective relating to the athletes performance, rather than providing a detailed validation case for CFD simulations. In contrast to this the experimental tools used in the SwinSIM project also allowed specific experimental test cases to be designed and conducted for this research. This approach has the advantage providing greater control over the experiment and the data acquired however the athletes used in this process were at a non-elite level. A combination of these two approaches provided a series of experimental test cases that replicate the different stages of analysis required to achieve the research aims and objectives.

Before providing details of the different cases used, a brief overview of the SwimSIM project is provided to give an indication of its breadth and scale. The tools and insight that have been developed through involvement in this work is also discussed.

3.1 Project SwimSIM

Project SwimSIM is the wider project sponsored by UK Sport and working with British Swimming, with the aim to increase the race performance of podium potential swimmers. The project has three PhD students, each focusing on a specific area of swimming research. In addition to this thesis the two other PhD projects are:

1. Phillips, C., 2013 ‘Musculoskeletal Modelling of Human Swimming for Technique and Performance Evaluation’.
2. Webb, A.P., 2013 ‘Identifying race time benefits of best practice in freestyle using simulation’.

All three PhD students have collaborated to develop equipment and testing methods to analyse the hydrodynamic performance of swimmers. The equipment developed, all being portable, includes: a tow system to measure swimming resistance over a range of speeds; a speed measurement system that measures the speed of a thin line attached to the swimmer; wave elevation measurement and a sensor network, which measures three-dimensional body kinematics. Data acquired from these systems is synchronised with video footage of the swimmer and presented back to the athlete on poolside. This system has provided both a research tool to support the PhD projects and also a rich learning environment for athletes and coaches.

This system has been developed over three years in conjunction with British Swimming. A key member of project SwimSIM was Jonty Skinner, who was appointed as technical advisor to British Swimming for 2009-2012. As an ex world record holder (100 m freestyle, 1976) and a coaching specialist, his involvement has bridged the gap between the engineering data and the improvement of swimming technique.

In total project SwimSIM has tested 103 participants over 1725 measurement runs, requiring 90 days of pool testing. This included 16 separate test sessions at different locations for British Swimming totalling 37 days. This resulted in 90 % of the London 2012 Olympic swimming team having their technique analysed.

Not all work conducted by SwimSIM has contributed directly to the aims of this study; however this involvement with British Swimming has provided scope for the vast testing program. Therefore equipment, testing procedures and improved knowledge of swimming hydrodynamics have been gained in addition.

Alongside the time devoted to experimental testing a significant input was required to develop the different experimental systems at the beginning of this PhD project. This included the design and construction of an in-line tension meter that measured the experimental force in the towline, a speed reel and mounting system and a moving camera buggy allowing underwater footage of the swimmer to be captured.

Ethical approval has been provided by the ethics committee of the Faculty of Engineering and the Environment (Approval Number: RGO7207). This covers the measurements conducted on swimmers, the acquisition of film and still photography and both the storage and sharing of data with British Swimming.

3.2 Experimental Method

The experimental test cases that are presented in this work were all conducted using the equipment and procedure developed as part of the SwimSIM project. They key components of the experimental set up used in this work are the instrumented tow system, the wave probe array and the moving camera system. The development of these systems was not part of the research presented in this thesis but a brief description of their capabilities and limitations is required.

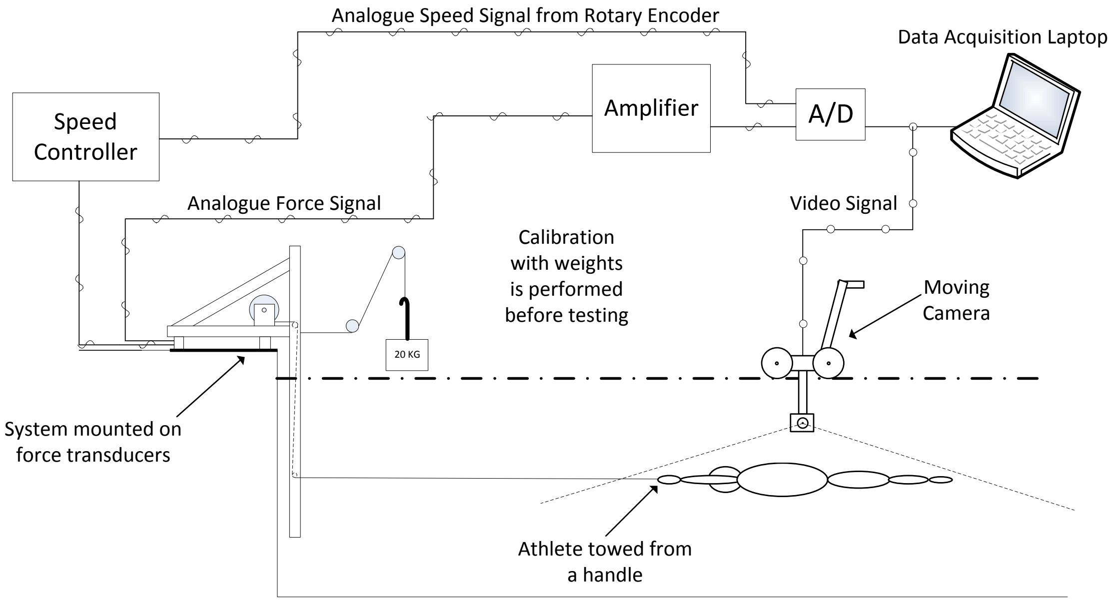

Figure 3-1 - Experimental set up (Webb, 2013)

The Instrumented tow system allows the swimmer to be pulled along the pool at a constant speed whilst the tow force is measured using three force blocks. The magnitude of the measured force is calibrated at the beginning of each session by applying a known force to the system. A moving camera allows a synchronised video feed to be acquired at the same time. A schematic of the generic experimental procedure and data acquisition system can be seen in figure 3-1. In all the test cases presented here the swimmer is attached to the tow line using a belt around their waist. This is necessary to allow the athlete to adopt realistic passive swimming positions or perform active swimming cases. However this non rigid connection to the tow system has the disadvantage of potentially affecting the instantaneous force measured by the system during unsteady active test cases. As the tow force varies the belt and swimmer deform reducing the magnitude of the force variation about the mean. More detail on the design and construction of the tow and data acquisition systems can be found in the other SwimSIM PhD theses (C. Phillips, 2013; Webb, 2013).

The synchronised video footage is used to determine the athlete's position in the water as it is impossible to physically measure this data through the tow line connection. This allows the body attitude and shape to be captured whilst swimming however doesn't currently allow accurate measurements of the body's depth in the water.

3.3 Passive test cases

Before a full self-propelled analysis of a swimmer could be conducted it was important to investigate the passive resistance components. However, as the ultimate aim was to simulate freestyle swimming, the passive cases needed to be as similar to freestyle as possible. To achieve this the athletes were towed on the surface of the water with their arms placed by their sides in an attempt to minimise the arm's impact on the flow. This is to provide a clean flow of water onto the head and shoulders of the athlete. It is hypothesised that this better represents the flow in freestyle than the traditional streamlined glide position simulated in (Sato & Hino, 2010), which is only used after a start or turn.

Before presenting the different test cases used it is helpful to define a few flow parameters which will be used to categorise the different cases.

Reynolds number

In a viscous flow the Reynolds number can be calculated as;

$$Re = \frac{UL}{\nu} \qquad 3\text{-}1$$

where U is the velocity, L is a reference length and v is the kinematic viscosity. The Reynolds number provides the ratio of the inertial forces to the viscous forces and therefore can be used to characterise the flow regime in terms of the impact of viscosity.

At low Reynolds numbers (typically below a critical Reynolds number of approximately 2 x10^3) the viscous forces dominate, damping out disturbances in the flow, producing laminar flow conditions. At high Reynolds numbers (typically $Re > 10^4$) the inertial forces dominate, creating unsteady eddies which cause turbulent fluctuation in flow velocity.

Froude Number

For free surface flows the Froude number can be calculated as:

$$Fn = \frac{U}{\sqrt{gL}} \qquad \text{3-2}$$

where g is the acceleration due to gravity, defining the velocity in terms of the wave pattern generated. As the Froude number increases so does the length of the waves generated. For a ship the reference length is defined as the water line length. This value is more difficult to define for a semi-submerged swimmer, in this study the reference length has been taken as the total length of the body (from head to toes). However it is acknowledged that this is likely to overestimate the Froude number.

The fundamental wave length can then be calculated based on the Froude number as;

$$\lambda_0 = 2\pi Fn^2 L. \qquad \text{3-3}$$

In the following section three different passive cases are presented. The first two are the primary cases providing two different body positions on the free surface. These two were selected because of the different flow features that develop around the bodies due to changes in speed and body position. Broadly speaking they represent the two extremes of free surface flows that can be observed around freestyle swimmers.

The third case is used to provide insight into the resistance for the active test case presented later. However this is not replicated using CFD.

3.3.1 Case N003 – head in line

The first passive test case was not specifically designed as part of this research but was taken from a previous study conducted as part of project SwimSIM. A series of tows were conducted with an elite level swimmer (Athlete N) near the free surface while the effects of changes in body position on resistance were investigated. The tow which best represented the athletes' freestyle body position (head in-line with the rest of her torso and close to the free surface) was chosen as an experimental validation case. A tow speed of 1.86 ms^{-1} was chosen as this was similar to her surface sprint speed, providing a Froude number of 0.43. Other key test case parameters are presented in table 3-1.

Table 3-1 –Experimental parameters for case N003

Length L (m)	1.86
Mean velocity V (ms^{-1})	1.86
Reynolds number Rn	3.46 x10^{6}
Froude number Fn	0.43
Fundamental wavelength λ_0 (m)	2.16
Estimated depth of athlete below the undisturbed free surface* (m)	0.17
Athlete height (m)	1.71
Athlete mass (kg)	62

*measured from the hip joint or groin

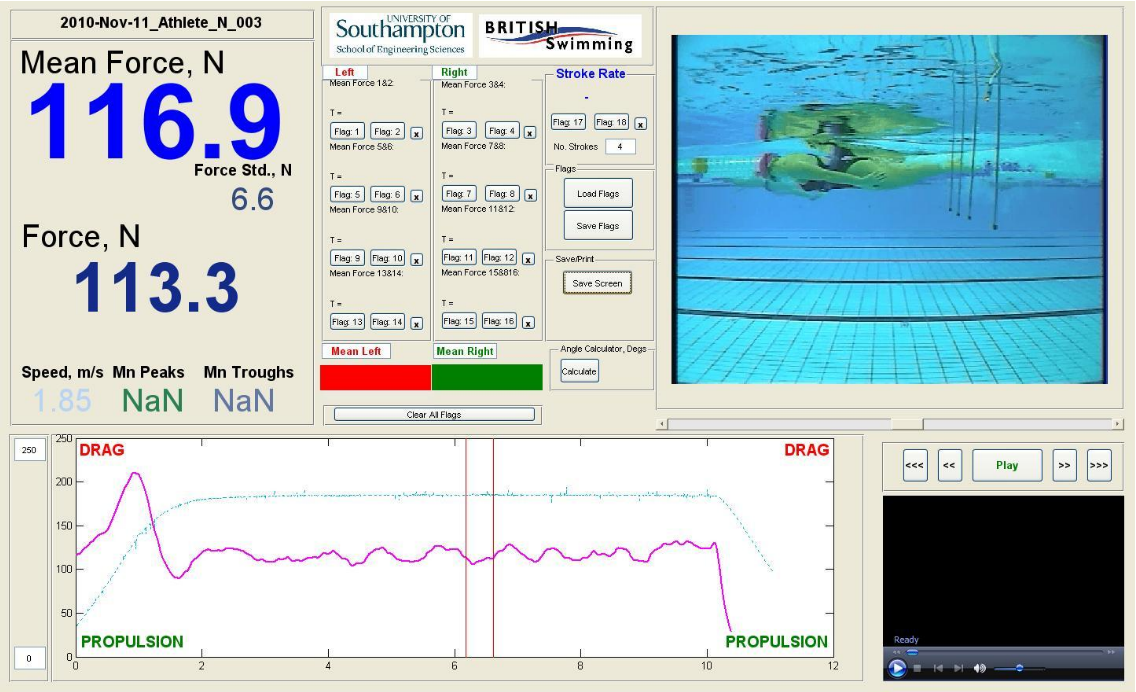

2010-Nov-11_Athlete_N_003

Mean Force, N 116.9

Force Std., N 6.6

Force, N 113.3

Speed, m/s 1.85

Mn Peaks NaN

Mn Troughs NaN

No. Strokes 4

Figure 3-2 – Speed and force traces for case N003 (head in-line), in blue and pink respectively. The mean tow force is presented in the top left of the SwimSIM feedback GUI.

The mean resistance was measured as 116.9 N (for details of the experimental uncertainty see (Webb, 2013)). Underwater footage was taken of this case along with longitudinal wave cuts at distances of 1.75, 2, 2.25 and 2.5 m from the athlete centreline. The force and speed traces, along with the mean values, can be seen in

figure 3-2, as presented to the athlete in the feedback GUI.

A comparison of the depth and attitude of the athlete while being passively towed compared to active swimming is provided in figure 3-3. Despite attempting to adopt the same posture a distinct difference in attitude is observed, although the depth at the hip appears to be the same. The lower head and shoulder position in the passive tow caused more water to flow up and over the head and shoulders before breaking over the legs. This deviation from the natural swimming position is due to the lack of lift, or vertical force normally generated as part of the propulsive stroke. However it can be observed that there are distinct similarities between the wave systems in each case.

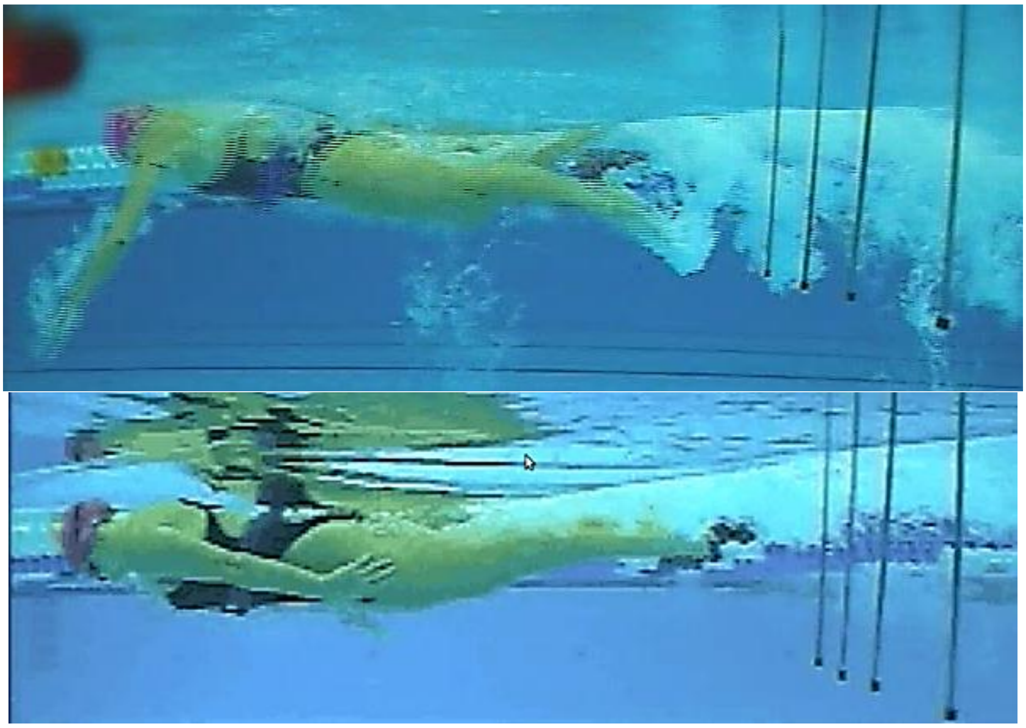

Figure 3-3- Comparison of Athlete N's depth and attitude whilst swimming (top) and whilst passively towed in case N003 (bottom)

Some of the key flow features observed in the passive case are identified below:

- the free surface remains smooth as it flows up and over the head and shoulders;
- a wave trough, or hollow, forms around the hips and thighs;
- a breaking wave forms over the legs generating an unsteady turbulent wake behind the swimmer.

The experimental wave cuts, measured from the four wave probes observed in figure 3-3, are presented in figure 3-4.

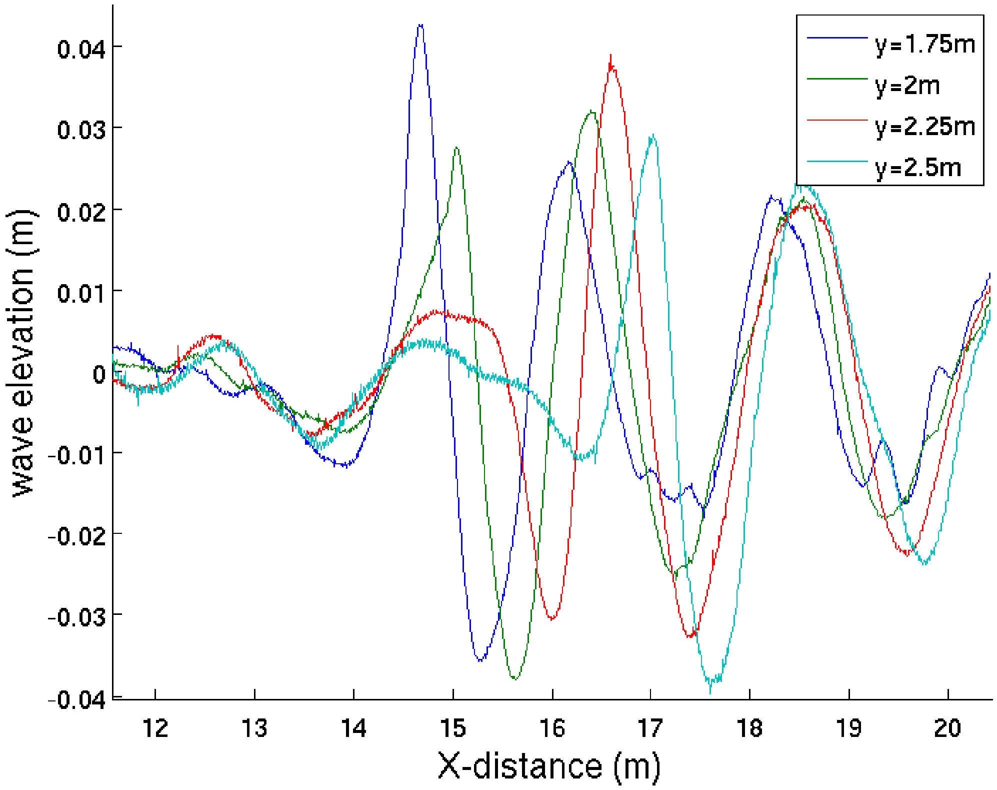

Figure 3-4 – Experimental wave cuts measured at different lateral spacings from the centreline for the passive case N003 (head in-line).

3.3.2 Case DA003 – head up

All of the remaining experimental test cases were specifically designed and conducted as part of the research presented in this thesis. The existing experimental method from project SwimSIM was used but the objective of these tests was to provide validation cases for different aspects of free style swimming.

The second passive case was conducted with a non-elite swimmer (Athlete DA) with the aim of better replicating the active freestyle body position during a passively towed case. In an attempt to force the body to sit higher in the water a pull-buoy (float) was placed between the athlete’s legs and the head was tilted back so that they were looking down the pool (see figure 3-5). The tow speed of 1.37 ms^{-1} was based on the free swimming speed of the athlete and was significantly less than that used in N003. The mean resistance was measured as 64.7N. Both above and underwater footage was taken of this case along with wave cuts at six different locations (1, 1.25, 1.5, 1.75, 2 and 2.25 m from the athlete centreline). The force trace, along with the mean value, can be seen in figure 3-5, as presented to the athlete using the SwimSIM feedback GUI.

Table 3-2 –Experimental parameters for case DA003

Length *L* (m)	1.86
Mean velocity *V* (ms^{-1})	1.37
Reynolds number *Rn*	2.55 x10^{6}
Froude number *Fn*	0.32
Fundamental wavelength λ_0 (m)	1.2
Estimated depth of athlete below the undisturbed free surface* (m)	0.17
Athlete height (m)	1.71
Athlete mass (kg)	62

*measured from the hip joint or groin

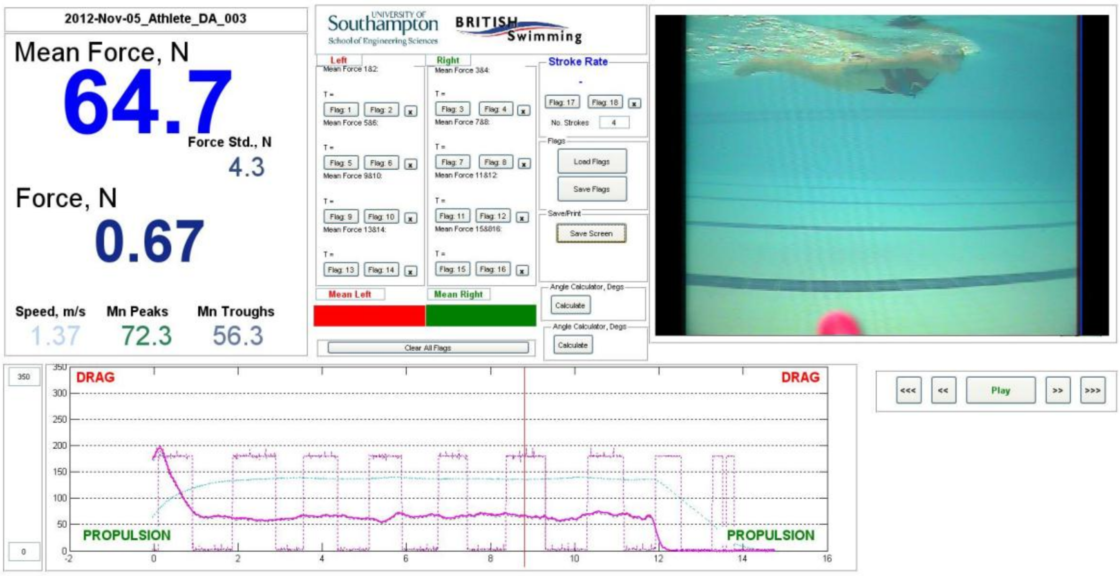

2012-Nov-05_Athlete_DA_003

Mean Force, N 64.7

Force Std., N 4.3

Force, N 0.67

Speed, m/s 1.37

Mn Peaks 72.3

Mn Troughs 56.3

No. Strokes 4

Figure 3-5 - SwimSIM feedback GUI for case DA003 (head up), with the force trace shown as a solid pink line at the bottom and the mean force presented in the top left.

A comparison of the depth and attitude of the athlete while being passively towed compared to active swimming is provided in figure 3-6. The passively towed position is a closer representation of the athlete DA's swimming position. The high head and shoulders adopted in the passive tow generate significantly different flow features compared to case N003 (head in-line).

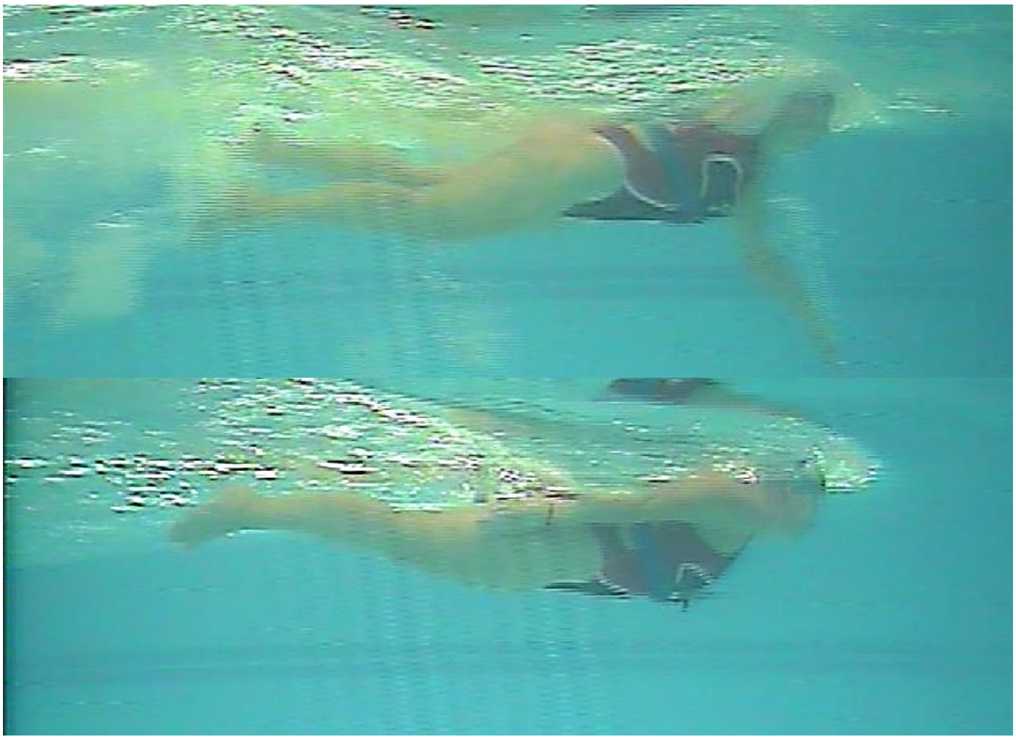

Figure 3-6 - Comparison of Athlete DA's depth and attitude whist swimming (top) and whilst passively towed in case DA003 (bottom).

From observing the underwater video footage and the surface footage (seen in figure 3-7) the following key flow features can be identified for the passive tow case:

- a bluff body breaking wave develops around the head;
- a large wave trough is formed around the torso, with the back partly submerged;
- a breaking wave that forms at the hips;
- a turbulent wake is observed around the legs.

The formation of the breaking wave at the hips (further forward than in case N003) could be due to the reduction in Froude number in this case (0.32 compared to 0.43 for N003). However the differences in body and head position are so significant that these could be dominating the changes in flow observed. The experimental wave cuts are presented in figure 3-8.

Figure 3-7 - Above water footage of case DA003

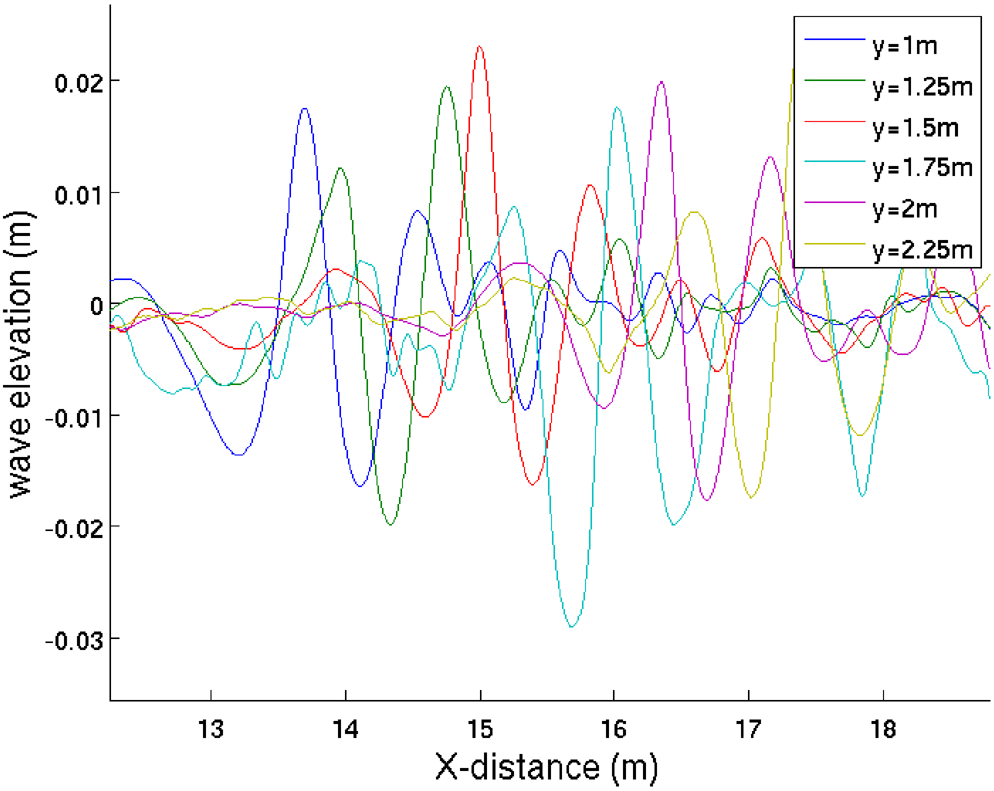

Figure 3-8 - Experimental wave cuts measured at different lateral spacings from the centreline for the passive case DA003 (head up).

3.3.3 Case C012 –passive version of propelled case

Table 3-3 –Experimental parameters for case C012

Length *L* (m)	1.93
Mean velocity *V* (ms^{-1})	1.47
Reynolds number *Rn*	2.84×10^6
Froude number *Fn*	0.34
Fundamental wavelength λ_0 (m)	1.38
Athlete height (m)	1.78
Athlete mass (kg)	66
Mean Tow force (N)	84.6

This test case is not simulated in this thesis but is included here as a passive comparison for the active test case, presented in section 3.4, which was conducted with the same Athlete.

Figure 3-9 – Passive towed position for Athlete C (case C012), provided for comparison with active case C009 (see Chapter 3.3).

3.3.4 Discussion

The two primary passive test cases (N003 – head in-line and DA003 – head up) represent the extremes of different flow regimes observed around a passively towed swimmer on the surface. These differences are caused by changes in tow speed and body position. In reality the flow features around a freestyle swimmer are likely to be somewhere in between the two. For instance it is common for water to alternate between flowing up and over the head and breaking around it while an athlete is swimming. It is intended that by simulating these two cases validation of the developed CFD methodology can be attempted across as wide a range of the free surface passive flow features as possible.

3.4 Propelled arms-only freestyle – Case C009

Table 3-4 –Experimental parameters for case C009

Length *L* (m)	1.93
Mean velocity *V* (ms^{-1})	1.56
Reynolds number *Rn*	3.01×10^6
Froude number *Fn*	0.36
Fundamental wavelength λ_0 (m)	1.56
Estimated depth of athlete below the undisturbed free surface* (m)	0.17
Athlete height (m)	1.78
Athlete mass (kg)	66

*measured from the hip joint or groin

The final experimental test case is of active swimming where the athlete does arms-only freestyle while being assisted by the tow system. The tow speed was set to the athlete's free swimming speed, providing the correct local flow for the arm stroke. The difference between the athlete's resistance *R* and thrust *T* is measured as the experimental tow force (*R-T*), see figure 3-10. This represents the lack of thrust and additional resistance due to the legs not being used.

This experimental set up allows real freestyle arm kinematics to be determined from experimental video footage, whilst measuring a time varying tow force (R-T). Therefore when replicated within a CFD methodology, this test case will allow the impact of real freestyle arm kinematics on the hydrodynamic forces to be to be assessed. It will also be possible to make a comparison with experimental data.

2012-May-21_Athlete_C_009

Mean Force, N 60.2

Force Std., N 21.2

Force, N 0.46

Speed, m/s 1.56

Mn Peaks 91.1

Mn Troughs 32.7

No. Strokes 4

Figure 3-10 - SwimSIM feedback GUI for case C009 (arm-only freestyle). Speed and force traces are provided in blue and pink respectively at the bottom. The mean force tow force (R-T) is presented in the top left.

A comparison of the adopted body position between normal freestyle, arms-only freestyle and a passive tow (case C012) is provided in figure 3-11. This indicates that the active depth and attitude of the head and torso are well replicated by the arms-only testing procedure. However there is an obvious difference in the position of the legs whilst performing arms only freestyle. The lower leg position in this case will cause a significant increase in the resistance compared to either the passive case or full freestyle swimming. The implications of this resistance increase will be discussed at greater length in Chapter 8, however it is helpful to highlight that the passive simulation C012 does not directly represent the passive resistance acting on the body in case C009.

Although difficult to see in the presented video snapshots, the free surface flow regime that develops around the head of athlete C in the active swimming case does appear to lie somewhere in between the two primary passive cases (N003 – head in-line and DA003 – head up). This helps to provide confidence that the two selected passive cases are suitable flow regimes for representing freestyle swimming.

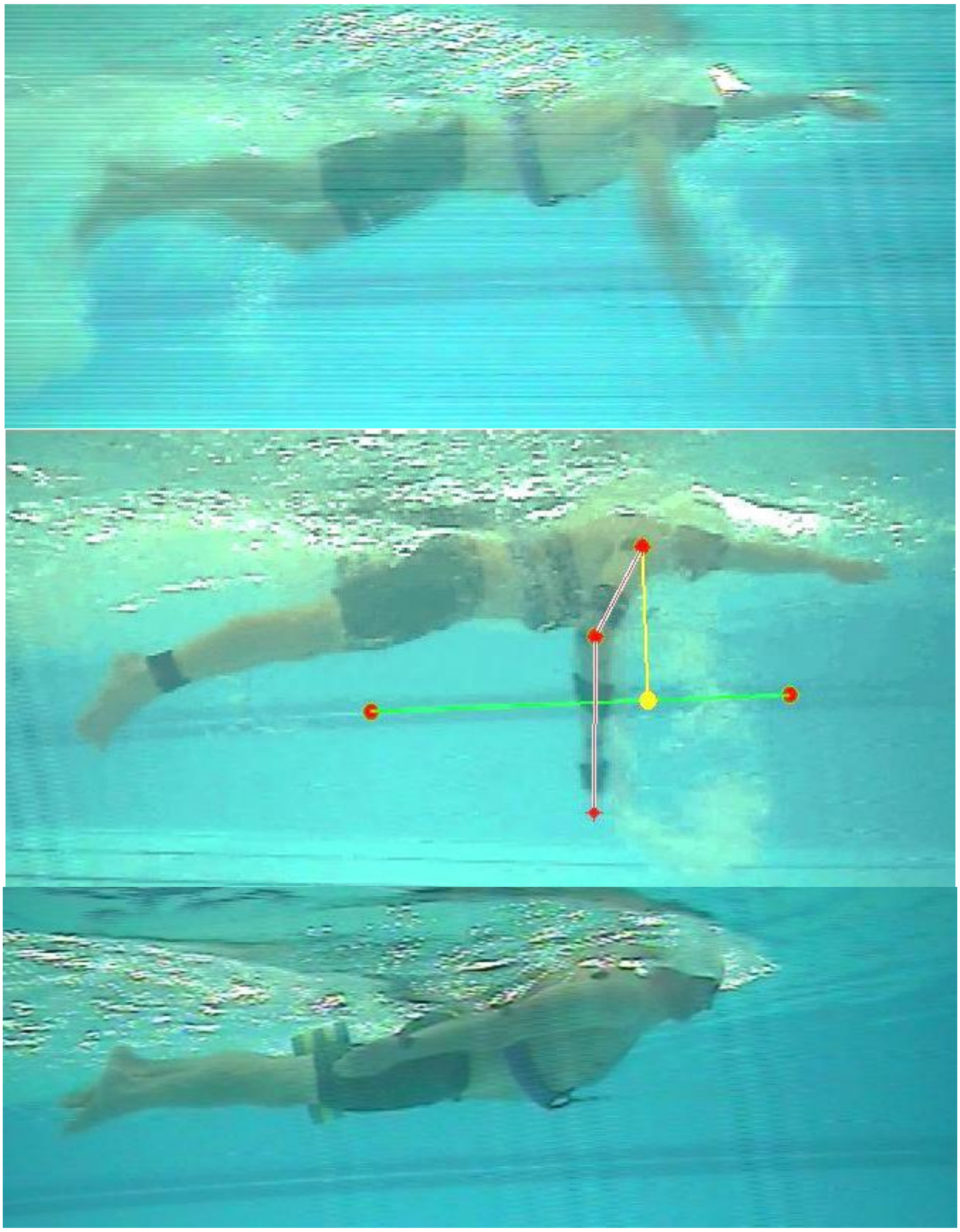

Figure 3-11 - Comparison of Athlete C's body position swimming normal freestyle (top), arms only freestyle in case C009 (middle) and during a passive tow in case C012 (bottom).

3.5 Conclusion

An experimental test case of a passively towed elite freestyle swimmer has been used from the other research activities of the wider UK Sport project SwimSIM. A series of additional experimental test cases have been conducted which break the full freestyle stroke down into the passive resistance of a swimmer on the surface and an arms-only freestyle case where the difference between the resistance and thrust is measured experimentally.

The two passive test cases will be used to investigate the passive resistance components of a swimmer on the water's surface through using a free surface CFD method. Comparisons can then be drawn between the numerical solution and the experimental data. This will build up confidence in the accuracy and validity of the developed methods.

The arm's kinematic data, measured from the arms-only freestyle footage from case C009, will be used to develop a body-force model that replicates the arm's impact on the fluid.

The arms-only freestyle case (C009) will ultimately form the basis of the final CFD analysis investigating the impact of the arm's kinematics on the resistance force of a freestyle swimmer.

The flow features that have been identified in the different experimental test cases help to inform the selection of suitable numerical methods to enable these case to be replicated using Computational Fluid Dynamics.

4. Simulating freestyle swimming

4.1 Challenges faced with simulating a freestyle swimmer

Before describing the different numerical tools that can be used to simulate a freestyle swimmer it is worth briefly discussing the difficulties that arise from such a complicated fluid dynamic problem.

Firstly the athlete geometries from the experimental test cases are very complex and it is unrealistic to presume that these will be exactly replicated within a simulation. The human body is able to perform a huge range of movements, each of them creating different muscle shapes which can then be deformed by external forces. Every attempt will be made to recreate the experimental conditions; however it should be acknowledged that even if the tested athletes were scanned this would still differ from the position adopted within the experiment, as shown by (Bixler et al., 2007). Accurate measurements of the swimmers depth and attitude in the water present another challenge in this process.

The complex flow features identified around the swimmers in chapter 3 offer significant challenges in themselves. The high curvature regions on the athlete’s geometry will cause the flow to separate off many parts of the body. This makes the boundary layer modelling crucial to the simulation accuracy as small changes in the separation points could have significant implications for the size of the separated regions and therefore the magnitude of the pressure resistance.

The free surface features identified around the swimmers represent significant free surface deformation compared to the size of the athlete. The complicated free surface flow that develops due to the semi-submerged nature of the body is likely to cause notable interactions between the different resistance components. The unsteady breaking waves that were identified in all the experimental cases create a significant challenge to simulate. This is due to the complex flow physics involved and the small scale of interface features such as bubbles and foam.

The unsteady flow features such as breaking waves and large turbulent eddies in the separated regions will create a larger computational demand due to time accuracy requirements and the need to provide mean force data over a period of time.

It is unrealistic to completely capture the physics of all aspects of this complex problem within an efficient simulation methodology. Therefore some approximations and simplifications will have to be made. It is important, however, to attempt to include as many aspects of the problem in the simulation as possible.

Provided there is an understanding of the effect and importance of any simplification made, a great deal can be learnt about the forces acting on a freestyle swimmer through the use of CFD methods. This chapter will outline the numerical methods used in the simulation and outline some of their limitations.

4.2 Applicable Computational tools used in Naval Architecture

Computational fluid dynamics (CFD) within naval architecture represents a well-established range of tools and techniques for providing numerical solutions to fluid flow problems. In general these different methods apply varying levels of simplification to the governing equations of fluid flow known as the Navier-Stokes equations. These represent the conservation of mass, momentum and energy (Versteeg & Malalasekera, 2007).

Potential flow simulations are where the fluid is assumed to be inviscid, greatly simplifying the flow. One commonly used application of these methods for ship design is estimating the wave pattern and wave resistance of hull forms. Thin Ship theory assumes that the body is slender and that the fluid motion is steady and irrotational, neglecting the effects of surface tension. The hull form is represented by planar arrays of Kelvin sources on the local centreline with the strengths determined from the hull geometry (Molland, A. F., Turnock, S. R., & Hudson, 2011). The wave system is then described as a series of Eggers coefficients which can be used to calculate the wave resistance based on the simulated far field wave pattern. The disadvantage of this method is that non-linear free surface effects such as breaking weaves are not included in the simulation; however it is computationally very efficient.

Thin Ship theory was used in this work to generate wave pattern and wave resistance estimates for the passive CFD geometries used. The simulation methodology used was from the original work of (Insel, 1990; Insel, M., Molland, A. F., & Wellicome, 1994) and was simply used to provide useful comparisons between experimental and viscous CFD predictions for the free surface deformation.

The Eggers coefficients defining the far field wave pattern can also be determined from experimental wave cuts, allowing the wave resistance to be demined for the passive experimental cases using the method presented in (Molland, A. F., Turnock, S. R., & Hudson, 2011).

Inviscid simulations fail to capture the boundary layer growth and shear related features of the flow. The most widely adopted viscous CFD method within engineering is based on solving the Reynolds Averaged Navier-Stokes (RANS) equations. This focuses on the time averaged properties of the flow, assuming that the effect of turbulence on these average properties can be represented as additional terms in the equations. For steady flow simulations this approach is widely used due to reasonably accurate results being provided at a modest computational cost compared to more advanced methods (Versteeg & Malalasekera, 2007). As engineering simulations are predominantly focused on determining mean flow values, such as ship resistance, a Reynolds averaged approach is often appropriate.

Unsteady RANS simulations (URANS) are also commonly used for unsteady flow problems. The large time scale unsteady flow features are physically simulated, whilst the effect of the small time scale turbulent features is represented by the additional terms in the URANS equations. Again this provides reasonably accurate results at a modest computational cost. However, RANS models are usually to dissipative for simulations of highly unsteady breaking waves(Yang & Stern, 2007). This is because the small length and timescales of the unsteady turbulent flow features are not resolved leading to some of the detailed flow physics associated with separation and air entrainment being lost. This tends to smear out large scale unsteady effects that can develop around complex bluff body geometries and breaking wave features.

More advanced CFD methodologies designed more specifically for large turbulent flow structures include large eddy simulations (LES) and detached eddy simulations (DES), a hybrid of RANS and LES. This separates out the large scale eddies, to be solved using the unsteady Navier-Stokes equations, whilst the small scale fluctuations are solved based on a mean flow approach. These types of methods require significant increases in computational cost due to the fine mesh and small time steps required (Versteeg & Malalasekera, 2007).

The main CFD method used in this work was URANS as this provided a good compromise between simulation fidelity and computational cost. However it is acknowledged that the free-surface separated flows observed around a swimmer would benefit from a LES/DES approach making this an interesting method to be investigated in the future.

4.3 Unsteady RANS Simulations

The aim of this work requires the application of established CFD methods to the sport of swimming rather than the development of numerical methods themselves. The purpose of this section, therefore, is not to fully explain the detailed working the applied URANS CFD code but to provide sufficient background to the methodology to explain some of the modelling decisions made and their impact of the simulated results. The underlying theory presented in this section is mainly taken from the books (Peric, M., & Ferziger, 2002; Versteeg & Malalasekera, 2007).

4.3.1 Turbulent Flow

The incompressible Navier-Stokes equations for a Newtonian fluid are provided in Cartesian tensor form with the continuity equation defined as

$$\frac{\partial u_j}{\partial x_j} = 0 \qquad 4\text{-}1$$

and the momentum equation defined as

$$\rho \frac{\partial u_i}{\partial t} + \rho \frac{\partial u_i u_j}{\partial x_j} = -\frac{\partial p}{\partial x_i} + \frac{\partial}{\partial x_j}\left(\mu\left(\frac{\partial u_i}{\partial x_j} + \frac{\partial u_j}{\partial x_i}\right)\right) + f_i \qquad 4\text{-}2$$

with x_i or (x, y, z) representing the coordinates, u_i or (u_x, u_y, u_z) the velocity components, μ the dynamic viscosity, ρ the fluid density and f_i the momentum source term representing external forces applied to the fluid. This provides the governing equations for unsteady incompressible flow.

In a viscous flow the Reynolds number, presented in equation 3-1, provides the ratio of the inertial forces to the viscous forces and therefore can be used to characterise the flow regime. At low Reynolds numbers (typically below a critical Reynolds number of approximately 2×10^3) the viscous forces dominate, damping out disturbances in the flow, producing laminar flow conditions. At high Reynolds numbers (typically $Re > 10^4$) the inertial forces dominate, creating unsteady eddies which cause turbulent fluctuation in flow velocity. Turbulent flows are characterised by unsteady eddies of many different length scales, effectively mixing the fluid and transferring momentum from one region to another.

To directly solve the unsteady Navier-Stokes equations requires a mesh and time step resolution small enough to capture the smallest, high frequency, turbulent fluctuation. This process is called Direct Numerical Simulation (DNS) however the computational requirements render it entirely impractical for most engineering simulations.

To enable a turbulent flow to be simulated numerically, the fluctuating instantaneous velocity is decomposed into a mean and time varying component. This is known as Reynolds decomposition and defines the mean flow as:

$$\bar{u} = \frac{1}{\Delta t}\int_0^{\Delta t} u(t)dt \qquad 4\text{-}3$$

where it is assumed that:

$$u = \bar{u} + u' \qquad \overline{u'} = 0 \qquad \overline{\bar{u}u'} = \overline{u'\bar{u}} = 0 \qquad 4\text{-}4$$

where u' represents the velocity fluctuation about the mean. For unsteady simulations the averaging period essentially becomes the simulation time step Δt providing a mean velocity, including the effects of turbulence, within that time step.

4.3.2 Unsteady Reynolds Averaged Navier-Stokes (URANS) Equations

By performing Reynolds decomposition on the Navier-Stokes equations (i.e. substitute equations 4-4 into equations 4-1 and 4-2) the following RANS equations are obtained.

$$\frac{\partial \bar{u}}{\partial x_j} = 0 \qquad \text{4-5}$$

$$\rho\frac{\partial \bar{u}_i}{\partial t} + \rho\frac{\partial \overline{u_i u_j}}{\partial x_j} = -\frac{\partial \bar{p}}{\partial x_i} + \frac{\partial}{\partial x_j}\left(\mu\left(\frac{\partial \bar{u}_i}{\partial x_j} + \frac{\partial \bar{u}_j}{\partial x_i}\right)\right) - \rho\frac{\partial \overline{u'_i u'_j}}{\partial x_j} + f_i \qquad \text{4-6}$$

The additional term in the equation, $\rho\frac{\partial \overline{u'_i u'_j}}{\partial x_j}$, is known as the Reynolds stress tensor which represents the effect that turbulence has on the mean flow properties within a given time step. The Reynolds stress tensor is comprised of six unknown independent variables, three normal stresses and three shear stresses. These Reynolds stresses are added to the principle unknown variables (u, v, w and p), providing ten unknowns with only four equations. This is known as the turbulence closure problem. Various different turbulence closure models have been developed to provide solutions to the Reynolds stresses allowing the URANS equations to be numerically solved.

4.3.3 Turbulence modelling

The turbulence model used in this work is the shear stress transport model (SST) developed by (Menter, 1994). This model belongs to a group of turbulence models commonly used in engineering known as eddy viscosity models. These are based on the Boussinesq assumption that the turbulence increases the effective viscosity μ to $\mu+\mu_T$, where μ_T is the eddy viscosity, allowing the Reynolds stresses to be calculated.

The SST model combines two different ways of calculating the eddy viscosity depending on the region of the flow. In the fully turbulent region, far from the wall, it adopts the standard two equation model k-ε, which solves two additional transport equations. The first is for the turbulent kinetic energy ($k = \frac{1}{2}\overline{u'_i u'_i}$) and second is for the dissipation of turbulent kinetic energy ε. This allows the eddy viscosity to be calculated as

$$\mu_T = \rho C_\mu \frac{k^2}{\varepsilon} \qquad 4\text{-}7$$

In the near wall region, however, this two equation model is transformed into the k-ω model (D. C. Wilcox, 1998) by substituting $\varepsilon = \omega k$, where ω is the turbulent frequency. This representation of the Reynolds stresses has been shown to provide better boundary layer modelling for adverse pressure gradients while reducing the sensitivity to boundary conditions through the use of k-ε further away from the wall. This makes the SST model the most generic of the eddy viscosity turbulence models and has been shown to give superior performance for zero or adverse pressure gradient boundary layers (Versteeg & Malalasekera, 2007). This improves the ability of the RANS simulations to accurately capture flow separation points over a complex geometry.

The SST has also been shown to better replicate the flow around ship hull forms compared to either zero equation models or the k − ε model, especially in capturing hooks in the wake contours at the propeller plane (Larsson, Stern, & Bertram, 2003).

4.3.4 Inlet and outlet boundary conditions

Solution of the RANS equations requires boundary conditions to be applied in order to solve the system of equations. There are two main types of boundary condition in CFD simulations: a Dirchlet boundary condition which specifies the values that must be taken on the boundary and a Neumann boundary condition which defines the gradient of a value on the boundary.

An inlet is a Dirchlet boundary condition where the inflow velocity and turbulence of the fluid is specified. An outlet is generally a Neumann boundary condition. If the outlet is placed far enough from the body to ensure the flow is fully developed so that no variation occurs in the flow direction, the flow gradients can be assumed to be zero in the flow direction.

4.3.5 Boundary layer modelling

The surface of the swimmer is defined as a no slip boundary condition. This ensures that there is no tangential fluid velocity on the wall, causing a boundary layer to grow due to viscosity driven shear forces. A boundary layer is defined as the region next to a wall where the velocity varies from zero on the surface to 99% of the free stream value at the edge of the boundary layer. Close to the wall, within a turbulent boundary layer, the mean flow velocity is dependent on the distance from the wall. This is known as the law-of-the-wall which can be described as:

$$u^+ = \frac{U}{u_\tau} = f\left(\frac{\rho u_\tau y}{\mu}\right) = f(y^+) \qquad 4\text{-}8$$

where u^+ and y^+ are the non-dimensional velocity and distance from the wall and u_τ is the friction velocity $\left(\sqrt{\tau_w/\rho}\right)$, calculated from the wall shear stress τ_w.

Experimental results show that boundary layers have a characteristic structure comprising of four regions:

- **the viscous sub-layer** is a narrow region, $y^+ < 5$, close to the wall in which the flow is highly retarded and the main forces at work are due to viscous shear. Within the viscous sub-layer it can be shown that there is a linear relationship between u^+ and y^+;
- **the buffer region** ($5 < y^+ < 30$), where turbulent and molecular viscosity are of equal importance;
- **the log law region** ($30 < y_+ < 500$), a turbulent region close to the wall where turbulent fluctuations dominate the mixing process. There is a logarithmic relationship between u_+ and y_+;
- **the wake or outer region** which extends from the log law region to the edge of the boundary, making up approximately 80% of the boundary layer. This is an inertia dominated region far from the wall.

To fully resolve the boundary layer physics within the fluid domain, the mesh has to be resolved down to a cell size that produces a y^+ value of approximately one. This allows each of the different zones in the boundary layer to be physically modelled. However this approach does require a high mesh density in the inner boundary layer region to capture the relevant flow physics. A best practice guide for marine flows (WS Atkins Consultants, 2003) recommends that at least 10 mesh points are placed within a $y^+ = 20$ from the wall.

An alternative approach to fully resolving the boundary layer is to use wall functions, which are designed to predict the mean fluid velocity for a point within the log law region of the boundary layer. This allows the flow variables to be directly related to the wall shear stress without directly resolving the intervening flow structure. This has the obvious advantage of significantly reducing the mesh density required as the first cell height off the wall only needs to achieve a y^+ of between 30 and 100. However the draw back of wall functions is that they are based on empirical relationships determined from flat plate and pipe flow boundary layers. Therefore wall functions have been shown to inaccurately model the adverse pressure gradients and separated regions found around complex geometries.

Both wall functions and fully resolved boundary layer simulations are investigated in this work to determine the impact boundary layer fidelity has on the solutions.

4.3.6 Free surface capture

The free surface interface is captured using a volume of fluid approach (VOF) where the volume fraction transport equation is defined as

$$\frac{\partial \varphi}{\partial t} + \frac{\partial (\varphi U_j)}{\partial x_j} = 0, \qquad 4\text{-}9$$

where φ is the volume fraction calculated as the volume ratio of water to air in a given cell (Peric, M., & Ferziger, 2002). The fluid density, ρ, and viscosity, μ, can then be calculated as

$$\rho = \rho_{air}(1-\varphi) + \rho_{water}\varphi \qquad 4\text{-}10$$

and

$$\mu = \mu_{air}(1-\varphi) + \mu_{water}\varphi \qquad 4\text{-}11$$

respectively.

Volume of fluid methods are currently the most commonly used method for free surface flows in ship hydrodynamics, making up approximately 70% of the submissions to a recent workshop on numerical ship hydrodynamics, Gothenburg 2010 (Larsson et al., 2010). This is due to its relatively simple implementation; the inherent conservation of mass if the volume fraction is conserved and the ability to cope with both complex geometries and free surface flow features, such as breaking waves. However due to the fact that they implicitly capture the water-air interface, these methods suffer from numerical diffusion in this region leading to smearing of the interface. Developments in VOF methodologies have mainly focused on trying to elevate this problem through the use of different approaches to interface advection. These can broadly be defined as geometric reconstruction techniques, where an additional explicit representation of the interface is based on an assumed functional form and algebraic techniques, where interface compression is added to try and maintain a sharp interface (Deshpande, Anumolu, & Trujillo, 2012). Although the geometric versions tend to provide a sharper interface they add considerable complexity and computational cost and therefore an algebraic form of the VOF methodology is still widely used. It should be noted however that the interface advection in VOF methods is an active area of research resulting in these methods improving continuously (Weymouth & Yue, 2010).

Other free surface methods include both surface tracking and level set approaches. Surface tracking modifies the computational grid to match the upper boundary to the free surface. This type of methodology is not applicable for complex and unsteady free-surface features such as wave breaking and also has difficulty modifying and moving the free-surface mesh around complex geometries (Wackers et al., 2011). Level set methods are closer to VOF methods in that they are applied on a static mesh. They apply a more complex formulation of the free surface interface which can provide a sharper resolution, however they have the disadvantage of not having mass conservation embedded in their formulation (Deshpande et al., 2012). With regard to capturing wave breaking neither VOF nor level set methods accurately capture the full physics of these flow features. However it is observed in (Wackers et al., 2011) that VOF methods do at least have the ability to attempt to capture foam and bubbly regions associated with breaking waves through dispersed volume fraction regions. This work also acknowledges the ability of VOF methods to calculate the bluff body breaking wave features found at the bow of hull-forms such as tankers.

4.3.7 Domain Discretisation

Solution of the RANS equations using the finite volume method requires that the simulation domain, around the geometry of interest, is discretised into a series of small finite volumes or cells. The discretised domain is usually referred to as the mesh.

There are many different software packages and techniques available to generate the mesh. In this work the script driven unstructured hexahedral based meshing software SnappyHexMesh is used. This allows local grid refinement to be placed at different regions of interest within the fluid domain allowing computationally efficient meshes to be developed. More detail is provided about the meshing process in Chapter 5 and in (OpenFOAM®, 2009).

Other meshing strategies available include structured grids, which have been shown to provide superior results to many solutions, however these are impractical to use on such a complex geometry as a human body.

4.3.8 OpenFOAM Flow Solver InterFOAM

OpenFOAM (Open Field Manipulation and Operation) is an open source CFD toolbox implemented in C++. It contains numerous applications and libraries, and it is nowadays extensively used in the scientific community. For a detailed description refer to the OpenFOAM website (www.openfoam.com) or the OpenFOAM user guide (OpenFOAM®, 2011). The advantages of using OpenFOAM as opposed to a commercial CFD code are:

- it is well set up for running large parallel jobs, not only within the code implementation but through the unlimited number of processors that can be used due to no licencing costs;
- the code and solvers themselves can be viewed and modified by the user, allowing for the inclusion of new features, such as bespoke body-force propulsion models, into existing solvers;
- being able to view the code also allows the user to see what is actually being done by the code, providing a transparency unavailable in commercial versions;
- there is a substantial and growing user group within the university and the Fluid Structure Interaction (FSI) research group with which to share knowledge and experience of using the software.

The disadvantage of using OpenFOAM is that it is a far less well documented code than commercial alternatives and thus it takes time to set up and adapt for specific purposes.

The two-phase OpenFOAM solver InterFoam is used in this work. This applies a homogeneous VOF approach using collocated grids and a Multidimensional Universal Limiter with Explicit Solution (MULES) approach for the volume fraction, applying a compression term to the interface. The solution of the momentum equation is provided using a Pressure Implicit with Splitting Operators (PISO) approach. Details of the solution algorithm along with extensive verification and validation data of the InterFoam solver is provided in (Deshpande et al., 2012). This work concluded that the InterFoam solver was comparable with other similar VOF methodologies, although it did suffer from greater interface diffusion than some geometric based interface advection methods.

The PISO algorithm for pressure-velocity coupling can be summarized as follows:

1. Set the initial conditions.
2. Begin the time-marching loop.
3. Assemble and solve the momentum predictor equation with the available face fluxes (and pressure field).
4. Solve the equation and explicitly correct the velocity field. Iterate until the tolerance for pressure-velocity system is reached. At this stage pressure and velocity fields for the current time-step are obtained, as well as the new set of conservative fluxes.
5. Using the conservative fluxes solve all other equations in the system. If the flow is turbulent, calculate the eddy viscosity from the turbulence variables.
6. Go to the next time step unless the final time has been reached.

Details of how the RANS equations can be discretised and solved using finite volume methods are presented in standard textbooks such as (Versteeg & Malalasekera, 2007)

4.4 Modelling the arm in self-propelled RANS simulations

There are essentially two different approaches that can be adopted to include the effects of the arm into the RANS simulations. The arm can be included in the simulation explicitly so that the flow around the physical arm geometry can be fully resolved. The other option is to simply include the effect the arm has on the fluid flow through the use of a body force model.

4.4.1 Explicit arm modelling

The main challenge presented with an explicit arm methodology is the arm's extensive range of motion. Simple mesh deformation cannot be used to simulate the arm's kinematics alongside the body. Therefore techniques such as adaptive re-meshing or overset grids are required.

Adaptive re-meshing provides the simplest solution to the problem with the simulation domain being repeatedly re-discretised as the arm moves through it with time. The solution from the previous mesh then has to be interpolated on to the new one and arm's motion included into the boundary conditions. Whilst this represents the simplest explicit methodology to develop it is likely to incur the largest computational cost due to the repeated re-meshing required.

Overset grids provide the most elegant explicit methodology, where a separate mesh is developed around both the body and the arm while rigid mesh motions are used to move the arm's mesh through the parent mesh around the body. A sophisticated algorithm is then used to interpolate data from one mesh to the other near the mesh boundaries, allowing both meshes to be used at the same time.

Each of these has their own drawbacks, such as varying levels of additional computational cost or complexity. However both of them suffer from a computational cost associated with the high mesh resolution required on the arm and the small time step required to capture the transient flow features.

The time step required for a stable unsteady simulation is related to the smallest cell size through the Courant number

$$C_r = \frac{U\Delta t}{\Delta x} \qquad 4\text{-}12$$

where U is the fluid velocity through the cell, Δx is the length of the cell and Δt is the time step (Peric, M., & Ferziger, 2002). Therefore, to maintain the same Courant number, any reduction in cell size required to simulate the flow around an arm results in a reduction in the time step and hence an increase in the total computational time.

Due to the fine mesh resolution required to accurately model a hand's geometry and the higher local flow velocities in this region, the time step will have to be significantly reduced compared to simulations of just the body. This can be observed by comparing the surface mesh density of 100,000 cells/m^2 used to model just a hand (Sato and Hino, 2003) with 32,000 cells/m^2 for the entire body (Lyttle and Keys, 2004). This would indicate a cell size three times smaller across the surface of the hand, although this could be significantly more if non-uniform cell sizes are taken into account. Another way of estimating the required cell size on a hand compared to the body is to calculate the change in cell size, normal to the wall, required to provide the same y^+ value on both the arm and body.

By taking the length of the respective geometries and the expected flow velocity it can be shown that the friction velocity on the hand is approximately twice that for the body (see Appendix 2 for details). As the y^+ is directly proportional to the friction velocity (see equation 4-8) the cell dimensions would need to be divided by two on the hand.

Based on these two quick assessments it would seem sensible to assume that a full arm simulation would require a minimum cell size of at least 2-3 times smaller than that required for just the body, but potentially far smaller. To maintain the same Courant number the time step would need to be reduced by the same amount. When you include the increased mesh size needed to resolve the arm, it is easy to see how computationally expensive full body simulations with moving arm geometries could become.

4.4.2 Body force models

The applications of body-force models have been extensively used to simulate the impact a propeller has on the flow behind a ship (Banks et al., 2010; A. B.

Phillips, 2009; A. Phillips, Furlong, & Turnock, 2010; Phillips, A. B., Turnock, S. R., & Furlong, 2009). A similar approach has also been adopted in reverse to remove energy from the fluid enabling tidal turbine wakes to be simulated (S R. Turnock, Phillips, Banks, & Nicholls-Lee, 2011). In all these examples of previously implemented body force models the location of the propulsive domain remains fixed. The proposed method of developing a generic body force model whose propulsive domain can move freely through the domain does not appear to have been implemented before.

The principle of using a body-force methodology here is that the physical geometry of the arm is not simulated. Instead a series of momentum source terms are added into the momentum equation represented as f_i in equation 4-6. This applies the momentum sources within the simulation domain, which represent the arm's location and the hydrodynamic force acting on it. This induces an acceleration vector which mimics the impact of the arm.

The advantage of adopting such an approach is that no mesh motion is required and the additional computational cost is minimal compared with the RANS solver (Banks et al., 2013). It should be highlighted however that this is an approximation of the flow induced by the arm. Its accuracy depends on the estimate of the fluid forces on the arm which are discussed in chapter 6. Therefore this is not an appropriate tool for investigating the detailed flow around the arm. It also has to be accepted that some of the detail flow structures generated by a real arm will not be captured. The discrepancy between the body-force model and an explicit representation will be most obvious in the immediate vicinity of the arm location.

There are no other examples of a body-force model being used within the swimming literature, making this study a novel application of a previously successful methodology from naval architecture. Another additional

4.5 Conclusion

A brief summary has been presented of the numerical methods that are suitable for modelling the experimental test case presented in chapter 3. A background has been provided of the implications that some of these numerical methods will have on the CFD solutions presented in the following sections of this thesis. It is acknowledged that the complexity of the experimental test cases means that the full flow physics cannot be captured in every detail. However key areas have been identified, such as free surface interactions and accurate boundary layer modelling, which are crucial to providing an accurate assessment of the resistance components on a freestyle swimmer. It is intended that by focusing on these features along with representing the impact of the arm, the aims and objectives of this research can be achieved.

5. RANS implementation for a passive swimmer

This chapter details the implementation of the numerical methods described in chapter 4 to the passive experimental cases presented in chapter 3. This will mainly focus on the development of a suitable meshing strategy to enable the key flow features associated with the boundary layer modelling and free surface interaction to be captured within the RANS methodology. This involves some individual mesh studies in these specific areas before a global mesh sensitivity study is performed on the final mesh structure. This provides the underlying RANS methodology that is then used to determine the resistance components of a freestyle swimmer in both passive and active simulations.

Before providing any detail of the RANS implementation the representation of the swimmer's body within the numerical domain should be discussed. Accurately representing the athlete's body is equally as important as the numerical methods if the developed implementation is to be validated against the experimental data.

5.1 Swimmer geometry

In order to simulate the conditions of the passive cases N003 (head in-line) and DA003 (head up) it was important to replicate the athletes' geometry as closely as possible. Because the athletes were towed with their arms by their sides the existing athlete scans available of swimmers were not appropriate. This is because these existing scans were of the athletes in a streamlined glide position. In lieu of generating new athlete scans a previously used geometry from the winter sport bob-skeleton was used as a basis geometry from which to start from, see figure 5-1. This provided a better match to the experimental conditions due to the position of the arms. This athlete scan ended up being the basis for all the simulated geometries in this work. The limitations of this process are discussed later and it is acknowledged that individual scans of the participating athletes would significantly improve the geometry generation process.

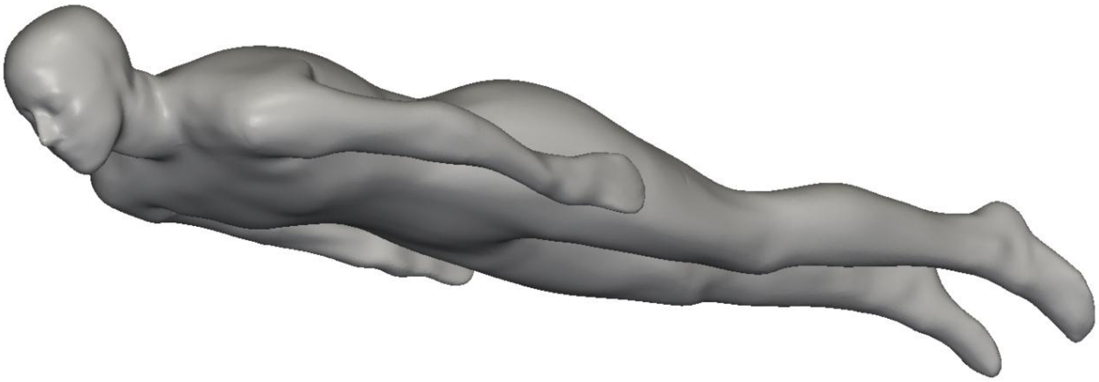

Figure 5-1 - Basis athlete geometry, originally from Bob-skeleton.

5.1.1 Geometry morphing and scaling

An in-house meshing tool called Adaptflexi (S.R. Turnock, 2004) was used in order to modify the basis athlete geometry so as to match the different case conditions. This has the capability to take an STL geometry and deform it in a number of different ways, most importantly performing joint rotations and variable scale factors along the body.

This process was scripted to take the basis athlete STL (scaled to a unit length of one meter) and perform a series of joint rotations about specified joint axes. Once the desired body shape and attitude was achieved the geometry was then scaled up to the correct dimensions based on the athlete's height. The details of the scripting process and the range of joint rotations achievable is provided in appendix 3. The outcomes of this process are presented for each simulation geometry.

5.1.2 Case N003 (head in-line)

Table 5-1 – N003 simulation geometry parameters

Length (m)	1.86
Surface Area (m^2)	1.727
Frontal Projected Area (m^2)	0.113
Volume (m^3)	0.0809
Density (kg/m^3)	776

The basis athlete geometry (figure 5-1) was deformed to match the position adopted during case N003, see figure 5-2. This geometry was created early in the methodology development, using joint rotations and a constant scaling factor for width and depth along the athlete‘s body. To provide consistency throughout the development process, this geometry has been maintained. There is, however, the possibility of a slightly closer fit between geometry and athlete if variable scale factors for depth and width were used, most noticeably on the thighs and head. It should also be observed that the athlete will have pulled their arms in close by their side during the experiment, whereas this is not the case with the simulation geometry. Despite this a satisfactory fit was generally achieved using this process.

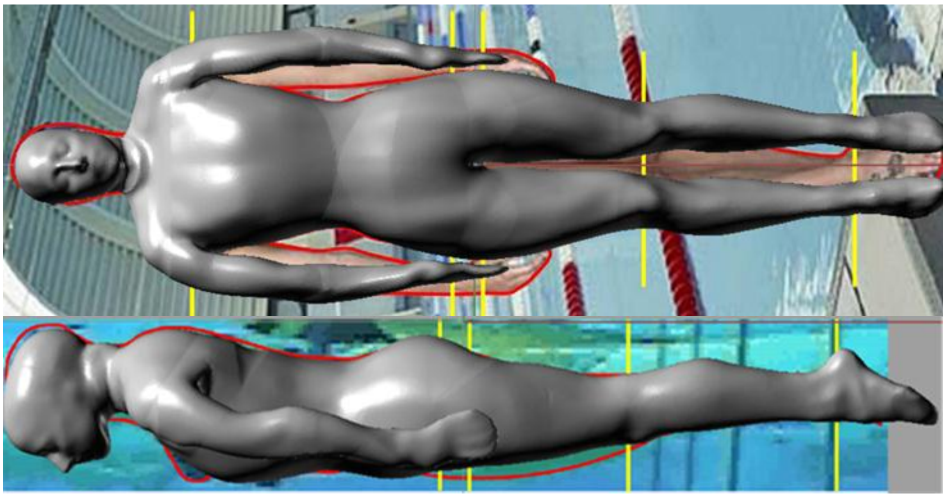

Figure 5-2 – N003 geometry compared to a head on photo (above) and underwater footage from experimental case (below). Body outlines have been drawn on the figures in red.

5.1.3 Case DA003 (head up)

Table 5-2 – DA003 simulation geometry parameters

Length (m)	1.86
Surface Area (m^2)	1.94
Frontal Projected Area (m^2)	0.127
Volume (m^3)	0.0867
Density (kg/m^3)	807

The geometry developed for the DA003 simulations required both joint rotations and variable scale factors to modify the basis athlete geometry sufficiently to match the experimental athlete’s profile (see figure 5-3). Scale factors were only applied in the vertical direction as the dimensions of the head on video footage were significantly distorted due to perspective (see figure 5-4). One of the most obvious discrepancies between the simulation geometry and athlete is the difference in the arm and shoulder position. This is due to the fact that the basis STL was generated from an athlete lying on their front. While applying joint rotations and scale factors can drastically change the simulation geometry, more complex joint motions such as those of the shoulders cannot currently be replicated. It just so happened that the scanned shoulder position shows a close agreement with case N003. The absence of horizontal scaling factors means that the ultimate volume of the athlete may not have been accurately represented, which will add to the errors associated with the arm and shoulder position.

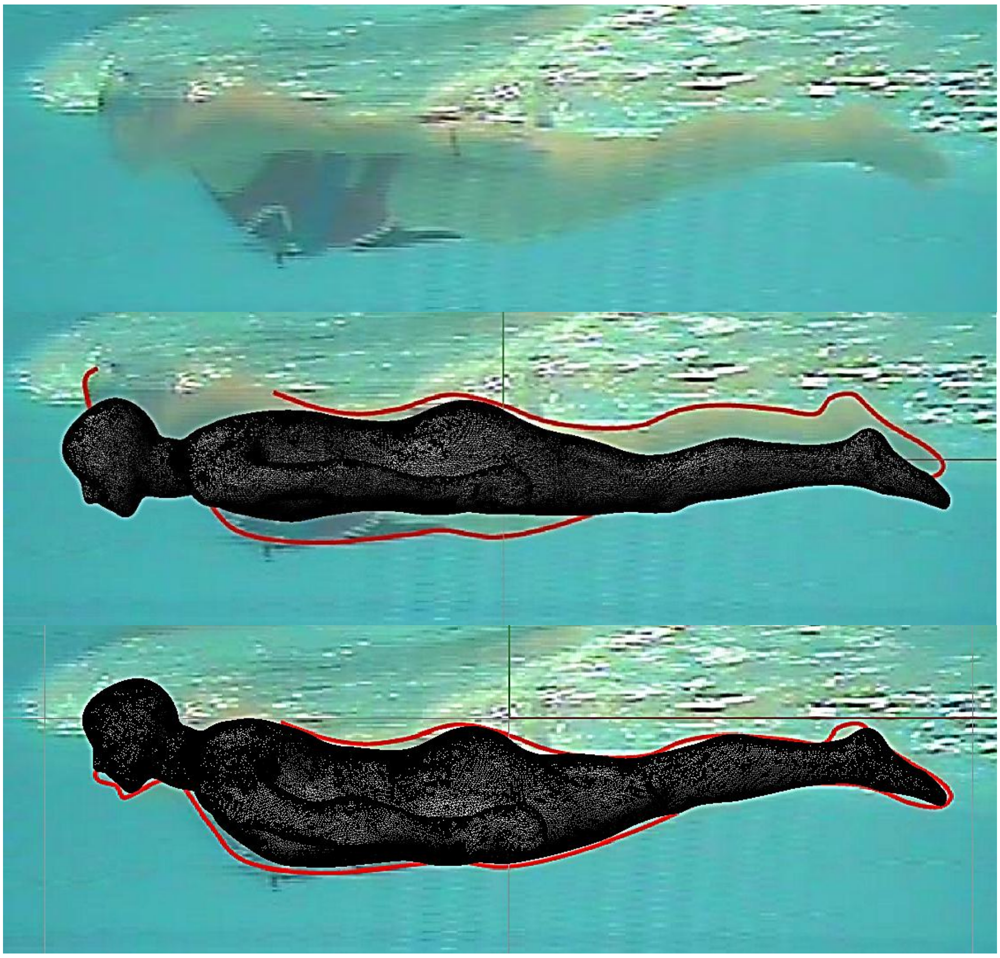

Figure 5-3 - DA003 simulation geometry (bottom) and basis athlete geometry (middle) compared to underwater footage from experimental case DA003 (top).

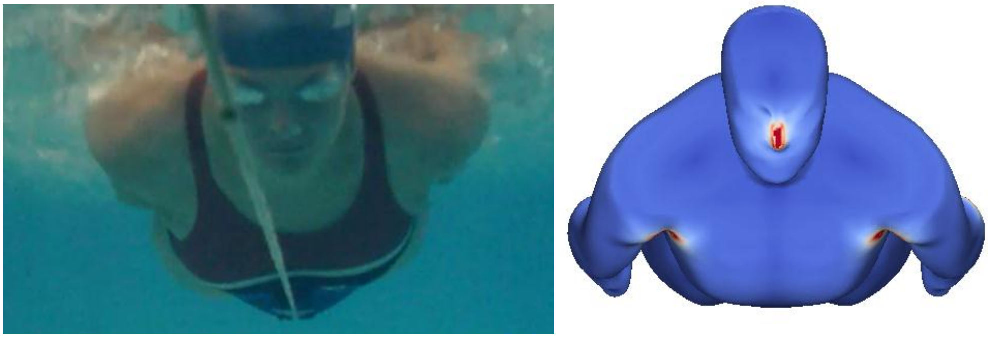

Figure 5-4 – Head on comparison of experimental and simulation geometry for case DA003 (head up).

5.1.4 Vertical position of geometry

The vertical position of the simulation geometry had to be judged by eye from the experimental footage, thus introducing another source of error to the simulated geometry. It is estimated that the vertical position of the swimmer will only be accurate to within ±0.02 m.

5.1.5 Conclusion

A great effort has been made to match the simulation geometries to those of the experimental cases. In general a reasonable fit has been achieved for the side-on profiles based on the experimental footage, however significant discrepancies have been identified within the body position that generates these profiles. These include the position and attitude of the athlete’s arms and shoulders and a more general lack of ability to scale the athlete’s width to account for differences in body shape. These discrepancies have been shown to have a significant effect on the posture of DA003 when viewed from head on. It should also be acknowledged that no attempt has been made to replicate the athlete’s hair and swimming cap arrangement.

To provide a better representation of the experimental cases would require scans of the individual athletes tested while they attempted to recreate their towed body position. This process in itself would not be without errors, as shown in the significant difference in experimental resistance for an athlete and a mannequin created from the same athlete’s body scan (Bixler et al., 2007). However a scanned geometry would provide a much closer representation than is currently achievable using the implemented morphing process.

5.2 Meshing technique

Once a simulation geometry has been generated it has to be represented within a numerical domain, creating a finite volume mesh of cells with which the RANS equations can be solved numerically. The distribution of cells within the numerical domain impacts on both the accurate resolution of the physical flow features and the computational efficiency. Some specific mesh refinement studies were required to achieve a suitable balance between the two. This mesh development process was conducted on the experimental case N003 (head in-line) before applying it to case DA003 (head up) in chapter 6.

The simulation domain represented three 2.5m lanes of a swimming pool, with (-3 to 11m) in the x-direction along the pool in the direction of the free stream velocity, (±3.75 m) in the y-direction across the pool width and (-2 to 1 m) depth in the z-direction. This provides a 14m long section of a 2m deep swimming pool three lanes wide.

An unstructured hexahedral mesh was created around the simulation geometry using the snappyHexMesh utility within OpenFOAM-1.6x (OpenFOAM®, 2009). Firstly a coarse block mesh was created, dividing the simulation domain into cells of 0.2 m in each direction. Regions were then defined with up to six levels of isotropic refinement (dividing the local cell dimensions by up to 2^6), gradually increasing the mesh density near the body whilst maintaining a cell aspect ratio of approximately one.

Refinement levels can be defined for different regions within the mesh. These regions were defined in three main ways:

- cells that intersect the surface of the STL geometry, providing the surface resolution;
- cells within specified distances from the STL surface, allowing the expansion rate of the mesh to be controlled;
- cells that lie within defined geometric shapes (such as boxes, cylinders and spheres), typically used for wake or free surface regions.

During each refinement process any cells within a zone marked for further refinement are split into eight equal parts.

Once the refinement stage is complete the cells contained within the STL geometry are removed. The nodes of the cells that remain adjacent to the STL are then snapped onto the STL surface, creating a smooth representation of the STL geometry within the mesh. This process is depicted in figure 5-5. For more details of how SnappyHexMesh works see (OpenFOAM®, 2009).

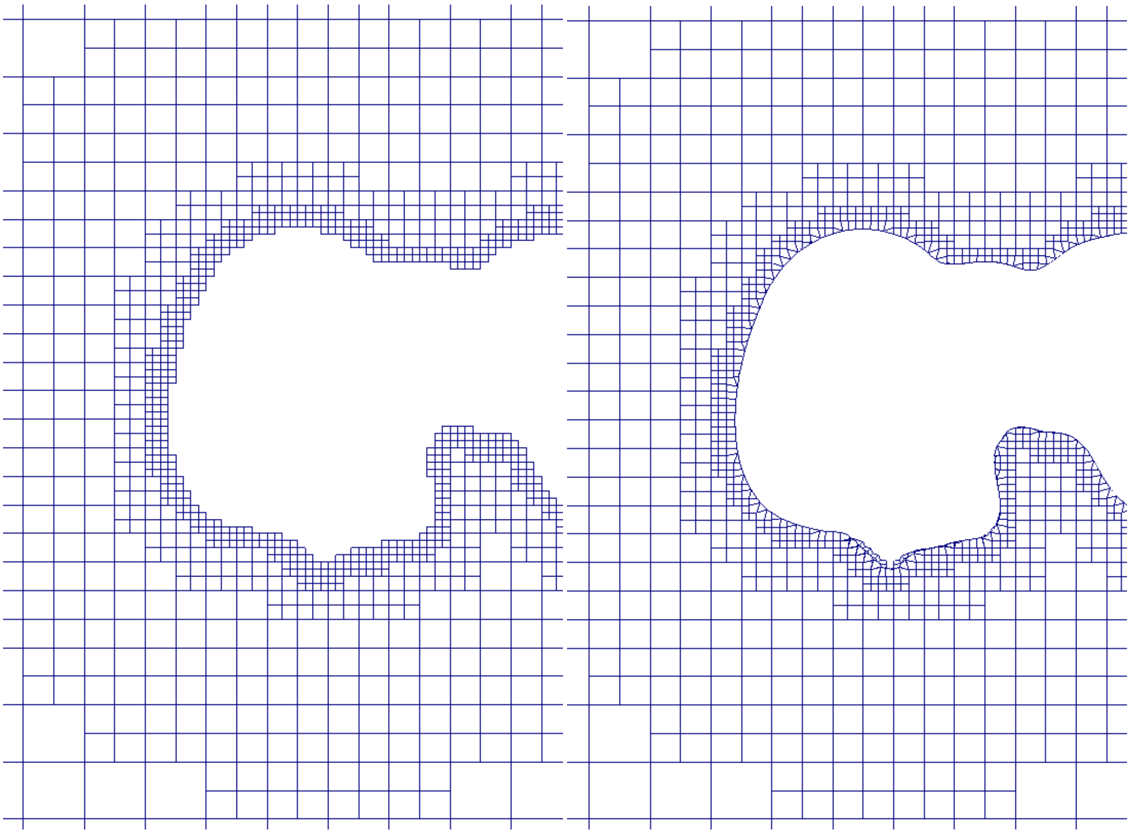

Figure 5-5 – SnappyHexMesh refinement process. Mesh after refinement with internal cells removed (left) and mesh with mesh nodes snapped to STL surface (right).

5.3 Boundary layer modelling

To provide greater control to the near wall region of the mesh, boundary layer cells were grown out from the body surface mesh, see figure 5-6. The structure of the layer mesh is defined by an outer cell thickness, an expansion ratio and the number of cells grown out from the wall. Where the layer mesh is grown the surrounding mesh is shifted out from the body to create space for the new cells. The quality of the mesh is then checked against predefined parameters and adjusted in an iterative manner to achieve the maximum layer growth possible (OpenFOAM®, 2009).

Two different types of near-wall layer mesh were created for case N003. Firstly, a layer mesh grown in a single stage (10 cells with expansion ratio of 1.2) was designed to give a y^+ equal to 40 on the body (suitable for use with a wall function (WS Atkins Consultants, 2003)). Secondly a layer mesh was grown in two stages, with 6 cells in the outer layer and then another 10 cells added inside these in the inner layer (see figure 5-6). The expansion ratio of the outer and inner layers were 1.5 and 1.2 respectively. The inner layer is designed to provide a y^+ of less than one on the surface of the body and provide 9 cells within a y^+ of 20 from the wall. This structure allows the boundary layer to be fully resolved, removing the need for a wall function. An example of these two types of mesh structures, along with the initial 'snapped' mesh, can be seen in figure 5-6.

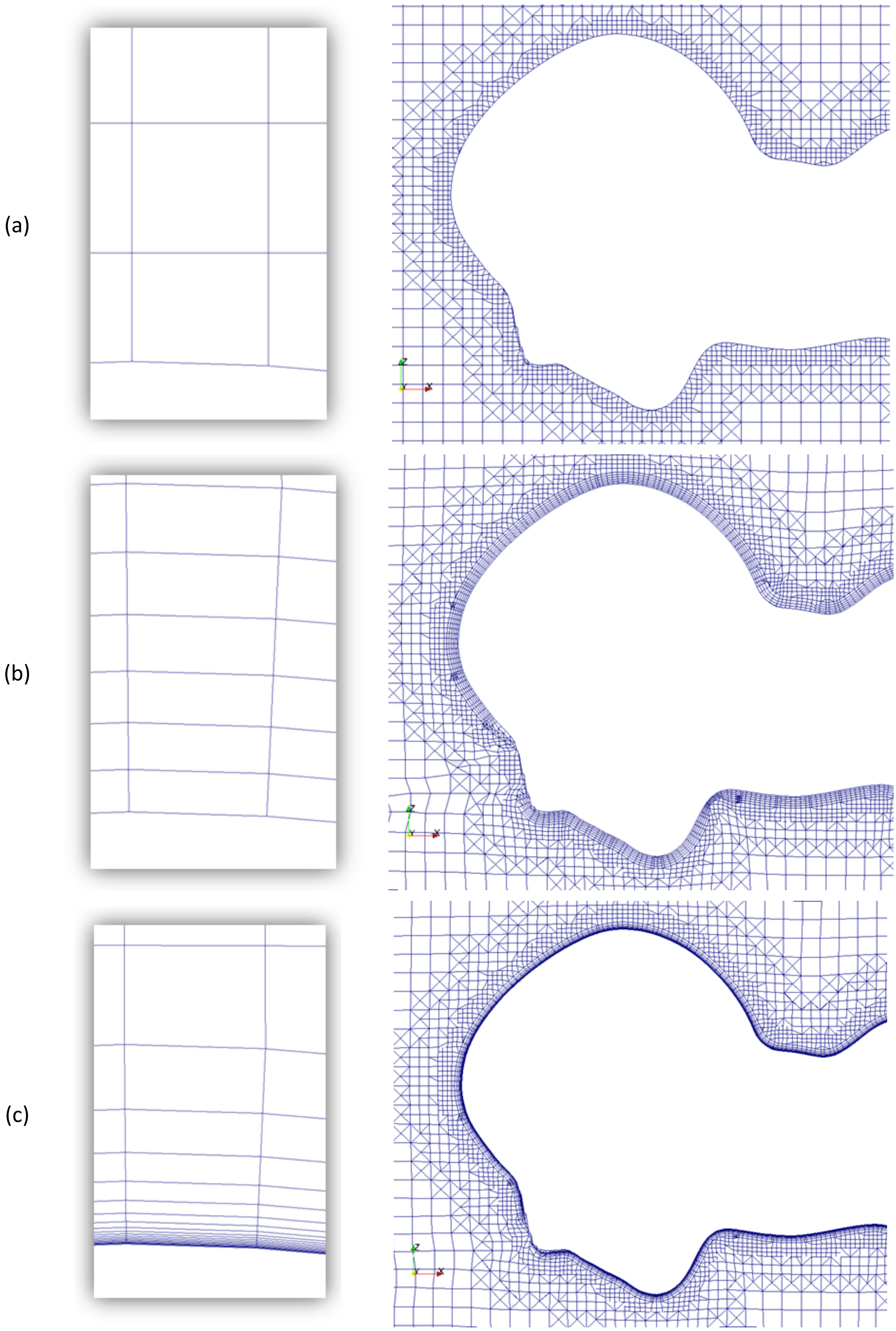

Figure 5-6 – Example of boundary layer mesh techniques: (a) snapped surface, (b) $y^+ = 40$ wall function layer, (c) $y^+ = 1$ fully resolved 2 stage layer.

The double layer process enables the cell expansion ratio within the inner boundary layer to be controlled without changing it throughout the entire layer structure. The importance of this is evident when we consider that as the layer mesh gets thicker (a consequence of having a small expansion ratio throughout the entire layer mesh) the increased displacement of the surrounding mesh can reduce the mesh quality sufficiently to stop localised layer growth entirely. This can give rise to patches of layer growth with a larger cell size in-between. In an attempt to avoid large step changes in near wall cell size, the layer mesh is tapered down as it approaches these points. This leads to significant regions of layer mesh being affected by locations where the layer fails to grow.

The two different types of boundary layer mesh were compared against a mesh without any additional layers. In all three cases additional mesh refinement was placed on the free surface (described later in section 5.4).

The impact of these different boundary layer meshes on the resistance acting on the body can be observed in figure 5-7. There is clearly a difference in both the skin friction (due to viscous shear stress on the body surface) and the pressure resistance components between the different meshes. In an attempt to understand the cause of these differences, the different components of resistance will be examined more closely.

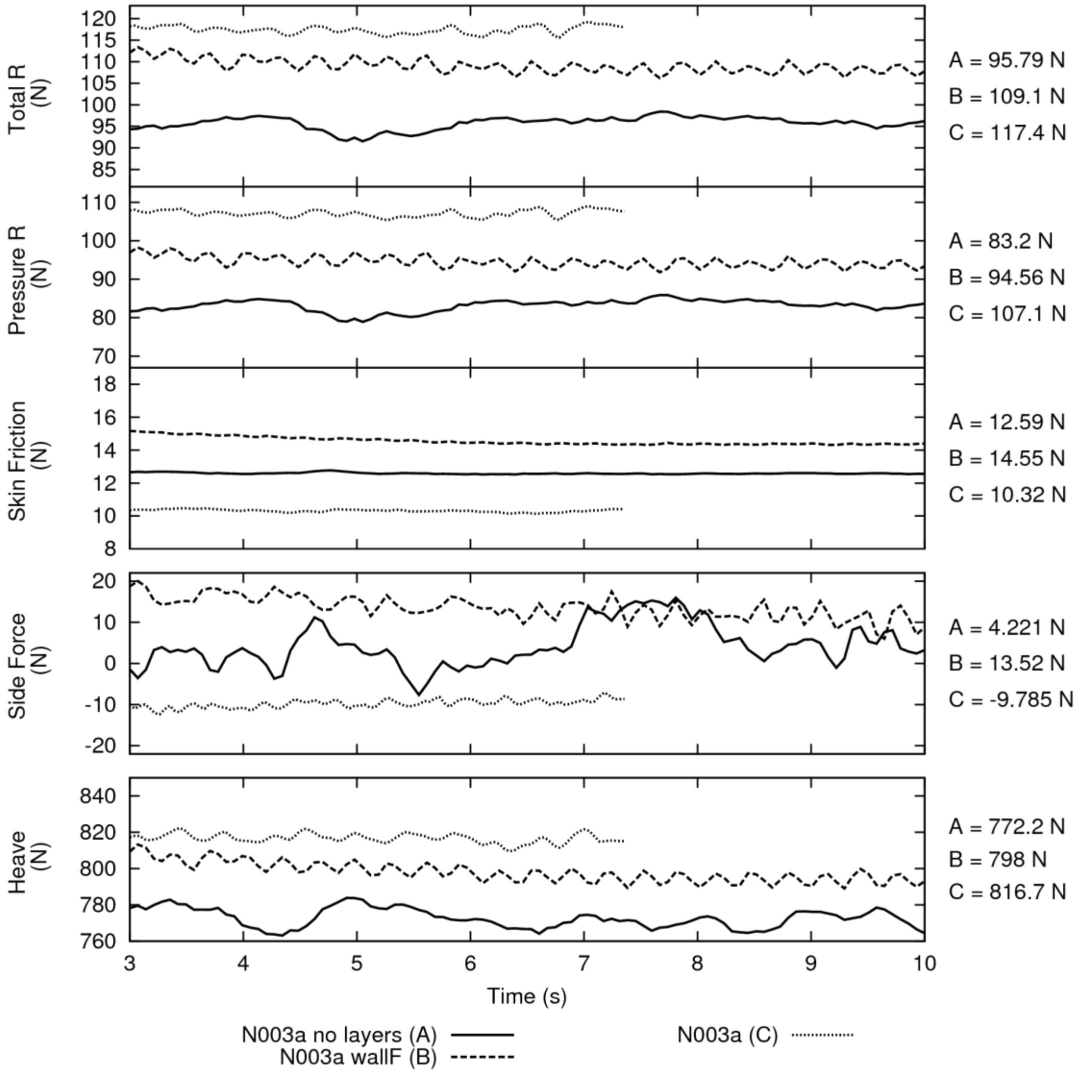

Figure 5-7 – Impact of different boundary layer mesh resolutions on the resistance components for case.

A local coefficient of skin friction resistance can be calculated as:

$$\mathrm{Cf\_x} = \frac{\tau_{\mathrm{w\_x}}}{\frac{1}{2}\rho U_0^2} \qquad 5\text{-}1,$$

where $\tau_{\mathrm{w\_x}}$ is the wall shear stress in the x-direction, ρ is the fluid density and U_0 is the free stream velocity. The wall shear stress can also be used to generate streamlines on the body which provides detail on the flow direction see figure 5-8.

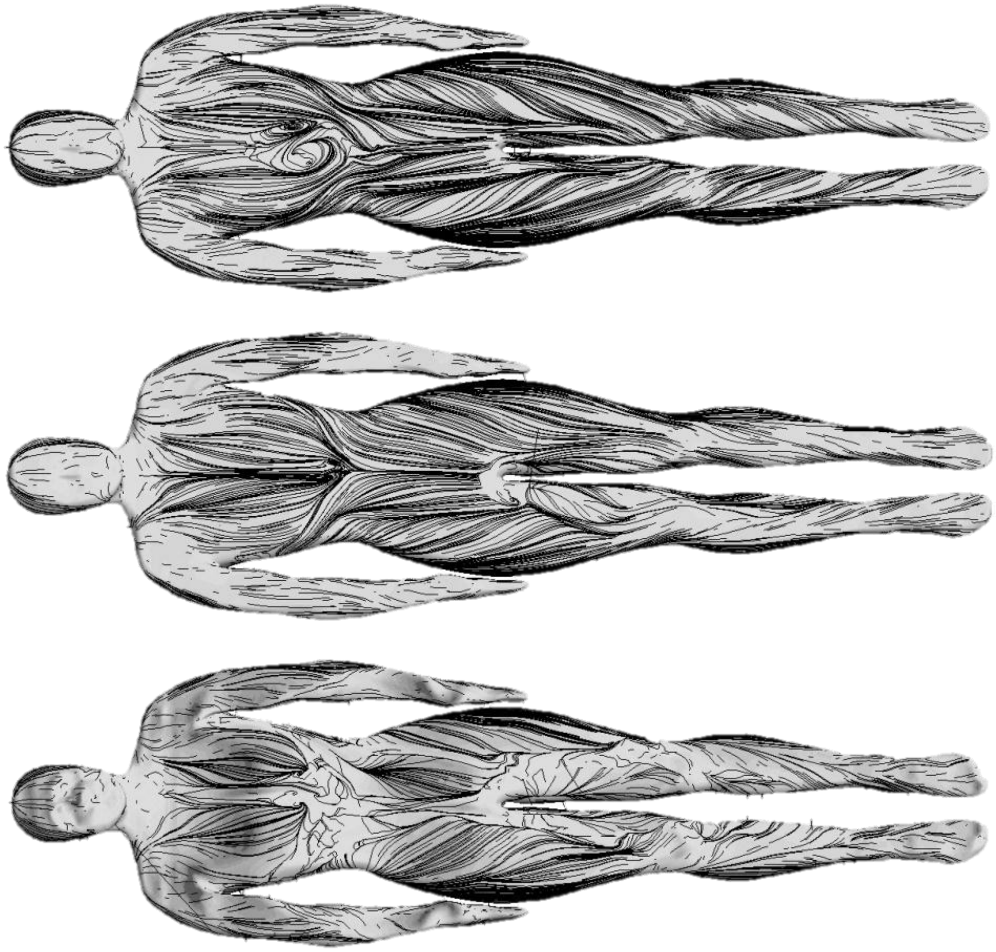

Figure 5-8 – Shear stress streamlines for different boundary layer resolutions viewed from below. No Boundary layer mesh (top), a wall function layer mesh (middle) and a fully resolved two stage layer mesh (bottom).

The most obvious differences between the near wall mesh resolutions can be observed in the surface streamlines. As the y^+ reduces, allowing more of the boundary layer physics to be captured, larger regions of separated flow appear on the body. This can be seen most clearly just beneath the chest, where the fully resolved boundary layer mesh captures a region of separation indicated by the reduced number of streamlines and the random nature of their direction. This represents the unsteady slow moving region of fluid that is created next to the body due to the boundary layer separating off the bottom of the chest. This has the impact of reducing the skin friction component of resistance while elevating the pressure resistance due to the increased size of the turbulent wake. A greater degree of asymmetry in the flow field is also observed as the boundary layer becomes better resolved. These asymmetries in the flow contribute to the significant variation in side force and are instigated by the non-symmetrical athlete geometry and instabilities in the flow. An example of this has been observed as vortical flow features originating from the head propagating down one side of the body.

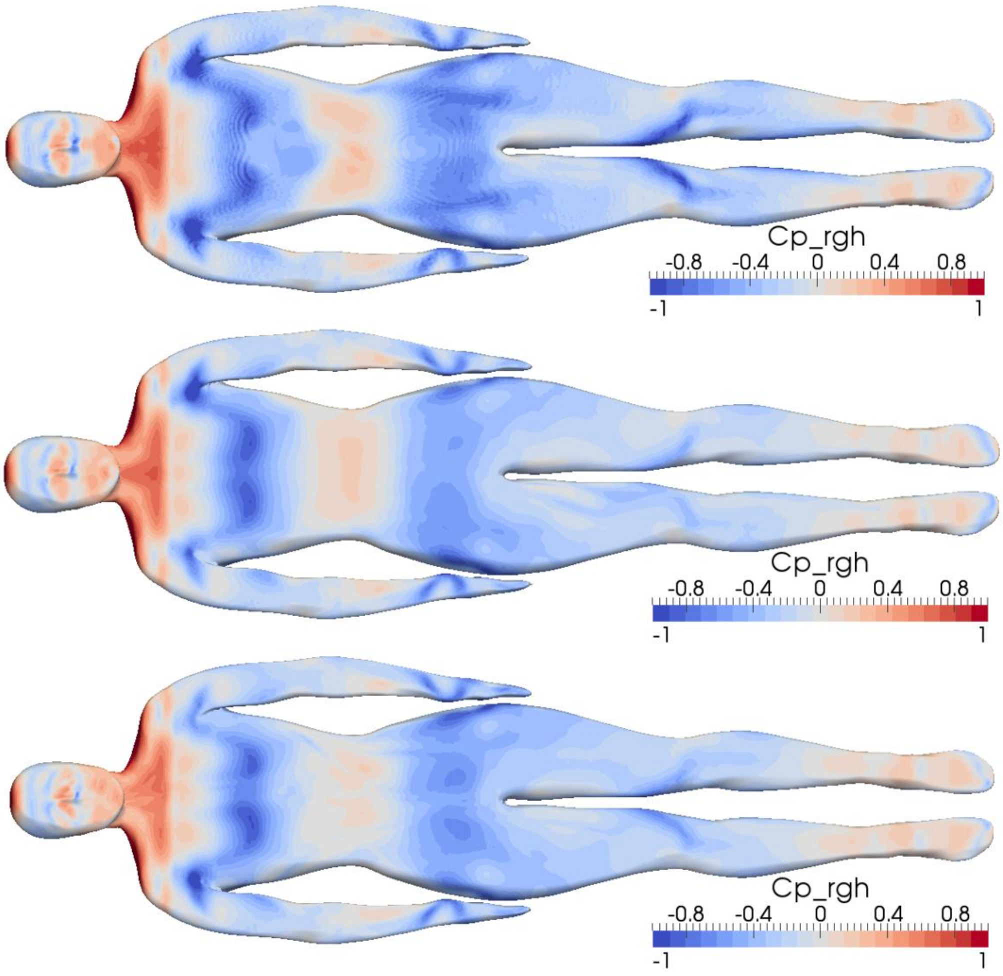

Figure 5-9 – Local coefficient of pressure (defined in equation 5-2) for no Boundary layer mesh (top), a wall function layer mesh (middle) and a fully resolved two stage layer mesh (bottom).

The pressure field around the swimmers body consists of both the dynamic pressure due to changes in the fluid velocity, and hydrostatic pressure associated with the depth below the free surface. The combined effects of the deformed free surface and the fluid velocity can be observed using a local coefficient of pressure defined as:

$$Cp\_rgh = \frac{p - \rho g h}{\frac{1}{2}\rho U_0^2} \qquad 5\text{-}2,$$

where *p* is the total pressure, g is the acceleration due to gravity and h is the distance from the undisturbed free surface. The hydrostatic pressure associated with the undisturbed free surface has been removed so that only the effect of the deformed free surface is observed.

The impact of the different boundary layer resolutions on the pressure field over the body can be seen in figure 5-9. The changes in pressure are much harder to identify but differences can be seen around the regions of separated flow, or other flow features observed in the surface streamlines. The effect these changes in pressure distribution have on the pressure resistance depends on their location on the body. To fully understand how these different pressure distributions result in changes to the pressure resistance a coefficient of pressure in the x-direction can be calculated as:

$$C_{px\_rgh} = C_{p\_rgh} S_n \tag{5-3}$$

where S_n is the surface normal in the x-direction. This provides a localised coefficient of total pressure resistance over the body. The impact of increases in separation on the pressure resistance can be seen in figure 5-10. As the boundary layer become better resolved the regions of high pressure resistance (low pressure behind the body) increase. This can be observed as increased regions of red behind the buttocks and in the armpits. A significant reduction in the pressure recovery (high pressure) on the feet is also observed as the boundary layer resolution increases.

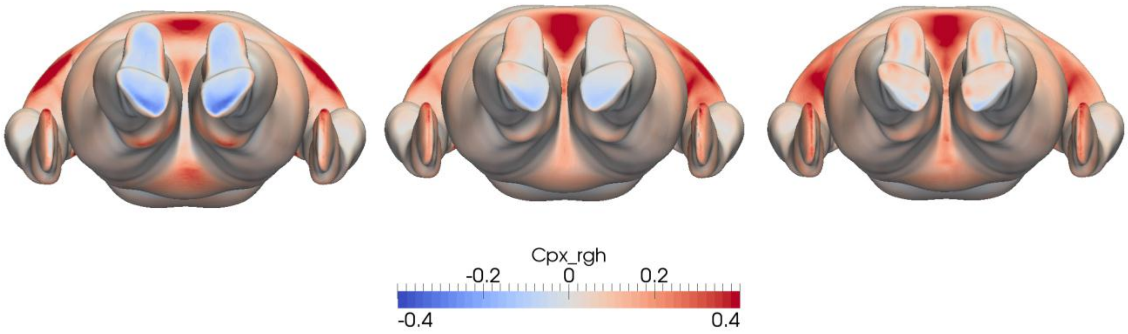

Figure 5-10 – Local coefficient of pressure resistance (defined in equation 5-3) for no boundary layer mesh (left), a wall function layer mesh (middle) and a fully resolved two stage layer mesh (right).

Based on the differences between different boundary layer modelling techniques it was concluded that a fully resolved boundary layer mesh was required to capture the complex separated flow observed around a swimmer's body. A brief study was conducted looking into the effect of increasing the mesh density within the inner boundary layer of a wall resolved mesh. This looked at increasing the number of cells within y^+ of 20 from 9 to 11 and 14. However this showed little change in resistance for a significant increase in mesh size. This correlates with the recommendation made in (WS Atkins Consultants, 2003) for at least 10 cells within a y^+ of 20 for a fully resolved boundary layer. Further details of this study can be seen in Appendix 4.

5.4 Free surface refinement

It has already been highlighted that the impact of the free surface interactions on the resistance components needs to be better understood. Therefore it is important that the interface between air and water is accurately captured within the simulations. Due to the fact that surface waves generally have small amplitudes compared to their wavelengths, the required cell size in the vertical direction is much smaller than those in the horizontal plane. Therefore it was decided to investigate the required vertical and horizontal mesh densities separately.

The primary aim of these investigations is to establish what mesh density is required to obtain an accurate representation of the free surface close to the swimmer. If the local free surface is well simulated than the pressure distribution over the body will be correct providing an accurate pressure resistance.

The simplest way to validate the local free surface deformation is to compare the simulated wave pattern against the experimental wave cuts. To achieve this requires the simulated waves to propagate out over the domain to the location of the wave probes. Achieving this wave propagation does not affect the local pressure distribution over the body but does allow direct experimental validation.

5.4.1 Vertical refinement study

To investigate the level of vertical refinement required for a swimmer a series of meshes were created with different levels of vertical refinement. To simplify matters this study was conducted without a boundary layer mesh and with a reduced level of refinement on the body surface. This allowed higher vertical refinement levels to be investigated while minimising the total mesh size. These meshes were created directly from the block mesh using the refineMesh utility to refine in the horizontal and vertical planes separately. This meshing process was developed by and is presented in (Bjorn, Turnock, & Hudson, 2012). This generated the high aspect ratio cells required for the free surface and standard square cells near the body. SnappyHexMesh was then used to remove the cells within the body and snap those left to the STL surface.

Three different vertical refinement levels (5, 6 and 7) were investigated, providing a vertical cell height of (6.25, 3.125 and 1.5625)x10^{-3} m, on the free surface. These three meshes can be seen in figure 5-11. The free surface was refined over an equal distance above and below the free surface due to the requirement to resolve the significant deformations observed up and over the head.

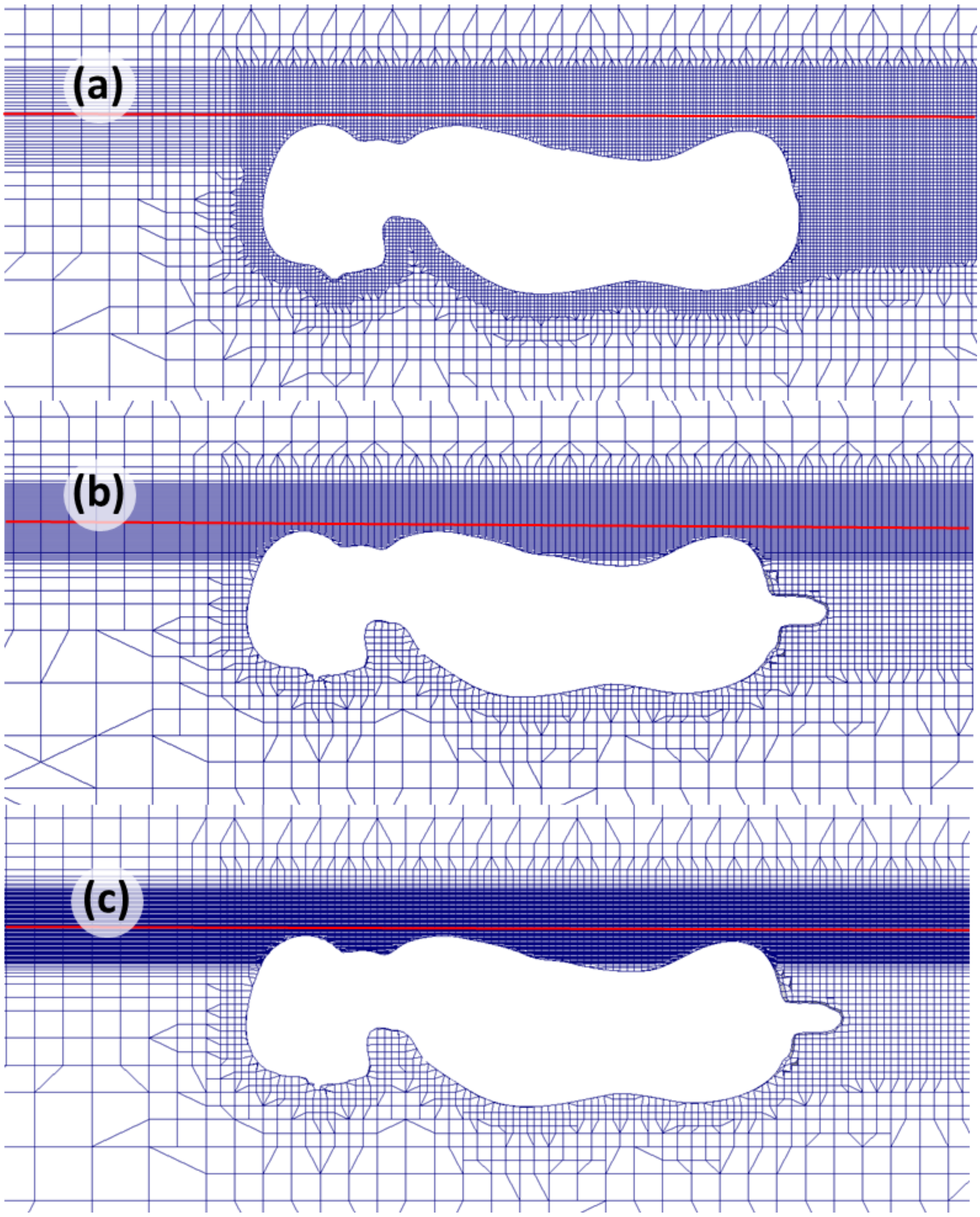

Figure 5-11 - Different meshes used for free surface vertical refinement study with refinement levels 5 (a), 6 (b) and 7 (c). The position of the nominal free surface is given in red.

The wave pattern generated by each mesh can be seen in figure 5-12. The two main impacts of the increased vertical refinement were to propagate the wave field a little further out behind the swimmer and to increase the entrainment of air from the breaking wave over the legs. This had the effect of making the free surface behind the swimmer more unsteady and disturbed. From the pictures of the experimental test cases (provided in section 3.2.1) it can be seen that in reality this region is extremely turbulent and unsteady with lots of entrained air bubbles.

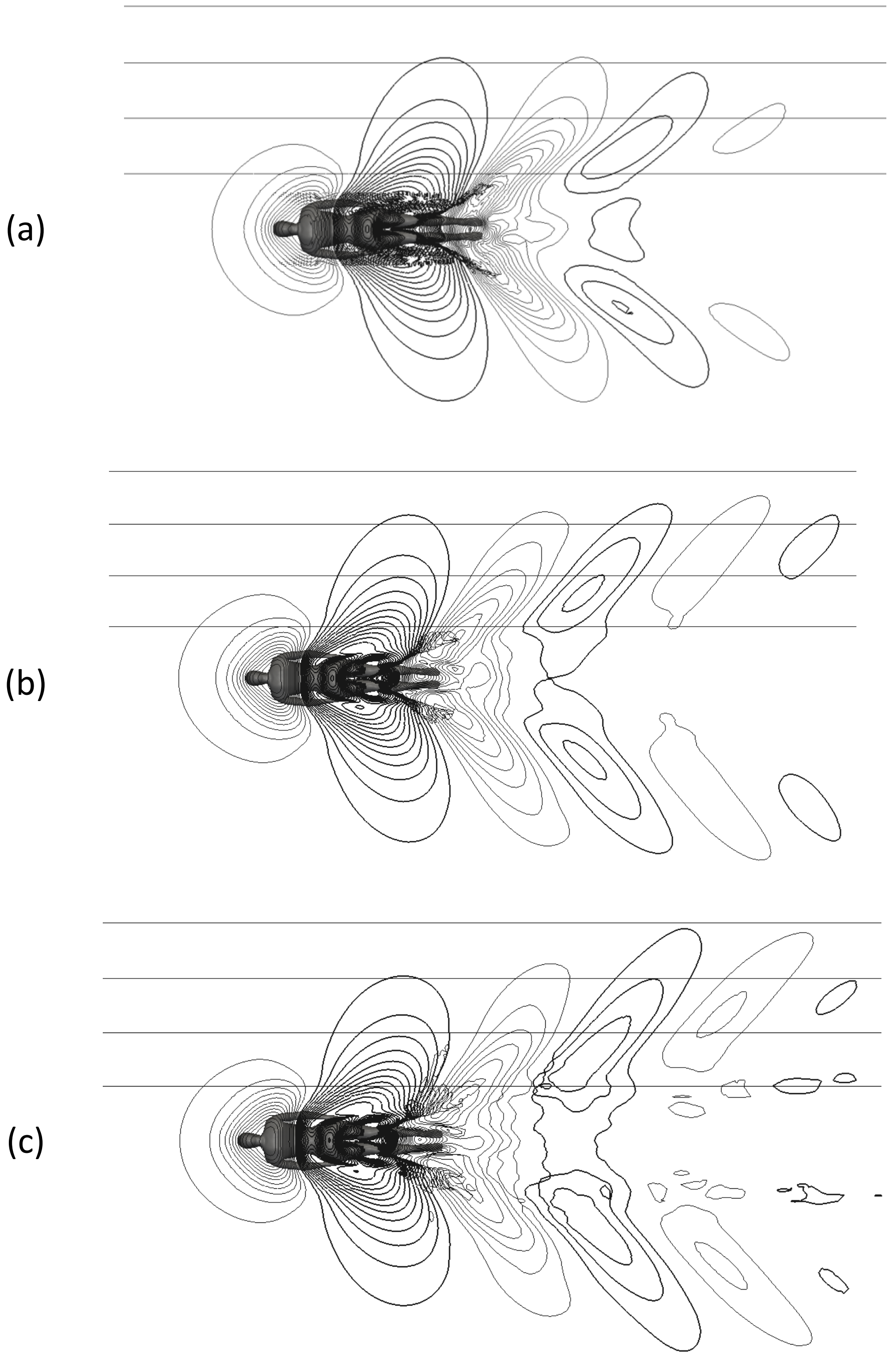

Figure 5-12 – Impact of vertical mesh refinement on free surface deformation, for case N003, with contours every ±0.005m (bold contours are wave troughs). Vertical refinements of 5, 6 and 7 are displayed in (a), (b) and (c) respectively. Wave cut positions at y=0.5, 1, 1.5 and 2 are also shown.

Both the increased wave propagation and the entrained air can be seen in the wave cuts presented in figure 5-13, which allows a direct comparison between the different meshes. The entrained air within the breaking wave around the feet can be seen as separate sections in the wave cut at y=0.5, for refinement level 7. The wave height is maintained more effectively at greater distances from the body with increased vertical refinement. The apparent lack of mesh convergence is due to the new physics of wave breaking and air entrainment being resolved with the increased mesh density.

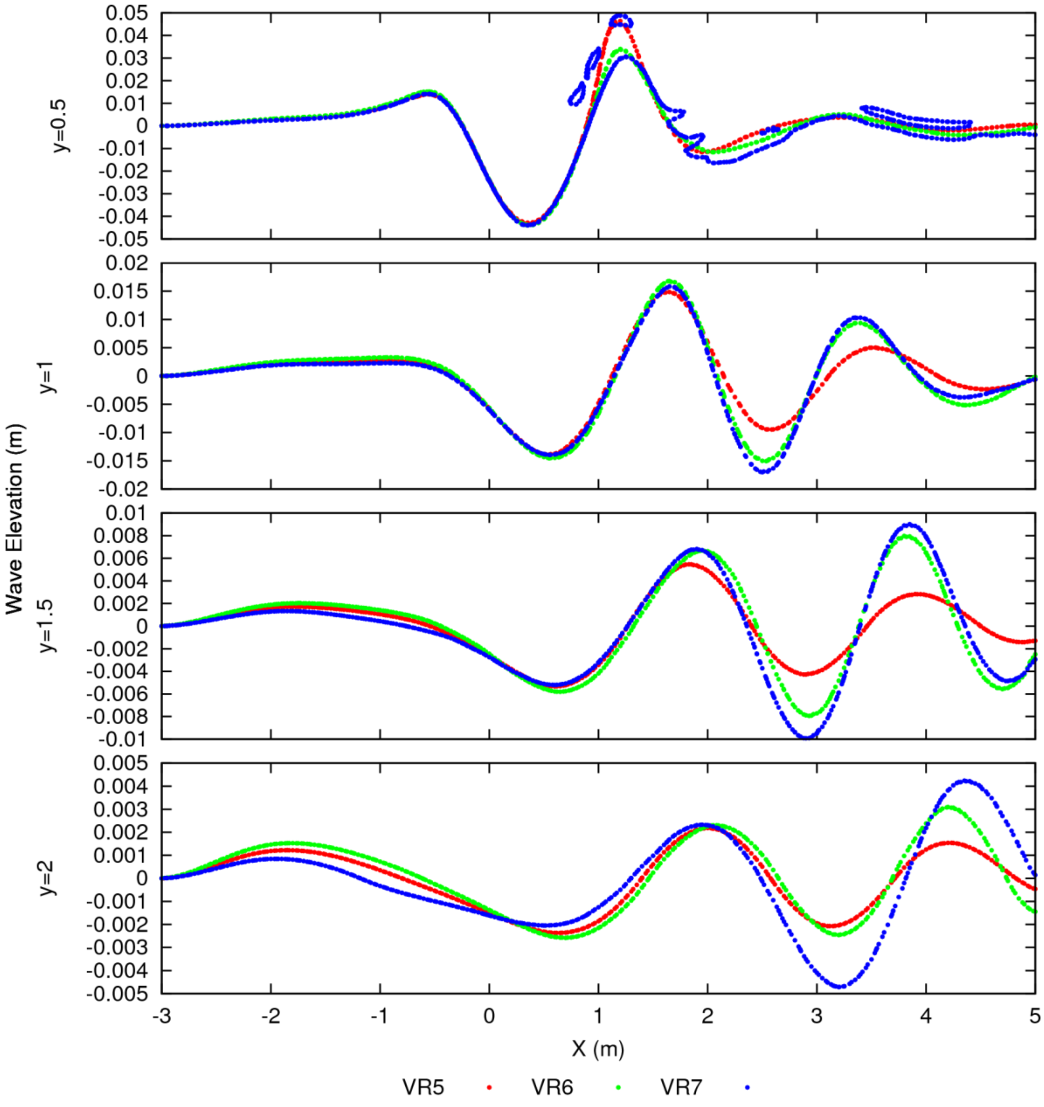

Figure 5-13 - Free surface wave elevation at four different lateral locations from the body centreline (depicted in figure 5-12). Different levels of vertical mesh refinement are displayed (5, 6 and 7) representing meshes (a), (b) and (c) respectively.

5.4.2 Comparison with thin ship/experimental results

Despite some improvements in wave propagation and free surface fidelity with increased vertical refinement, the observed far field wave amplitude from all three meshes is significantly smaller than that measured experimentally (presented in section 3.2.1).

The experimental wave cut two metres from the body centreline corresponds to the outer wave cut in figure 5-12 and figure 5-13. However by this point in the simulations the waves have almost entirely dissipated. Therefore to enable some comparison to be made to the experimental data, thin-ship theory has been used. Thin-ship theory provides an inviscid solution for the wave pattern using the same geometry as used in the full RANS simulations (see chapter 4.2 for more details). The comparison of the simulated wave cuts to thin ship and the outermost experimental wave cut can be seen in figure 5-14 Thin-Ship theory appears to capture the general shape and position of the first wave trough, although there are some marked differences in the wave amplitude. However as the Thin-Ship solution is inviscid it will fail to capture any wave breaking, which would lead to it over predicting the wave heights. It also appears from the shape of the wave cuts that the experimental data for y=2 m has a better fit to the Thin-Ship data at y=1.5 m. This could indicate that the athlete had veered off from the centreline in the experiment. This comparison tells us that the thin-ship solution can capture the correct wave shape but will over predict the amplitude. This allows us to then make comparisons between the CFD data and the thin-ship solution closer to the swimmer's body.

Close to the body the CFD simulation captures the stern wave position and shape with a reasonable degree of accuracy, allowing for the expected reduction in amplitude compared to the thin-ship prediction. It is clear however that beyond the first wave cut the simulated waves are being dissipated artificially. It is also apparent that increasing the vertical free surface refinement has little impact on this process. This indicates that something else is responsible for the lack of wave propagation.

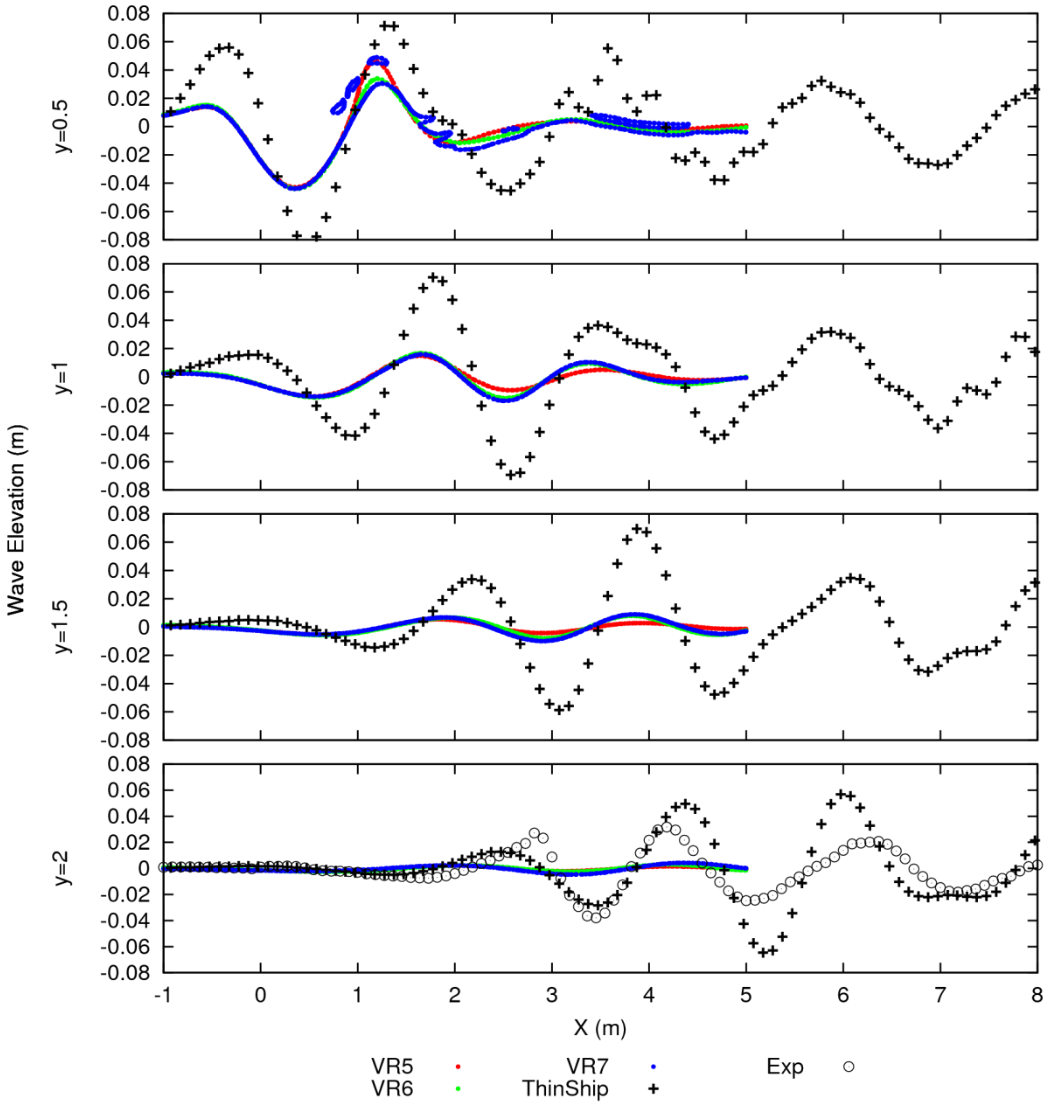

Figure 5-14 – Impact of vertical mesh refinement on free surface wave elevation at four different lateral locations from the body centreline. Different levels of vertical refinement (5, 6 and 7) are displayed VR5, VR6 and VR7 respectively, whilst experimental and thin-ship data is represented by data points.

5.4.3 Comparison to G2010 Mesh statistics

The current mesh settings were compared to those used in the Gothenburg 2010 submission (Banks et al., 2010) in an attempt to understand which features of the mesh may be affecting the wave propagation. In the work submitted to this workshop a simulated wave pattern for a container ship is presented that agrees closely with both experimental wave cuts and free surface contour plots. The research paper that formed part of this submission is included in Appendix 1. The non-dimensional mesh parameters that were used are provided in figure 5-15. The horizontal cell dimensions are presented as the number of mesh points per fundamental wavelength (ppwl) along the static water line. This can be calculated as

$$ppwl = \frac{2\pi(Fn)^2}{\Delta x/_{Lpp}} \qquad 5\text{-}4.$$

The vertical cell height (Δz) is divided by the length of the ship (Lpp). The location within the domain is provided relative to the ship length.

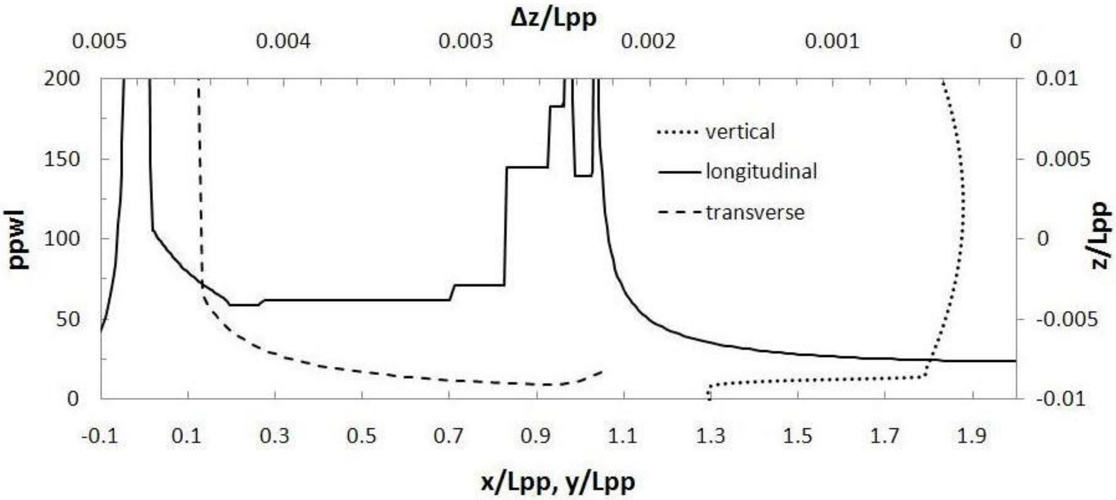

Figure 5-15 - Non-dimensional cell sizes used in the Gothenburg 2010 submission for wave pattern around a container ship.

From figure 5-15 we can determine that a vertical cell size of Δz/Lpp equal to 0.0003 was used (see axis along the top of the figure and the dotted line). This equates to approximately 33 cells over the experimental wave height. However, most of the other submissions (Larsson et al., 2010) had values of Δz/Lpp in the range of 0.001 to 0.0005 (10-20 cells over the wave height).

Table 5-3 provides the same non-dimensional mesh statistics for different refinement levels applied to case N003. A vertical refinement level of 6 or 7 provides a greater number of cells across the wave height than was used in the Gothenburg 2010 submission indicating that a vertical refinement level of 6 should be adequate for wave propagation throughout the domain. This explains why refining beyond this point produced little change.

Table 5-3 - Mesh parameters for different refinement levels for case N003 (length 1.86 m, velocity 1.86 $^{ms-1}$,measured wave height 0.14 m).

Refinement Level	cell size (m)	ppwl	Δz/Lpp	cells/wave height
1	0.1	22.15832	0.053763	1.4
2	0.05	44.31663	0.026882	2.8
3	0.025	88.63326	0.013441	5.6
4	0.0125	177.2665	0.00672	11.2
5	0.00625	354.5331	0.00336	22.4
6	0.003125	709.0661	0.00168	44.8
7	0.0015625	1418.132	0.00084	89.6

If we look at the horizontal mesh parameters typically presented at Gothenburg, 50 to 75 cells per fundamental wave length (ppwl) were used by submissions in the longitudinal direction alongside the hull. This increased to 150-200 at the bow and stern and drops off to approximately 20 further astern of the hull (see figure 5-15 and (Larsson et al., 2010)). In comparison the meshes used in the vertical refinement study have a horizontal refinement level of 2 over the majority of the free surface. In table 5-3 we can see that this equates to 44 cells per fundamental wavelength (based on a fundamental wave length of 2.2m, using a body length of 1.86 m). However as previously discussed in Chapter 3.3 it is clear that for a swimmer much of their body is partially submerged which may significantly reduce their effective length. This appears to be observed in both cases N003 and DA003 where the dominant stern wave system is generated forward of the feet. This would have the overall effect of reducing the number of cells per fundamental wavelength for the same refinement level. With this in mind it appeared that the horizontal refinement level used in the vertical refinement study was lower than that used in Gothenburg and that this should be investigated further.

5.4.4 Horizontal refinement study

A new series of meshes were created with a vertical refinement level of 6 on the free surface and horizontal refinement levels of 2, 3 and 4 respectively. Due to the greater impact horizontal refinement has on the total mesh size this refinement was limited to regions of the free surface where the waves were expected to propagate. The three resulting meshes can be seen in figure 5-16.

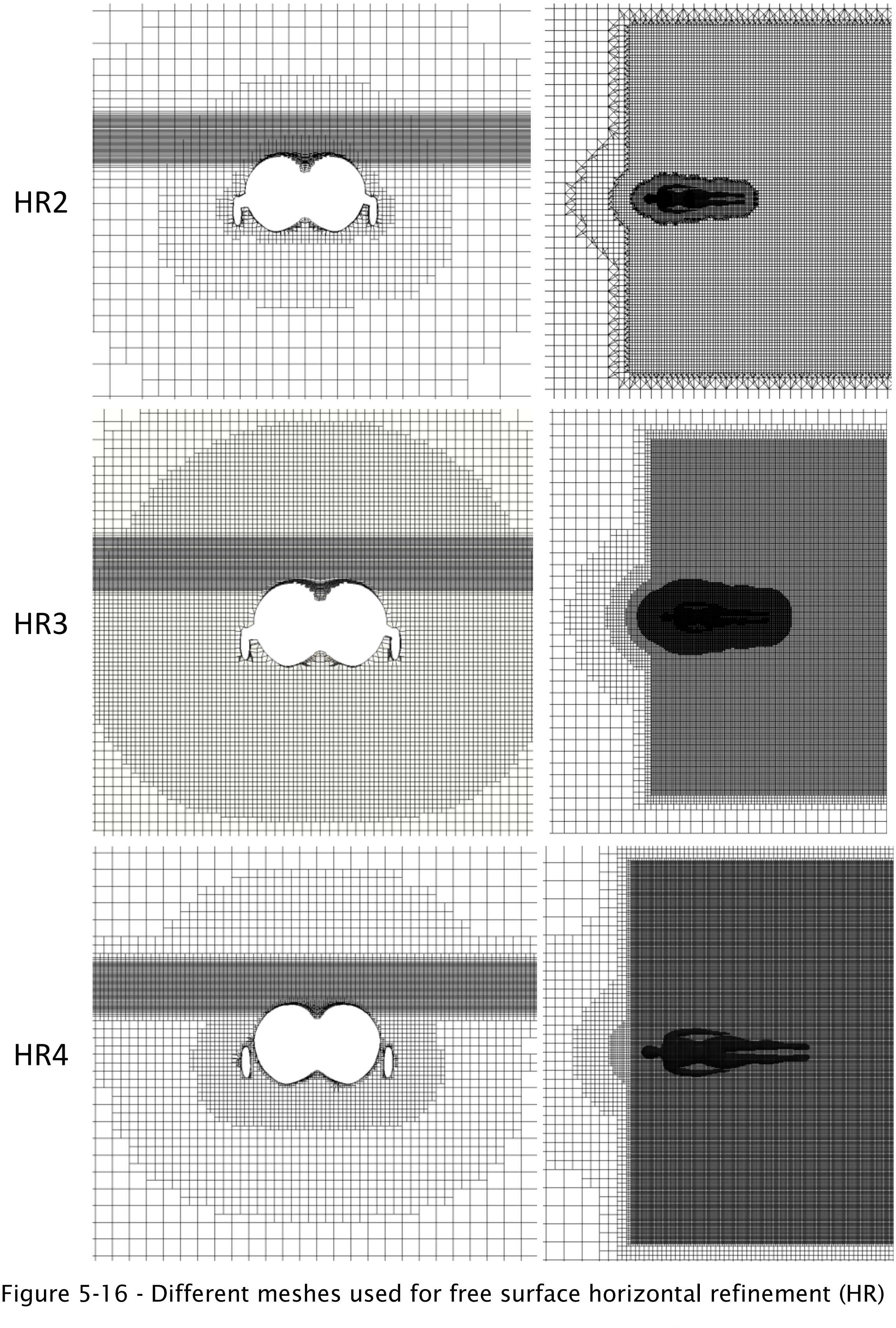

Figure 5-16 - Different meshes used for free surface horizontal refinement (HR) study with refinement levels 2, 3 and 4. Transverse view of the mesh at the hips on the left and view from above on the right.

The impact of the horizontal mesh refinement on the free surface deformations can be viewed in terms of free surface contour plots in figure 5-17 and wave cuts in figure 5-18. The surprising outcome of this study is that the coarsest horizontal refinement of 2 actually produces the largest wave elevations away from the swimmer. In fact this mesh (HR2) appears to generate a significantly different wave field compared to all the other simulations. Key differences can be observed in the form of the breaking wave field over the legs. The rooster tail type wave that is generated in the finer meshes does not form in HR2. Instead a much broader wave field appears to form with a larger diverging wave angle from the centreline. This propagates much further through the domain, as can be seen in the first appearance of a simulated wave in the y=2 m wave cut in figure 5-17. This poses the question why a lower mesh resolution would appear to generate a wave profile that agrees better with experimental and thin-ship data.

Bases on observations of the simulated free surface features it is hypothesised that wave breaking is dissipating energy from the wave pattern, preventing it propagating out through the domain.

Although there appears to be more wave breaking in HR2 than the other cases, it can be seen that this actually occurs further away from the body. Close to the swimmer the free surface appears to form uneven humps and hollows rather than the rooster tail type wave that forms on the finer meshes. Indeed as the horizontal refinement is increased the rooster tail type wave becomes more clearly defined. It is therefore thought that the wave propagation observed in case HR2 is actually due to the mesh being coarse enough near the swimmer to prevent sharply defined breaking waves to form. This would explain why increasing the refinement level on the free surface has little impact on the wave propagation throughout the domain.

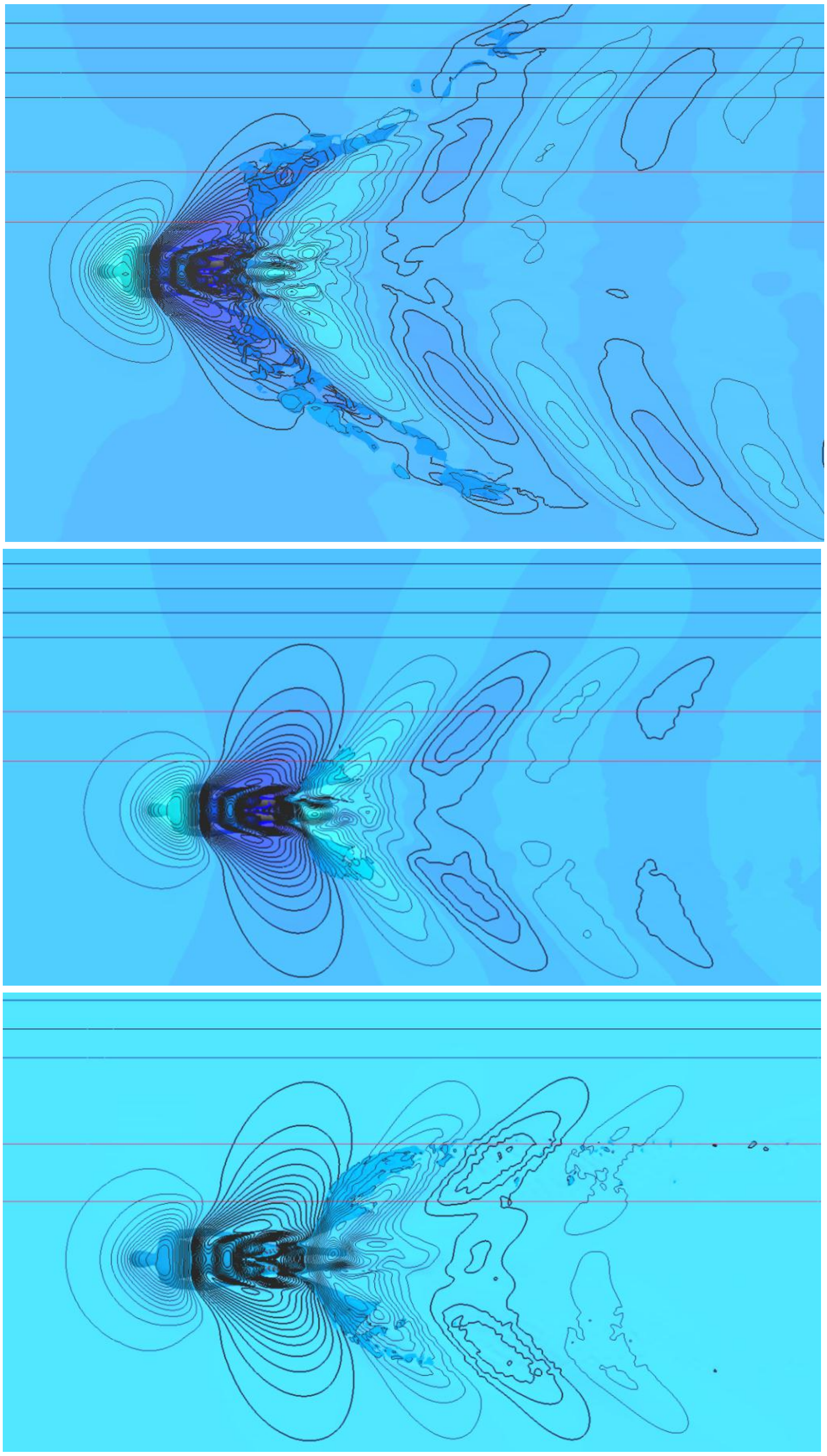

Figure 5-17 – Influence of horizontal mesh refinement on the free surface deformation, with contours every ±0.005m (bold contours are wave troughs). Horizontal refinement levels HR2 (top), HR3 (middle) and HR4 (bottom).

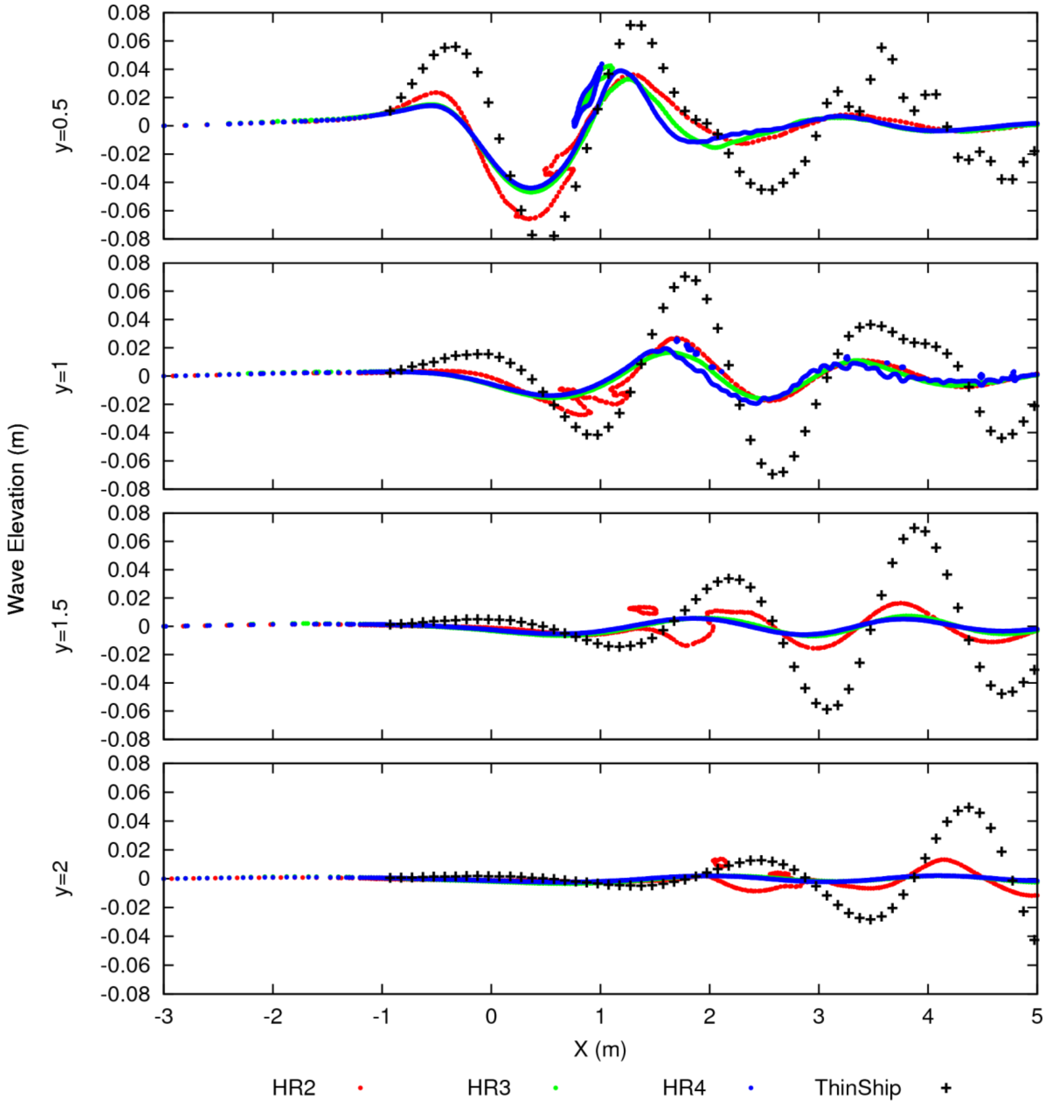

Figure 5-18 - Impact of horizontal mesh refinement on free surface wave elevation at four different lateral locations from the body centreline. Different levels of horizontal refinement (2, 3 and 4) are displayed as HR2, HR3 and HR4 respectively, whilst thin-ship data is represented by data points.

5.4.5 Conclusions

The inability of the implemented volume of fluid method to fully simulate the physics of the breaking wave field was identified as a potential weakness of the free surface method. However as long as the local free surface flow is simulated well enough to initiate the correct breaking wave features this should indicate the correct pressure force is captured on the body. Therefore it appears that the free surface flow will have to be validated based on the local free surface features observed in the experimental test cases, rather than comparisons with experimental wave cuts.

It was decided to maintain the free surface refinement levels at 6 in the vertical direction and 2 in the horizontal direction as increasing the mesh resolution over the entire free surface is unlikely to result in any improvements in wave pattern resolution. Greater mesh refinement was placed close to the geometry to ensure the pressure and local free surface field is correctly captured.

5.5 Separated zones

Due to the bluff body nature of a swimmer's body the flow is largely dominated by separated regions. This gives rise to the large unsteady wake region that is observed behind the athlete in both passive cases (see section 3.2). So far the mesh refinement process has focused on the near wall region and the free surface. Therefore the final stage of mesh development is to put an additional refinement region behind the swimmer to enable this turbulent wake to propagate downstream. The refinement distances out from the surface of the body were also increased to ensure separated regions and the local free surface features, were correctly captured.

5.6 Final Mesh Structure (N003a_A)

The final mesh structure combined the best features of the different mesh investigations providing:

- refinement levels of 6 on the body and 5, 4, 3 and 2 within a distance of 0.03, 0.1, 0.4 and 0.8m off the body;
- a double layer mesh, fully resolving the boundary layer down to a $y^+=1$ on the wall;
- a horizontal refinement level of 2 within a bounding box of ((-1.5, -1, -0.1)(3, 1, 0.1)) on the free surface;
- a vertical refinement level of 6 on the free surface;
- and a wake refinement level of 4 within the bounding box ((0, -0.3, -0.3)(4, 0.3, 0.1)).

The details of this final mesh structure along with each of the meshes used in this thesis are presented in Table 5-4 in section 5.2.6.

SnappyHexMesh is unable to apply uni-directional refinement, so the free surface refinement had to be applied separately. The simplest way to achieve this, whilst still maintaining the boundary layer mesh was to add the vertical refinement after running SnappyHexMesh. This way the boundary layer mesh is unaffected.

This process is achieved using the refineMesh utility built into OpenFOAM1.6x, which allows refinement in a single direction. To allow a uniform vertical refinement level to be generated over the free surface the selection of cells has to take account of their current refinement level. Therefore the cells to be refined are selected based on two parameters; firstly their distance from the free surface and secondly; their refinement level (provided by snappyHexMesh). This allows multiple vertical refinements to be made, gradually bringing the entire free surface to the same vertical refinement level while maintaining the original horizontal levels. This process can be seen in figure 5-19.

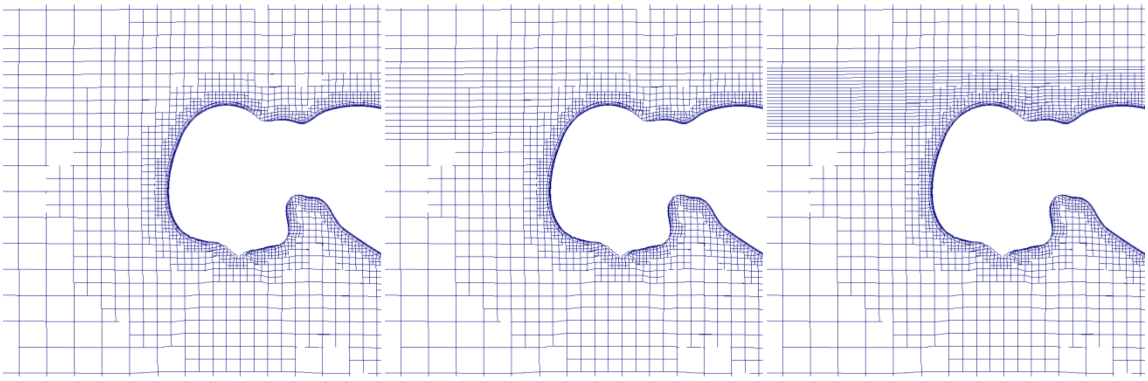

Figure 5-19 – Free surface refinement process from left to right.

The entire meshing process can be summarised as the following stages:

1. Create a blockMesh of uniform cell size.
2. Refine the mesh based on defined refinement levels and zones.
3. Remove any cells contained within the swimmer geometry STL.
4. Snap the remaining cell nodes to the surface of the geometry.
5. Grow the outer boundary layer zone of cells out from the geometry's surface.
6. Grow the inner boundary layer zone of cells out from the geometry's surface.
7. Refine the free surface region in stages until uniform vertical refinement levels are achieved:
    a. Select cells near the free surface.
    b. Discard those cells with the desired vertical refinement level.
    c. Refine selected cell in the vertical direction.
    d. Repeat stages a-c.

The resulting mesh structure can be seen in figure 5-20.

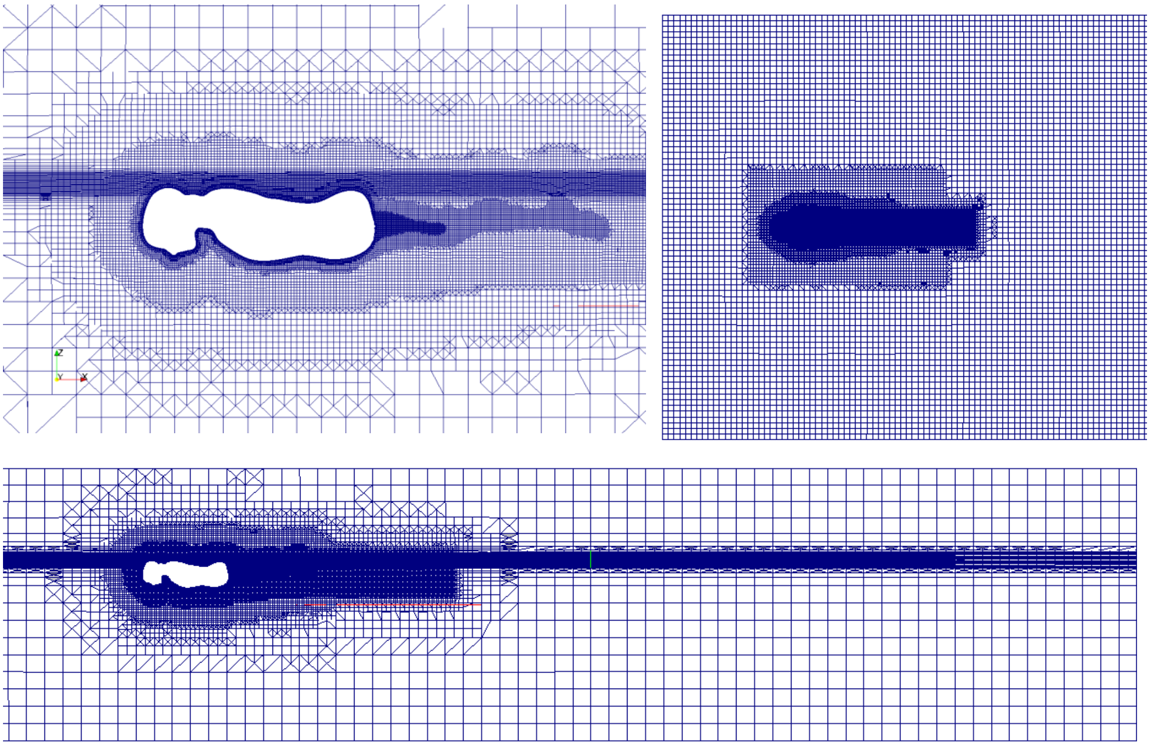

Figure 5-20 - Final mesh structure (N003a_A) viewed from both the side (left and bottom) and above looking at the undisturbed free surface (right).

5.6.1 Global mesh refinement study

To enable the final mesh structure to be assessed in terms of grid uncertainty a series of meshes were generated, maintaining the underlying structure but varying the mesh density as uniformly as possible. This was achieved by changing the basis cell size within the original blockMesh by a factor of √2. The refinement process that is then conducted on this blockMesh remained exactly the same as outlined in section 5.2.4.

Due to the sensitivity of the layer growth process to the surface mesh density a few modifications were required to build the new meshes. In the fine mesh only the outer boundary layer mesh was modified to reduce the expansion ratio by a factor of √2. The inner layer settings were unaltered to achieve the same surface coverage of the boundary layer mesh.

The two coarser meshes failed to consistently build the two stage layer mesh. Therefore a single stage wall resolved boundary layer mesh was implemented with the mesh density adjusted accordingly to the √2 reduction in cell size.

In all the mesh refinement study meshes a $y^{+}=1$ on the surface of the swimmer was used.

5.7 Different meshes used throughout thesis

To allow a comparison to be made between the different meshes used in this work the key parameters used to create them are summarised in table 5-4.

Table 5-4 - Meshes used

Mesh	Description	No of Cells (M)	Base Cell Size (m)	Refinement levels (RL) for different locations				Boundary Layer Mesh	CPUh/s *
				Distance of RL 6,5,4 & 3 from body (m)	Wake Box	Free Surface			
						Vertical	Horizontal		
Mesh Development:									
N003a	Wall resolved BL	4.63	0.2	0.01, 0.02, 0.1 & 0.2	None	6	2	2 zones (y+ = 1)	1320
N003a_wallF	wall function	2.5	0.2	0.01, 0.02, 0.1 & 0.2	None	6	2	Single zone (y+ = 40)	1350
N003a no layers	No boundary layer mesh	1.52	0.2	0.01, 0.02, 0.1 & 0.2	None	6	2	None	120
VR5	FS vertical refinement 5	2	0.2	RL 5 on the body	None	5	2	None	
VR6	FS vertical refinement 6	1.8	0.2	RL 4 on the body	None	6	2	None	
VR7	FS vertical refinement 7	3.33	0.2	RL 4 on the body	None	7	2	None	
HR2	FS horizontal ref. 2	1.85	0.2	RL 4 on the body	None	6	2	None	
HR3	FS horizontal ref. 3	5.6	0.2	RL 4 on the body	None	6	3	None	
HR4	FS horizontal ref. 4	10.4	0.2	RL 5 on the body	None	6	4	None	
Mesh Sensitivity:									
N003a_A_Vcoarse	√2 mesh reduction	0.72	0.4	0.01, 0.04, 0.2 & 0.4	Yes	6	2	Single zone (y+ = 1)	50
N003a_A_coarse	√2 mesh reduction	1.85	0.283	0.01, 0.04, 0.2 & 0.4	Yes	6	2	Single zone (y+ = 1)	170
N003a_A	Final Structure	5.7	0.2	0.01, 0.04, 0.2 & 0.4	Yes	6	2	2 zones (y+ = 1)	2160
N003a_A_fine	√2 mesh refinement	14.6	0.141	0.01, 0.04, 0.2 & 0.4	Yes	6	2	2 zones (y+ = 1) refinement applied to outer zone only	13550
Final Meshes:									
N003a_A	N003 on surface	5.7	0.2	0.01, 0.04, 0.2 & 0.4	Yes	6	2	2 zones (y+ = 1)	2160
N003a_A-1m	N003 submerged	5.5	0.2	0.01, 0.04, 0.2 & 0.4	None	6	2	2 zones (y+ = 1)	1800
DA003_A	DA003 on surface	6.85	0.2	0.01, 0.04, 0.2 & 0.4	Yes	6	2	2 zones (y+ = 1)	2380
DA003_A-1m	DA003 submerged	6.46	0.2	0.01, 0.04, 0.2 & 0.4	None	6	2	2 zones (y+ = 1)	3170
C009	N003a but with extra refinement for arms	4.63	0.2	0.01, 0.02, 0.1 & 0.2	None	6	2	2 zones (y+ = 1)	1084

* CPU hours per second of absolute simulation time (on average 5-10 seconds of flow simulated to produce time averaged results)

5.8 Numerical Modelling

The numerical settings used within the RANS simulations are outlined in table 5-5. These were maintained across the full range of simulations presented in this work.

The turbulence boundary conditions applied on the surface of the swimmer were automatic wall functions that switch on if the y^+ is greater than a value of 5 (i.e. outside the viscous sub-layer). When the y^+ is less than 5 they switch off and the boundary layer is fully resolved.

Table 5-5 - Numerical settings

Property	**Mesh**
Type of mesh	Unstructured (Hexahedral)
No. of elements	5.7M for N003a_A
y+ on the body	Approximately 1
	Domain physics:
Fluid	Homogeneous water/air multiphase, kOmegaSST turbulence model
Inlet	Free stream velocity of 1.86m/s, buoyantPressure, k = 0.1 m^2s^{-2}, omega = 2 s^{-1}
Outlet	*U*=Zero gradient, *P*=static pressure
Bottom/sides	Wall with velocity set to free stream value U_0 , buoyant pressure
Top	Opening
body	Wall with no slip condition, buoyant pressure, automatic kqRWallFunction and omegaWallFunction
	Solver settings (interFoam):
Transient scheme	1st order Euler
Grad (U) Scheme	cellLimited Gauss linear 1
Div (U)	Gauss linearUpwind grad(U)
Pressure coupling	PIMPLE (in PISO mode)
Convergence criteria	P 1e-7, U 1e-8, k 1e-8, omega 1e-8
Multiphase control	Volume fraction coupling
Timestep control	max Courant No = 0.4, max Volume fraction Courant No = 0.4, No of alpha sub-cycles = 2.
	Processing Parameters:
Computing System	IRIDIS High Performance Computing Facility (University of Southampton)
Run type	Parallel (108 Partitions run on 9x12 core nodes each with 22 Gb RAM)
Wall Clock time	72 hours for 3.89 seconds of passive free surface simulation (N003a_A)

5.9 Mesh Sensitivity

The global mesh refinement study was conducted to assess the impact of mesh density on the simulated results. By evaluating how the forces on the body change as the mesh density is increased the potential error associated with the domain discretisation process can be visualised. Unfortunately this process was hampered by the meshing technique adopted. The ability of snappyHexMesh to grow layers out from the surface mesh on the body depends on the cell size on the body relative to the surface curvature. Therefore as the surface mesh resolution decreases it becomes harder to grow a continuous boundary layer mesh over the surface of the body.

5.9.1 Variation in hydrodynamic forces

The mean forces acting on the body for each mesh were calculated from the final three seconds of simulation, see table 5-6. In each case this period represented a variation of the forces about a steady mean.

Table 5-6- Mean forces on the swimmers body for varying mesh densities.

Mesh	No of cells (M)	Resistance (N)			Side force (N)	Heave (N)
		Total	Pressure	Viscous		
N003a_A_Vcoarse (i)	0.72	108.6	96.72	11.92	5.923	788.2
N003a_A_coarse (ii)	1.85	112.2	98.64	13.57	-2.774	786.9
N003a_A (iii)	5.7	115.6	106	9.566	-9.754	804
N003a_A_fine (iv)	14.6	117.6	108	9.669	-6.69	816.3

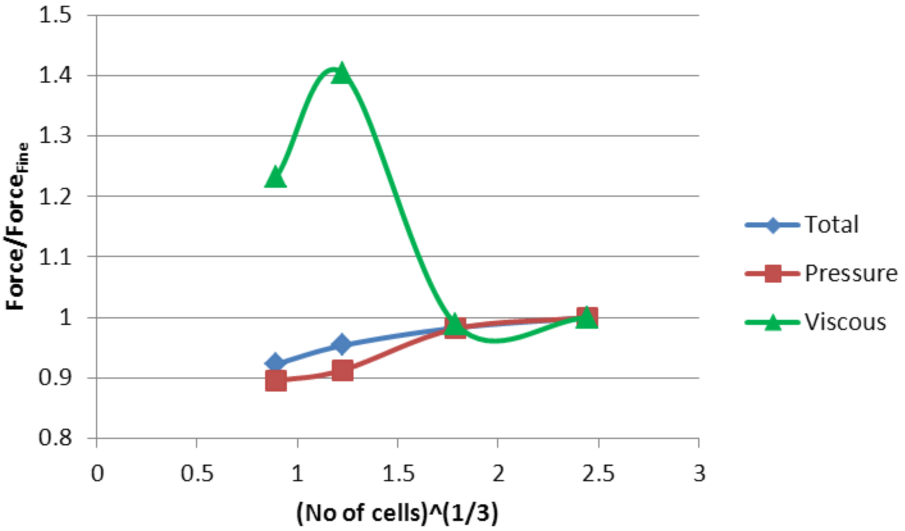

Figure 5-21 - Variation of resistance with mesh density.

The relative change of the resistance components compared to those of the finest mesh (iv) can be visualised in figure 5-21. Despite the apparent convergence of the pressure, and therefore the total resistance, there appears to be oscillation in the viscous resistance. This is best understood by looking at surface layer mesh grown in each case.

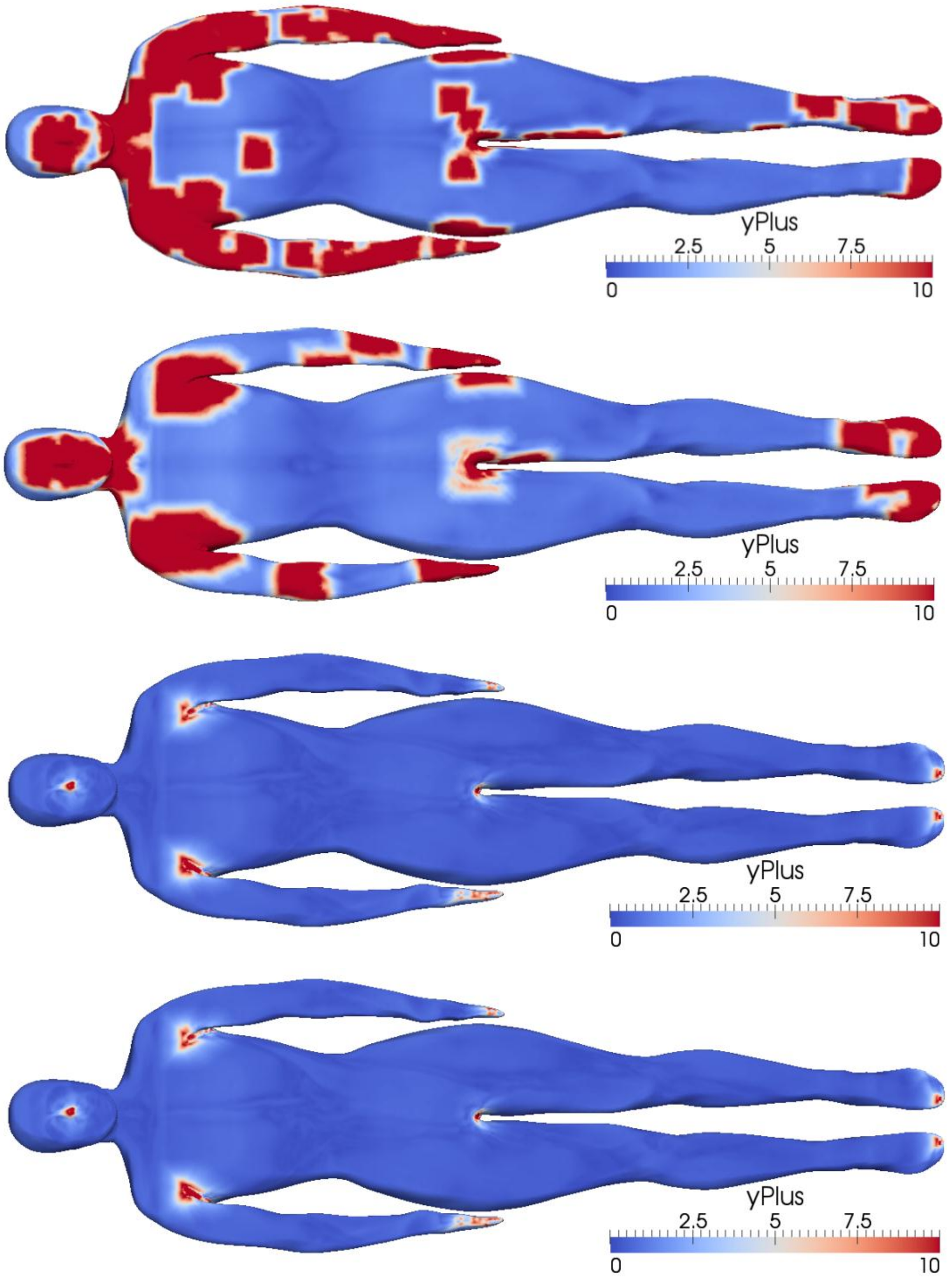

Figure 5-22 - y^+ for different mesh density cases, from top to bottom (i), (ii), (iii) and (iv).

One of the effects of increasing the cell size of the surface mesh over the body is the reduced resolution of high areas of curvature. As the relative angle between surface cells increases it becomes more difficult to build a comprehensive layer mesh over the entire body. This leads to the areas without a layer mesh increasing in size and occurrence. This can be seen in figure 5-22 as increased areas of high y^+ values on the coarser meshes. Mesh (ii) still maintains good layer growth over most of the torso and legs; however with the coarsest mesh (i) layer mesh growth starts to break down at random points over the torso and legs.

The effect of the breakdown in layer mesh growth on skin friction can be seen in figure 5-23 as patches of reduced skin friction coefficient, corresponding to the areas of increased y^+. The effect of globally reducing the mesh density (and therefore increasing the cell expansion ratio within the layer mesh) appears to increase the skin friction magnitude where the layer mesh is present. This is most obvious on the chest between meshes (ii) and (iii) and potentially explains the larger skin friction value for mesh (ii) before the effects of failed layer growth dominate in mesh (i).

The changes in skin friction over the body ultimately indicate differences in the boundary layer physics being captured in the simulations. The most significant effects of this are observed in the locations of flow separation from the body, visualised by shear force streamlines in figure 5-23. Where the streamlines converge to a single line this indicates that the boundary layer has separated from the surface at this point. The separated region is then characterised by unsteady and vortical streamlines and low or negative skin friction. Again the most significant differences in these features occur between meshes (i) to (iii). This is most noticeable in the separation under the chest but also along the legs, where far more complex flow features are observed in the two finer meshes.

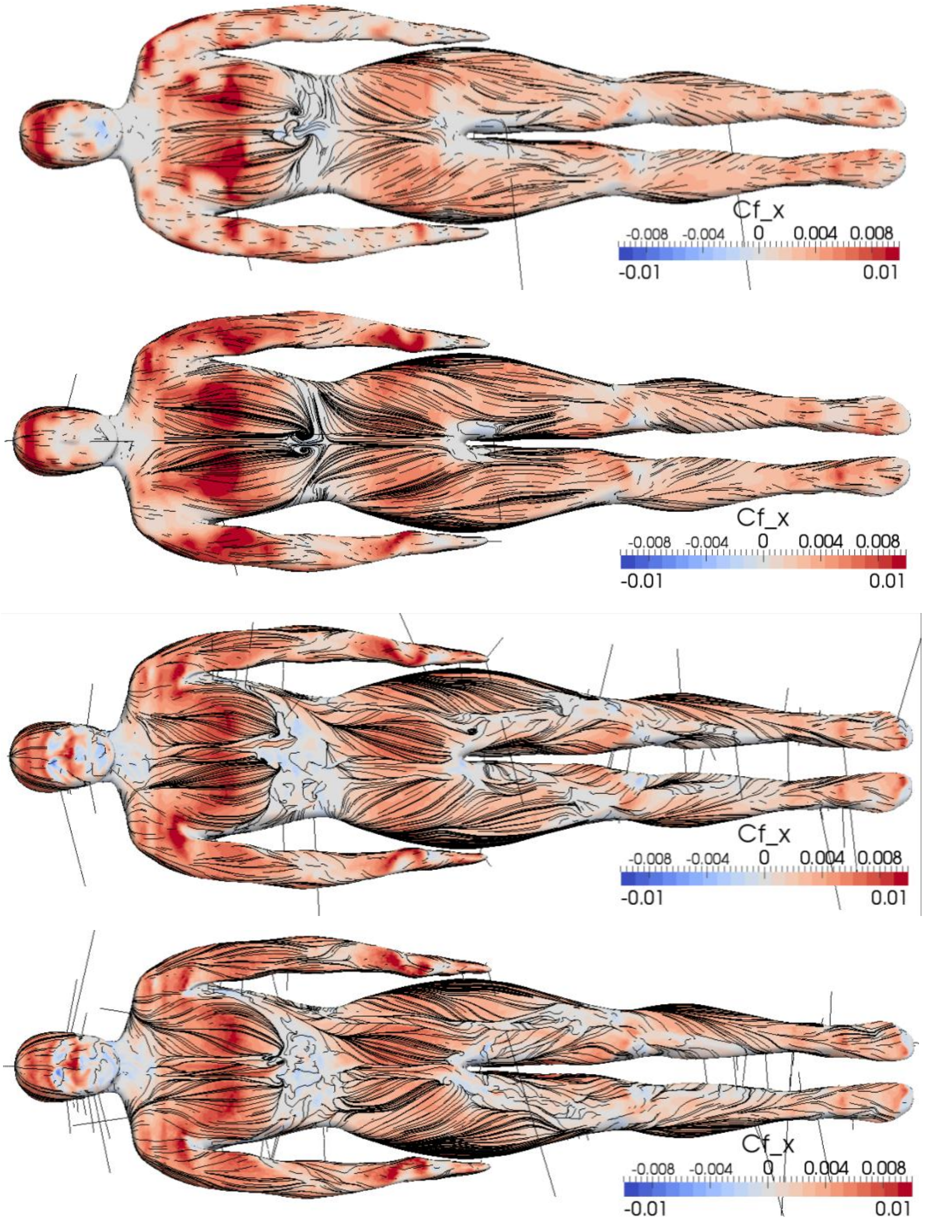

Figure 5-23 – Instantaneous coefficient of skin friction (defined in equation 5-1) and shear stress streamlines for different mesh density cases, from top to bottom (i), (ii), (iii) and (iv).

Changes in the skin friction with mesh density correspond to changes in the pressure field, depicted in figure 5-24. A reduction in pressure is observed on both the chest and armpits for both the coarser meshes (i) and (ii). This indicates a higher flow velocity in this region. The increased complexity of separation features over the torso and legs can also be observed in two finer meshes (iii) and (iv).

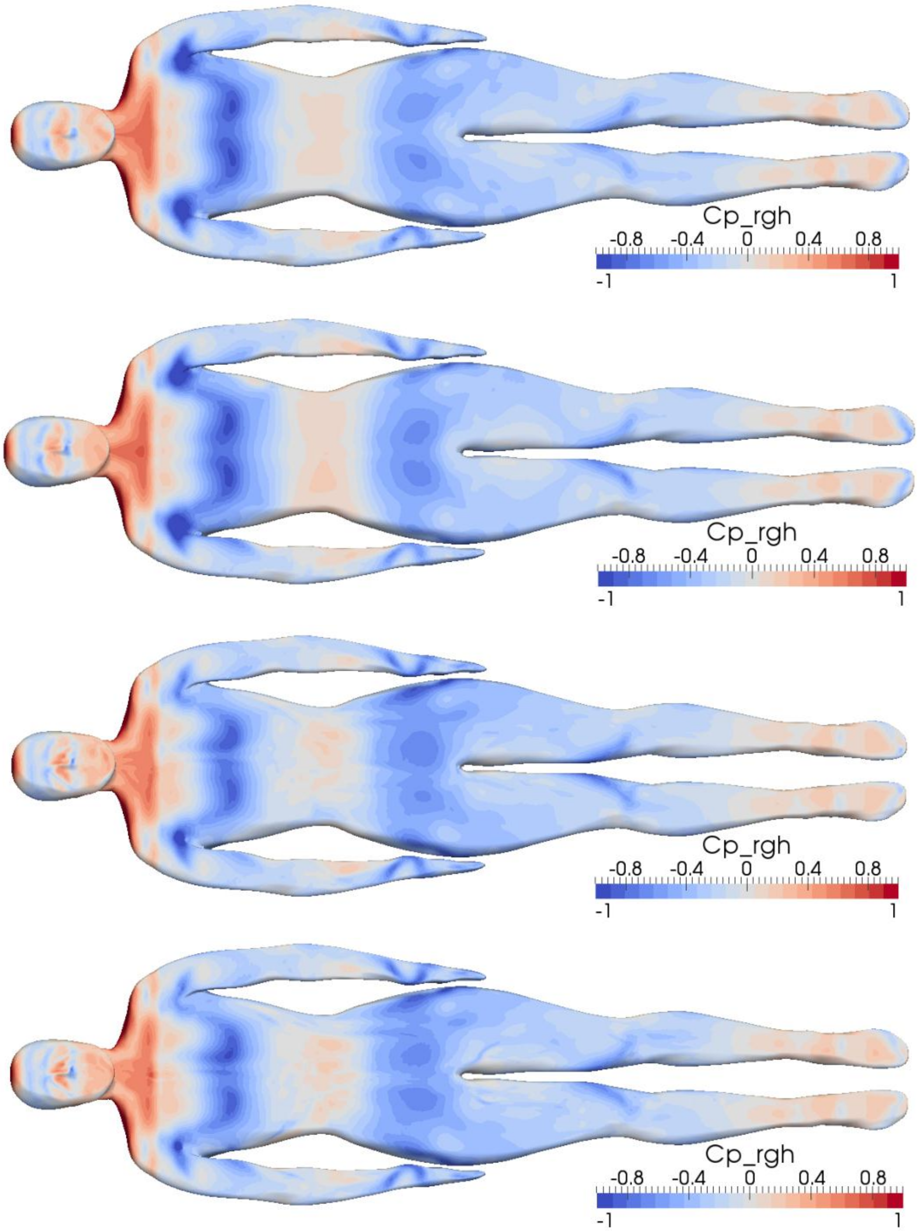

Figure 5-24 - Instantaneous coefficient of pressure for different mesh density cases, from top to bottom (i), (ii), (iii) and (iv).

5.9.2

5.9.3 Variation in free surface deformation

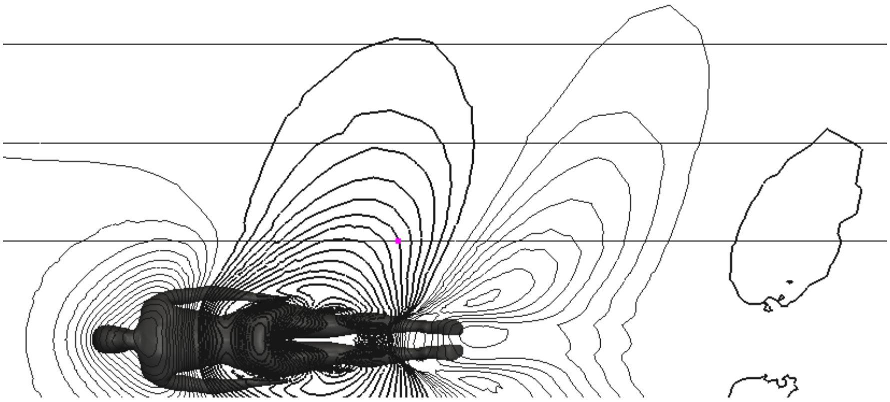

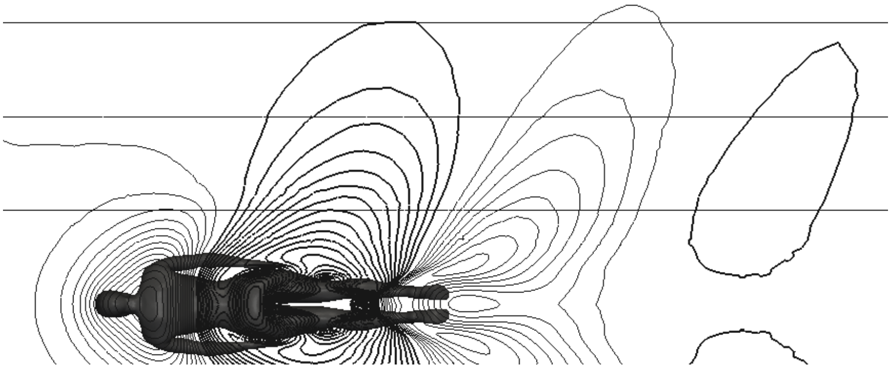

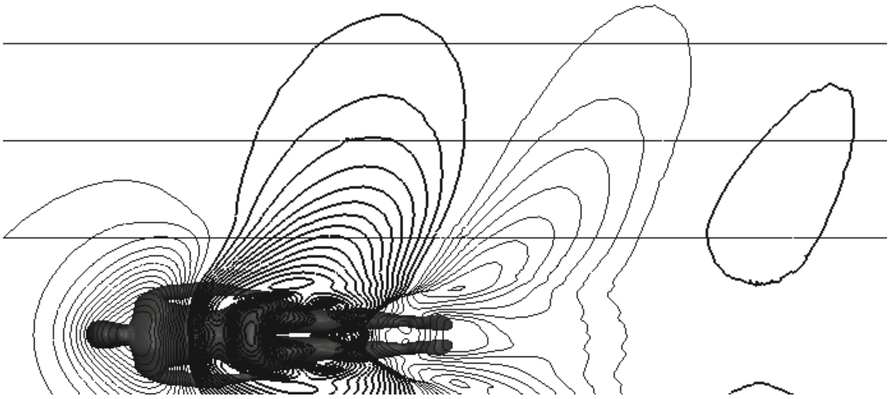

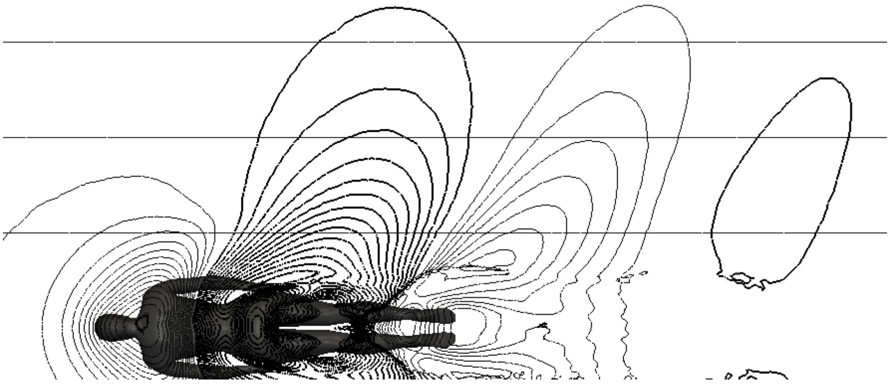

Figure 5-25 - Free surface deformation with contours every ±0.005m from the static free surface (bold contours are wave troughs). for different mesh density cases, from top to bottom (i), (ii), (iii) and (iv).

The free surface contour plots for the four different meshes can be seen in figure 5-25. As the mesh density increases the free surface deformations gradually increase in magnitude; however this has very little impact on the propagated wave pattern. Some local changes can be observed near the body, most strikingly the shape of the wave field generated over the lower legs.

From the free surface snap shots it would appear that grid independence has not yet been reached for the free surface resolution. It should be noted, however, that these are instantaneous deformations of an inherently unstable process and that some of the variation may be due to this.

5.9.4 Summary

The greatest discrepancies between the different meshes occur between the three coarser grids (i – iii). Increasing the mesh density above that used in mesh (iii) appears to have only a small impact on the simulated results. A visual inspection of the variation in resistance components indicates that the simulations are converging on a grid independent solution. It can also be observed that the significant increase in density between meshes (iii) and (iv) produced relatively small changes for a six fold increase in the computational cost (see table 5-4). Therefore it was concluded that the additional computational cost of the fine mesh density (iv) was not justified for the minor improvements in fidelity. The final mesh structure presented in section 5.2.5 was therefore used as the basis mesh structure for the future investigations.

5.10 Conclusion

In this chapter the implementation of the RANS methodology for free surface passive swimming simulations is described. The generation of suitable simulation geometries is described and the limitations of the current geometry morphing process discussed. An inability to correctly replicate the shoulder and arm position of the athletes used for the experimental test cases is identified. This is due to the complex range of motion available in the shoulder joints. A more general assessment of the athlete posture was provided by side-on profile comparisons. A good replication of the experimental athlete profile was achieved in the simulation geometries through the use of joint rotations and vertical scale factors. Although a significant effort was made to match the experimental athlete geometries as closely as possible it is acknowledged that obtaining athlete specific body scans would improve this process.

A series of specific mesh development studies were conducted into the impact of boundary layer resolution and free surface mesh refinement. It was concluded that a fully resolved boundary layer mesh was required to capture the complex separation features that develop over the swimmer's body. Both the vertical and horizontal mesh refinement on the free surface was investigated. A lack of wave propagation throughout the simulation domain was attributed to the large amplitude wave breaking features that occur around the swimmer's legs in case N003. This appears to artificially dissipate the energy from the wave system and is identified as a weakness of the implemented volume of fluid methodology in the openFOAM solver InterFoam. This dissipation of wave energy makes direct comparison between simulated and experimental wave cuts impossible. However comparisons were made using thin-ship data between the near field simulated data and the far field experimental wave cut data. This indicated that the correct wave shape and position was being simulated near the swimmer's body, however further verification of this method will have to be based on local free surface features identified from experimental footage.

The final mesh structure developed from the specific investigations was subjected to a global mesh sensitivity study. Visual inspection of the variation in resistance components indicated that the simulations were converging on a grid independent solution. This allows a greater degree of confidence that no further increases in mesh refinement are required.

The developed RANS methodology described in this Chapter will now be applied to both the passive and active test cases detailed in Chapter 3. This will allow the resistance components of a freestyle swimmer to be determined and the impact of free surface interaction assessed.

6. Passive resistance of a swimmer

In order to correctly simulate the forces acting on a freestyle swimmer it is important to establish that all the different resistance components are correctly captured. Before conducting propelled freestyle simulations, which will include the impact of the swimmer's arms, it is important to build confidence in the implemented CFD methodology. This will be achieved by recreating the passive experimental cases N003 (head in-line) and DA003 (head up), presented in Chapter 3.2, using the developed methodology outlined in in Chapter 5.

By focusing on the passive resistance components first the problem is simplified, allowing a better comparison to be made to experimental data. A detailed understanding of the resistance components on the free surface was also identified as a key objective if the ultimate aims of this research were to be achieved.

The lack of detailed understanding of how the free surface interacts with the resistance components was identified in the previous CFD literature. Therefore an additional deeply submerged simulation was conducted for each of the experimental cases (N003 and DA003). In these two submerged cases the simulation geometries developed in Chapter 5.1 were submerged to a depth of 1m. By comparing the simulated results of these deeply submerged cases with the surface simulations of N003 and DA003 the impact of the free surface on the resistance components will be assessed.

6.1 Free surface features

Before examining the forces on the swimmers' bodies the simulated free surface deformations will be compared to the free surface features identified in the experimental video footage from both cases. This is an important step in validating the free surface methodology implemented and will build confidence that the pressure field around the swimmer is correctly simulated.

In both test cases important features in the free surface deformation near the swimmer have been replicated in the simulations. For case N003 (head in-line), the free surface flow regime is dominated by the high Froude number (0.43) and low head position. This caused the water to flow smoothly up and over the head before dropping down and breaking over the legs. The similarities in the simulated flow and the experimental footage can be seen in figure 6-1.

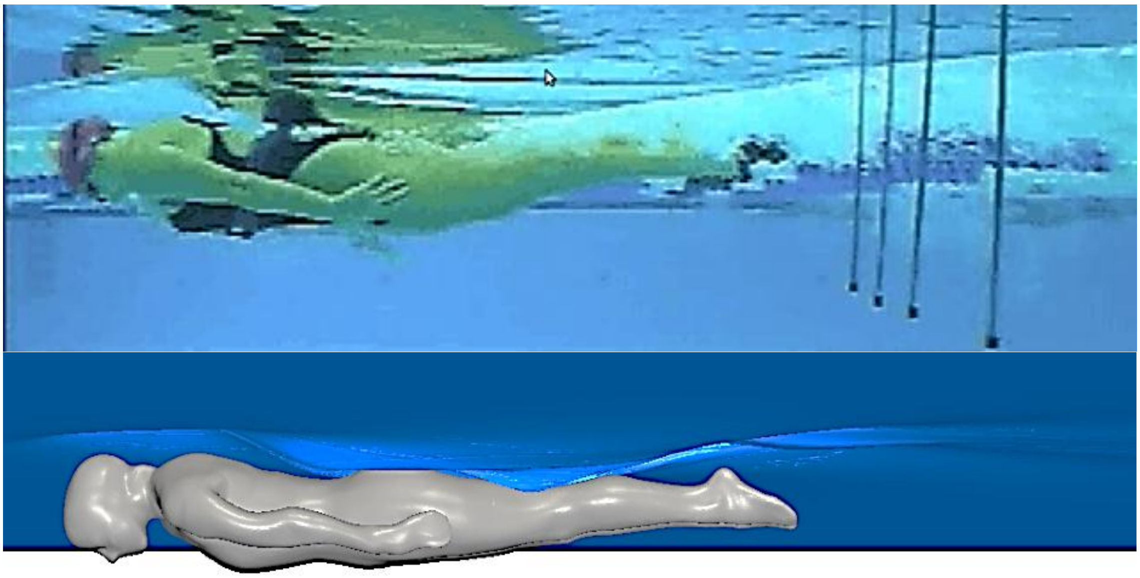

Figure 6-1 -Free surface comparison with experimental underwater footage for case N003 (head in-line).

The most significant difference between the simulation and experiment is the nature of the free surface after the breaking wave. In the experimental footage it is clear that the air water interface becomes extremely disturbed and broken with lots of entrained air and bubbles. This makes it difficult to see exactly where the breaking wave is located. The free surface visualisation from the simulation is produced as an iso-surface where the volume fraction is equal to 0.5 (exactly half water and half air). Therefore much of the detailed complexity is not visualised. This highlights one of the intrinsic weaknesses in the volume of fluid method for free surface flows around a swimmer, as the complex flow physics involved in breaking waves is difficult to capture. However it is felt that the main features of the free surface flow near the body are well captured using this methodology.

In case DA003 the lower Froude number (0.32) and raised head position lead to significantly different flow features compared to N003. Firstly the water breaks around the head creating a bluff body type bow wave, which pushes the water ahead of it rather than parting it. This feature is well replicated in the simulation and can be compared to both the above and underwater footage in figure 6-2 and figure 6-3. Again the main difference in the bow wave simulation is the lack of unsteady broken water. However the general shape of the wave and the dry back half of the head are well captured.

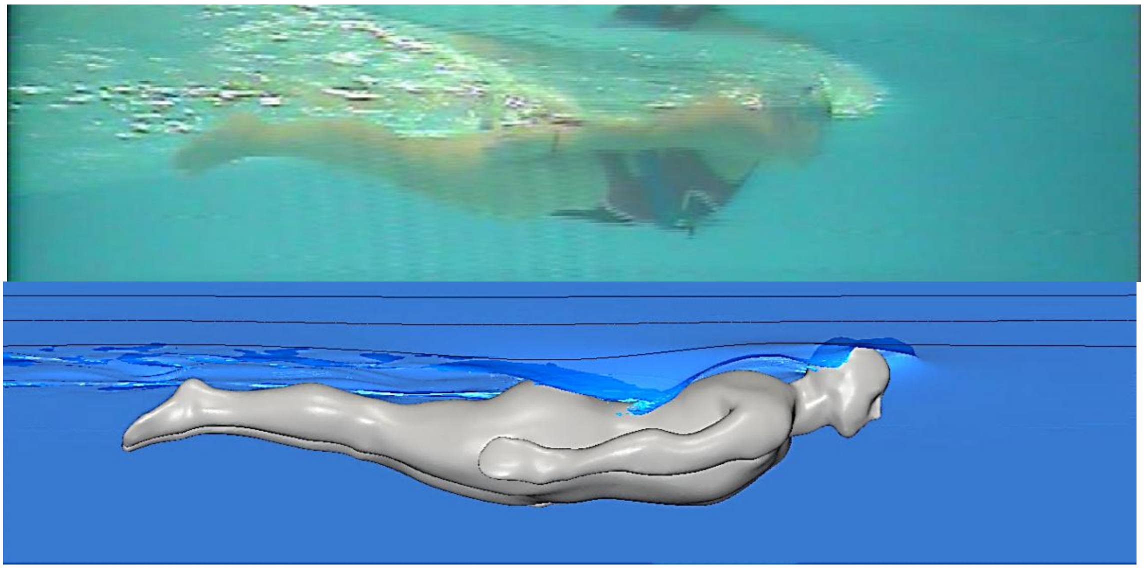

Figure 6-2 - Free surface comparison with experimental underwater footage for case DA003.

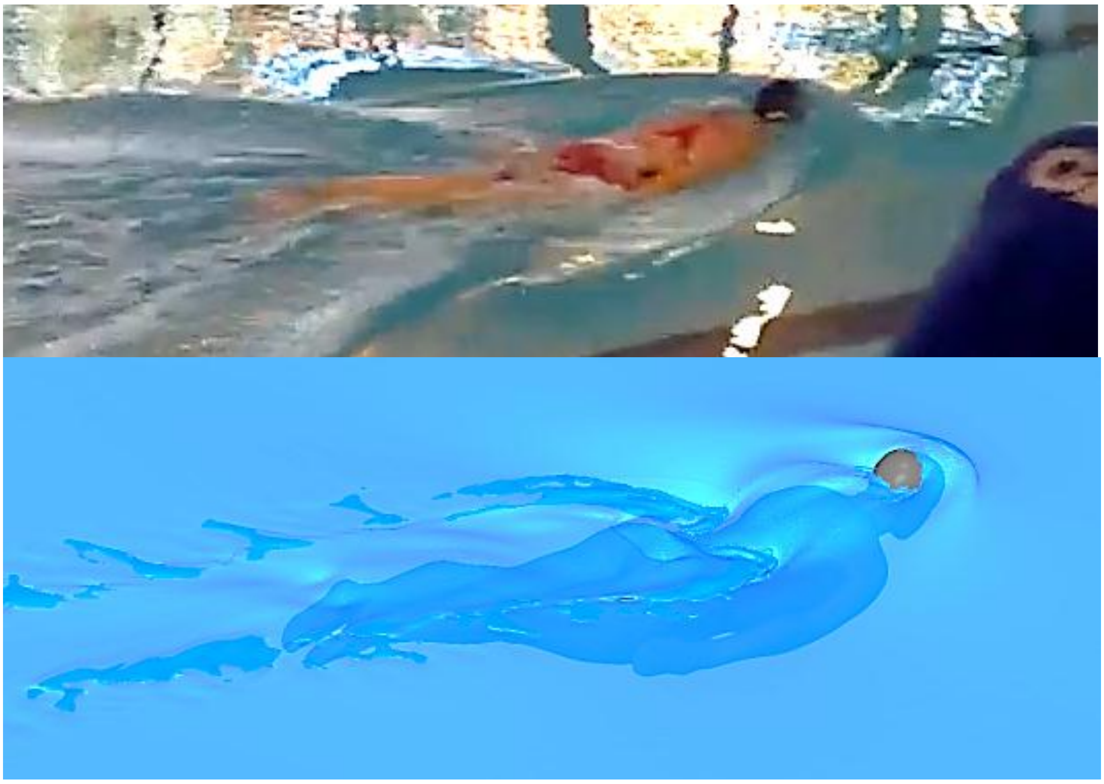

Figure 6-3 - Free surface comparison with experimental above-water footage for case DA003.

One of the key differences between the free surface in the experiment and the simulation is the amount of water flowing over the athlete's back. In the above water footage the athlete's back appears to have only a small amount of unsteady broken water flowing over it. In the simulation there is a significant amount of water flowing over the back. The most likely reason for this discrepancy is the difference in the geometry's arm and shoulder position. Figure 6-2 shows that the simulation geometry has significantly lower shoulders and arms than those of the athlete. This is likely to encourage water to flow up and over the shoulders rather than around them, allowing more flow over the back. This discrepancy in the geometries is currently a weakness of the STL morphing process (see section 5.1.3 for more detail). There is also the likelihood of some discrepancy in the vertical position of the athlete geometry, which would also have an effect on the free surface flow.

The most significant wave feature in case DA003 is developed from around the hips (much further forward then in case N003). This appears to be best replicated in the underwater comparison, showing a similar origin to the breaking wave (slightly forward of the hips). However the above water footage shows the breaking wave on either side of, and slightly behind the hips as well as into the small of the back. The CFD free surface visualisation from above the water appears to place the breaking wave slightly ahead of the experimental footage (Figure 6-3). This discrepancy could be due to a number of different factors. The increased flow over the back could be changing the formation of the breaking wave. Indeed in the experimental above-water footage it appears that the breaking waves on either side of the hips occur just after the arm, whereas the arms are much deeper in the simulation. This causes them to have less impact on the free surface in this region. Another aspect of a breaking wave feature is its inherently unstable nature; this means some discrepancies could be due to the time at which the images (both experimental and simulated) are taken. Finally the free surface visualisation method used in the simulations can in itself be slightly deceiving. The iso-surface plotted does not provide a distinction between unsteady broken water and 'solid' water that we naturally perceive in video footage. This appears to provide a definitive interface between air and water within the simulation, which is not actually the case.

In general the free surface flow features observed in case DA003 appear to be well captured. However some clear discrepancies have been identified between the simulation and the experiment. It is believed that these differences are primarily a consequence of the errors in the shoulder and arm position, rather than the free surface methodology.

The fundamental free surface flow regimes of two very different passive cases have been well replicated by the implemented CFD methodology. This provides confidence that the simulated pressure field around the swimmer geometries is being well captured. However the significant implications of errors within the simulation geometries have been highlighted.

6.2 Impact of free surface on velocity field

Before looking at the different resistance components in detail it is helpful to try and visualise the velocity field generated around a swimmer's body, both deeply submerged and near the free surface.

6.2.1 Case N003 (head in-line)

Figure 6-4 provides a comparison of the axial velocity field at different locations along the same geometry, with and without the free surface. The locations with lots of velocity contours represent regions of fluid that have been slowed down by the presence of the swimmer. This allows regions of separated or stagnated flow to be identified, for instance behind the head or between the arms and legs. It is also possible to identify a vortex feature coming off the chin and gradually weakening as it passes under the body.

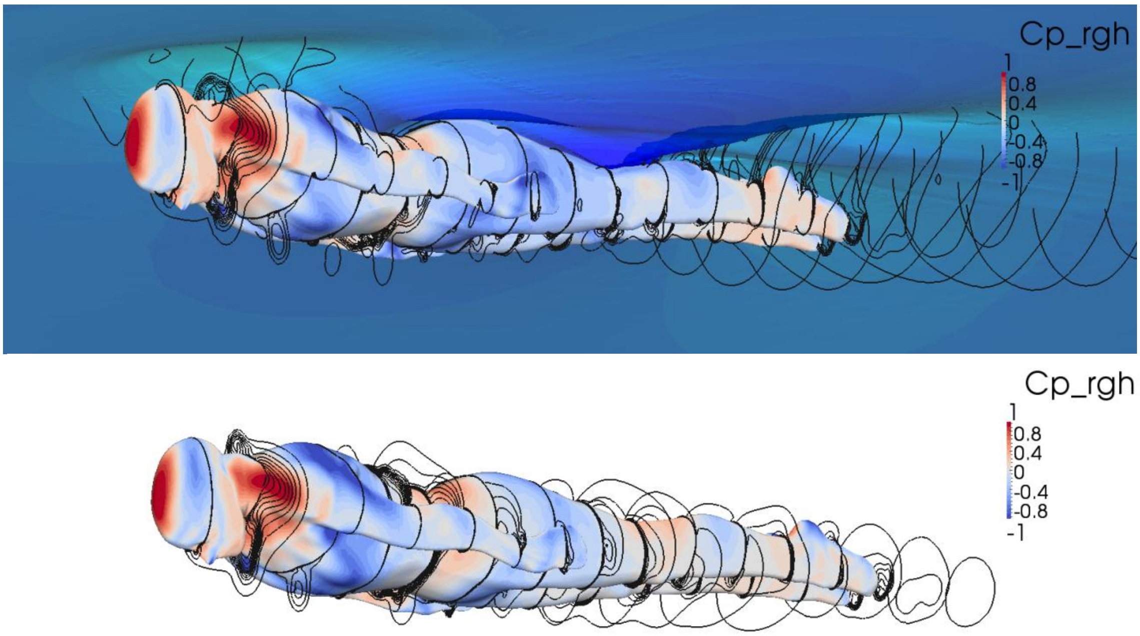

Figure 6-4 - Relative axial velocity contours (u/U_0) for N003 near the surface (above) and deeply submerged (below). Contours: -0.3 to 0.9 in steps of 0.1.

The impact of the separated regions on the resistance will be discussed in more detail later; however it is important to understand the huge influence the free surface has on these features. The impact of the flow up and over the head and shoulders of the swimmer on the surface has two distinct impacts on the separated regions. Firstly the wake behind the head is moved up and expanded compared to the deeply submerged case. Secondly a separated region in the small of the back and between the arms can be observed in the submerged case. In the surface case this is removed as the free surface drops down over the back maintaining attached flow. It is even possible to see distinct differences between the two cases underneath the swimmer, drawing attention to the fact that the free surface influences the entire velocity and pressure field around the body. This identifies the difficulty of performing a neat separation of resistant components.

6.2.2 Case DA003 (head up)

The velocity field generated around the DA003 Geometry can be seen in figure 6-5. It is clear that in both the surface and submerged cases significantly more separation occurs compared to N003. This corresponds to a body posture and attitude that presents a far less streamlined profile to the flow due to the arched back, high head position and the attitude of the legs. It should also be noted that this geometry has a larger volume for the same length compared to N003.

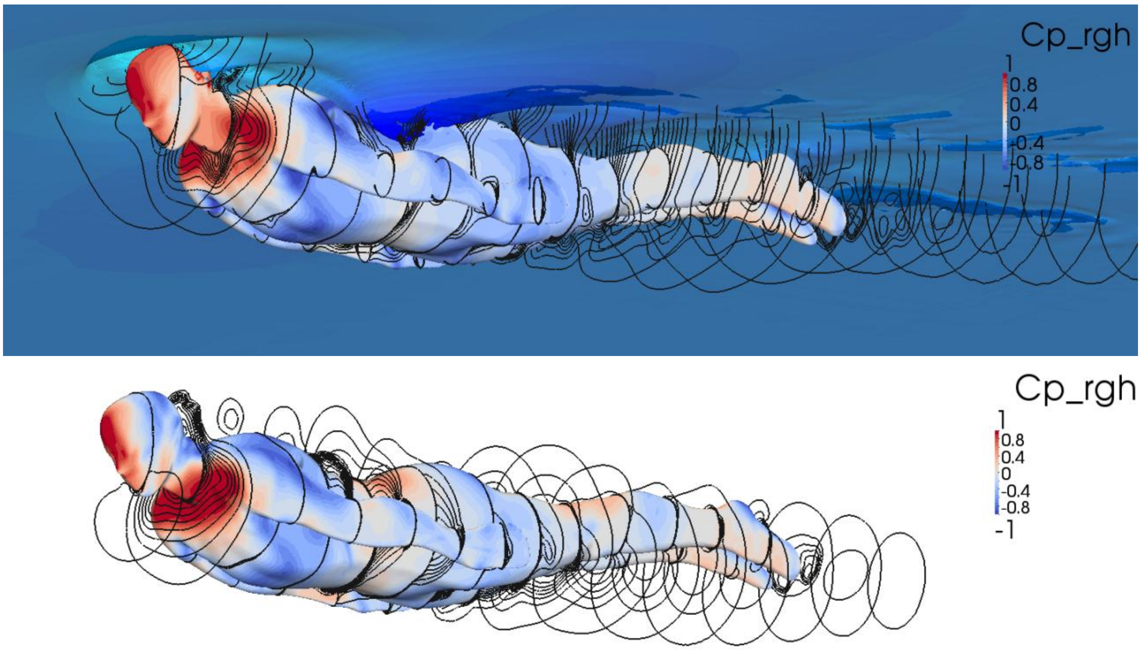

Figure 6-5 - Relative axial velocity contours (u/U_0) for DA003 near the surface (above) and deeply submerged (below). Contours: -0.3 to 0.9 in steps of 0.1.

The interaction of the free surface with the velocity field is even more pronounced for this case. The flow around the head and shoulders changes entirely near the free surface, directing the wake from the chin down and under the chest. Likewise, the back of the head running dry essentially eliminates the wake and vortex observed in this region in the fully submerged case. The breaking wave at the hip results in a large wake region with a deep velocity deficit that encompasses most of the legs.

It should be noted that the lack of wake development downstream of the deeply submerged cases is partly due to the lack of wake refinement boxes in these meshes. This does not affect the mesh resolution near the body or the generation of the wake; however it will prevent it propagating downstream.

6.3 Resistance components of Case N003 (head in-line)

The forces acting on the athlete’s body (for both the surface and submerged case) can be seen in figure 6-6 and are displayed in table 6-1. The average total resistance for the surface case was 115.6 N. This compares to an experimental resistance of 116.9N, providing close agreement in terms of total resistance. To understand the detail of how well the simulation matches the experimental case we have to consider the individual resistance components.

Table 6-1 - Comparison of CFD force components for case N003 with experimental and thin-ship data.

Resistance (N)	ITTC'57	Exp	Thin Ship	CFD submerged @ -1m	CFD on the surface (N003a_A)		
					Force	%	Coefficient*
Skin Friction	10.87			8.35	9.566	8.28	0.049
Pressure:				92.71	106	91.70	0.540
P-Viscous (form)				92.71	71.64	61.97	0.365
P-wave		34.36	34.85	-	34.36	29.72	0.175
Total		116.9			115.6	100	0.589

*coefficient calculated using frontal projected area, values in red are estimated

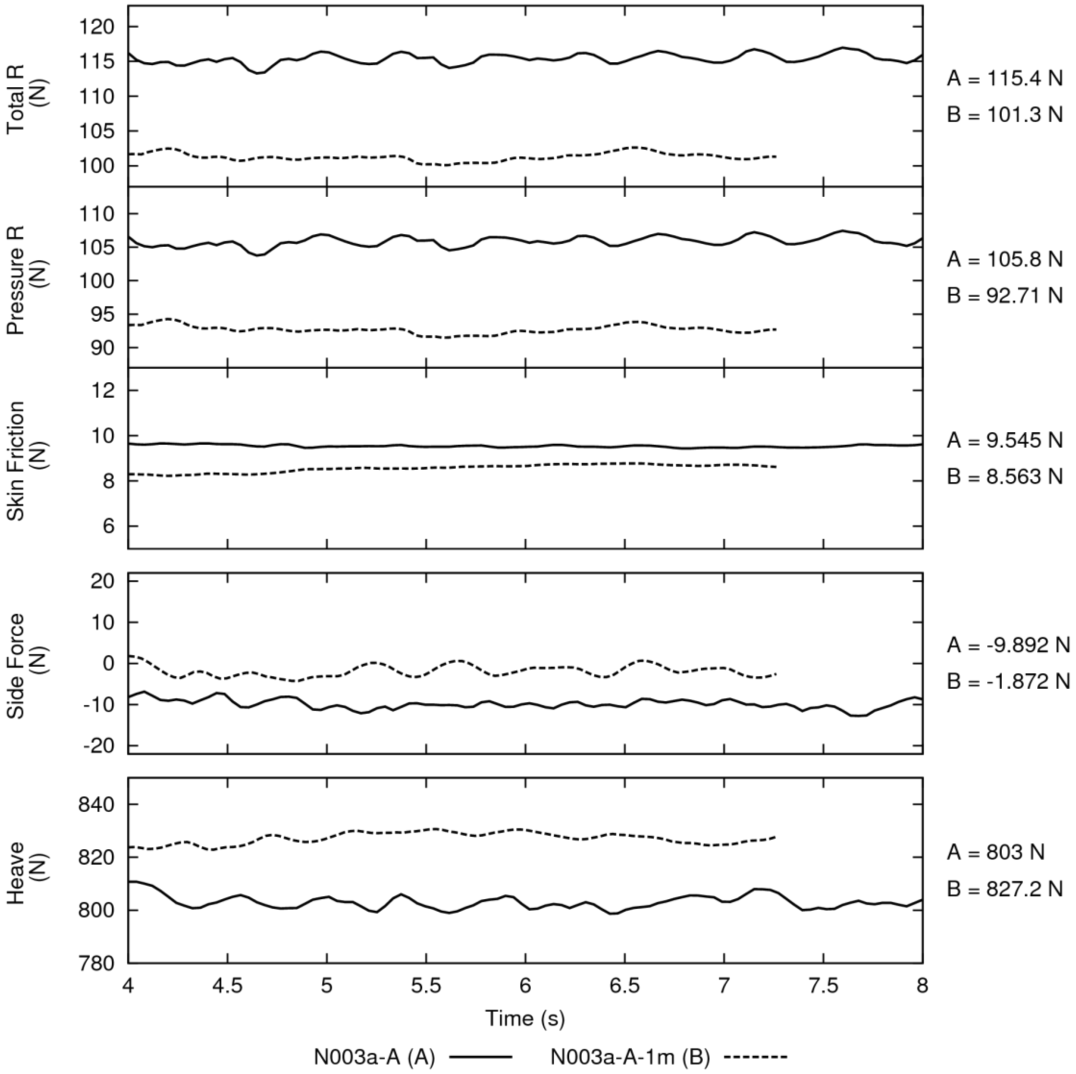

Figure 6-6 - Forces acting on athlete geometry for simulated case N003, at experimental depth (N003a-A) and deeply submerged (N003a-A-1m). Time averaged values are given on the right.

6.3.1 Skin Friction

The skin friction on the body is due to the development of the viscous boundary layer. This frictional force can be estimated based on the wetted surface area S_w and a coefficient of frictional resistance C_f, which was estimated using the ITTC'57 skin friction correlation line (Molland, A. F., Turnock, S. R., & Hudson, 2011):

$$C_f = \frac{0.075}{(\log R_e - 2)^2} \quad 6\text{-}1.$$

The skin friction resistance can therefore be calculated as:

$$R_f = \frac{1}{2} \rho S_w U_0^2 C_f \quad 6\text{-}2,$$

where the surface area for the N003 simulation geometry is 1.727 m^2 and the free stream velocity is 1.86 ms^{-1}. This provides an estimate of the viscous resistance as 10.87 N compared to 9.57 N from the CFD simulation on the surface and 8.35 N from the submerged case. This comparison can also be seen in table 6-1.

The difference in simulated skin friction compared to the ITTC estimate is likely to be caused by the complex separation zones that develop over the swimmer's body. The distribution of skin friction and the regions of separated flow can be seen in figure 6-7 through the use of shear stress streamlines. After the flow separates from the body a region of reduced, or even negative, shear stress is observed due to the eddies and recirculation in the flow. The separated zones have the ultimate effect of reducing the surface area over which the boundary layer develops, whereas the ITTC'57 correlation line is based on ship hull forms with mainly attached flow.

In the surface case the influence of the free surface causes the water to flow up and over the head, accelerating down the back and over the hips. This gravity driven flow removes the adverse pressure gradient you would expect to find behind the shoulders, keeping the flow attached all the way to the back of the knees. At this point the dominant wave system originates with a breaking wave, causing the flow to separate entirely over the calves.

Surface:

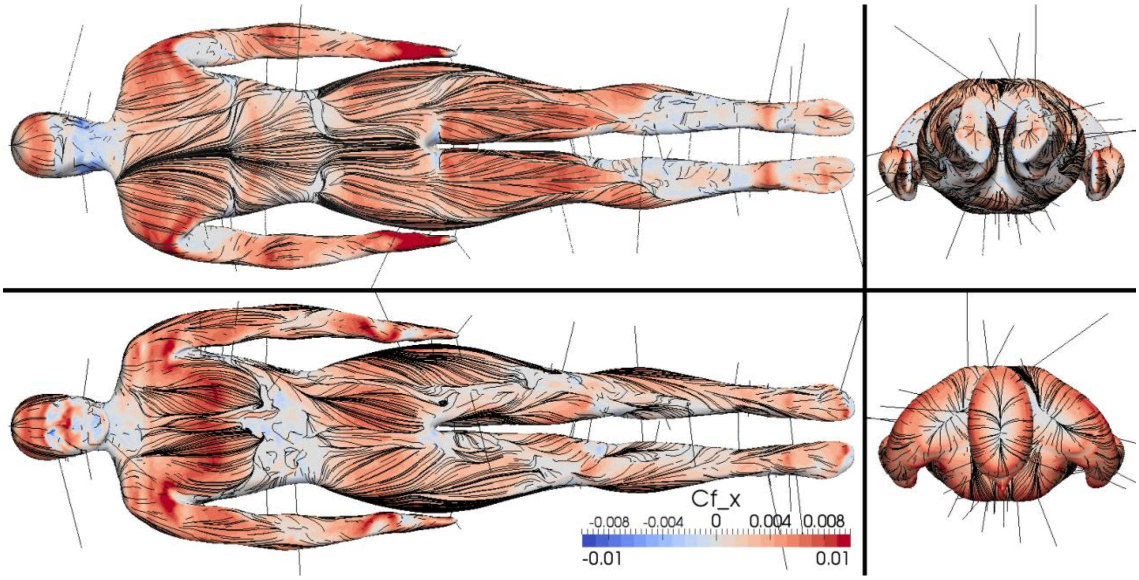

Submerged:

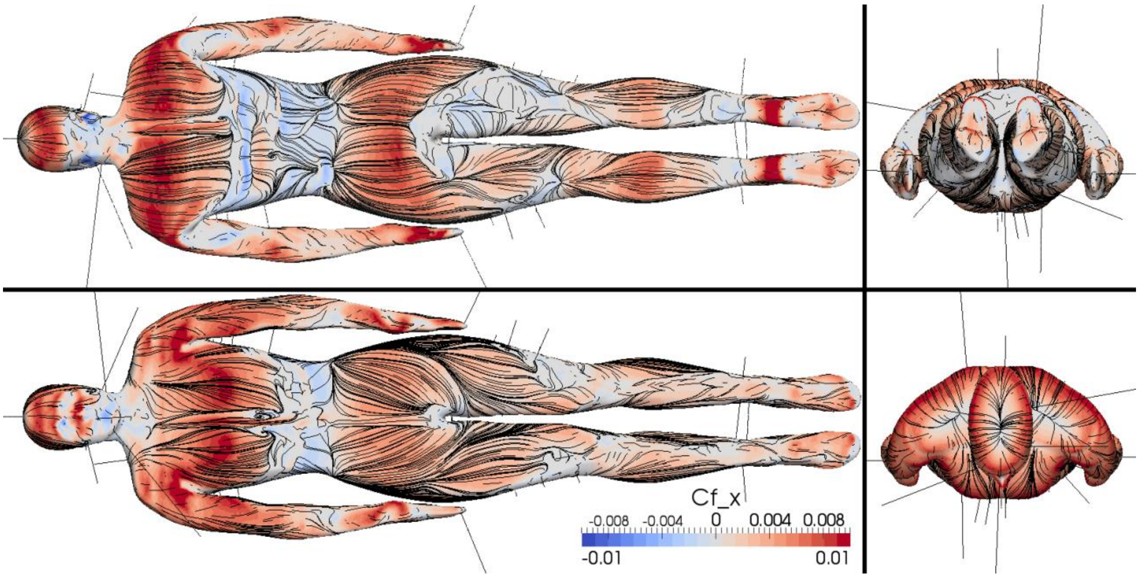

Figure 6-7 – Local coefficient of frictional resistance for N003 on surface (top) and submerged (below).

In contrast the fully submerged case has significant flow separation behind the shoulders and buttocks. This causes the submerged case to have a greater proportion of separated flow compared to the surface case, explaining why the skin friction reduces at a greater depth.

6.3.2 Pressure Resistance

The pressure resistance acting on the body is made up of two main components; the wave resistance and the form drag (or resistance due to separation). The combined effect of these on the pressure field can be viewed in figure 6-8. The static pressure of the undisturbed free surface has been removed as defined in equation 5-2. Therefore, for the fully submerged case, where the free surface deformation is negligible, this becomes purely the dynamic pressure. Increased pressure indicates lower velocities and vice-versa. For the surface case the pressure coefficient represents the combination of dynamic pressure and the hydrostatic effect of the deformed free-surface.

The deeply submerged case indicates the large stagnation pressures associated with the head and shoulders, along with the low pressure regions associated with the flow accelerating over regions of high curvature such as the shoulders, chest and hips. A sharp pressure change is also observed over the heels, as the flow stagnates on the back of the heel then sharply accelerates over the top of it before separating. The other previously identified separated regions are characterised by higher pressures than the surrounding areas due to the reduced flow velocity within these recirculating wake regions.

The surface case exhibits many of the same flow features, offset by the hydrostatic impact of the free surface. For instance the reduced pressure associated with accelerating the flow up and over the head and shoulders is offset by the increased hydrostatic head due to the elevated free surface in this region. Likewise the high pressure, associated with the concave curvature of the top of the hips stagnating the flow, is reduced due to the low free surface elevation in the small of the back. Interestingly the wake region created over the lower legs by the breaking wave field has the effect of significantly reducing the fluid velocity over the heels (see figure 6-4). This reduces the pressure variation observed in the submerged case.

Surface:

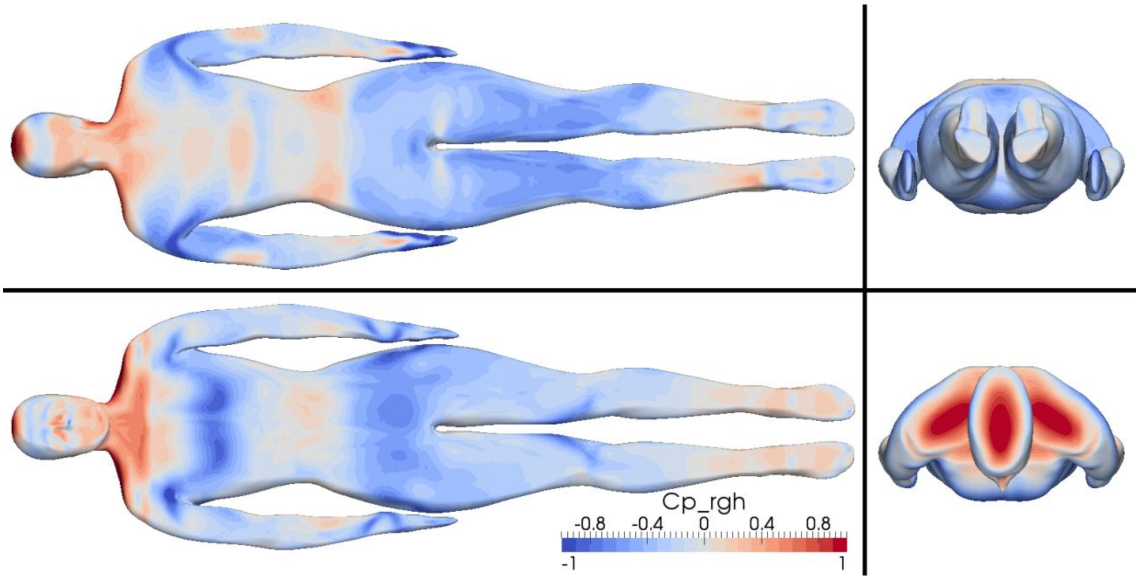

Submerged:

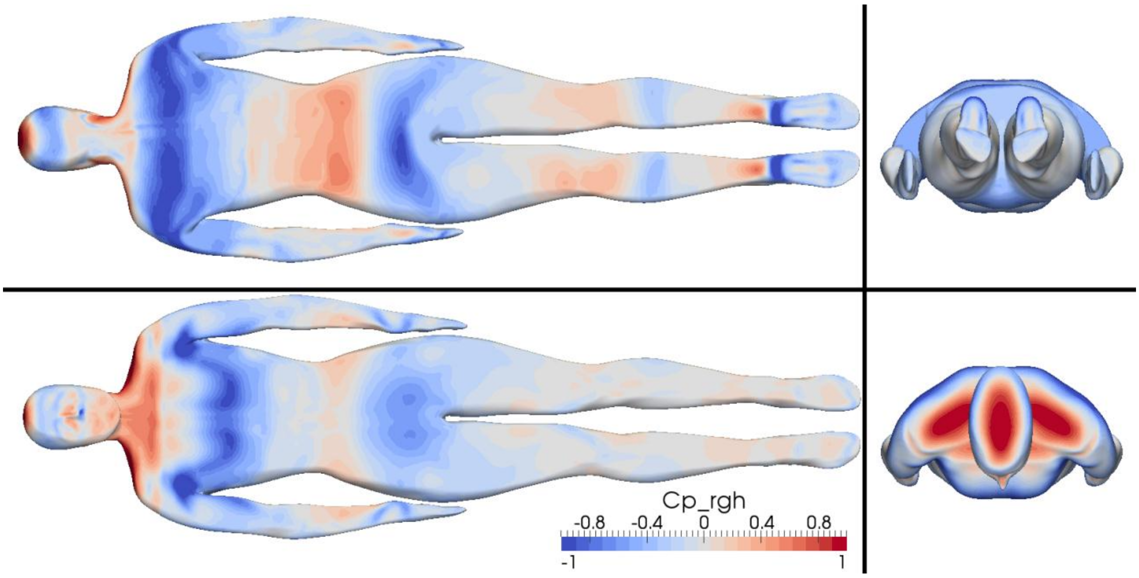

Figure 6-8 - Pressure coefficient (as defined in equation 5-1) for N003_A, on surface (top) and submerged (below).

The impact of these different pressure distribution on the resistance can be seen in figure 6-9.

Surface:

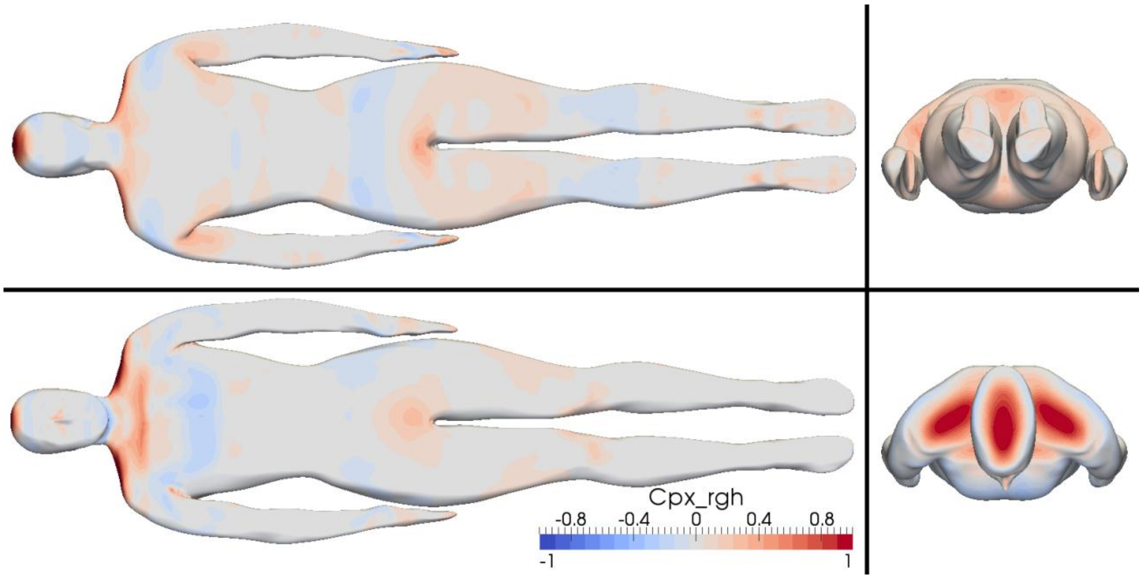

Submerged:

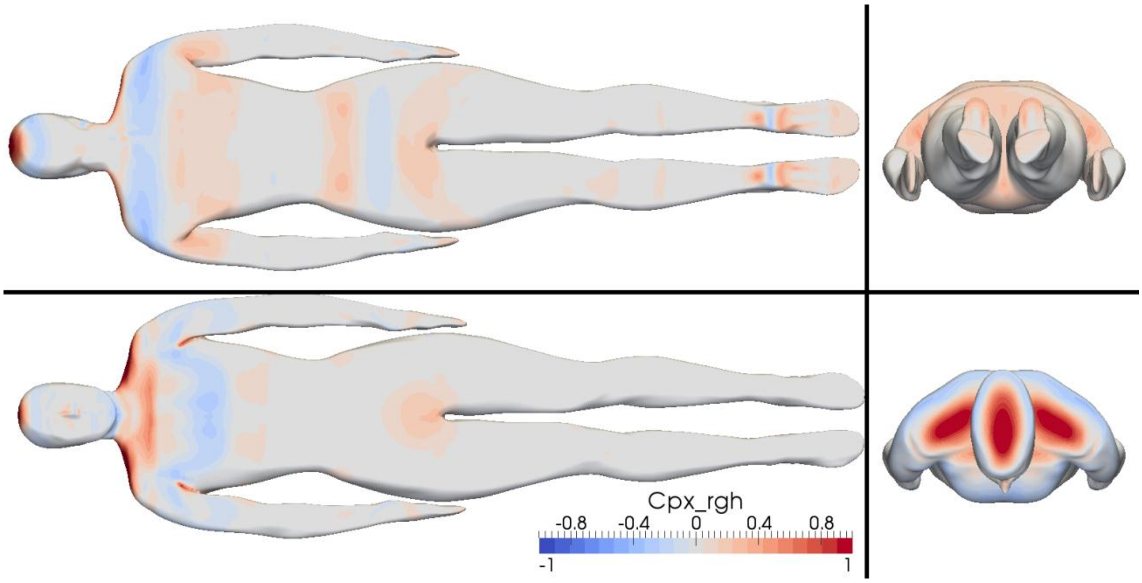

Figure 6-9 – Pressure resistance coefficient (as defined in equation 5-3) for N003_A, on surface (top) and submerged (below).

The increase in pressure resistance for the surface case (displayed in table 6-1) can be seen most clearly by comparing the views from ahead and behind the swimmer. From both these views the surface case has an increased proportion of positive pressure resistance. This is due to the elevated free surface over the head and shoulders increasing the hydrostatic pressure on the forward facing surfaces in this region. The opposite effect occurs around the hips and thighs, where the drop in the free surface elevation reduces the pressure on the backward facing surfaces in this region. It should be noted however that in the region of the swimmer's back the impact of the free surface is to reduce the local pressure resistance, not increase it. This is due to the combined effect of changes in the hydrostatic pressure and the suppression of separation in this region.

6.3.3 Pressure Resistance due to Waves

The wave resistance has a purely pressure component captured in the developed wave pattern and a viscous-pressure component due to wave breaking within the near field. It has already been documented that the near field, or local, free surface features appear to correspond well with experimental footage. However the wave pattern that develops from this is failing to propagate out over the simulation domain (see figure 6-10). This has been discussed at greater length in section 5.4. For the purpose of this section it can just be stated that the simulated wave resistance cannot be validated using the experimental wave cuts as the simulated waves dissipate too quickly. Therefore it is impossible to verify that the near field free surface deformations are the same magnitude as those observed in the experimental case. However the use of thin-ship theory allowed the position and shape of the near field waves to be compared to the experimental data to a limited extent (see 5.4(ii)). This appeared to correlate well. The additional visual comparison of the local flow features supports the assumption that the component of pressure resistance due to wave making is captured on the body but not propagated throughout the domain. This assumption allows the pressure resistance to be broken down into wave drag and the viscous-pressure (or form) drag. Both analysis of the experimental wave cuts and thin-ship simulations provide wave resistance values of approximately 34N.

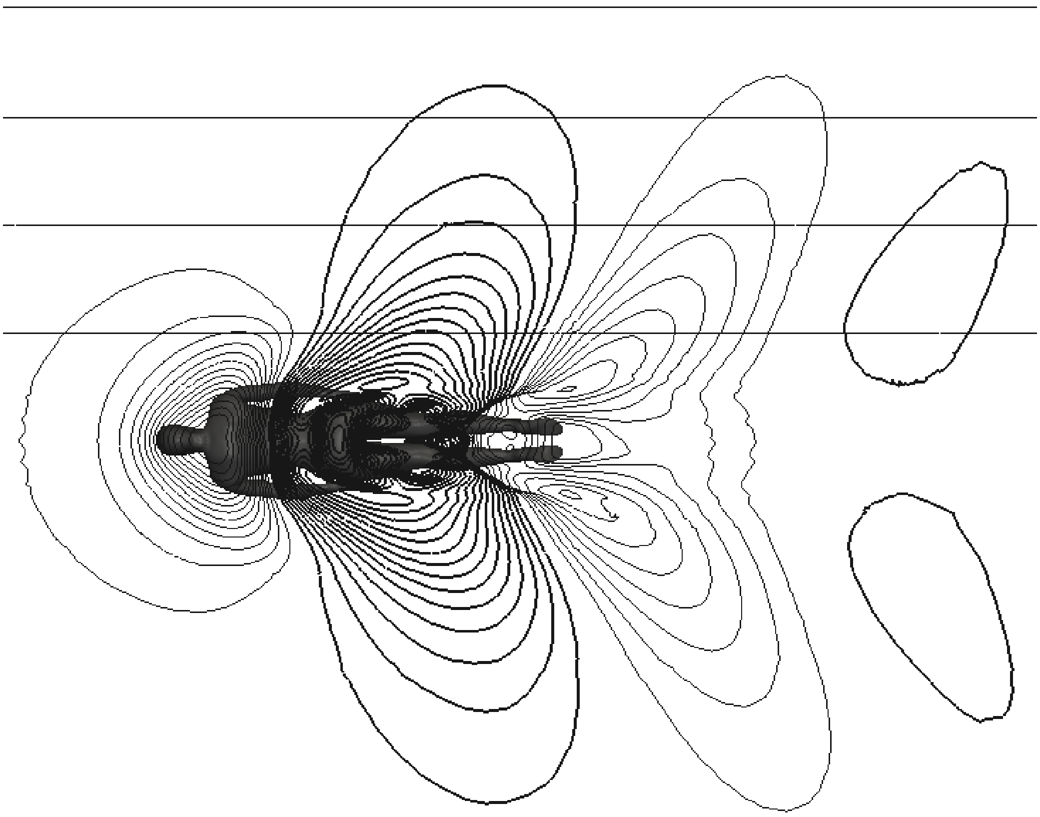

Figure 6-10 - Free surface elevation with contours +-0.005, for N003

6.3.4 Viscous pressure resistance

The viscous pressure drag represents the change in pressure over the body due to the effects of viscosity. Sometimes referred to as the form drag, this component of resistance includes the effects of separation. If we assume that the wave resistance measured experimentally is correctly captured in the pressure field over the body, we can subtract this from the total pressure resistance to provide an estimate of the viscous pressure resistance for case N003a_A. These values can be seen in red in table 6-1, denoting that they are estimated values instead of direct measurements. This would indicate that the form drag is approximately 72 N when the swimmer is on the surface (accounting for 62% of the total resistance). This is significantly less than the 92 N simulated for the fully submerged case. This change would appear to be explained by the large areas of separation observed behind the shoulders and buttocks in the fully submerged case which don’t appear in the surface case.

6.4 Resistance components of Case DA003 (head up)

The forces acting on the body in case DA003 (for both the surface and submerged case) can be seen in figure 6-11 and table 6-2. The time averaged total resistance from the surface simulation was 78.88 N, 22% greater than the experimental value of 64.7 N. Surprisingly the total resistance increased even further for the fully submerged case, appearing to indicate that the influence of the free surface can actually reduce the resistance. To understand where these apparent discrepancies come from the individual resistance components will again be analysed.

Table 6-2 - Comparison of CFD force components for case DA003 with experimental and thin-ship data

Resistance (N)	ITTC'57	Exp	Thin Ship	CFD Submerged @ -1m	CFD on the surface (DA003-A)		
					Force	%	Coefficient*
Skin Friction	7.03			4.427	7.597	9.63	0.064
Pressure				82	71.28	90.37	0.600
P-Viscous (form)				82	42.83	54.30	0.361
P-wave		28.45	31.72	-	28.45	36.07	0.240
Total		64.7			78.88	100	0.664

*coefficient calculated using projected frontal area, values in red are estimated

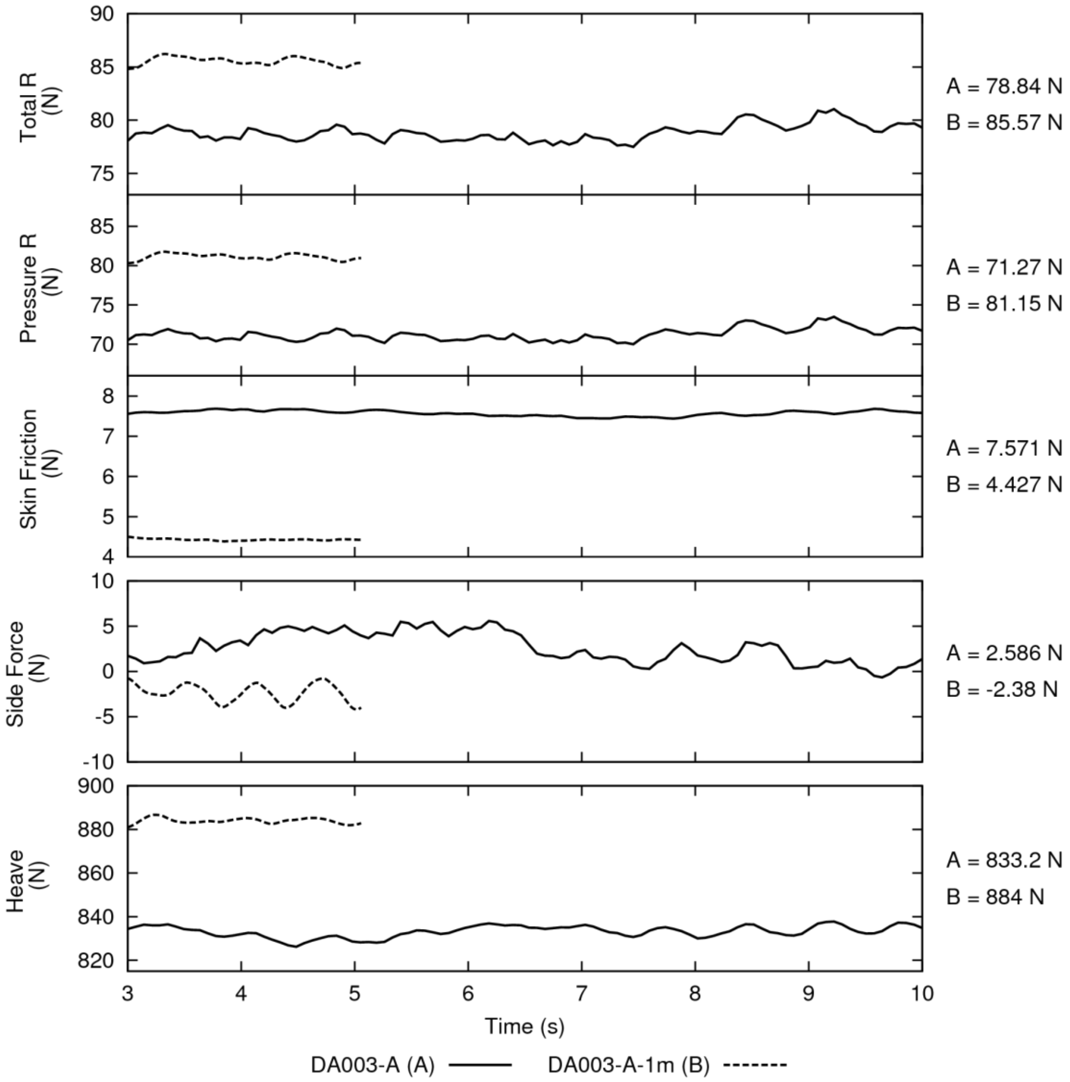

Figure 6-11 - Forces acting on athlete geometry for case DA003. Time averaged values are given on the right.

6.4.1 Skin friction

The frictional resistance was estimated to be 7.03 N based on the ITTC formulation described in equations 6-1 and 6-2 (based on an athlete length of 1.86 m, velocity of 1.37 ms^{-1} and wetted surface area of 1.94 m^{2}). The frictional resistance simulated for case of DA003 on the surface was 7.6 N and 4.4 N when deeply submerged. The reason for this large reduction in the skin friction can be seen in figure 6-12. The case on the surface appears to have fully attached flow over almost the entire torso, whereas the fully submerged case has large separation regions behind the chest and shoulders as well as underneath the thighs. The breaking wave system that develops around the hips on the surface case produces a separated region on the back of the thighs with two eddies. These create a noticeable region of negative skin friction between the legs as the flow recirculates. In spite of this there is a significant increase in separation on the submerged case, which has the obvious impact of reducing the surface area over which the boundary layer grows, generating skin friction. Indeed in many of the separated regions the skin friction is negative due to flow recirculation.

Apart from affecting the flow separation, the interaction of the free surface appears to have increased the skin friction magnitude around the shoulders and arms. This would indicate that the flow is accelerated to a higher velocity in these regions when the athlete is on the surface as opposed to deeply submerged. In the experimental case however, less water was observed to flow up and over the shoulders, and the water that did appeared to be broken and unsteady (see section 6.1). This fundamental difference in the flow regime in this location could have had a significant impact on the skin friction resistance on the shoulders and back. A smaller volume of water, moving more slowly and erratically than in the simulation would indicate that the experimental skin friction would be reduced in this region. This sort of discrepancy is likely to form part of the explanation as to why the simulated resistance is larger than the experimental case.

Surface:

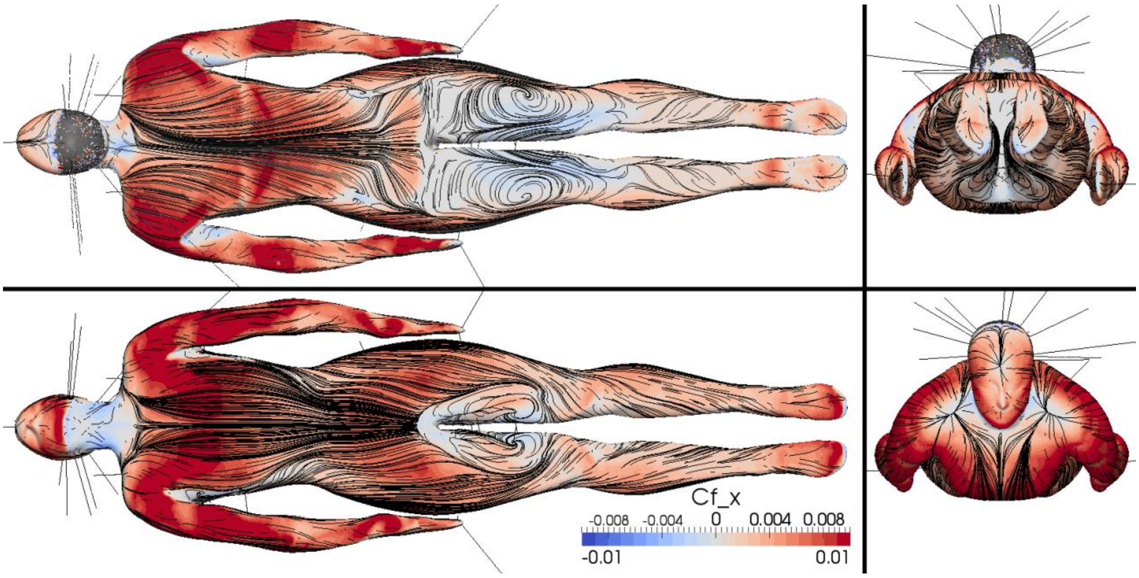

Submerged:

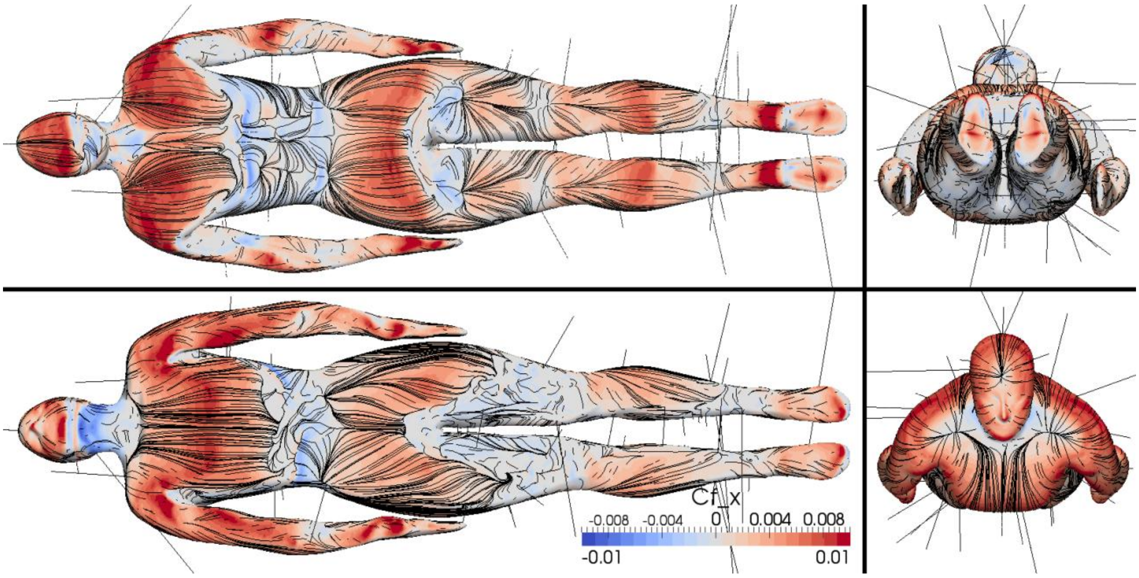

Figure 6-12 – Local coefficient of frictional resistance for DA003, on surface (top) and submerged (below).

6.4.2 Pressure Resistance

The distribution of pressure over the body for both the surface and submerged cases of DA003 can be seen in figure 6-13. As with case N003 the hydrostatic pressure associated with the undisturbed free surface has been removed, leaving the combined effects of the dynamic pressure and the deformed free surface height.

The deeply submerged case shows most of the same flow features as the deeply submerged N003. This includes the high stagnation pressure on the head and shoulders and low dynamic pressure where the flow is accelerated. The regions of separated flow can also be identified as sharp increases in the local pressure coefficient. The wake that develops behind the head can be observed in this manner creating a region of higher pressure down the centre of the upper back.

In the surface case only the pressure coefficient in the water phase has been presented, indicating the portion of the head that is running dry. The increase in pressure due to the bluff body wave system around the head can be seen as an increase in pressure on the front half of the head. This is due to the combined effect of the flow stagnating as it cannot flow up and over the head and the increase in free surface elevation, which in turn raises the hydrostatic pressure. Another consequence of this bow wave system is to direct the flow under the swimmer, reducing the stagnation pressure on the front of the chest due to the presence of the wake under the chin. This influence of the free surface on the velocity field was previously discussed in section 6.2 and can be seen in figure 6-5.

Other obvious free surface features can be observed in the pressure field on the surface case of DA003. A high pressure region on the upper back denotes a local peak in the free surface elevation, as the flow around either side of the head combines before flowing down the back and breaking around the hips. This results in a significantly lower pressure in the small of the back and on top of the hips compared to the deeply submerged case. Again, it should be pointed out that the difference in the free surface flow over the back in the experimental case (see section 6.1) is likely to have changed the pressure field in this region when compared to the surface simulation. This could therefore provide a contribution to the discrepancy in total resistance.

Surface:

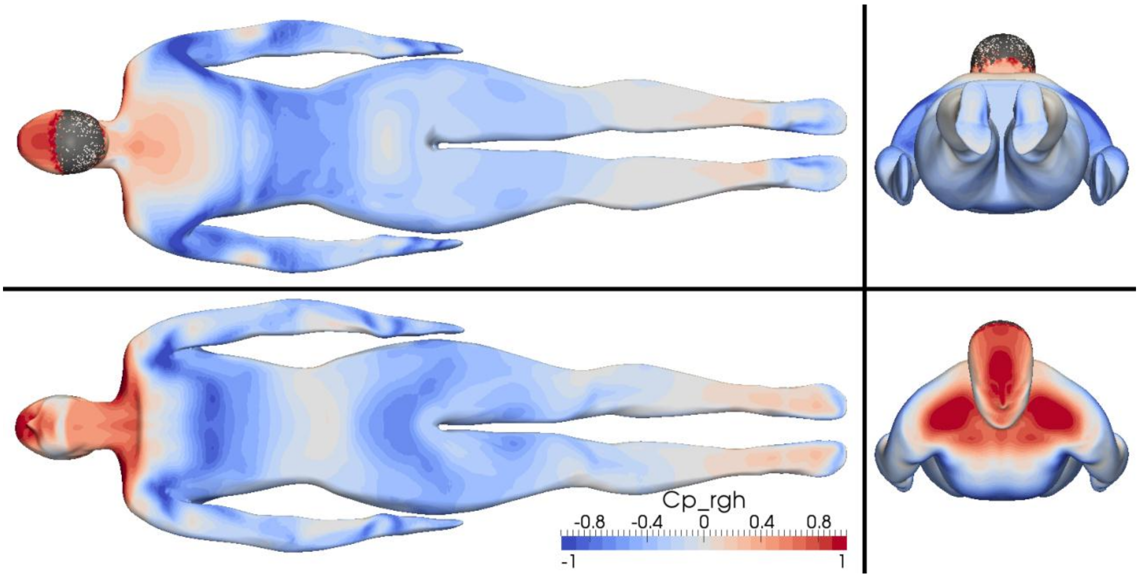

Submerged:

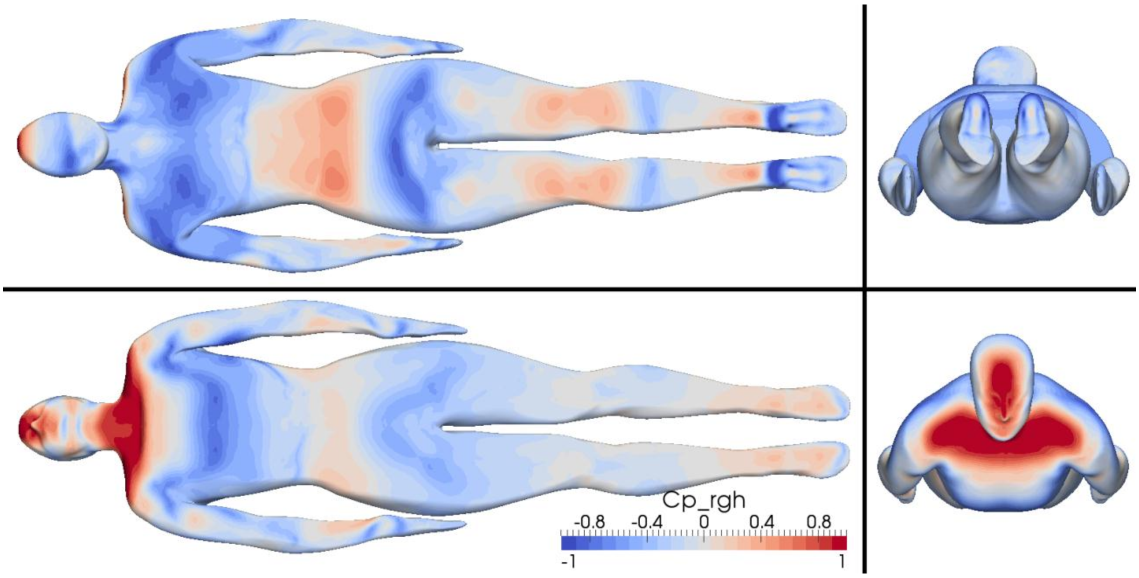

Figure 6-13 - Local coefficient of pressure (defined in equation 5-2) for DA003, on the surface (top) and submerged (below).

The effect of the different simulated pressure distributions on the total pressure resistance can be seen in figure 6-14. The main differences observed are the changes to the stagnation pressure on the head and chest and an increase in resistance around the hips in the deeply submerged case.

Surface:

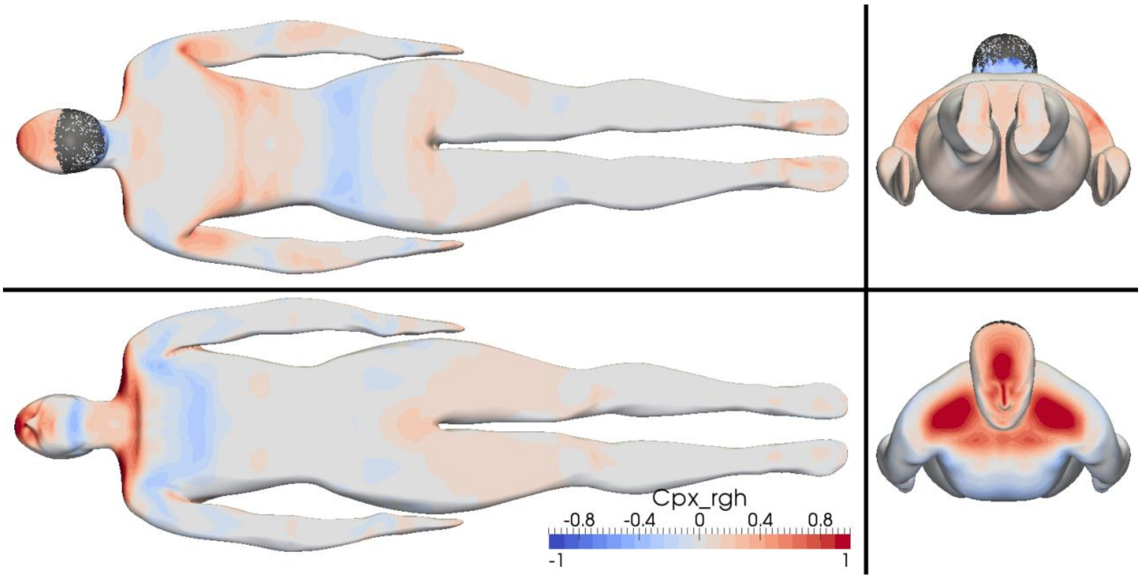

Submerged:

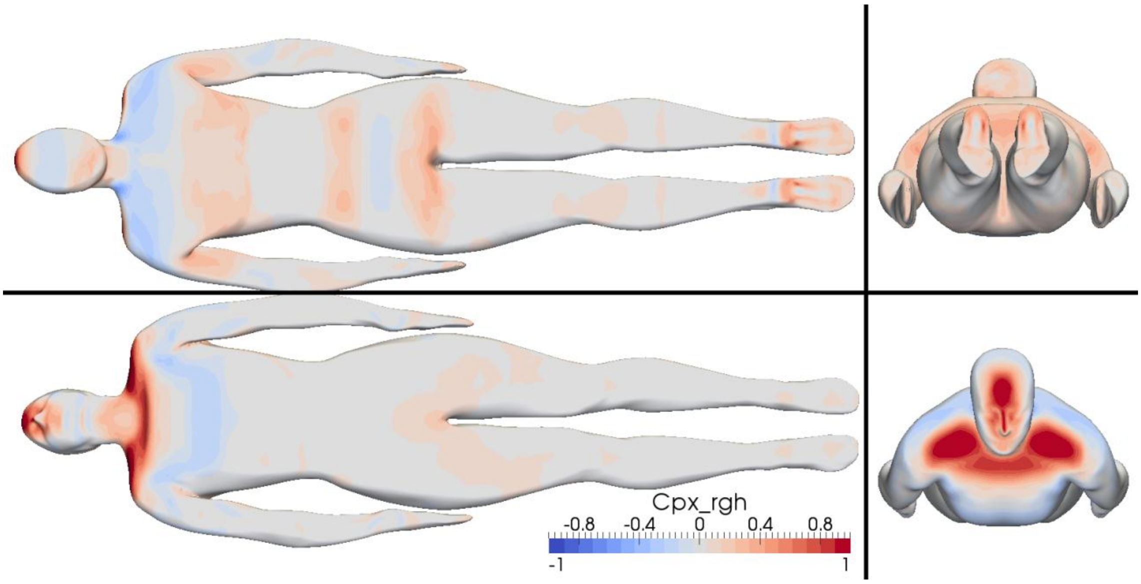

Figure 6-14 - Pressure resistance coefficient (as defined in eq 5-3) for DA003_A, on surface (top) and submerged (below).

6.4.3 Pressure resistance due to waves

Due to the reduced Froude number and the body position of case DA003, far more wave breaking was observed in the experimental case. Increased wave breaking appears to dissipate the energy in the wave system, preventing the simulated wave pattern propagating out over the simulation domain. This has already been discussed at greater length in section 5.4, however the implications for the simulated case can be seen in figure 6-15. The well-defined bluff body wave system around the head can clearly be seen along with the breaking wave at the hips. However the wave system beyond this point is almost entirely dissipated and so despite obtaining experimental wave cuts closer to the swimmer than in N003, it was still not possible to validate the simulated wave resistance against these. Again, the best indication that the pressure resistance is being modelled correctly is the observed similarities in the local free surface features discussed in 6.1. Unfortunately, despite these similarities there are also discrepancies within the free surface features, such as the volume of water flowing down the back of the swimmer and the exact location of the breaking wave field. It is unclear how much these observed differences are likely to affect the simulated wave resistance; however the strong interaction observed between the free surface and the other resistance components indicates that they will have some impact. Without investigating this further the only method for splitting the pressure resistance up is to once again assume that the experimental resistance of 28.45 N is correctly captured within the pressure field on the body. The over prediction of the thin-ship wave resistance is likely to be due to the significant amount of wave breaking that was observed in this case, which will not be correctly captured in this invicid simulation.

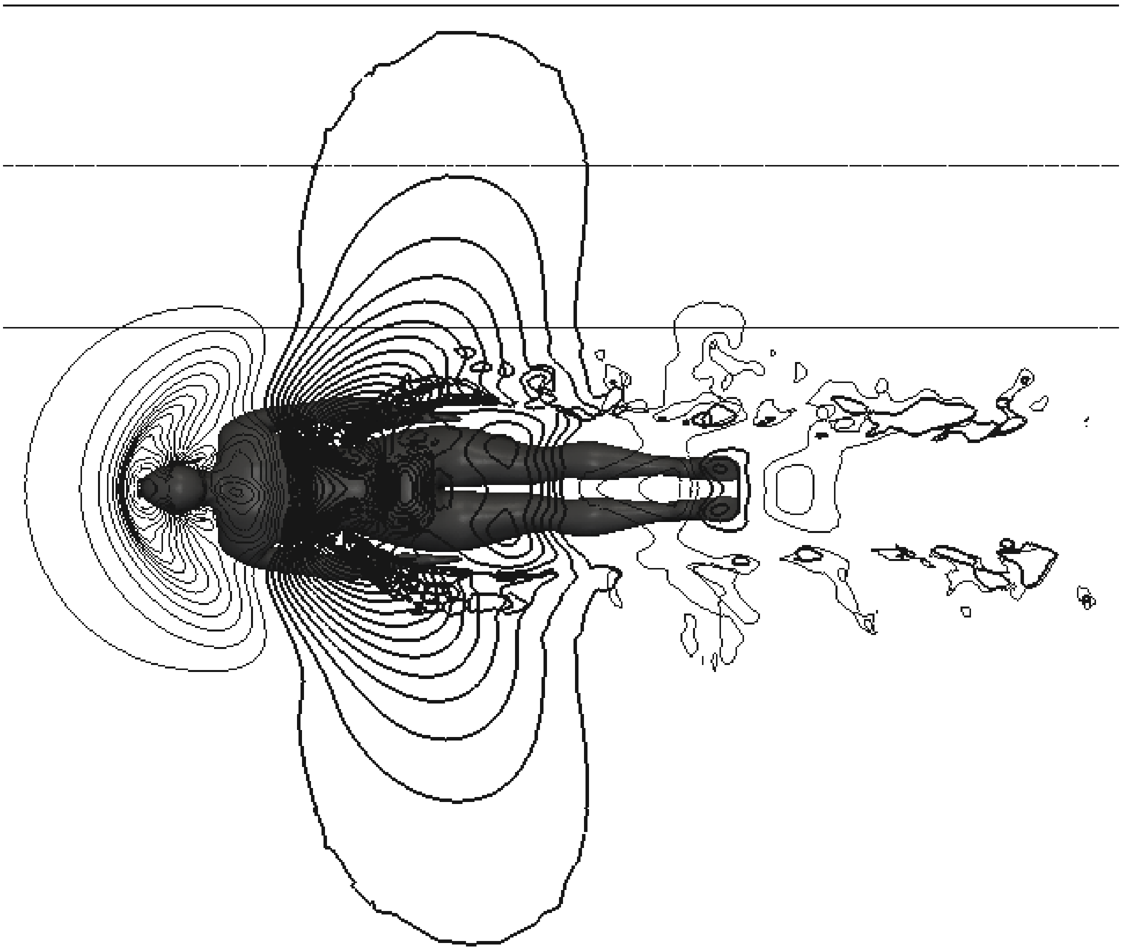

Figure 6-15 - Free surface elevation with contours +-0.005 m, for DA003. Negative deformation is shown with bold contours.

6.4.4 Viscous pressure resistance

If we assume that the wave resistance that was measured experimentally is correctly captured in the pressure field over the body, we can subtract this from the total pressure resistance to provide a simulated form drag of 43 N. These estimated values can be seen in red in table 6-2. This would indicate that the form drag, including the effects of separation, accounts for approximately 54% of the total resistance for the surface case. The form drag for the fully submerged case is approximately twice this at 82 N, encompassing the entire pressure resistance. This seems plausible when you consider the vast increase in the flow separation on the submerged case depicted in the surface streamlines provided in figure 6-12.

Another representation of the impact of bluff body separation on the resistance can be made by observing the wake (velocity deficit) associated with each case (see figure 6-16). The presence of the free surface effectively removes the large wake regions that develop behind the head, shoulders and buttocks of the submerged case. This helps to explain why the resistance of the submerged case actually increased, despite generating no waves.

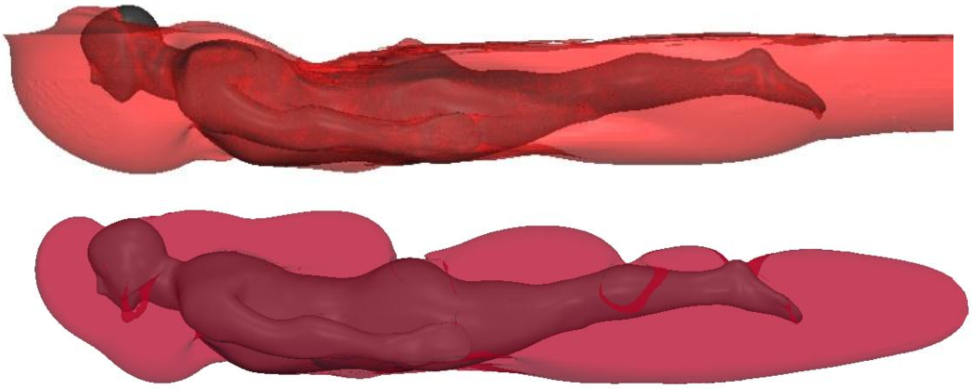

Figure 6-16 - Surface contour of axial velocity deficit ($u/U_0=0.9$) for DA003_A, on surface (top) and submerged (below).

6.5 Discussion

On the whole, the simulation of N003 appears to correspond well with the experimental case. In particular the local free surface features and the total resistance value has been well replicated. This provides justification for the assumption that the experimental wave resistance is correctly simulated, despite the artificial dissipation of wave energy due to wave breaking. The experimental wave resistance was then used to provide a viscous pressure resistance, or form drag, of 71.6 N accounting for 62 % of the total resistance. The pressure resistance for the fully submerged case was 92.7 N, accounting for 92% of the total resistance. This significant reduction in form drag in the surface case is due to the influence of the free surface maintaining attached flow over the majority of the swimmer's back and thighs. This suppresses large regions of separation observed in the fully submerged case. This interaction emphasises that the impact of the free surface is far more complex than simply adding on a wave making resistance component. The free surface interaction causes changes to both the form and frictional components of resistance.

It should be noted that although every effort has been made to recreate the experimental conditions, there are several aspects of the simulation geometry that differ from the experiment, such as the distance of the arms from the body and the dimensions of the head and thighs. These discrepancies will have added errors into the simulation, however it is felt that the fundamental flow features present in the experimental case have been captured.

A much larger discrepancy was observed between the experiment and the simulation of case DA003, with the CFD providing a total resistance 20% greater than the experiment. Despite many of the fundamental free surface flow features being well replicated there were also some significant disparities in the simulated surface flow field. The most obvious difference was an increase in the volume of water flowing over the back and shoulders. These differences in the simulation indicate that the experiment was less well replicated by CFD in this case. There are a number of potential factors that could have contributed to this. Firstly differences in the simulation geometry compared to the experiment were greater for case DA003 (head up) than in case N003 (head in-line). This is due to the significant change in the experimental athlete position in DA003 from the basis STL geometry. It has already been identified in Chapter 5.1.3 that the arm and shoulder position for DA003 could not be matched using the implemented geometry morphing techniques. It is unclear exactly what impact this will have had on the total resistance; however it seems likely that the lower shoulder and arm positions observed in the simulation were the main cause of large volumes of water flowing down the back. This created a significant difference in the free surface flow field compared to the experimental case. This will undoubtedly have had an impact on all the resistance components due to the strong interaction of the free surface on the velocity and, therefore, the pressure field. The difference in the shape of the projected area is also likely to have had an effect of the pressure field around the body.

In addition to the difference in arm and shoulder position between DA003 and the basis STL there were also key differences in both the body shape and posture. As a result of this significant joint rotations and scale factors were used to match the geometry to the experimental footage (see section 5.1.3 for more details). Although this process provided a good match to the athlete outline in the side-on underwater footage, there could be significant differences in the breadth of the swimmer and generally body shape. This would have led to differences in the volume of the geometry compared to the tested athlete, changing both the surface area (affecting skin friction) and the projected area (affecting the form drag). In contrast, much smaller alterations had to be made to the original STL geometry to match the experimental case N003. In this case there was the added advantage of having both profile and side-on pictures of the athlete with which to scale the geometry. It should be noted that any attempt to try and validate the athlete volumes using their mass is made complicated by the unknown volume of air within their lungs.

Besides the issue of obtaining the correct volume for the geometry, small differences in the local shape and curvature could have a significant impact on the local flow such as points of separation and the free surface deformation. In hindsight it was fortunate that the original STL geometry matched the athlete in N003 reasonably well, helping to provide a close match between experimental and simulated resistance.

Another potential cause of geometry error is the vertical position of the body. This had to be determined by eye from the underwater video footage and is therefore likely to have an error of approximately +-0.02m associated with it. Obviously this could have affected either of the passive resistance cases. Indeed if we compare the simulated heave (vertical) force with the athlete weight (803 N and 608 N respectively for N003 and 833 N and 685 N respectively for DA003) it is clear that both simulations are generating more vertical force than their weight. This would suggest that both geometries should be higher in the water. It is important to point out however that small changes to the swimmer's attitude or body shape could change the amount of lift force generated. Likewise, errors in the geometry volume will obviously change the buoyancy force generated.

Another potential reason for the discrepancy in DA003's total resistance is errors in the wave resistance. In both passive resistance cases there was an obvious dissipation of the energy in the wave system, preventing it from propagating out over the simulation domain. However there was a marked decrease in the wave propagation in case DA003. This is thought to be due to the increase in wave breaking close to the body compared to N003. The inability of the implemented free surface method (VOF) to accurately capture the flow physics of breaking waves has already been discussed with regard to wave propagation. However it is possible that in DA003 this process happened close enough to the body to inhibit the local pressure field's accurate development. In N003 this process occurs near the feet and behind the swimmer, decreasing the likelihood of it affecting the accuracy of the local pressure field. However, the similarities between the local free surface features and the experimental footage would indicate that the local pressure field was captured around the torso. The experimental footage of the free surface over the legs shows only unsteady turbulent wake features, indicating that the wave dissipation is unlikely to have a significant impact on the forces in this region. It seems likely that a more significant factor affecting the wave resistance accuracy was the discrepancy in arm and shoulder position between the simulated geometry and the experimental case.

The comparison between surface and submerged examples of both passive cases has highlighted the complex interaction of the free surface on the different resistance components, making it clear that the wave making resistance cannot be assessed simply by comparing the resistance of a swimmer when they are on the surface with when they are deeply submerged.

The complexity of the resistance components on the surface highlights the need for greater understanding of how body shape can ultimately affect surface resistance.

Another benefit of simulating the deeply submerged cases is that it provides an opportunity to compare these results with other simulated data of swimming geometry in a similar position. (Marinho, 2009) simulated a male athlete geometry, with their arms by their side, without the effect of a free surface. The drag coefficients and percentages from this study and the deeply submerged cases for N003 and DA003 are displayed in table 6-3. Case N003-1m would seem the best case to compare due to a similar head and body position being adopted and free stream velocity being used (DA003 was at a lower velocity than the range conducted in (Marinho, 2009)). It can be seen that the relative proportions of friction to form drag are very similar, however there is a significant difference in the drag coefficients. This could be due to the differences in body shape between a male and female geometry. Interestingly the pressure drag coefficient is better matched by case DA003 which is characterised by increased flow separation.

These comparisons help to provide confidence in the developed CFD methodology to capture the correct shear stress distribution and points of separation.

Table 6-3 - comparison of friction and form drag

	DA003-1m		N003-1m		Marinho	
Resistance	coeff	%	coeff	%	coeff	%
Frictinal	0.037291	5.12	0.042567	8.26	0.061	7.96
Form Drag	0.690736	94.88	0.472626	91.74	0.701	92.04
Combined	0.728027	100.00	0.515193	100.00	0.762	100

6.6 Conclusion

An unsteady RANS methodology has been used to simulate the passive resistance components for two different experimental test cases of swimmer on the free surface. In both cases complex free surface features close to the swimmer have been well replicated. The discrepancies that were observed appear to be due to errors in the simulation geometry when compared to the experiment. In both cases the initiation of wave breaking was found to dissipate energy from the wave system preventing it from propagating out over the simulation domain. This prevented the simulated waves from being validated against experimental wave cuts.

The first simulated case (N003) not only captured the local free surface flow but reproduced the total experimental resistance to within 1%. This total resistance was made up of 8.3% skin friction and 91.7% pressure (30% wave and 62% form drag). The second case (DA003) over-estimated the total resistance by 20%. However this is believed to be in part due to the inaccuracies of the simulated geometry, causing a different free surface flow regime over the athlete's back. The total resistance was made up of 9.6% skin friction and 90.4% pressure (36% wave and 54% form drag). This case highlights the importance of using accurate geometries and the need to obtain athlete specific scan data with the correct body posture. Ultimately it should be accepted that this process will always provide some inaccuracies and therefore CFD validation data should, if possible, be acquired using a manufactured mannequin with controlled attitude and depth to ensure consistency.

For both experimental cases additional simulations were conducted with the same geometry at a depth of 1m. This allowed a comparison to the surface simulation to be made to assess the impact of the free surface on the different resistance components. In both cases the interaction of the free surface was found to change the boundary layer growth and points of separation on the swimmer's body entirely. In general the free surface maintained attached flow over the swimmer's back, suppressing separation. This emphasises the complex effect of the free surface on the flow around a swimmer, making it impossible to assess wave making resistance from the difference in total resistance between two different depths.

Taking into account the aims of this thesis it is believed that the developed methodology has been shown to capture the different resistance components of a passive swimmer on the surface. It has been shown to replicate two very different free surface flow regimes and therefore should provide a reliable basis for assessing the impact an arm has on the resistance of a freestyle swimmer.

7. Development of a propulsion model

7.1 Introduction

So far the focus of the presented work has been on simulating the resistance components of a passive swimmer on the surface. However to understand how the hydrodynamic forces vary on a freestyle swimmer throughout a stroke, the impact of the arm on the fluid has to be included. The computational challenges associated with physically modelling the arm were discussed in Chapter 4.4, resulting in the decision to represent the arms using a body-force method. This allows the impact the arm has on the fluid to be captured within a simulation using the same RANS methodology developed for a passive athlete geometry.

As the arms generate the majority of the propulsion (Marinho, Barbosa, Mantha, Rouboa, & Silva, 2012) and the legs are unlikely to affect the flow over the head and torso of the athlete, no attempt was made to simulate the legs.

7.2 Body Force Implementation of arms

The swimmer's arms can be represented by adding momentum sources into the simulation domain that represent the impact the arm has on the fluid. The strength and direction of these source terms are determined from the force acting on the arm as it moves through the water.

7.2.1 Force estimation

To calculate the forces acting on the arm, it is viewed as a foil capable of generating both lift and drag as it moves through the water. Using a quasi-steady blade element approach this foil is split up into a series of n elements of length δl. The hydrodynamic forces acting on each blade element can be seen in figure 7-1, where F_L is the lift force and F_D is the drag force.

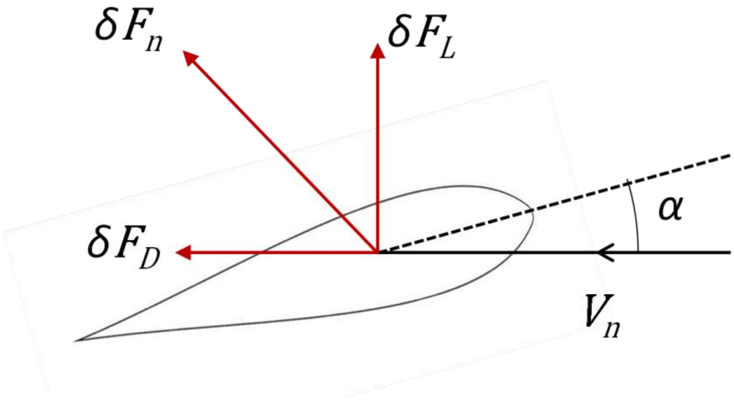

Figure 7-1 - Forces acting on an individual blade element.

The lift and drag vectors acting on each blade element (normal to the blade) are defined as

$$\delta\overline{F_L} = \left(\frac{1}{2}\rho|V_n|^2 C_l c\delta l\right)\left(\widehat{V_n} \times \widehat{AB}\right) \qquad 7\text{-}1$$

and

$$\delta\overline{F_D} = \left(\frac{1}{2}\rho|V_n|^2 C_d c\delta l\right)\widehat{V_n} \qquad 7\text{-}2$$

respectively, where V_n is the velocity vector of the fluid (normal to the blade), c is the blade chord and $\widehat{AB}$ is the unit vector along the blade's span. Therefore $\left(\widehat{V_n} \times \widehat{AB}\right)$ provides a unit vector perpendicular to both the normal velocity and the blades span.

The lift and drag coefficients, C_l and C_d, are defined by the angle of attack α of the individual blade element to the normal velocity vector. The force vector normal to the blade is therefore

$$\overline{F_n} = \sum_{i=1}^{n} \delta\overline{F_n} = \sum_{i=1}^{n} \delta\overline{F_L} + \delta\overline{F_D} \qquad 7\text{-}3$$

The normal velocity observed by each blade section is calculated from the relative motion of the arm and the fluid. This is described in more detail in sections 7.3.2 and 7.5.1 as the kinematic model was refined.

This quasi-steady methodology does not take account of the unsteady effects of the arms' acceleration or the 3D effects of radial flow down the arm. The impact of these simplifications is likely to be significant and therefore potential methods of including some of these effects into force coefficients are discussed later in this chapter. The main benefit of adopting a quasi-steady approach at this stage it that it allows a generic propulsion model to be created.

7.2.2 Applying momentum source terms within OpenFOAM

The blade forces are applied to a propulsive domain, representing the region of fluid the arm is acting on during that time step. Its location and size is determined by the arm's location (provided by the kinematic model) and its dimensions, such as blade length *l* and chord *c*. The propulsive domain is then divided up into sectors of length *δl*, representing individual blade elements.

The coordinates of each cell within the fluid domain are calculated relative to the paddle location, determining which cells are within a given sector of the propulsive domain and providing accurate sector volumes.

The current simulation time is used to calculate the position of the blade, based on kinematic data for a single stroke cycle and a defined stroke rate. The velocity of the blade is calculated based on the blade position from the previous time step. The normal force (*δFn*) is then calculated for a blade element, with length and chord equal to the sector dimensions. The momentum source term for each cell within that sector is calculated as

$$f_i = \frac{\delta \bar{F}_n \varphi}{V_s} \,, \qquad 7\text{-}4$$

where φ is the cell's volume fraction and V_s is the sector volume. Therefore source terms are only applied while the blade is in the water (φ=1), automatically taking account of the dynamic free surface. The source terms are stored within a volume vector field, with each cell outside the propulsive domain set to zero. These are then added to the momentum equation (4-6) within the OpenFOAM solver interFoam (OpenFOAM®, 2011). The total blade force is determined for each time step by multiplying each cell's source term with its cell volume and summating over the propulsive domain. The instantaneous thrust is then acquired by resolving this force vector into the direction of the swimmer's motion (equal and opposite to the free stream velocity vector U_0).

To enable both swimmer's arms to be simulated, two separate body force models were added to the interFoam solver. This provides the potential for different arm kinematics to be simulated.

7.3 Kayak paddle validation case

Before conducting simulations of a swimmer's arm, a simplified test case of a rotating kayak paddle was conducted. This provided a comparison to unsteady experimental data of a rotating kayak paddle, including free surface interactions (Ellison & Turnock, 2010). This case provided the opportunity to validate the proposed methodology using simplified kinematics and blade properties.

7.3.1 Experimental data

A marathon kayak paddle was mounted on an instrumented pivot mechanism attached to a towing tank dynamometer (Figure 7-2). This allowed lift, drag and rotation angle to be recorded against time. A constant torque was applied to the paddle via a dropping weight allowing the dynamic forces generated by the blade to be measured against time.

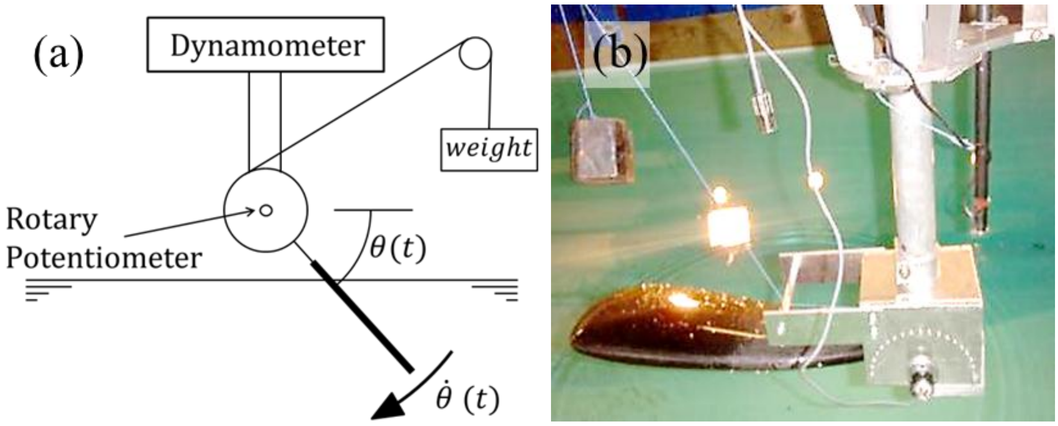

Figure 7-2- Schematic (a) and picture (b) of dynamic paddle experiment.

The experimental data for a blade angle of attack of 90 degrees to the flow (i.e. a purely drag based stroke) can be seen in figure 7-3. A discontinuity in the angle data (t = 2.5 s), is thought to be due to a dead spot on the rotary potentiometer and not the flow physics. This error gets amplified when the angular velocity is calculated.

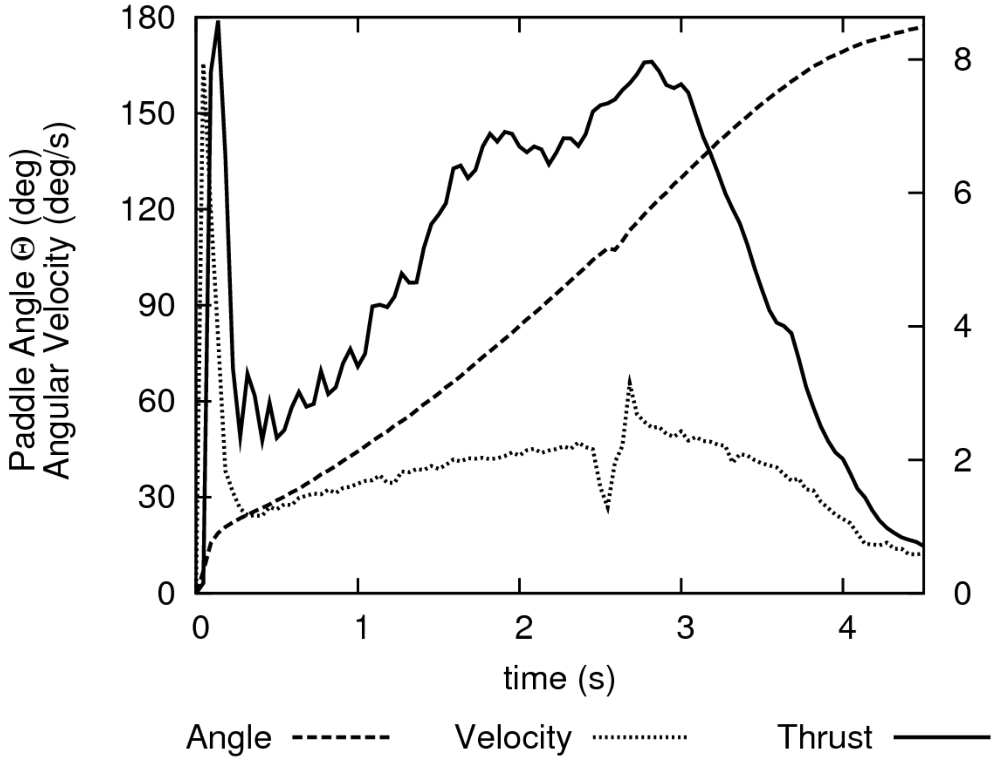

Figure 7-3 - Experimental data for a rotating paddle (Ellison & Turnock, 2010).

7.3.2 Paddle kinematics

The paddle's motion is described by pure rotation $\dot{\theta}$ about a fixed point (see figure 7-4). The angle of rotation θ is measured from the horizontal, ahead of the point of rotation (therefore it increases throughout the stroke).

The kinematic data for the paddle model was provided as a series of blade rotation angles θ over a full stroke cycle of 360 degrees. The data from 0-180 degrees was sampled at a constant time interval from the experimental data. This effectively removes the discontinuity in the experimental data. The blade recovery (not performed in the experiment) was provided by assuming a constant angular velocity with the same time interval. This angle data for a full paddle stroke was then put through a Butterworth filter to smooth the transition from experimental to interpolated data.

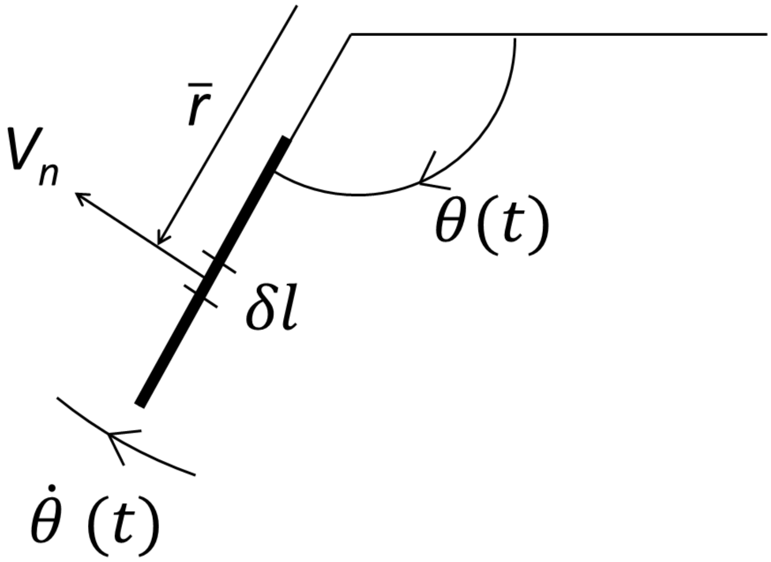

Figure 7-4 - Free body diagram of paddle kinematics.

The velocity magnitude encountered normal to a blade element with a radius vector $\bar{r}$ is given by

$$V_n = (\dot{\theta} \times \bar{r}) \cdot \hat{n}, \qquad 7\text{-}5$$

where $\hat{n}$ is the unit vector normal to the blade calculated as

$$\hat{n} = \hat{\dot{\theta}} \times \hat{r}. \qquad 7\text{-}6$$

The normal velocity is then used in equations 7-1 and 7-2 to calculate the forces on the blade.

7.3.3 Blade parameters

Due to the polar coordinate system used to provide the blade kinematics, the propulsive domain was defined as an arc swept by the paddle. Its location in time is provided by the paddle's centre of rotation and angle of rotation *θ(t)*.

Its dimensions are derived from the paddle length (or radius) *l*, chord *c* and an arc angle (or swept angle) *δθ*. The propulsive domain is then divided up into sectors of length *δl* with an inner radius to account for the length of the paddle handle, see figure 7-5.

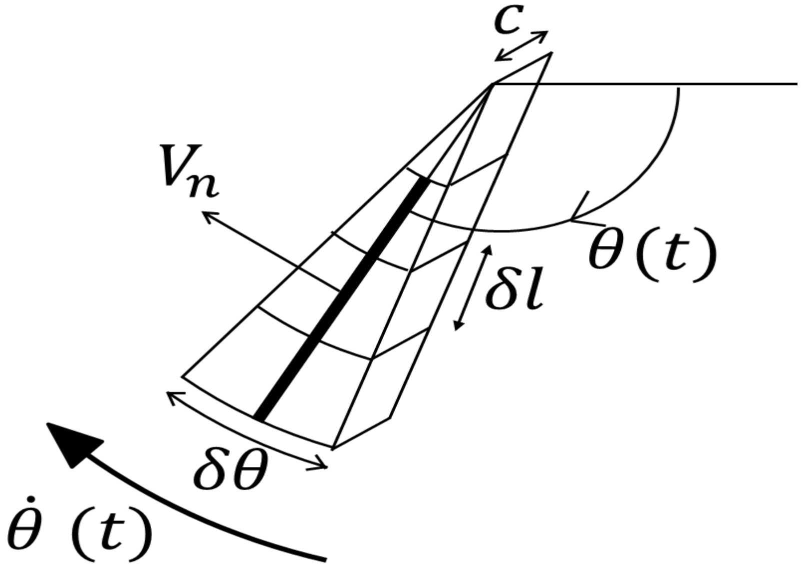

Figure 7-5 - Schematic of paddle propulsive domain divided into sectors.

In the body force simulation of the experiment the paddle was represented as a square plate of the same length and chord (0.54 and 0.2 m respectively). A propulsive domain of swept angle (*δθ*) equal to 20 degrees was divided into 8 radial divisions, with an inner radius of 0.1m. The centre of rotation was placed 0.1m above the free surface. Due to the constant angle of attack of 90 degrees a fixed drag coefficient was used and the lift coefficient was set to zero.

7.3.4 Numerical model

The numerical settings used for the simulation were the same as those provided in Chapter 5.4.

7.3.5 Results

The experimental data was best replicated by a drag coefficient of 2.4 over a range of rotational velocities. This is larger than the maximum value of 1.75, recorded in steady translation paddle experiments (Sumner, D., Sprigings, E. J., Bugg, J. D., & Heseltine, 2003), and 1.2 for a flat plate (Hoerner, 1965). These three simulation cases can be seen in figure 7-6 along with a constant angular velocity case for the flat plat, demonstrating the importance of the varying paddle velocity. The increase in the unsteady drag coefficient could be due to a number of factors. Firstly the unsteady effects of the variable velocity and interactions with the free surface are likely to have a significant impact. Secondly the flow regime around a rotating paddle is likely to be different from one translating. Finally the 3D effects of the blade having a finite length, causing different flow at the root and tip, will cause significant differences compared to a 2D blade element approach. These differences are modelled as a Goldstein correction when using a similar methodology to model marine propeller blades (Molland, A. F., Turnock, S. R., & Hudson, 2011).

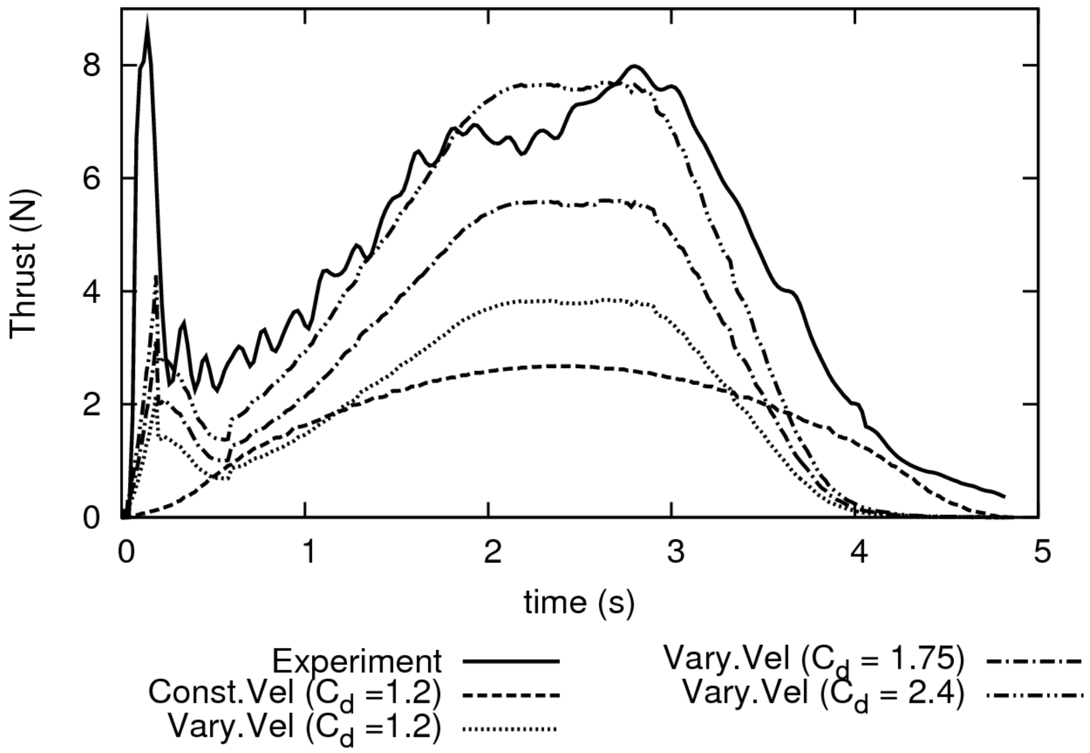

Figure 7-6 - Thrust generated by the paddle model compared with experimental data.

In order to check the induced velocities in the fluid domain were correct, a simple momentum analysis was performed over a control volume encompassing the propulsive domain. By monitoring how the average axial velocity U_x varied within the control volume, the axial force applied to the fluid was calculated and found to agree closely with the calculated thrust.

7.3.6 Conclusion

The kayak paddle simulation has shown that a blade element approximation of an unsteady paddle stroke can provide a good representation of the forces produced by the blade. It is recognised, however, that to achieve the correct force magnitude the drag coefficient used in the simulation had to be tuned to the experimental data. It is therefore concluded that provided some effort is made to tune the force magnitude to the simulated conditions the developed blade element methodology is suitable for simulating the forces generated by a swimmer's arm.

7.4 Self-propelled kayak case study

Before developing a propulsion model for a freestyle swimmer's arm it is helpful to apply the developed kayak paddle model within a self-propelled simulation. This provides a simplified test case of the methodology required to investigate active freestyle swimming.

7.4.1 Introduction

The difference between medal positions in sprint kayak is often as little as tenths or even hundredths of a second (London2012, 2012). The competitors speed is determined by balancing the thrust produced by the paddle and the resistance of the kayak hull. The resistance is comprised of skin friction (due to the viscous boundary layer) and pressure resistance (containing form drag and wave resistance) (Molland, A. F., Turnock, S. R., & Hudson, 2011). For kayak designers to help provide performance gains the resistance has to be minimised allowing greater speeds to be achieved for the same propulsive power.

Jackson (Jackson, 1995) estimated the different components of resistance acting on a sprint kayak, along with the thrust generated by the paddler, in order to identify potential areas for performance improvement. The design of sprint kayaks and canoes has primarily focused on optimising the hull form for minimum calm water resistance. This has been achieved using empirical data and a thin ship approach (L Lazauskas & Tuck, 1996; Leo Lazauskas & Winters, 1997) and through the use of Computational Fluid Dynamics (CFD) and tank testing (Bugalski, 2009). The surge velocity of rowing shells was investigated both numerically and experimentally indicating the significant effects of the unsteady motion on the total resistance (Alexander Day, Campbell, Clelland, Doctors, & Cichowicz, 2011). It was concluded that a good representation of the surge motion of the hull could be replicated in a towing tank and could therefore be used to further minimise the unsteady resistance of hull designs for rowing shells and kayaks.

Research has also been conducted into blade designs in paddle sports, including both experimental, analytical and CFD studies (Morgoch & Tullis, 2011; Ritchie, Faizal, & Selamat, 2010; Sumner, D., Sprigings, E. J., Bugg, J. D., & Heseltine, 2003). A lack of agreement between CFD methods was attributed to the lack of free surface in the CFD simulations. The importance of free surface effects and unsteady motion on blade forces was demonstrated through CFD and experimental simulations of oar blades in rowing (Leroyer, Barré, Kobus, & Visonneau, 2010; Sliasas & Tullis, 2010). The impact of viscosity was found to be very limited.

Despite individual research into hull design and paddle propulsion no one has investigated their flow interactions. A kayak paddle operates close to the side of the hull generating large local velocities which may have an impact on the hull hydrodynamic forces. However as these paddle induced interactions have never been evaluated it is unclear if they need to be included in a hull optimisation process.

7.4.2 Self-propelled simulations

To assess the extent of the interaction between the paddle and hull the developed body force model of a kayak blade was implemented on both sides of a K1 sprint kayak, with the left hand paddle 180 degrees out of phase from the right. The kayak geometry used was taken from the Eagle kayak by Ted Van Dusen, which was the base for many modern hull shapes (Bugalski, 2009).

The length, beam and draught were 5.2 m, 0.38 m and 0.12 m respectively, giving a displacement of 80 kg. The hull pitch angle was fixed at zero and the velocity set at 5 ms^{-1} ($F_R = 0.7$), calculated as an average speed based on race times for the women's K1 200m event (International Canoe Federation, 2011).

7.4.3 Meshing technique

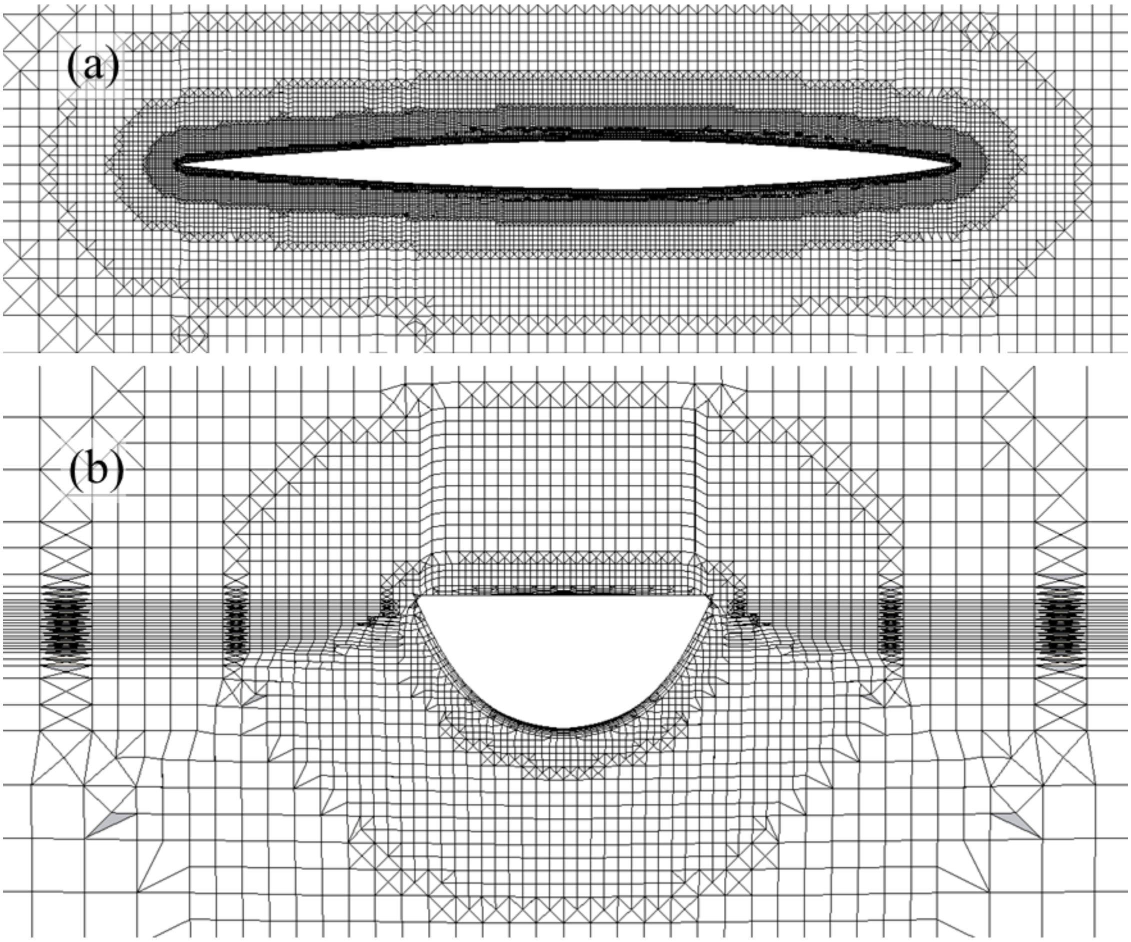

Figure 7-7 - Mesh structure seen on a horizontal plane at the water line (a) and a vertical plane at amidships (b).

An unstructured hexahedral mesh around the kayak was created using the snappyHexMesh utility within OpenFOAM, with dimensions of 20 m, 16 m, 12 m. Firstly a coarse block mesh was created with cells of 0.5 m in each direction. Regions were defined with up to six levels of isotropic refinement (dividing the local cell dimensions by up to six), gradually increasing the mesh density near the hull, whilst maintaining a cell aspect ratio of approximately one. Uni-directional refinement was applied perpendicular to the free surface to provide good wave pattern resolution, whilst minimising mesh size.

Boundary layer elements were grown out from the kayak surface mesh to provide a first cell height of approximately 0.0005 m. This places approximately 10 cells within the predicted boundary layer with an estimated y^+ of 40 allowing the viscous boundary layer to be captured using wall functions (WS Atkins Consultants, 2003). The developed mesh structure can be seen in figure 7-7.

7.4.4 Numerical model

The solver settings and simulation parameters can be found in table 7-1.

Table 7-1 – Numerical settings for self-propelled kayak study.

Property	Mesh
Type of mesh	Unstructured (Hexahedral)
No. of elements	Approximately 1.2M
y+ on the hull	Approximately 50
	Domain physics:
Fluid	Homogeneous water/air multiphase, kOmegaSST turbulence model
Inlet	Free stream velocity of 5m/s, buoyantPressure, k = 0.1 m^2s^{-2}, omega = 2 s^{-1}
Outlet	*U*=Zero gradient, *P*=static pressure
Bottom/sides	Wall with velocity set to free stream value U_0 , buoyant pressure
Top	Opening
Hull	Wall with no slip condition, buoyant pressure, kqRWallFunction, omegaWallFunction
	Solver settings (interFoam):
Transient scheme	1st order Euler
Grad (U) Scheme	cellLimited Gauss linear 1
Div (U)	Gauss linearUpwind grad(U)
Pressure coupling	PIMPLE
Convergence criteria	P 1e-7, U 1e-8, k 1e-8, omega 1e-8
Multiphase control	Volume fraction coupling
Timestep control	max Courant No = 0.4, max Volume fraction Courant No = 0.4
	Processing Parameters:
Computing System	IRIDIS High Performance Computing Facility (University of Southampton)
Run type	Parallel (24 Partitions run on 2x12 core nodes each with 22 Gb RAM)
Wall Clock time	88 hours for 19 seconds of naked hull simulation 24 hours for 5.4 seconds of Self-propelled simulation

7.4.5 Naked hull resistance

The naked hull resistance of the passive kayak was determined from a surface integration of the shear stress and pressure over the hull, providing skin friction and pressure resistance respectively. These individual force components, along with their total, are presented in table 7-2. An estimate of the skin friction is also provided using the ITTC'57 correlation line (Molland, A. F., Turnock, S. R., & Hudson, 2011) using the static wetted surface area of 1.692 m^2. The pressure or residuary resistance (combined form and wave drag) is also provided using an experimentally determined coefficient of residuary resistance obtained from a K2 kayak (Wolfson Unit for Marine Technology and Industrial Aerodynamics (WUMTIA), n.d.). Finally, thin ship theory (Insel, M., Molland, A. F., & Wellicome, 1994) provides a numerical estimate of wave resistance, assuming potential flow. The general agreement between the individual components of resistance provides some confidence that the flow is being correctly modelled. The resulting free surface deformation can be seen in figure 7-8.

Table 7-2 - Resistance components from naked hull simulation and other sources.

Resistance (N)	ITTC'57	Experimental	Thinship	CFD
Skin Friction	55.02	-	-	59.06
Pressure or Residuary (Wave and Form)	-	14.26	-	16.00
Wave	-	-	15.10	-
Total	-	-	-	75.05

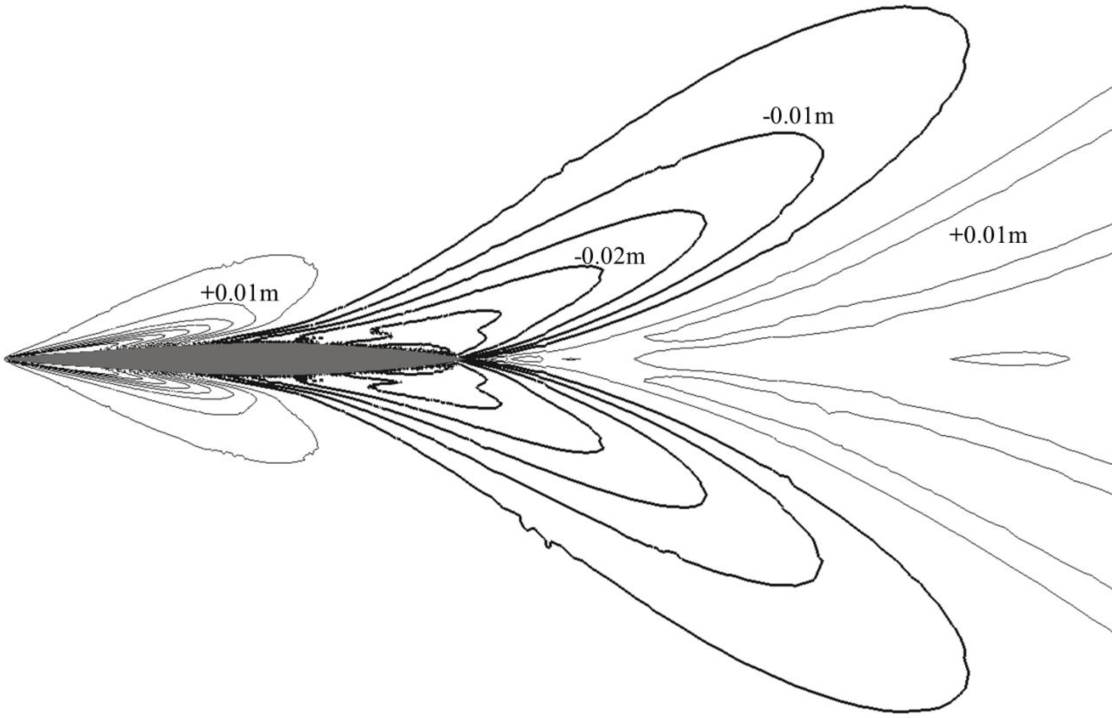

Figure 7-8 - Naked hull free surface deformation with contours every ±0.005m from the static free surface (bold contours are wave troughs).

7.4.6 Simulated K1 Paddling technique

To represent an athlete's paddling technique as closely as possible the paddle length and centre of rotation were taken from stroke data presented in (Kendal & Ross, 1992). The blade dimensions were as previously used for validating the paddle force model. This provided a propulsive domain with outer and inner radius of 0.97 m and 0.52 m respectively and a swept angle ($\delta\theta$) of 10 degrees. The coordinates for the centre of rotation were chosen as (0 m, ±0.35 m, 0.54 m), relative to the centre of the kayak (on the waterline), to best simulate the early drag based phase of the stroke. This was based on the blade entry position presented in (Kendal & Ross, 1992) however neglects the lateral translation of the blade from this point. The resultant volume of water swept by one blade can be seen in figure 7-9.

Two different paddling techniques were simulated based on different angular velocity profiles. Stroke profile A is a simplified technique which maintains a constant angular velocity throughout the entire stroke. Stroke profile B has a varying angular velocity prescribed to match the simulated thrust profile with paddle force traces measured in experimental field tests using sprint kayak athletes (Wolfson Unit for Marine Technology and Industrial Aerodynamics (WUMTIA), n.d.)).

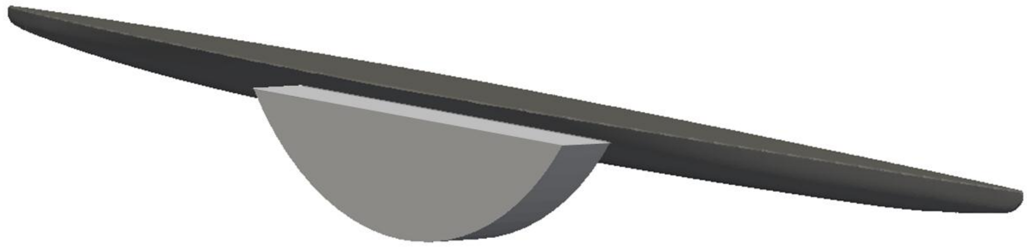

Figure 7-9 - Volume swept by the time varying position of the propulsive domain alongside the kayak's hull.

To gain insight into how the paddle and hull interact, three different lateral positions for the propulsive domain were used. The centre of the paddle was off-set from the hull centreline by 0.35, 0.50 and 0.65 m, corresponding to 0.16, 0.31 and 0.46 m from the maximum beam, see figure 7-10.

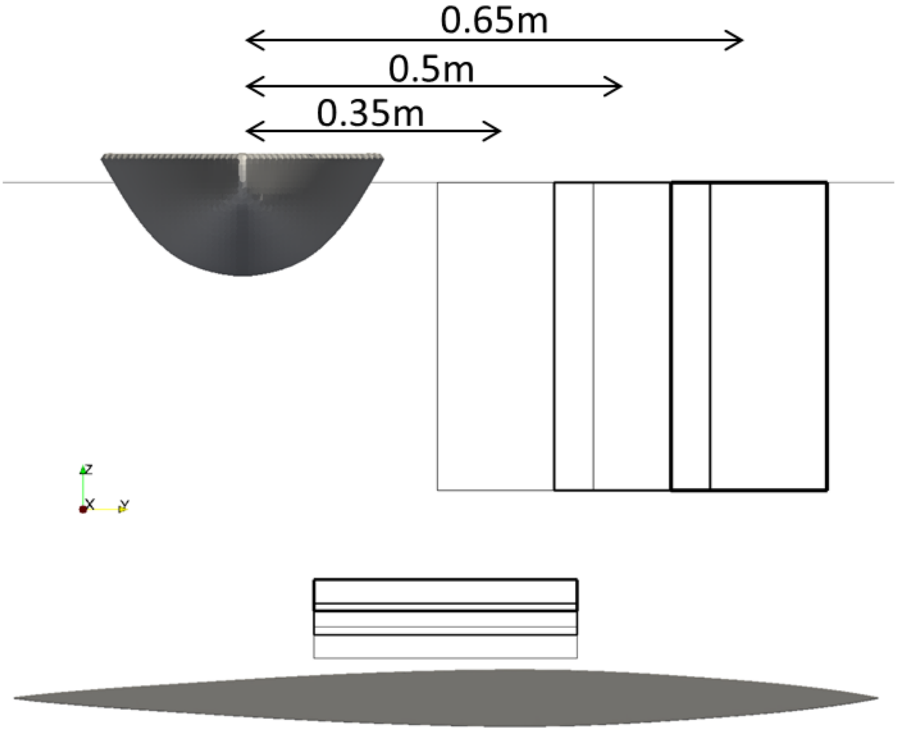

Figure 7-10 - Position of the volume of water swept by propulsive domains of different lateral spacing's, indicated by increasing line weights.

7.4.7 Stroke rate

To simulate a self-propelled kayak the average thrust generated by the paddle has to equal the average hull resistance. The required stroke rate, or stroke period t_{stroke}, was determined by simulating the two different stroke techniques without the kayak for a range of angular velocities until the average thrust was within 1 N of the naked hull resistance. This resulted in a stroke rate of 67 and 60.45 cycles/min, producing approximately 74 and 76 N of thrust for stroke profile A and B respectively.

7.4.8 Effect of paddle on the local flow

The self-propelled simulations continued from the converged solution of the naked hull. The increase in computational cost for a given simulation time was 8 %.

The impact the paddle model has on the free surface can be seen in figure 7-11. The distinctive depression due to the right and left paddle strokes can be seen at t/t_{stroke} = 0.25 and 0.75 respectively. These travel downstream with time creating an unsteady wave pattern that appears similar to those observed behind K1 kayaks.

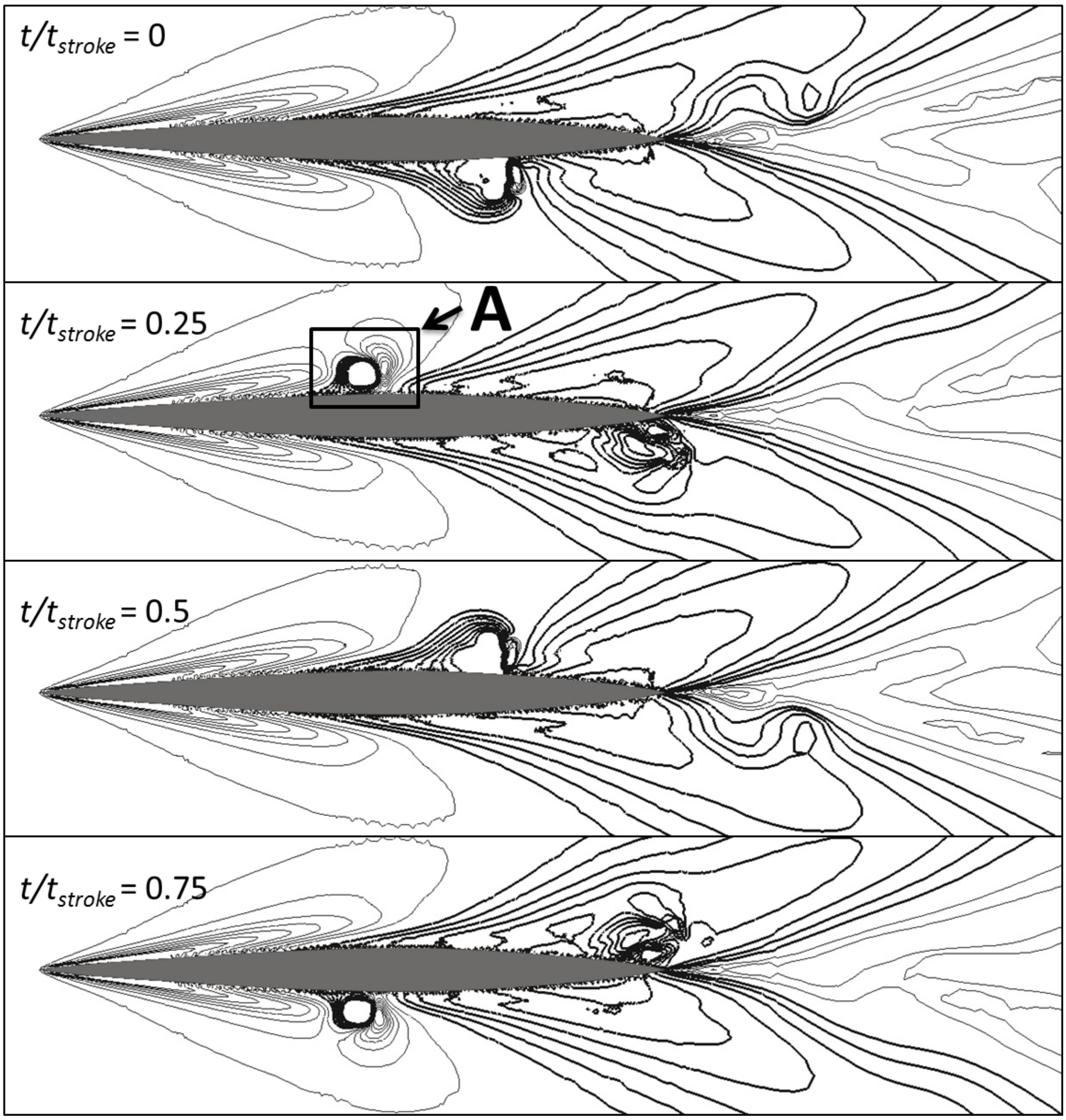

Figure 7-11 - Self-propelled free surface deformation with contours every ±0.005m from the static free surface (bold contours are wave troughs), for different relative stroke times (t/t_{stroke}), for stroke profile (A) offset 0.35m from the kayak centreline.

The impact the paddle has on the local velocity can be seen in Figure 11. At a depth of 0.1 m the proximity of the hull's boundary layer can be seen to modify the flow speed due to the no slip boundary condition. Upstream and downstream of the paddle the axial velocity is increased near to the hull, however, between the paddle and the hull the flow actually recirculates around the edges of the propulsive domain due to the difference in pressure and free surface height. The impact of the dynamic free surface can be seen in figure 7-12 (a) as the trough created behind the blade draws fluid in from the sides. It can be seen in figure 7-12 (b) that at a greater depth this no longer occurs.

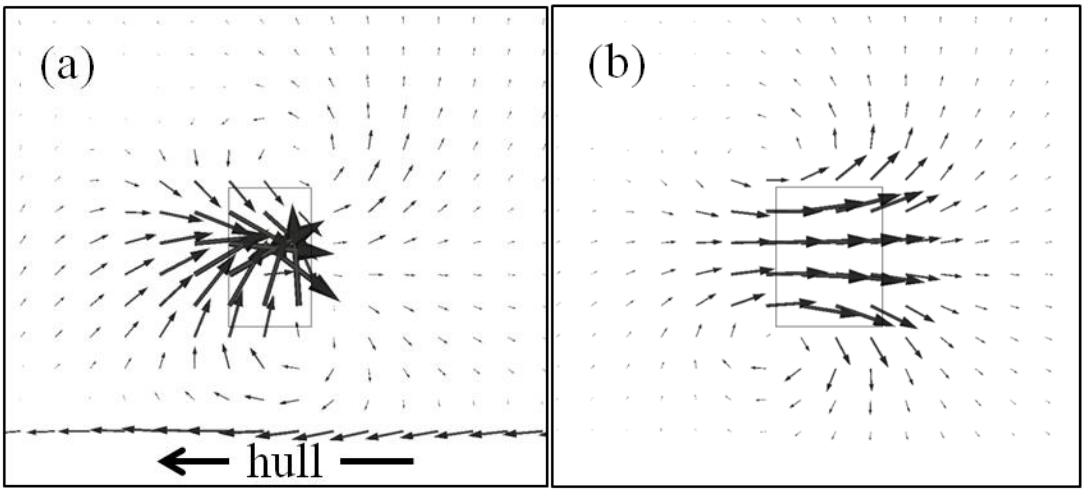

Figure 7-12 - Change in velocity from the free-stream value U_0, due to right paddle stroke (θ = 90 deg, t/t_{stroke} = 0.25). Values taken on a horizontal plane at location A in figure 7-11, at a depth of 0.1m (a) and 0.3m (b). The location of the propulsive domain at each depth is shown by an outline.

7.4.9 Comparison of different stroke techniques

The impact of the two different paddling techniques on the thrust and hydrodynamic forces acting on the kayak can be seen in figure 7-13. The reduction in thrust during the middle of paddle stroke (A) is due to the forward velocity of the kayak reducing the local fluid velocity normal to the blade when the paddle is vertical. In reality an athlete does not maintain a constant angular velocity but would naturally compensate for the effect of the kayaks forward motion by accelerating the blade through the middle of the stroke. The effect of varying the rotational velocity in this manor can be seen in technique (B). The interaction of the free surface with the paddle model has affected the average thrust generated by the two paddling techniques in opposite ways, decreasing A while increasing B from the values in section 7.4.7. This indicates that in the future the stroke rate should be determined within the self-propelled simulation.

The variation in total resistance is small with a maximum increase of less than 1 N from the naked hull case. As the paddle accelerates the flow alongside the hull, an increase in the frictional resistance may be expected. In-fact the average frictional resistance is reduced, potentially due to the recirculation of fluid between the hull and the paddle seen in figure 7-12 (a), effectively reducing the free stream velocity near the hull. It is clear from the free surface deformation in figure 7-11 that the paddle model affects the pressure field resulting in the observed increase in pressure resistance. This increase is predominantly observed during the paddle entry phase (t/t_{stroke} = 0.125), but is minimised with technique (B) by entering the water at a lower angular velocity.

The net result for technique (A) is an increase in average self-propelled resistance of 0.05N from the naked hull case, whilst decreasing by 0.12 N for technique (B). This indicates that that paddle interactions may help to reduce resistance in some cases. Overall a 0.23% reduction in self-propelled resistance is observed between paddling technique (A) and (B).

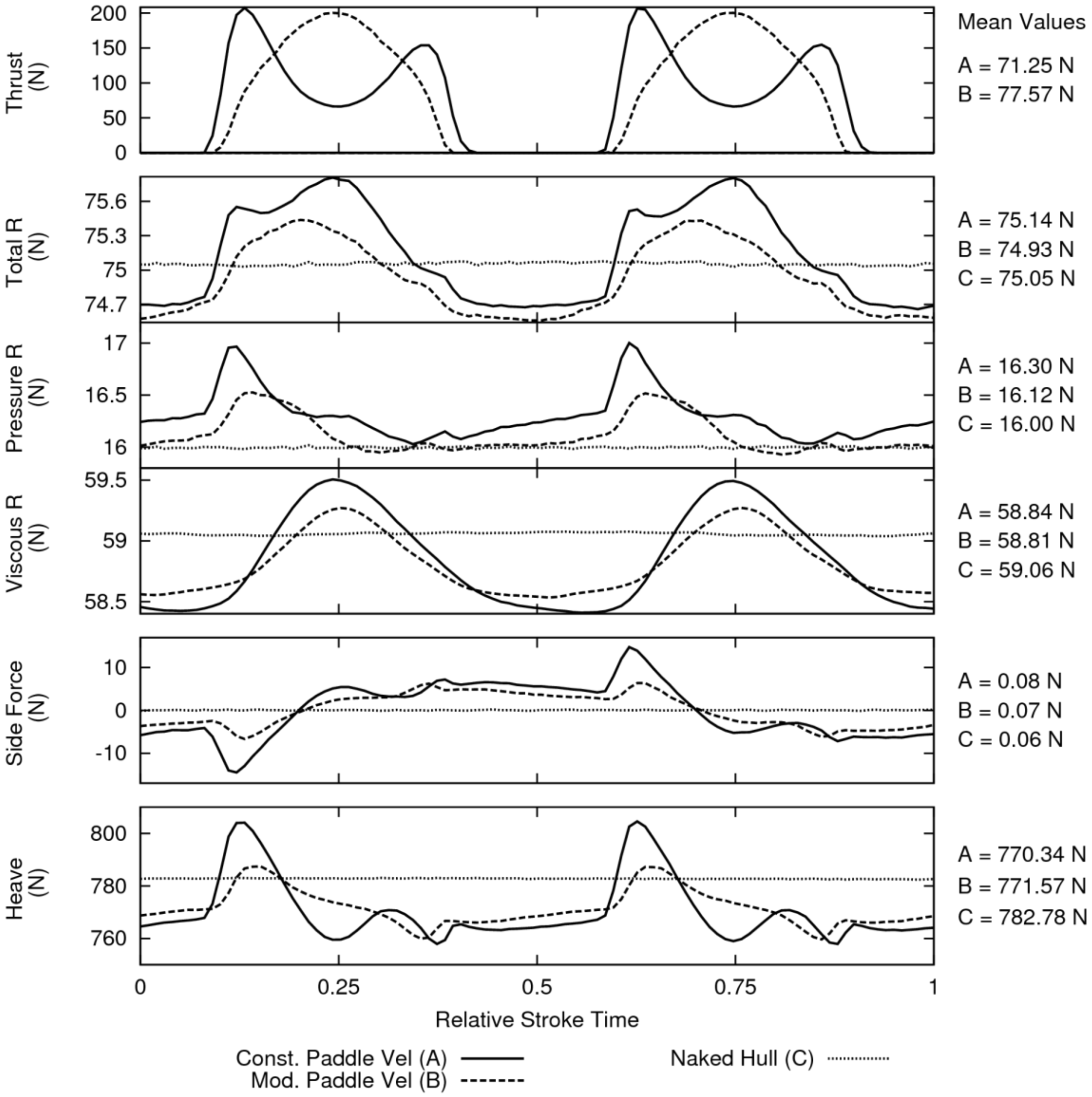

Figure 7-13 - Hydrodynamic and hydrostatic forces for two self-propelled kayaks with different paddling techniques for a paddle offset of 0.35 m and the naked hull (towed case).

The variation in both the side and vertical forces, due to the changes in the pressure field, are more significant than the change in resistance. As the fluid is accelerated the pressure drops pulling the kayak in that direction. This results in a side force fluctuation that lags behind the paddle model by approximately a quarter of a stroke, due to the accelerated flow moving down the hull after the paddle exits. A general decrease in the hydrodynamic lift is also observed, except when the paddle enters creating a high pressure region beneath it. The moments generated by these time varying hydrodynamic forces can be seen in figure 7-14. Both self-propelled cases exhibit a bow up (positive) pitch moment, due to the accelerated flow passing along the aft half of the hull, reducing the local pressure.

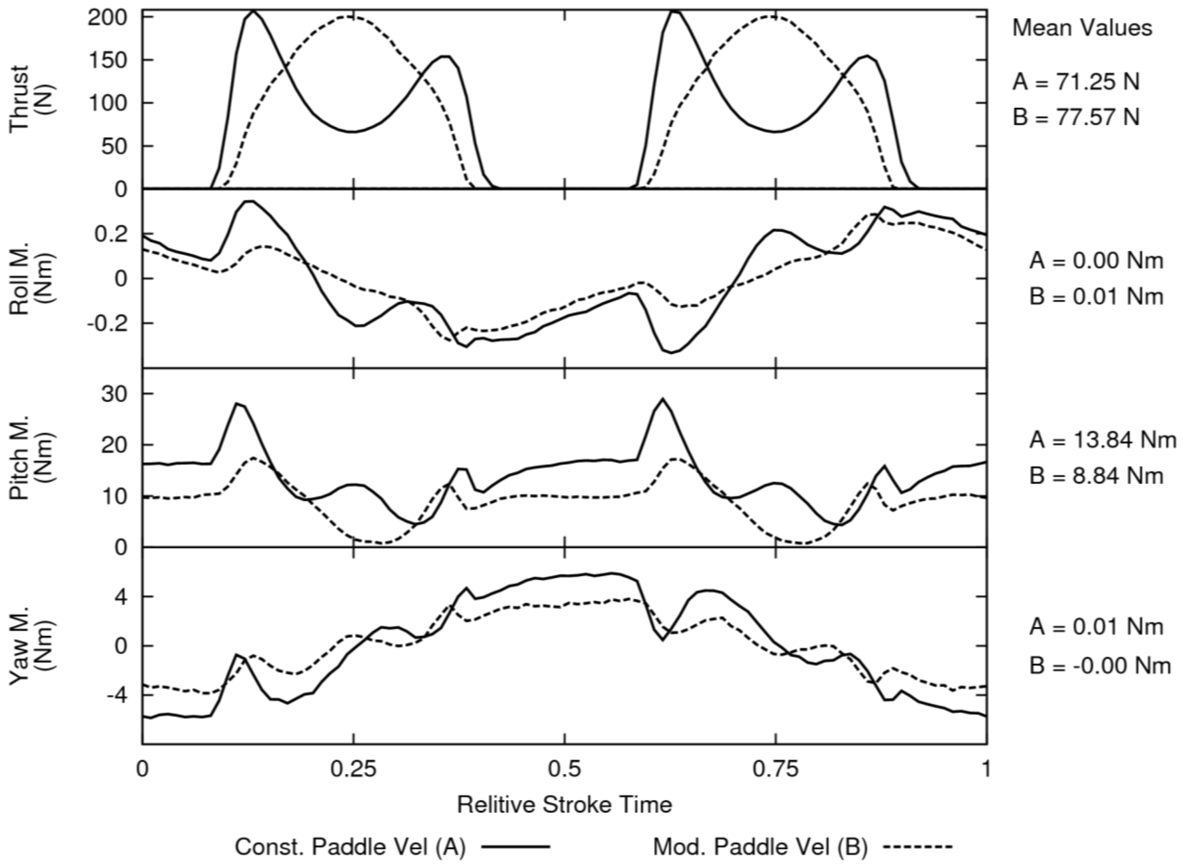

Figure 7-14 - Variation in self-propelled hydrodynamic moments, from naked hull case, for paddling technique's A and B offset by 0.35 m from the hull centreline.

7.4.10 Effect of paddle off-set

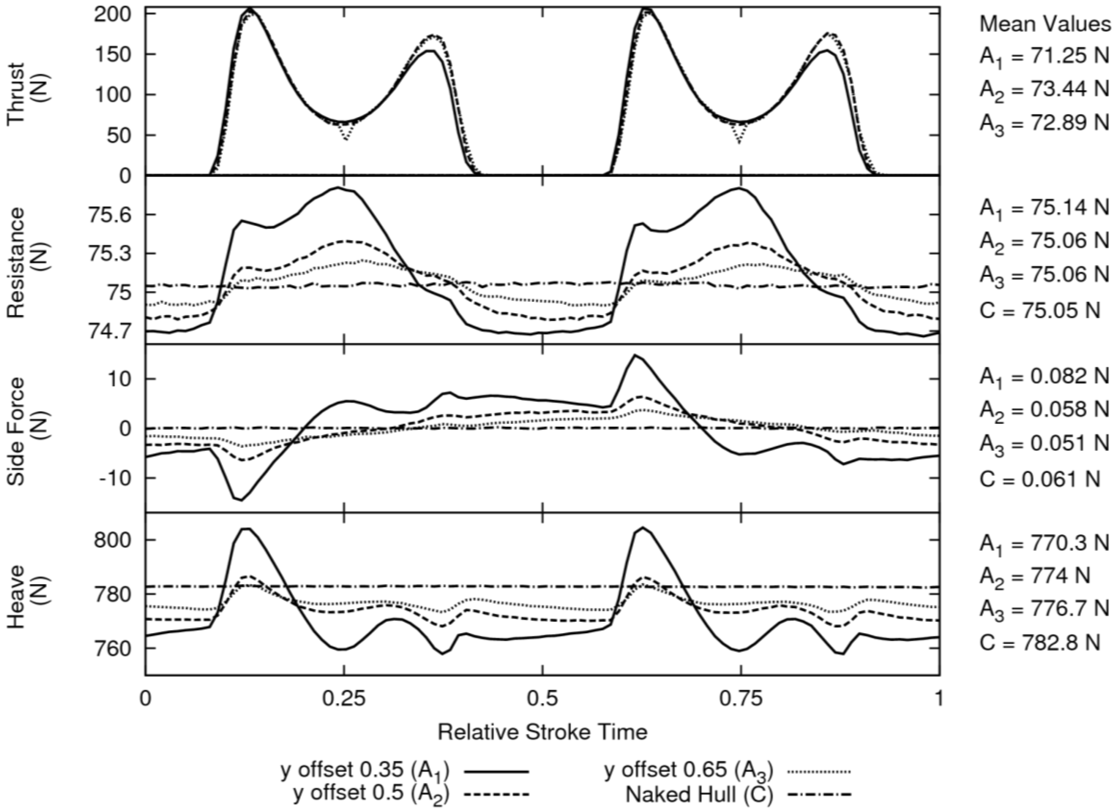

Figure 7-15 – Impact of paddle proximity on hydrodynamic forces for a constant velocity paddling technique (A).

It can be seen in figure 7-15 that the magnitude of the force, and therefore moment, variation reduces as the paddle offset is increased. This highlights the need to correctly model the blade path during the stroke, but also implies that the developed methodology could provide coaches and athletes with insight as to how their technique impacts on their resistance.

7.4.11 Effect of fixed attitude of kayak

Due to the fixed attitude of the hull, it is likely that the full impact of the paddle on the self-propelled resistance has not been captured. A first order, quasi-static approach can be used to estimate the resulting heave and pitch motions based on balancing the hydrostatic restoring forces against the measured hydrodynamic values (Comstock, 1976). It can be seen in figure 7-16 that the resulting motions are relatively small compared to those that may be expected due to the motion of an athlete's body. However, it can easily be deduced that the average increase in draught for a paddle offset by 0.35m, rotating at a constant angular velocity, was 1.15mm. This would result in an increased wetted surface area of approximately 0.0124 m^2. It therefore follows that the increased resistance, calculated using the ITTC'57 skin friction coefficient (Molland, A. F., Turnock, S. R., & Hudson, 2011), would be approximately 0.4 N (0.5 % of the naked hull resistance).

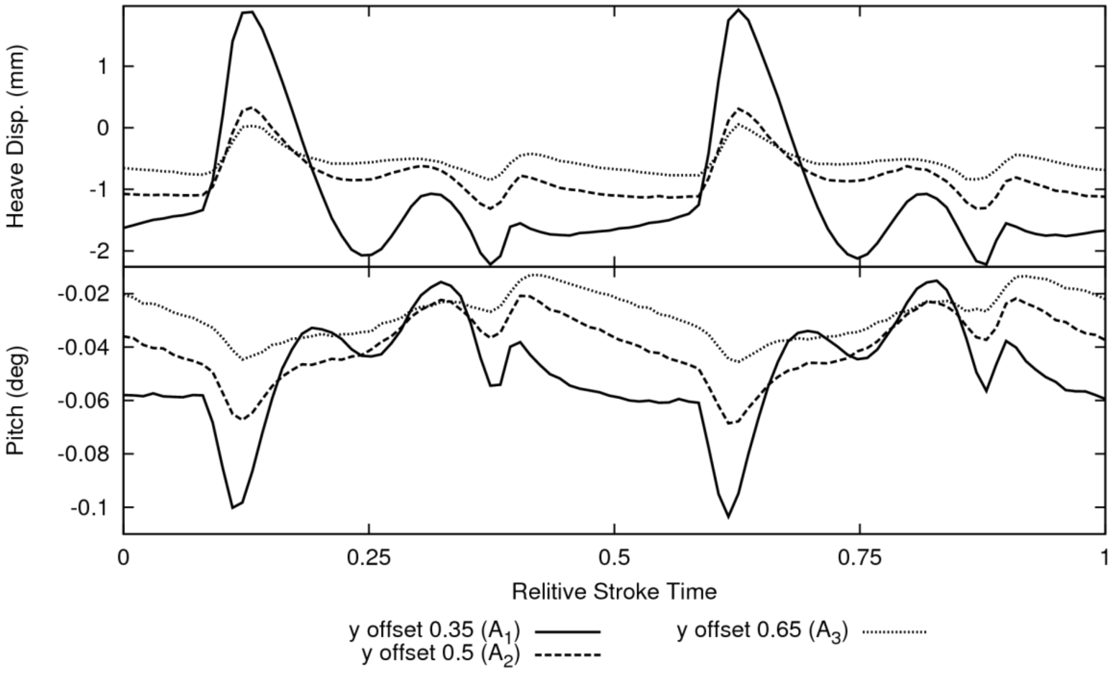

Figure 7-16 – Estimated paddle induced heave and pitch motions, for paddling technique (A) with different paddle offsets.

Due to the small magnitude of the pitch variation it seems unlikely that this would have a significant impact on the resistance, however it is possible that the yaw and sway motions could have more impact due to the induced drag associated with an angle of attack.

It should be acknowledged that some unsteady aspects of the kayak motion have not been assessed in this work. This includes the unsteady surge velocity and athlete induced motions of the hull. The variation in kayak hull velocity has been reported to be as low as 4% by Jackson (Jackson, 1995) or vary between 5 and 14% depending on the athlete (Kendal & Ross, 1992). However as a velocity variation of over 50% in a rowing shell causes only a 3% increase in resistance

(A. Day, Campbell, Clelland, & Cichowicz, 2011) the impact of surge velocity in kayaking is likely to be small but potentially as significant as the hydrodynamic interactions investigated here. There is no published data on the impact of athlete induced heave and roll motions however visual observations indicate that these could also be significant.

7.4.12 Potential impact on race time

In this study a 0.23% difference in self-propelled resistance was observed between different paddling techniques (A) and (B), while an estimated 0.5% increase could occur due to paddle induced draught increases. But are these interactions significant enough to be considered in kayak design or athlete technique?

Jackson (Jackson, 1995) estimated that an increase in total resistance of 0.7% (1% of frictional drag) would reduce a kayak's speed by 0.27%. If this is applied to the average speeds calculated from the winning times at the 2012 Olympic games the race times are increased by approximately 0.1 s, 0.3 s and 0.5 s for the 200m, 500m and 1000m Kayak events respectively. As the differences between medal positions are often as little as tenths or even hundredths of a second (London2012, 2012), it would appear that reductions in resistance of just fractions of a percent are worth pursuing.

7.4.13 Conclusions

The self-propelled resistance of a fixed K1 kayak has been estimated using a body force representation of a paddle stroke within an unsteady, free-surface, URANS simulation. A mathematical model calculates the momentum source terms used to simulate the impact of the paddle, using a blade element approach, validated against experimental data. This developed methodology has allowed the unsteady interactions between a paddle and hull to be investigated for the first time, whilst increasing the computational cost from a calm water simulation by just 8 %. The unsteady free surface and pressure fields are captured and propagated downstream allowing new insight into the paddle induced hull forces.

A case study, looking at how blade and hull interactions varied with different paddling techniques and lateral paddle positions, was conducted to assess the potential impact of these interactions on performance. A strong relationship between magnitude of paddle induced forces and paddle-hull proximity indicates the developed methodology could be used to investigate the impact of different paddling techniques on hydrodynamic forces. This could be achieved by including blade translation and lift forces into the current methodology to provide a more realistic stroke representation.

The paddle interactions produced a maximum resistance variation of approximately 1.6 % of the naked hull resistance but a change in average resistance of just 0.16 %. However a 0.23 % difference in self-propelled resistance was observed between different paddling techniques, while an estimated 0.5 % increase could occur due to draught increases caused by low pressure regions of accelerated flow. An estimate of small changes in resistance on race times indicates that reductions of even a fraction of a percent could make the difference between medal positions at the Olympics.

Despite the paddles impact on resistance being small, the minimal increase in computational cost is such that the developed methodology, potentially including athlete induced motions, could be viable as a design tool for optimising kayak hull shapes for the unsteady flow conditions found whilst racing.

This case study can be viewed as a simplified version of the active swimming problem, providing confidence in the implemented body force methodology for unsteady propulsion simulations.

7.5 Forces on a freestyle arm

To enable the developed methodology to simulate a freestyle arm several modifications were made. Firstly, the kinematic model had to be able to simulate a much wider range of motion compared to that of a rotating paddle. Secondly, varying lift and drag coefficients needed to be included, depending on the local angle of attack of the arm. Finally, the effect of the swimmer's forward motion was included.

7.5.1 Freestyle Arm kinematics

The freestyle arm kinematics were taken from the experimental test case C009, presented in Chapter 3, and measured as a series of Euler joint angles for the elbow and the shoulder. These joint angles describe the arm position through a series of rotations, about the joint centres. This is from a reference arm position which is in the direction of the swimmer's motion, with the palm face down (i.e. as the arm enters the water). The rotations are applied in the order XZY (roll about the longitudinal x-axis, yaw about the vertical z-axis and pitch about the transverse y-axis). The lower arm joint angles are relative to the upper arm and are therefore applied first before the entire arm is rotated about the shoulder.

C

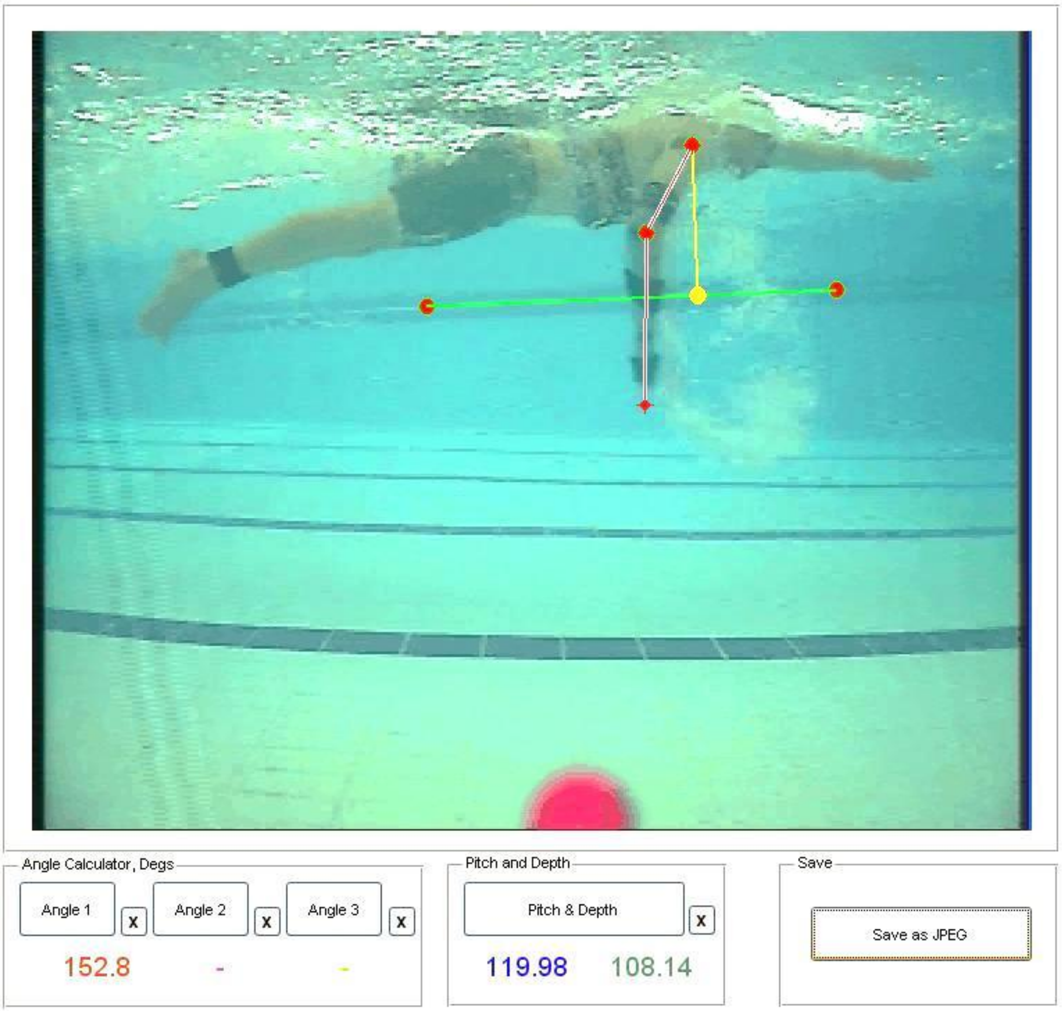

152.8 - -

119.98 108.14

Figure 7-17 - Manual digitisation process for acquiring pitch joint angles.

The pitch angles were measured from the side-on underwater footage taken during the experiment (x-z plane). The digitisation process can be seen in figure 7-17, where the pitch angle of the upper arm is measured as 119.98 deg, compared to the horizontal reference provided by the far-edge of the pool. The depth of the shoulder joint is measured in pixels, compared to the same horizontal reference. The angle between the lower and upper arm was measured as 152.8 degrees, which represents a relative pitch angle of -27.2 degrees.

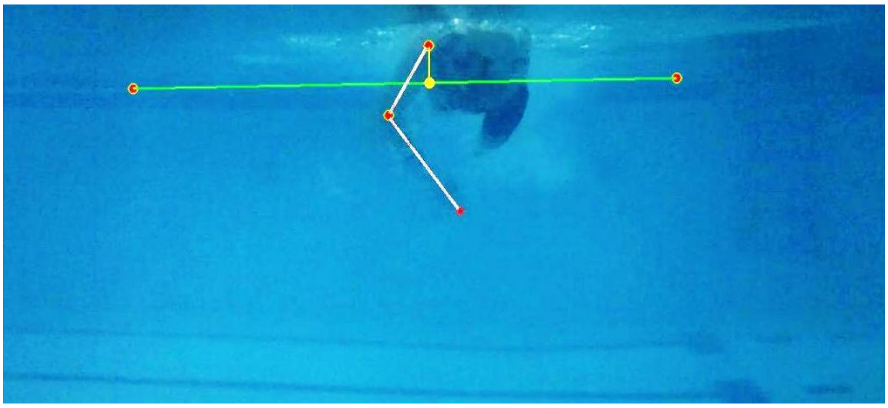

Figure 7-18 - Manual digitisation process for acquiring yaw joint angles

The same process was conducted to obtain yaw angles for as much of the propulsive stroke as possible. Head-on footage of the same athlete swimming freestyle was used (see figure 7-18). However yaw angles can only be measured accurately from this view whilst the arm segments are within the y-z plane. This is due to the yaw rotations being applied before the pitch rotations in the rotation sequence. Without footage from above or below the full arm motion could not be digitised, therefore the yaw angles were manually altered for pitch angles near 0 and 180 degrees (hand entry and exit) so that the arm kinematics visually matched the video footage.

The beginning of the stroke cycle was defined as the right hand entry, which coincided with a zero pitch angle for the upper arm. The joint angles for the arm recovery phase of the stroke (above the water) are linearly interpolated back to the hand entry position. The yaw and pitch angles for the full stroke cycle were smoothed using a Butterworth filter and can be seen in figure 7-19. The roll angle, defining the arm orientation (applied first in the rotation sequence) was fixed at a zero degrees. This was due to the difficulties in determining this angle from the video footage.

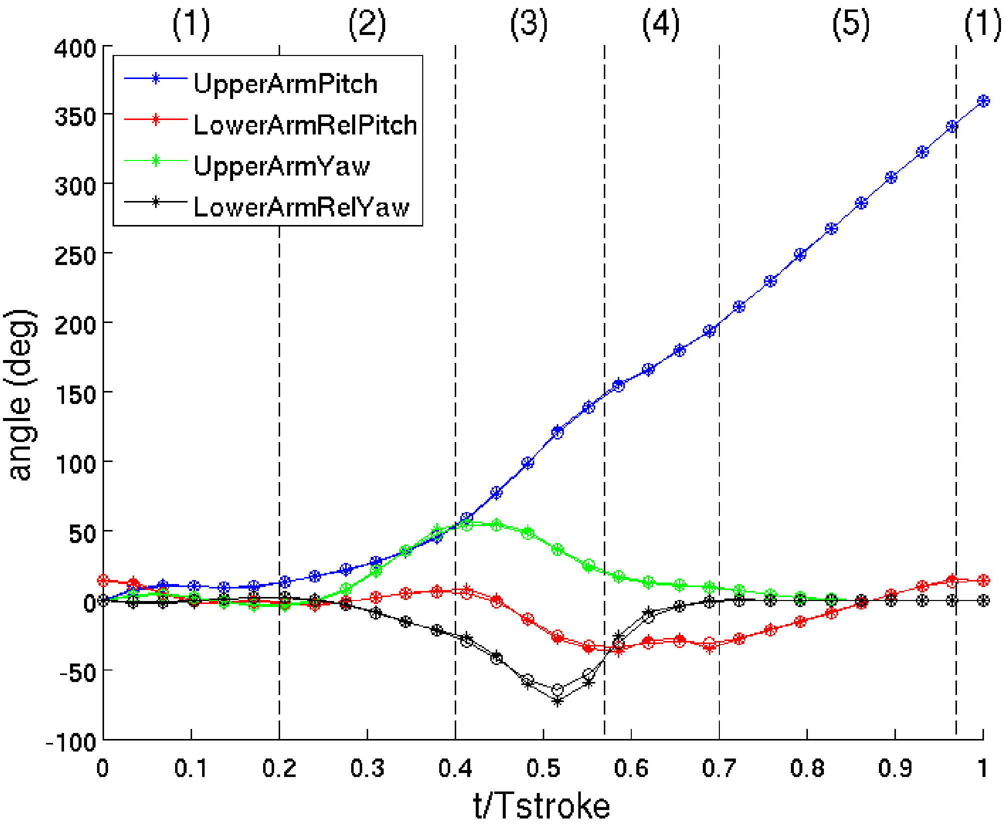

Figure 7-19 - Yaw and pitch joint angles for upper and lower arm, raw data (crosses) and after smoothing (circles).

The arm stroke can be split up into the following different phases (labelled on the relevant figures):

1. **Hand entry.**
2. **Outward sweep.**
3. **Inward sweep.**
4. **Hand exit.**
5. **Arm Recovery.**

The shoulder location (defining the centre of the joint rotations) was determined from the variation in shoulder depth in pixels, re-dimensioned using a known distance on the swimmers body. A similar approach allowed the surge motion (distance in the x-direction) to be estimated. The sway motion (distance in the y direction) was assumed to be zero. The variation in shoulder location can be seen in figure 7-20.

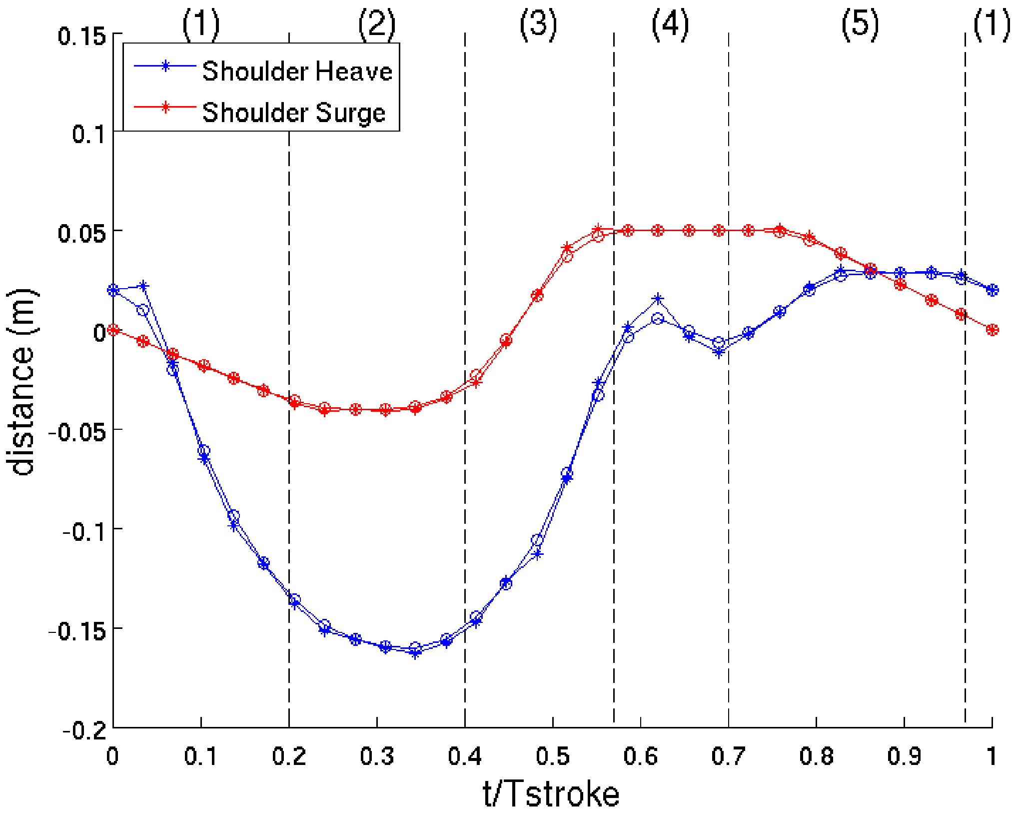

Figure 7-20 - Shoulder heave and surge motion.

To simplify the input of the kinematic data into the OpenFOAM solver, the Euler angles were converted into a list of joint locations in Cartesian coordinates based on the length of the different arm sections. The length of the upper arm was measured as 0.3 m and the lower arm (including the hand) was 0.4 m. This provided the position of the elbow and finger tips, at regular time intervals, throughout a complete stroke cycle. The orientation of the combined lower arm and hand was provided by a unit vector α_0 pointing out through the thumb, normal to the arm. This conversion was completed using quaternion rotations from the reference arm position. The resultant upper and lower arm locations during the underwater phase of the stroke, can be viewed in figure 7-21. It should be noted that a shoulder hub radius of 0.05m was removed from the top of the upper arm.

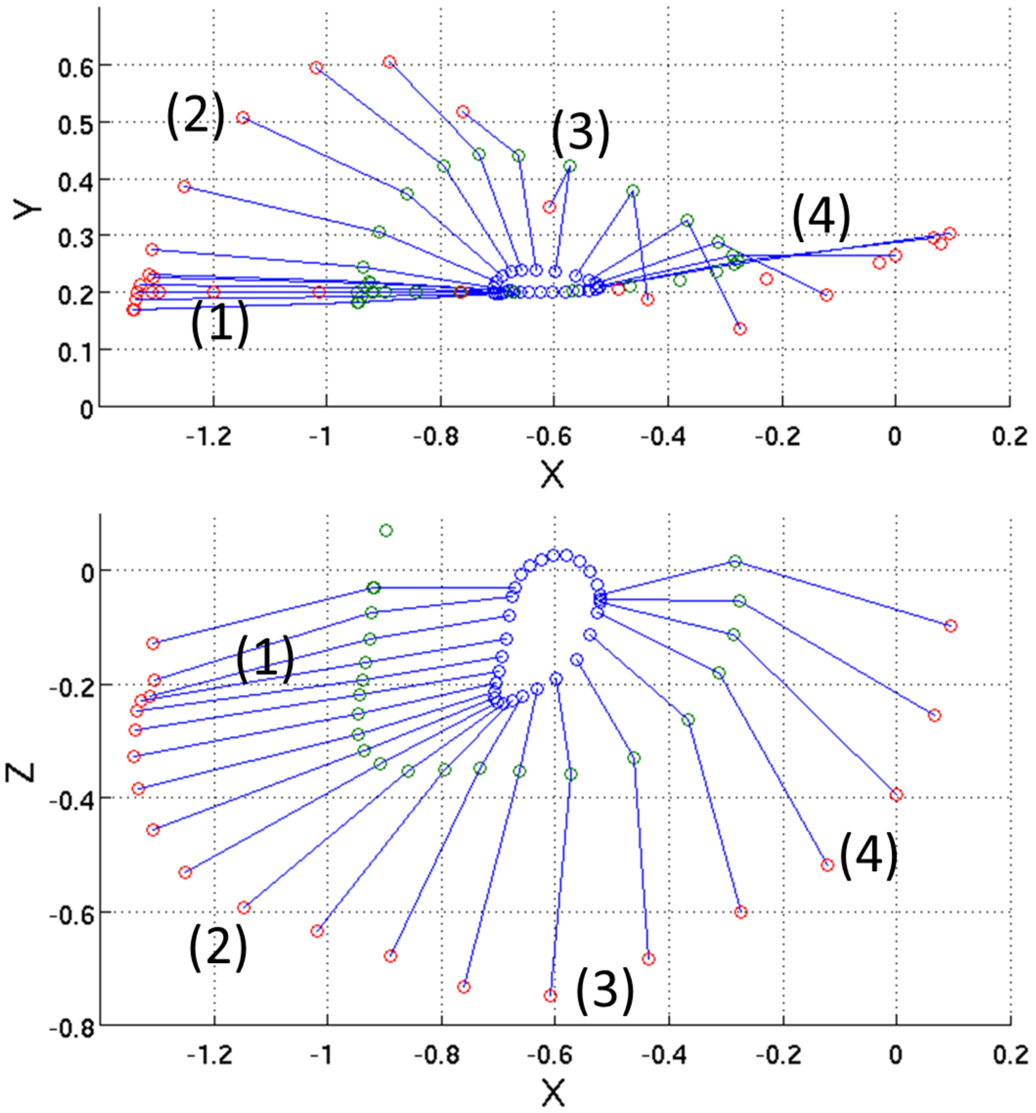

Figure 7-21 – Arm segments locations for the right arm viewed from above (top) and the side (bottom).

The different stroke phases can now be defined in terms of the arm position:

1. **Hand entry**. The hand enters the water moving at a significant velocity after the arm recovery. The arm then slows down and remains roughly aligned to the flow as the body roll increases the right shoulder depth.
2. **Outward sweep**. The arm moves outwards and pitches down.
3. **Inward sweep**. The forearm sweeps back in underneath the upper arm whilst both the shoulder and upper arm move backwards.
4. **Hand exit**. The hand pushes back towards its exit from the water
5. **Arm Recovery**. The arm moves through the air back to the beginning of the stroke cycle.

To simplify the freestyle arm model, only the lower arm and hand were simulated, but as a single arm section. This captures the greatest proportion of the propulsion generated by the arm due to the increased velocity of the hand (Keys,M. et al., 2010). The left arm kinematics were created by mirroring those of the right arm in the x-z plane and shifting their phase by 180 degrees.

The experimental kinematics for the right arm are shown to be well captured by the arm model through comparison to the experimental video footage in Chapter 8.3.

7.5.2 Determining the normal velocity on the arm

The body force calculations described in section 7.2 require the normal velocity vector of the fluid to calculate the fluid forces. For the freestyle arm model this process was made more generic by defining the kinematics of a given section of arm (e.g. lower arm and hand) by two points (A and B) and the unit vector α_0 providing the orentation. This provides the potential for multiple sections of the arm to be modelled independently in the future.

For each time step within the simulation the body force model calculates the relative stroke time t/T_{stroke} , where T_{stroke} is the stroke period of one complete cycle. This value is then used to interpolate the values of A, B and α_0 from the input kinematic data using a 3rd order interpolation method. The positions of A and B from the previous time step provide the velocity vectors V_A and V_B. Therefore linear interpolation provides the velocity of each blade element within the solution domain V_{armRel}, i.e. relative to the swimmer.

The actual fluid velocity observed by the blade is therefore given by

$$V_{arm} = V_{armRel} - U_0, \qquad 7\text{-}7$$

where U_0 is the free-stream velocity of the fluid in the simulation domain. The component of the observed fluid velocity normal to the blade is given by

$$V_n = V_{arm} - \left(V_{arm} \cdot \widehat{AB}\right)\widehat{AB}, \qquad 7\text{-}8$$

where $\widehat{AB}$ is the unit vector from A to B (i.e. along the blade span).

The angle of attack of a given blade element is provided by

$$\alpha = \cos^{-1}\left(\frac{V_n \cdot \widehat{\alpha_0}}{|V_n|}\right), \qquad 7\text{-}9$$

with the sign of α provided by the sign of $\left(V_n \cdot \left(\widehat{\alpha_0} \times \widehat{AB}\right)\right)$.

For the experimentally recorded stroke rate of 42.8 rpm, and tow speed of 1.56 ms^{-1}, the normal velocity and angle of attack for the blade element nearest the finger tips can be seen in figure 7-22 and figure 7-23. Again the previously defined stages of the stroke have been labelled on the figures and can be characterised as:

1. **Hand entry.** The hand actually starts to enter the water at the end of the arm recovery resulting in the high velocity. The rotation quickly slows down causing any slight motion from side to side to result in a large change in angle of attack (observed in figure 7-23.)
2. **Outward sweep.** The first peak in normal velocity is caused by the combined effect of pitch and yaw rotation moving the arm down and outwards. This causes the angle of attack to increase towards 180 degrees as the little finger becomes the leading edge of the foil.
3. **Inward sweep.** The second peak in normal velocity occurs as the shoulder and upper arm accelerate backwards at the same time as the lower arm rotates back in under the swimmer. This moves the angle of attack in the opposite direction as the thumb becomes the leading edge.
4. **Hand exit.** As the hand pushes back towards its exit from the water most of the normal velocity comes from the pitch rotation providing an angle of attack close to 90 degrees.
5. **Arm Recovery.** A much larger normal velocity is observed as the arm moves back through the air to the beginning of the stroke cycle.

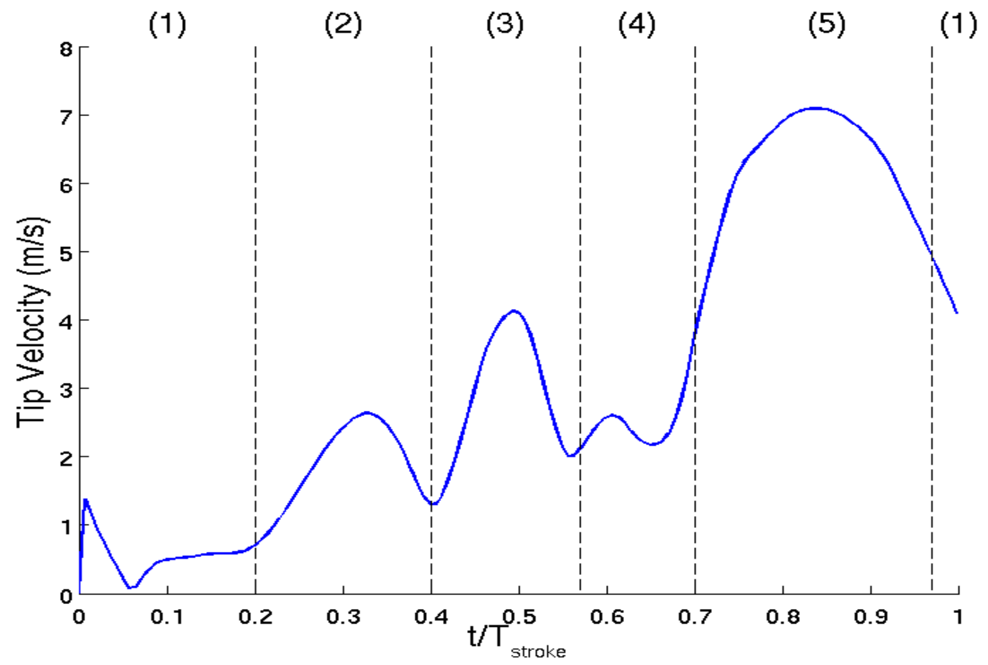

Figure 7-22 – Normal velocity experienced near the fingers throughout one stroke cycle.

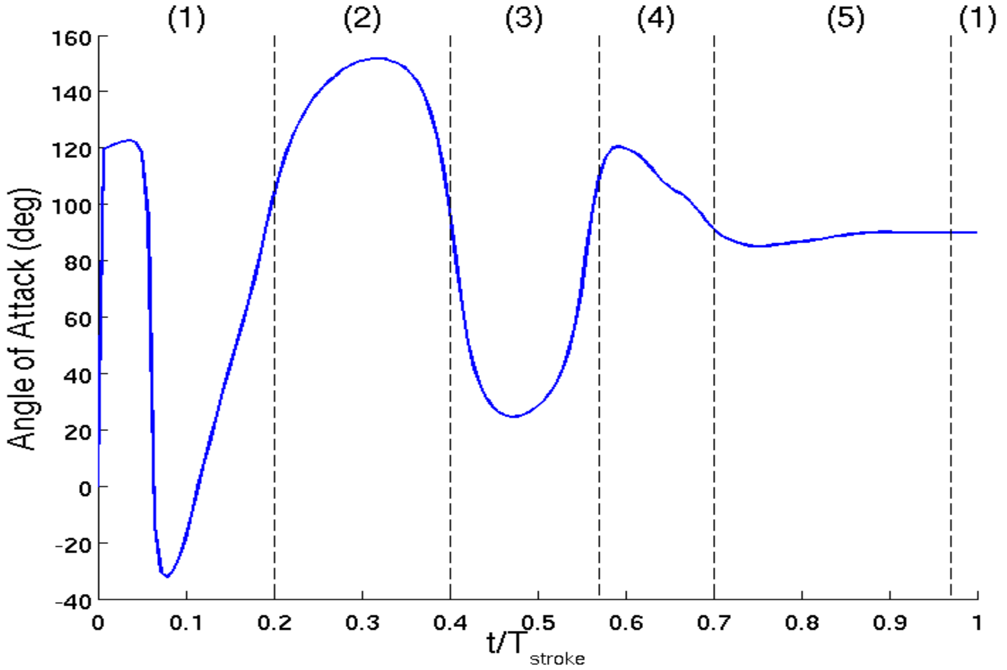

Figure 7-23 – Angle of attack experienced near the fingers throughout one stroke cycle.

7.5.3 Angle of attack

Lift and drag coefficients for a hand at various angles of attack were taken from (Bixler & Riewald, 2002). These values, along with estimated values for negative angles of attack, can be seen in figure 7-24.

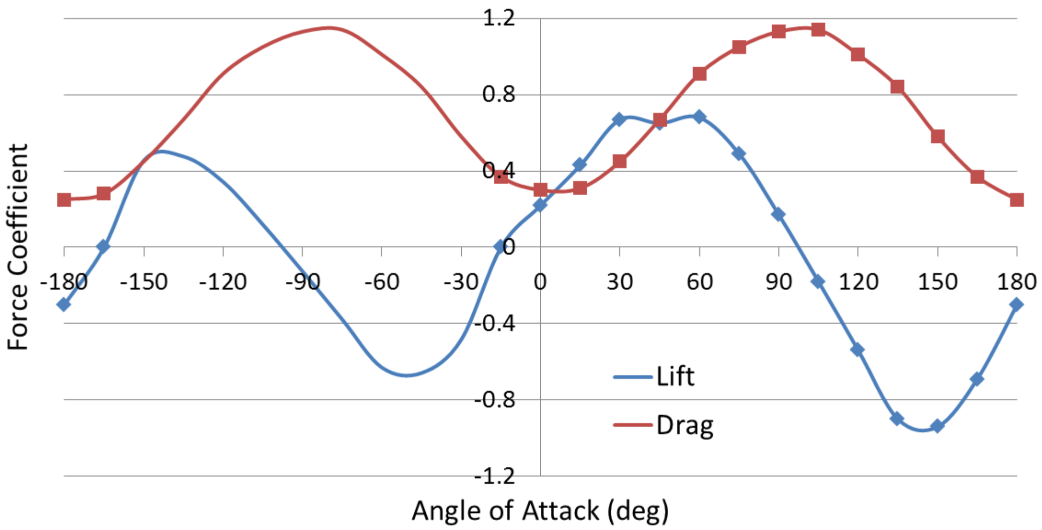

Figure 7-24 – Lift and drag coefficients for a hand taken from (Bixler & Riewald, 2002) are indicated by data points, with estimated values for negative angles of attack depicted with lines.

The decision to apply coefficients for a swimmer's hand to the entire fore arm was made on the basis that the hand experiences a larger normal velocity than the arm, causing it to generate a greater proportion of the total force. Therefore it was more important to correctly simulate the hand over the forearm. The effect of this, however, is that the forces generated nearer the elbow will be artificially large, particularly the lift force; due to the arm having a significantly reduced lift coefficient (Bixler & Riewald, 2002).

7.5.4 Arm width

The width of the arm obviously varies significantly down its length, especially around the hand and wrist. However in the arm model it is assumed to stay constant and is used to tune the thrust magnitude to correspond with the variation in experimental tow force data.

The experimental tow force (swimmer's resistance *R* minus the generated thrust *T*) in case C009 varied by approximately 80N (see Chapter 3.3 for force trace). Therefore a maximum thrust value approaching this would seem sensible. The mean tow force was 60.2 N at an average tow speed of 1.56 ms^{-1}.

An estimate of the average thrust produced in the experiment can be obtained by attempting to predict the resistance acting on the athlete. Experimental case C012 measured a resistance of 84.6 N on athlete C at a tow speed of 1.47 ms^{-1} (see chapter 3.1). Assuming resistance is proportional to velocity squared provides a passive resistance of 95 N for athlete C at the same tow speed as case C009. The difference between this resistance and the experimental tow force provides an estimate of 35 N for the mean thrust.

A series of different blade chord dimensions were tested to try and match the simulated thrust with the experimental tow force data. The maximum thrust produced, along with the average thrust from both arms within 1 stroke cycle, is presented in table 7-3. As it was not possible to directly match both the maximum thrust and the predicted mean thrust from the experiment, a compromise of a blade chord of 0.075 m was selected. This produced a mean thrust of 33N and a peak thrust of 100 N.

Table 7-3 - Impact of blade chord on thrust magnitude

Blade chord *c* (m)	Max projected area (m^2)	Average thrust (N)	Max thrust (N)
0.1	0.04	44	130
0.09	0.036	39.98	120
0.08	0.032	35.54	108
0.07	0.028	31.1	94
0.06	0.024	26.66	80

7.5.5 No of blade elements required

The number of blade elements used within the arm model were varied from one to eight, whilst maintaining all other parameters the same. Figure 7-25 demonstrates that a minimum of 4 blade elements are required to represent the forearm and hand, producing 99% of the thrust that 8 blade elements would produce.

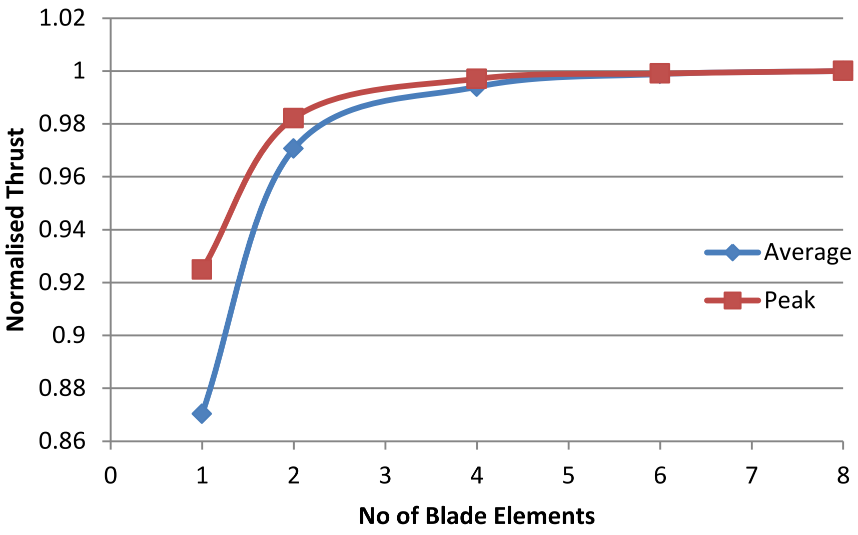

Figure 7-25 –Effect of the number of blade elements on thrust magnitude.

7.5.6 Forces acting on the arm

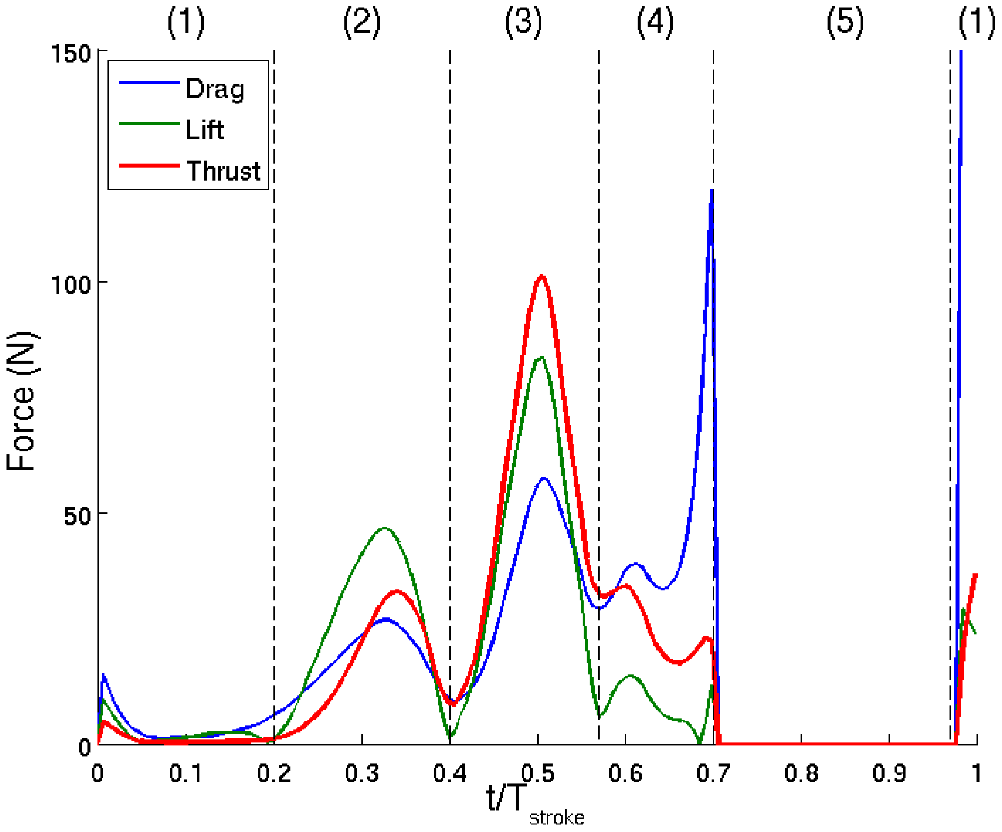

Figure 7-26 – Hydrodynamic forces generated by a single arm during one stroke cycle.

The lift and drag forces and the resultant thrust profile for a single arm with blade chord of 0.075 m is given in figure 7-26. The lift and drag forces along with the total normal force are plotted in vector format in figure 7-27, providing a visual representation of where the forces are generated within the stroke.

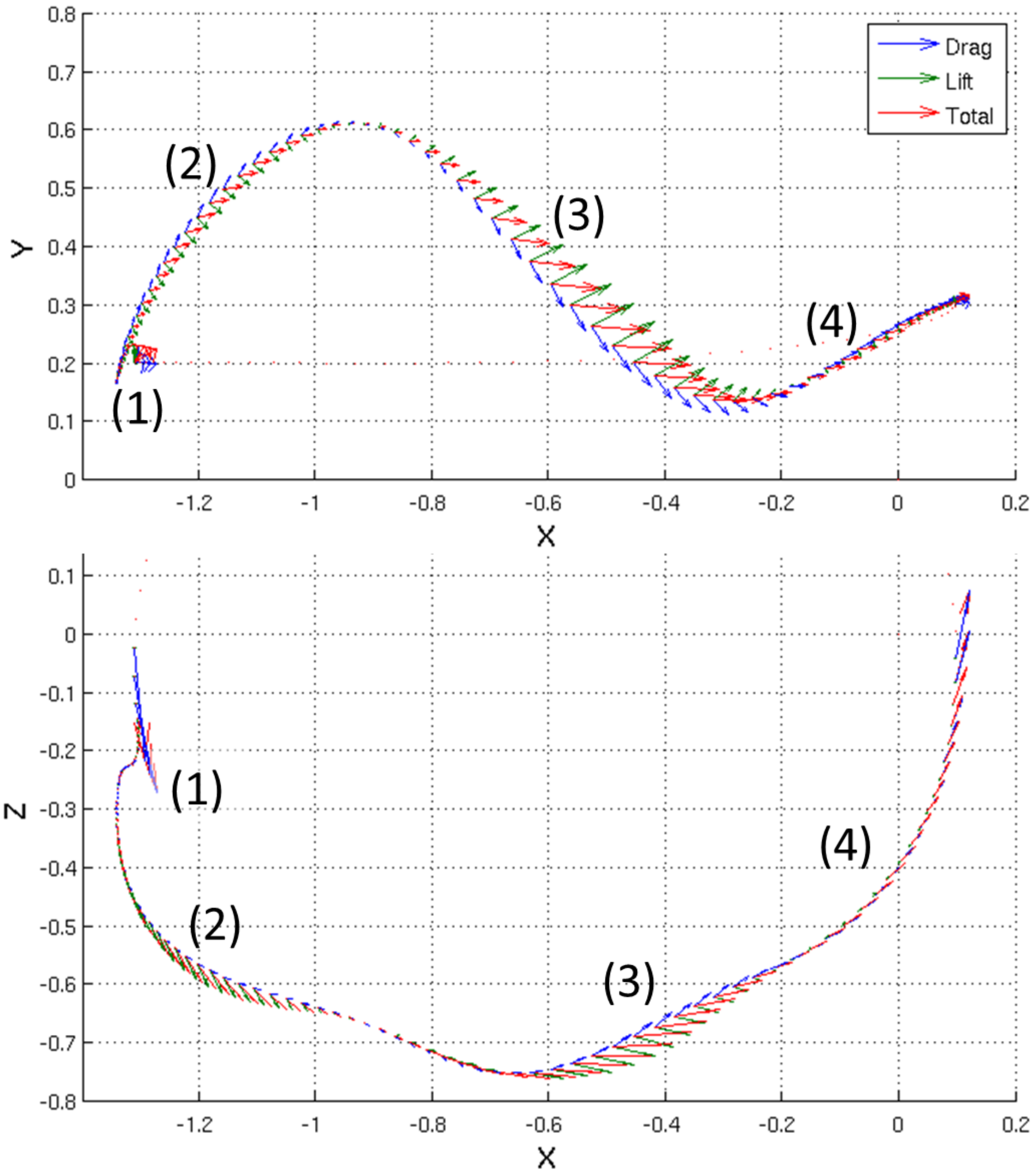

Figure 7-27 - Force vectors for combined hand and forearm, plotted at the fingertip location, viewed from above (top) and the side (below).

The previously defined phases of the stroke are labelled on the figures and can be characterised in terms of the forces generated as follows:

1. **Hand entry.** The hand enters the water moving at a significant velocity generating a large drag force. This occurs at the end of the stroke cycle. The arm then slows down and remains aligned to the flow as the body roll increases the right shoulder depth. This produces little force due to the negligible normal velocity.

2. **Outward sweep**. As the arm moves outwards and pitches down, both lift and drag are generated. However, from the vector plots it can be observed that the total force generated by the arm has a significant downwards component. Therefore only a portion of the total force is converted into thrust. This improves towards the end of the outwards sweep, resulting in the first meaningful contribution to thrust.
3. **Inward sweep**. As the forearm sweeps back in underneath the swimmer the greatest thrust is generated. The combination of increased lift, due to the angle of attack, and a peak normal velocity, result in a large normal force that is almost entirely converted into thrust.
4. **Hand exit**. As the hand pushes back towards its exit from the water the resultant force is dominated by drag due to the small amounts of translation. As the hand approaches the water's surface, less of the total force is converted into thrust, due to the high vertical component.
5. **Arm Recovery**. As the arm moves through the air back to the beginning of the stroke cycle, no force is generated as aerodynamic resistance is ignored.

The forces generated will obviously be specific to the athlete's kinematics that have been simulated and it should be remembered that this was a non-elite athlete. However, it is still useful to compare the simulated forces with other previously published data. If we consider the general shape of the thrust trace, it is observed that it is dominated by the large peak in thrust associated with the inward sweep. Similar large propulsion peaks can be observed in the full body swimming simulations presented in (Keys,M. et al., 2010). One of the stroke techniques assessed by (Sato & Hino, 2003) also produces a sharp peak in thrust produced by the hand in a similar phase of the stroke. However, this technique also produces a significant amount of thrust as the hand approaches its exit. Taking account of the kinematics of the hand that were used in the simulation, this is primarily due to the hand orientation, converting the large drag force into thrust. Due to the hand and arm being combined in the kinematic model presented here, this level of fidelity cannot be achieved during this phase of the stroke.

7.5.7 Impact of hand orientation

It was impossible to determine the exact hand orientation (or roll angle of the arm) from the video footage, therefore the reference angle of attack was fixed at 90 degrees in the presented force results. In order to quantify the impact the angle of attack could have on the fluid forces generated, a series of different reference angles of attack were investigated. This allows an attempt to be made at quantifying the potential error associated with differences in hand orientation, between the experiment and simulated arm model.

Five different reference angles of attack were tested (70, 80, 90, 100 and 110 degrees). These represent the angle of attack if a pure pitch rotation was applied. The different thrust profiles generated by each case can be seen in figure 7-28. As one might expect the thrust produced during both the outward and inward sweep of the arm can be increased from the basis 90 degrees case previously examined. The maximum thrust was increased by 20% on the inward sweep with a reference angle of attack of 110 degrees.

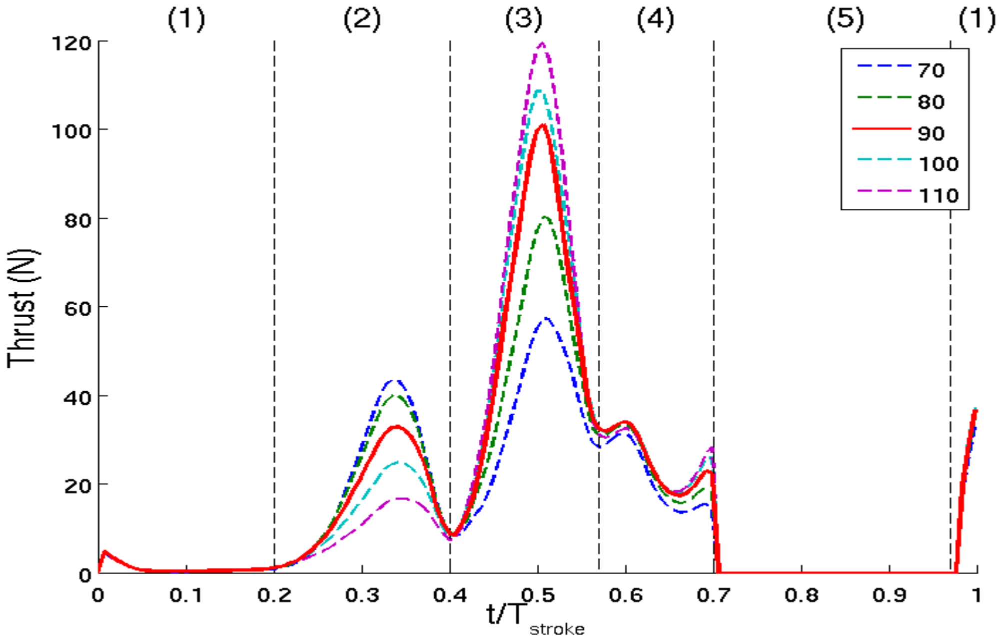

Figure 7-28 - Effect of arm orientation (reference angle of attack) on thrust produced

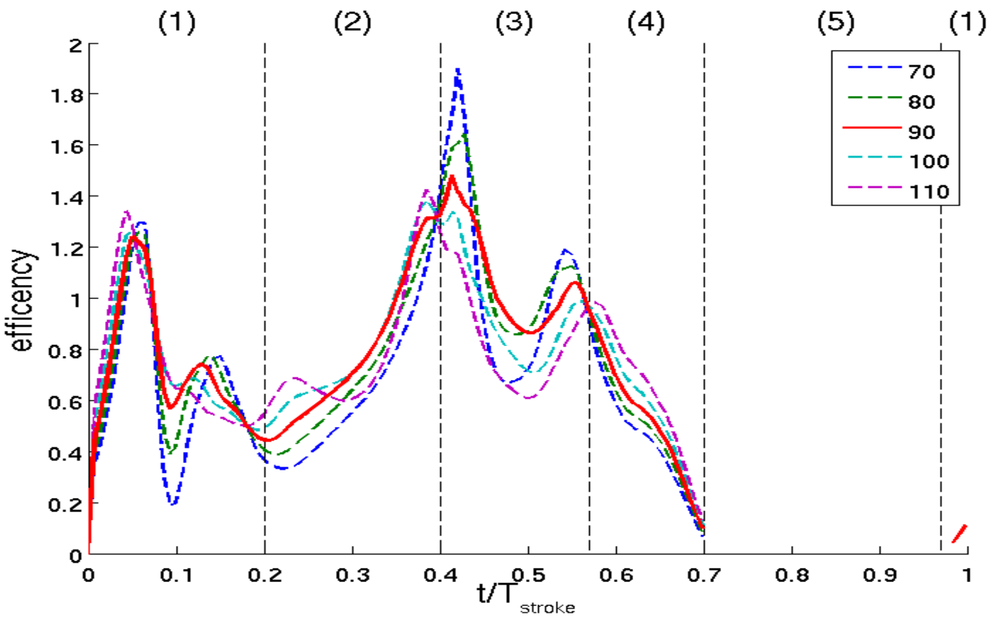

Figure 7-29 - Effect of arm orientation (reference angle of attack) on stroke efficiency.

Looking at the thrust alone does not give much indication as to whether the correct angle of attack is being used. Therefore a hydrodynamic propulsive efficiency was defined as the useful power-out of the arm divided by the hydrodynamic power-in. This is calculated as:

$$\eta = \frac{TU_0}{F_D V_n}, \tag{7-10}$$

where T is the thrust, U_0 is the swimming speed, F_D is the drag force on the arm and V_n is the normal velocity of the arm.

Figure 7-29 shows that the potential increases in thrust available through varying the arm orientation comes at a cost in terms of efficiency. In both the inward and outward sweep phases of the stroke (labelled 2&3) it can be observed that the maximum thrust is achieved at the lowest efficiency.

The point of this study was not to try and optimise the swimming stroke but to try and replicate the propulsive forces generated by athlete C in the experimental case C009. It is interesting however that the reference angle of attack of 90 degrees provides the best propulsive efficiency for both peaks in thrust. This would indicate that any potential changes in hand orientation at these points in the stroke are likely to be small so as to maintain a high propulsive efficiency. Indeed the increase in power required to generate the greater thrust values may not be physically possible for the athlete to deliver.

It is likely, however, that the arm orientation is not correctly captured in other phases of the stroke. It would seem sensible that the body would naturally adjust the arm orientation to maintain a good propulsive efficiency. However, it can been assumed that these discrepancies in other phases of the stroke will have an even smaller impact on the thrust generated, due to the smaller normal velocity in these phases. Therefore we can assume that the potential error associated with not being able to accurately capture this aspect of the kinematics is small relative to the impact of arm position and velocity.

7.5.8 Discussion

Many simplifications have been made to enable a freestyle arm model to be developed. It is worth discussing some of these in order to understand the limitations of this methodology and provide insight as to what should be improved on in the future.

The adopted approach is a quasi-steady one, based on lift and drag coefficients obtained from steady conditions and an instantaneous normal velocity. Studies have shown that the unsteady effects of acceleration have a significant impact on the arm forces generated (Rouboa et al., 2006; Sato & Hino, 2003). However, it is hoped that by tuning force magnitudes to experimental data some of these unsteady effects are accounted for. This approach was shown to work well for the unsteady thrust profile in the kayak paddle validation case in section 7.3.

The arm's kinematics were determined using a manual digitisation process from underwater footage. Comparisons of the simulated arm position and the same video footage made in Chapter 8.3 agree well. Nevertheless this process could be improved by using a more sophisticated kinematic acquisition system such as wireless sensors. One area of the kinematics that it was difficult to determine was the velocity of the arm as it entered the water. This is affected by two factors. Firstly, the arm position is only know once the arm is in the water, therefore the velocity of the arm before this point cannot be determined for this experimental test case. It is also likely that the arm slows down significantly during this entry process. The second factor is the accuracy of the shoulder location, which is defined as a variation in heave and surge motion about a fixed point. Therefore any vertical error in this fixed point location changes where the free surface sits within the defined kinematics. As this fixed point was determined by eye from the side on video footage there is a degree of error in this process (±0.02 m). The combined effect of these two factors makes it possible for the arm to enter the water at a different velocity from that of the experiment. When you consider that the fluid forces involved with a free surface impact are highly non-linear, it is not hard to imagine that the simulated arm forces at arm entry will differ from the experiment.

The swimmer's arm is currently modelled as the combined effect of the forearm and hand. This simplification has two main draw backs. Firstly, the lack of upper arm effects being captured. Although the upper arm will be moving at a lower velocity than the forearm, it will still be having an effect on the fluid. Due to its low rotational speed it is likely that some of it at least is actually contributing to the drag of the swimmer, rather than generating propulsion. The full body swimming simulations concluded that the net force on the upper arm was close to zero over the stroke (Keys,M. et al., 2010). This would indicate that its contribution to thrust may not be important, but the effect it has on the fluid may interact with the resistance acting on the body and head. Indeed, due to the close proximity of the upper arm to the athlete's body, the impact on the swimmer's hydrodynamic forces may be significant despite the small thrust values likely to be generated.

The second drawback of combining the forearm and hand is that this removes some of the complexity in different hand and arm orientations within the stroke kinematics. One example of this is the hand position as the arm pushes back towards its exit from the water (4). During this phase of the stroke the athlete keeps the hand perpendicular to the direction of movement to maximise the thrust generated from the drag force. This is achieved through flexion of the wrist joint which cannot be currently modelled.

Separately modelling the hand and forearm would allow specific lift and drag coefficients to be used for the different sections of the arm. In the current method the coefficients from a swimmer's hand have been used for the entire lower arm. This will have increased the lift produced in both the outwards and inward sweep phases of the stroke, resulting in the peak thrust value being over estimated.

An attempt has been made to tune the force magnitudes to the variation in experimental tow force using the blade chord. This will be revisited in chapter 8 once the resistance from the simulated case C009 is evaluated. It is hoped that by tuning the force magnitudes in this way the correct mean thrust value can be achieved, whilst the underlying physics of the arm kinematic model will ensure that it is distributed in a realistic manner.

7.6 Conclusion

A generic arm propulsion model has been created that uses experimental arm kinematics of a freestyle swimmer to generate the hydrodynamic forces acting on the arm. These propulsive forces are applied to the fluid domain using a body force model that varies in both time and space. The force magnitude of the propulsive model is tuned to the experimental forces measured during the test case C009. This approach has been shown to work effectively for simulating the unsteady forces generated by an unsteady rotating kayak blade. Simulations of a self-propelled kayak have also been implemented using this methodology.

There are many future modifications that could be made to increase the accuracy of the arm force calculations. However, the basic underlying flow physics of a free style arm stroke is suitably well captured to enable the different propulsive phases of a free style arm stroke to be identified. This allows its impact on the hydrodynamic forces acting on a swimmers body to be assessed in detail for the first time.

8. Propelled freestyle simulation

This final chapter of the thesis combines the two previously developed methodologies for passive resistance of a swimmer with the body-force arm model to perform a propelled freestyle simulation. This aims to replicate the experimental test case C009 where athlete C does arms-only freestyle whilst being assisted by the tow system. Therefore this experimental case is not fully self-propelled as the generated thrust is less than the resistance; due to the lack of propulsion from the legs. The difference between the resistance and the thrust (R-T) is measured as the force in the tow line. The tow speed was determined from the athlete's free swimming speed. Therefore the hydrodynamics of the arm stroke should replicate the athlete's normal freestyle technique. The benefit of using an arms-only test case is that the experimental tow force measured can be compared to the simulated R-T value.

8.1 Passive simulation

Before conducting the self-propelled simulation it is important to understand the passive flow field that develops around the C009 geometry. This not only provides a passive resistance with which to compare the self-propelled forces, but also allows the effect of the arms on the flow to be identified. The passive resistance of C009 is also required to provide an accurate estimate of the required mean thrust from the propulsion model.

8.1.1 Geometry

The simulation geometry for C009 was generated from the basis athlete STL using the method described in section (5.2.1). However as the athlete's arms will be simulated using the body force model, they needed to be removed from the geometry. To maintain the effect of the shoulders on the flow, the arms were removed from just below the armpit. The resulting basis STL geometry for propelled cases can be seen in figure 8-1.

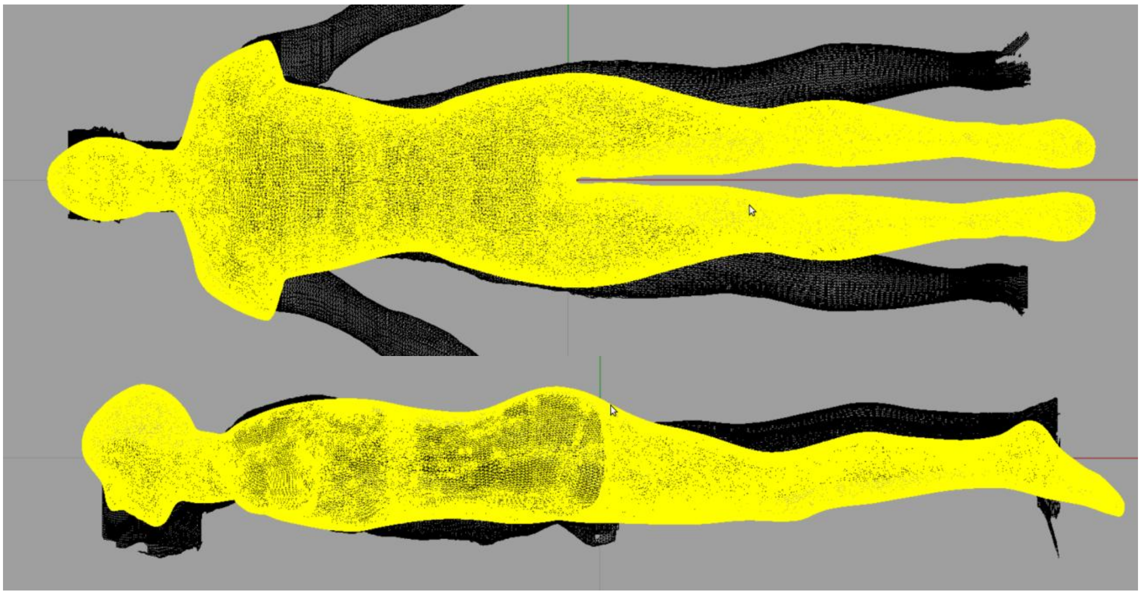

Figure 8-1- Comparison of basis propelled STL geometry (yellow) and a crude scan of Athelete C (black)

Having established the importance of correctly matching the simulation geometry to the experiment, a crude body scan of athlete C was obtained. Unfortunately this could not be used to generate the simulation geometry directly, however it was used to determine how the basis geometry needed to be modified, see figure 8-1. This identified that the basis geometry already matched athlete C in depth (z-direction), however there were marked differences in both the slope of the shoulders and the curvature of the hips. These were both modified through the use of a combination of variable lateral scale factors along the swimmers length and a local morphing function in the longitudinal direction. The modified body shape can be seen in figure 8-2.

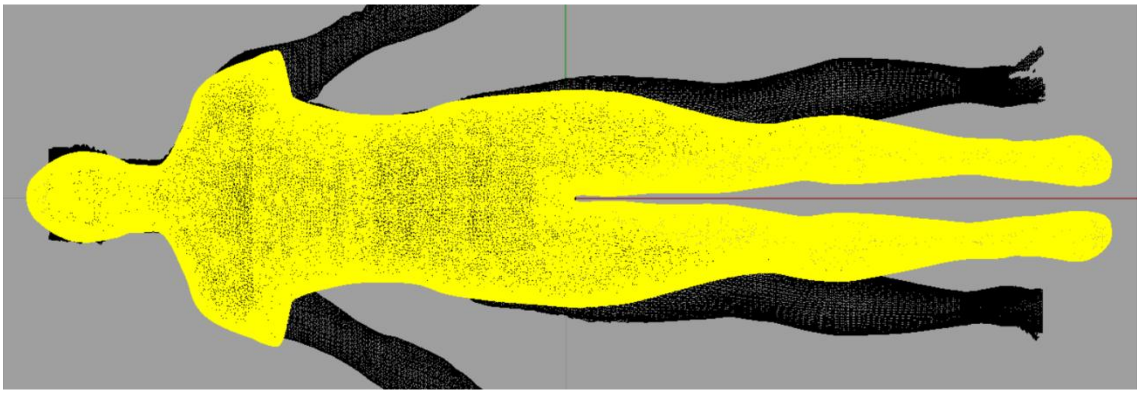

Figure 8-2 – Basis geometry modified for athlete C body shape (yellow) compared to crude scan of athlete C (black).

The final stage was to use joint rotations to match the athlete's attitude adopted in the experimental case. As the athletes roll will not be simulated, the geometry was generated to match the athlete at a neutral roll phase of the stroke. The final simulation geometry for C009 can be seen in figure 8-3.

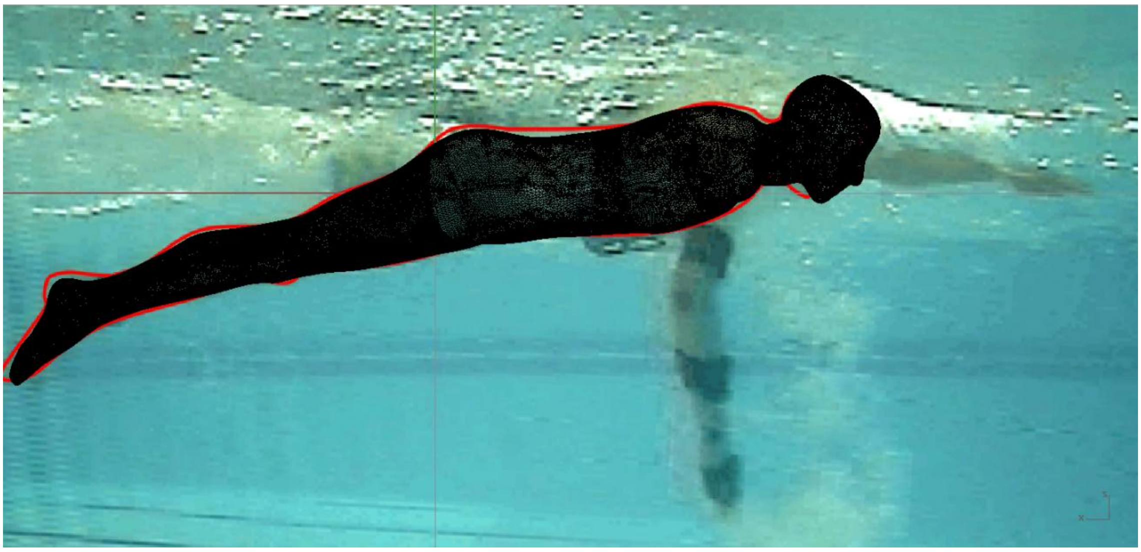

Figure 8-3 – Comparison between simulation geometry and experimental athlete attitude for case C009.

8.1.2 Meshing

The meshing strategy adopted was based on the previous mesh N003a (see Chapter 5.3.6). This applies the same mesh structure as used in the passive cases in Chapter 6, but without a refinement box for the wake and slightly reduced refinement distances out from the body. In addition to this, a new refinement zone was added to encompass the region through which the arm model would operate.

8.1.3 Results

The developed free surface around the passive geometry can be seen in figure 8-4 and figure 8-5. The comparison to the experimental footage from C009 is added purely to demonstrate that similar free surface flow features are observed. Notably the water flows up and over the front part of the head, just making it over the top, before dropping sharply down the back of the head. In the experimental footage a similar trend can be seen, but with the flow behind the head being unsteady and broken. In both figures the free surface drops sharply down the back, appearing to consist of only a small amount of water with breaking wave features on either side of the hips. Again this region appears very broken and disturbed in the experimental footage. The main difference between this simulation and the other passive cases presented in chapter 6 is the position of the legs. In C009 the legs are much lower in the water, which minimises their influence on the free surface.

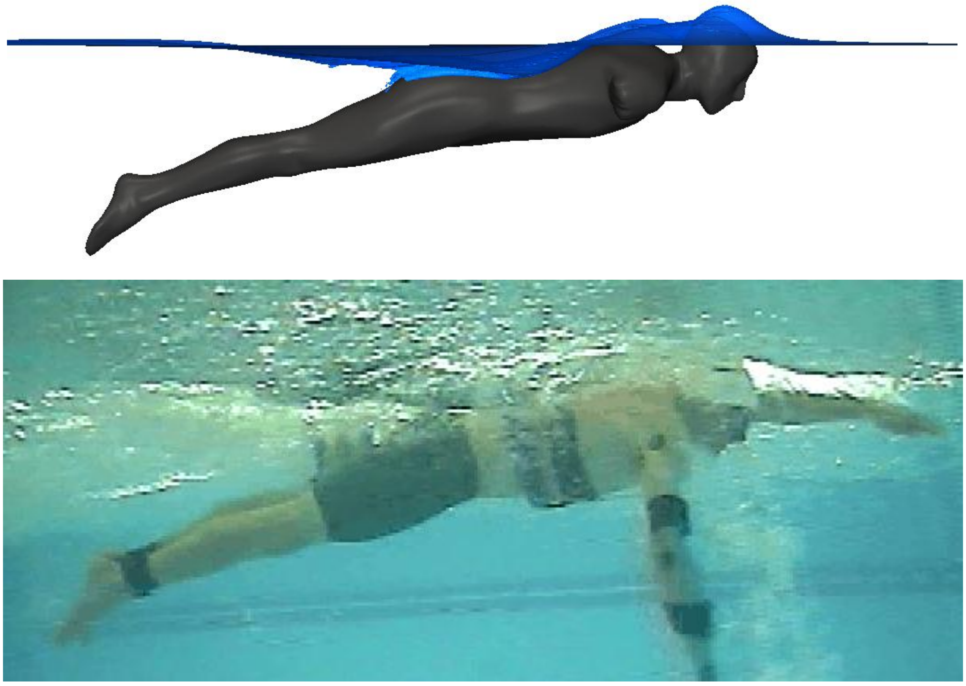

Figure 8-4 - Comparison between passive free surface and experimental footage of case C009.

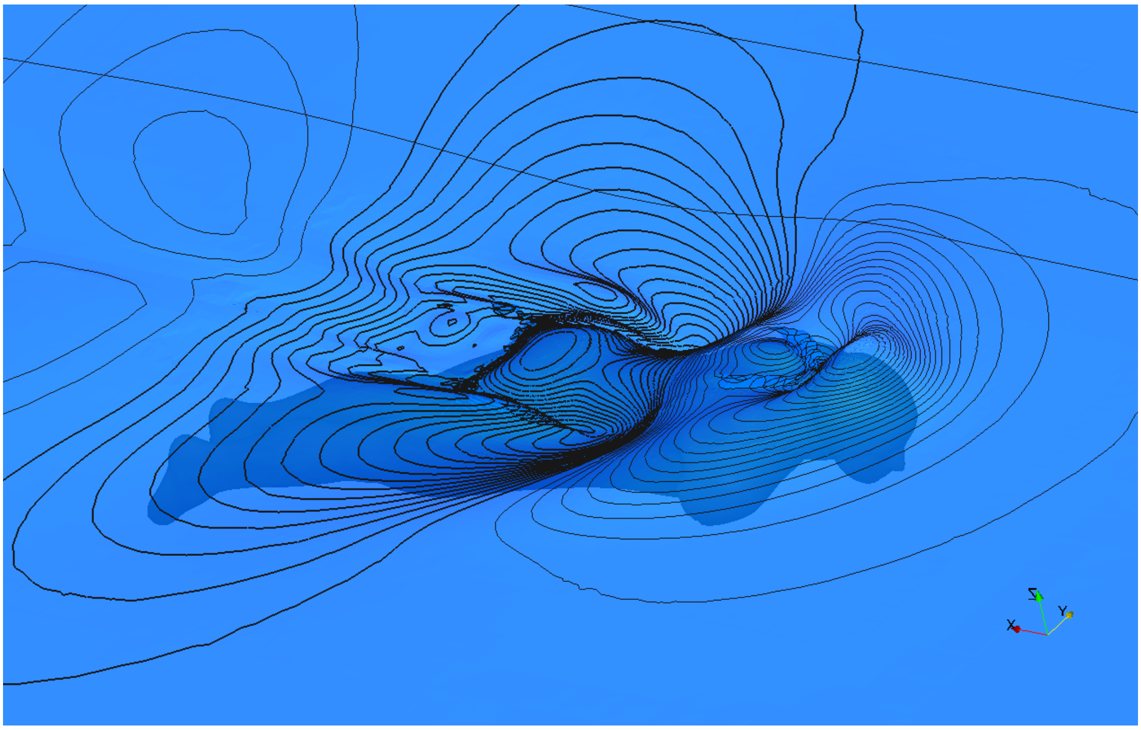

Figure 8-5 – Passive free surface deformation for Case C009, contours +-0.005 m.

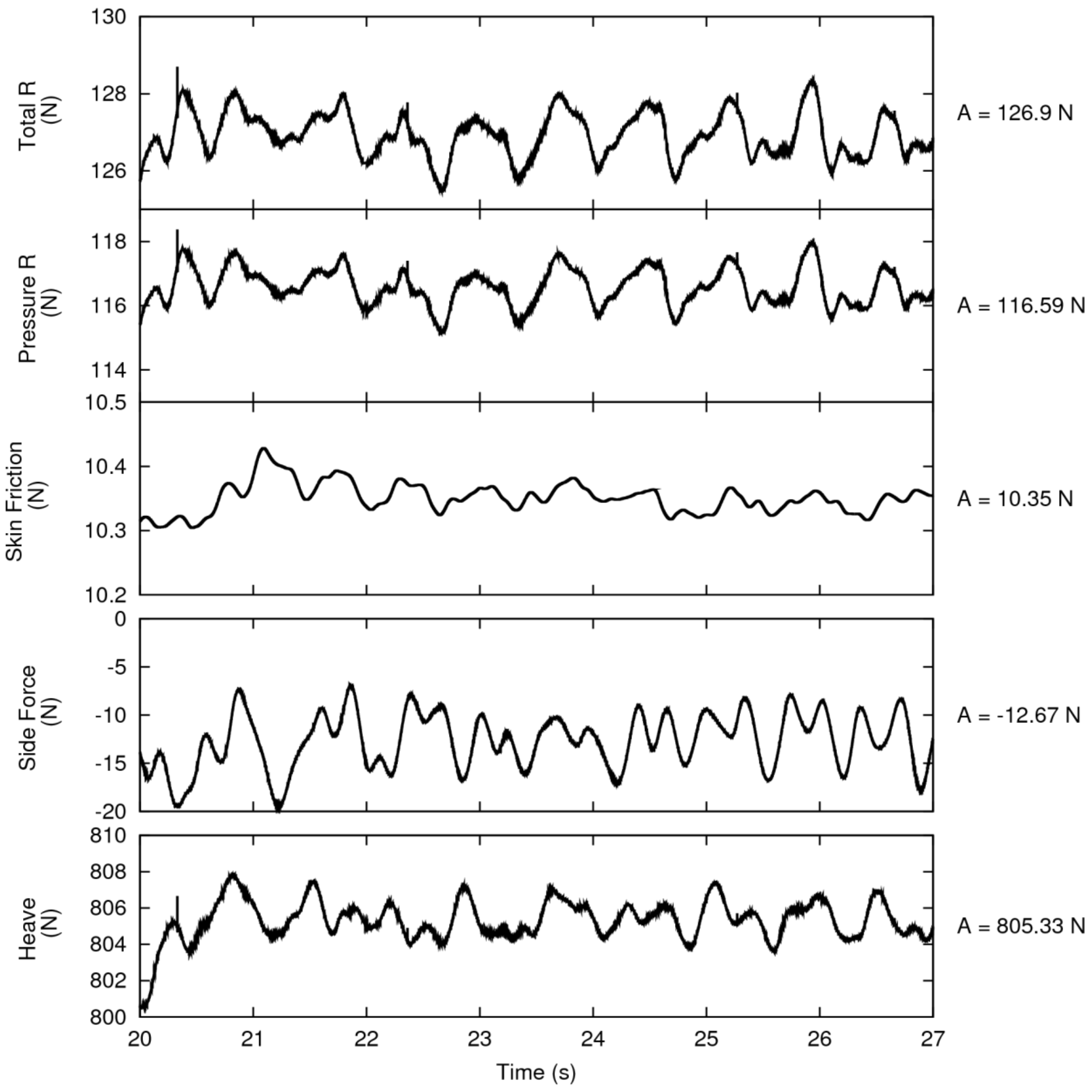

Figure 8-6 – Simulated passive forces for case C009, with time averaged values presented on the right.

The passive forces simulated for case C009 are presented in figure 8-6. A previous prediction of the passive resistance in this case was made by scaling the resistance from a passive experimental case for the same athlete (case C012 in Chapter 3), which was conducted at a slightly different speed. By assuming the resistance is proportional to velocity squared, the passive resistance for C009 was predicted as 95 N (see Chapter 7.4.3 for more details). This resistance prediction is significantly less than the simulated resistance for this geometry. On further inspection of both cases (C009 and C012, see Chapter 3) it is clear that the reason for this increase is due to the different attitude adopted by the athlete whilst doing arms-only freestyle as opposed to a passive tow. The leg position in case C009 (arm-only) is much lower than C012 (passive) and increases the projected area by approximately 47%. This increased projected area will increase the amount of flow separation in the region of the legs. If we scale the experimental resistance from case C012 (passive) by both projected area and velocity, using a standard drag coefficient approach, we obtain a predicted passive resistance for C009 (arm-only) of 140 N. This method is likely to over predict the frictional resistance, which is related to surface area not projected area. Moreover, differences in the free surface flow regime due to attitude will not have been captured. However, this does provide some confidence that the simulated passive resistance of 127 N for C009 is at least sensible.

The increase in separation, due to the attitude of the legs, can be seen in the shear stress streamlines presented in figure 8-7. The entire area behind the buttocks and legs is characterised by low or negative skin friction and unsteady turbulent streamlines. The rest of the torso presents mainly attached flow apart from on the neck and under the armpits.

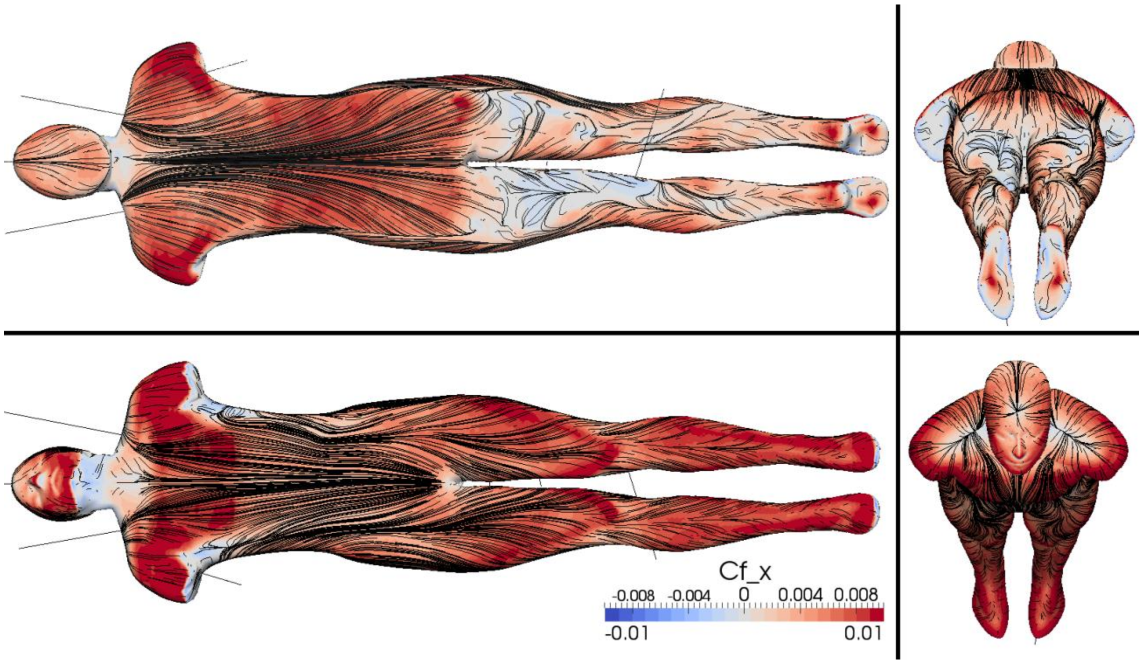

Figure 8-7 – Local coefficient of frictional resistance, with shear stress streamlines, for the passive simulation of case C009.

In figure 8-8 all the regions of separated flow can be seen as areas of low pressure on the backward facing surfaces. High pressure stagnation areas are observed on the head, shoulders and the front of the shins and feet. A high pressure region is also observed on the top of the head and shoulders due to the elevated free surface in this region.

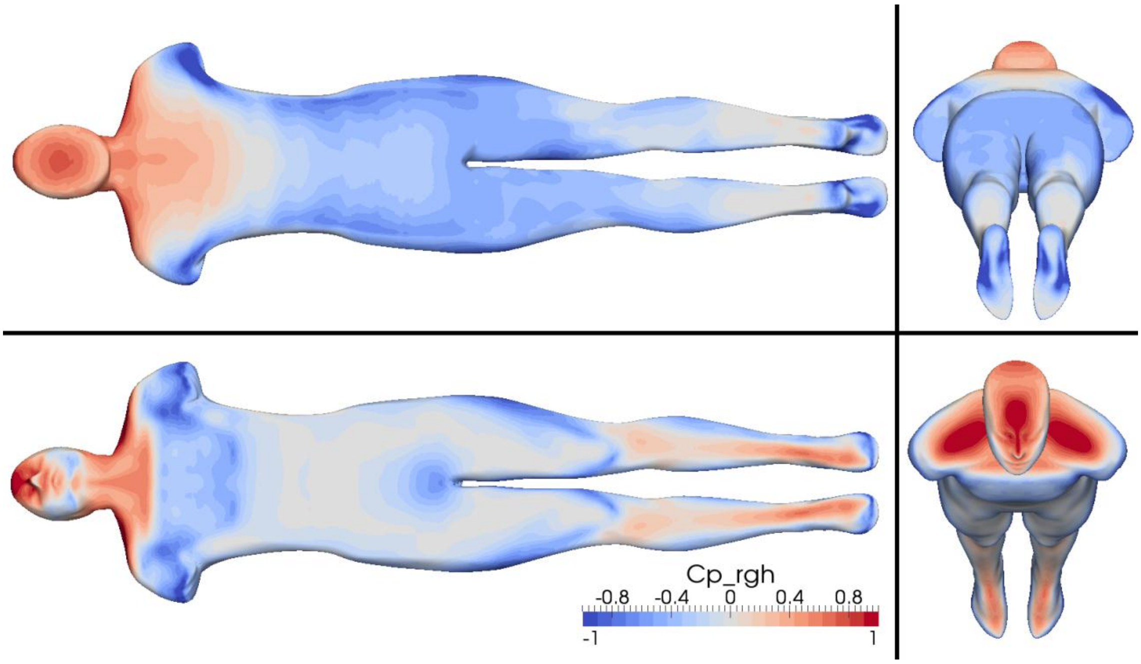

Figure 8-8 – Local coefficient of pressure (as defined in equation 5-2) for the passive simulation of case C009.

8.1.4 Conclusion

The methodology for passive swimming simulations presented in chapter 5, was used here to provide a passive solution to the geometry of the arms-only freestyle case C009. The resulting passive resistance is significantly greater than passive experiments for the same athlete, due to the different attitude adopted whilst swimming arm-only freestyle.

This simulation provides the initial conditions for a propelled freestyle simulation, allowing the impact of the arms on the hydrodynamic forces on the body to be determined.

8.2 Arm Propulsive Model

The propulsion model described in Chapter 7.5 provides a maximum instantaneous thrust of 100 N and mean thrust of approximately 33 N. These thrust magnitudes were tuned using the arm width to match the variation and average experimental tow force (R-T) measured in case C009. However this was based on a predicted passive resistance of 95 N, obtained from scaling the passive resistance from case C012. Due to the significant change in the athlete's leg position whilst arms-only swimming the resistance was increased by approximately 30 N compared to the passive tow prediction. This provided a passive resistance of 127 N for the C009 geometry (arms-only freestyle). Therefore it became clear that the current thrust generated by the arm model (33 N) would only account for half the thrust required to provide a simulated tow force (R-T) of 60N, which was measured experimentally.

To recreate the propelled experimental test case (C009) the propulsion model needed to generate twice as much thrust compared to the version presented in chapter 7. There were two possible options for increasing the generated thrust for the given stroke kinematics; either increase the arm width or the force coefficients used. It was decided that the current arm width (0.075 m) provided a good representation of the lower arm dimensions and proximity to the athlete geometry (see figure 8-9). Therefore the magnitude of the lift and drag coefficients were doubled to generate a larger mean thrust. The consequence of this is that the maximum instantaneous thrust produced is approximately twice the variation in experimental tow force (R-T). Potential reasons for this apparent disparity are discussed later in this chapter, however It is felt that the new propulsion model (producing 66N of mean thrust) best replicates the experimental test case by attempting to match the mean tow force measured.

Both versions of the propulsive model (mean thrust of 33 N and 66N) were used to simulate the arms only freestyle case C009 to provide an indication of how the arm induced variations vary with thrust magnitude. However detailed analysis is only provided for the new propulsion model (66N) as this should recreate the experimental test case more accurately.

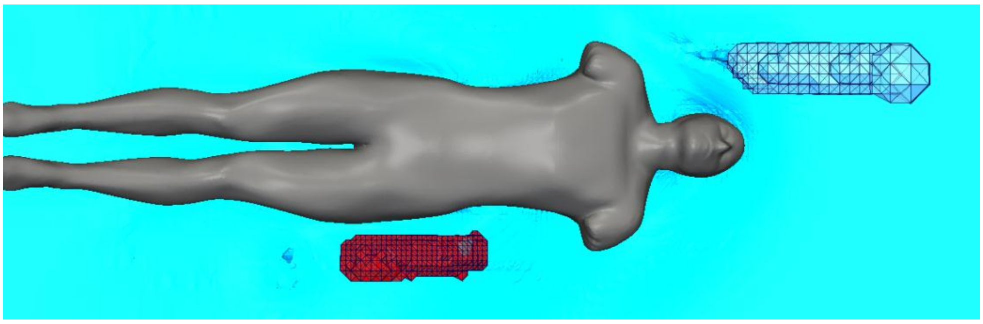

Figure 8-9 – Arm propulsive domains, viewed from below to provide proximity to athlete

8.3 Propelled resistance of case C009

The passive simulation of case C009 was used as the initial condition for both the propelled simulations conducted for this case (C009_SP_33N and C009_SP_66N). The only change between these two simulations is the magnitude of the lift and drag coefficients used. In both cases one full stroke cycle was conducted before analysing the second. This provided time for the impact of the arm stroke on the unsteady fluid flow to develop before it was assessed. The additional computational cost of the propelled simulations compared to the passive case was 8% and 28% for the 33N case and 66N case respectively. The increase in computational cost between the two propelled cases is due to the increased magnitude of arm induced velocities and pressure differentials reducing the solution time step and increasing the solution time.

The time varying forces produced by the arm model and measured on the athlete geometry, can be seen for one full stroke cycle in figure 8-10. The stroke starts with the right arm entering the water ahead of the swimmer, which coincides with the main propulsive phase of the left arm. Due to the fact that the simulated stroke kinematics are the same for both the left and right arms, the variation in thrust and resistance components are repeated during a complete stroke cycle. The impact of the arms on the flow will only be assessed during the main propulsive phase of the right arm in order to avoid repetition. The key points within the stroke cycle that will be analysed in detail are marked with red lines at different relative stroke times(t/T_{stroke}= 0.3, 0.4, 0.5, 0.6 and 0.7).

The position of the arms and the effect they have on the fluid can be seen for each of these key times in figure 8-11. This provides an overview of the stroke kinematics relative to the forces measured on the body along with a temporal and spatial representation of how the arm model affects the local flow. Detailed analysis of the fluid flow and the forces on the body will be conducted at each of these times to provide insight into how the arms produce the variation in hydrodynamic forces observed in figure 8-10. This analysis will only be conducted on case C009_SP_66N.

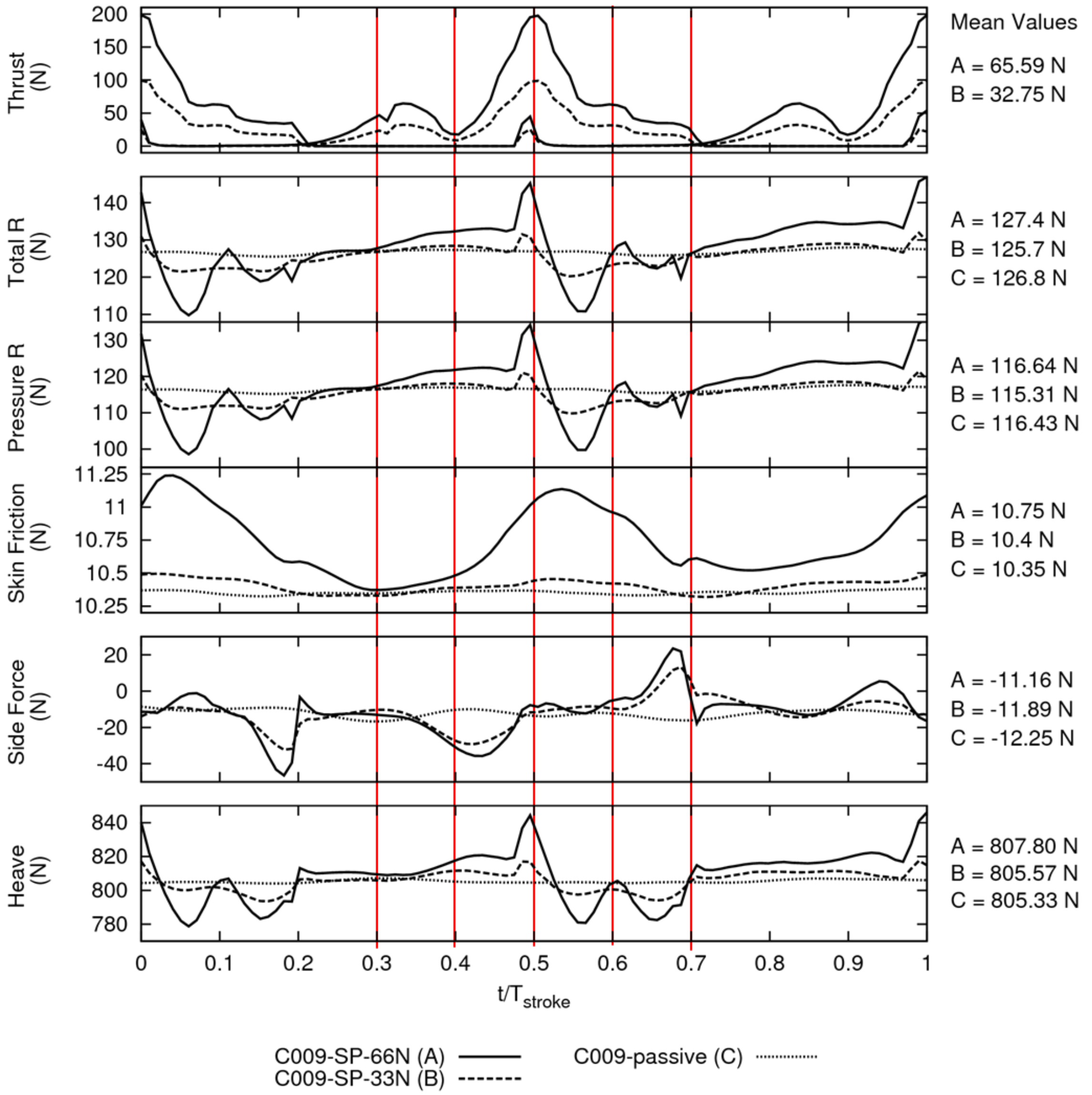

Figure 8-10 – Thrust produced and hydrodynamic forces acting on the athlete, over one stroke cycle, for both self-propelled and passive simulations of C009.

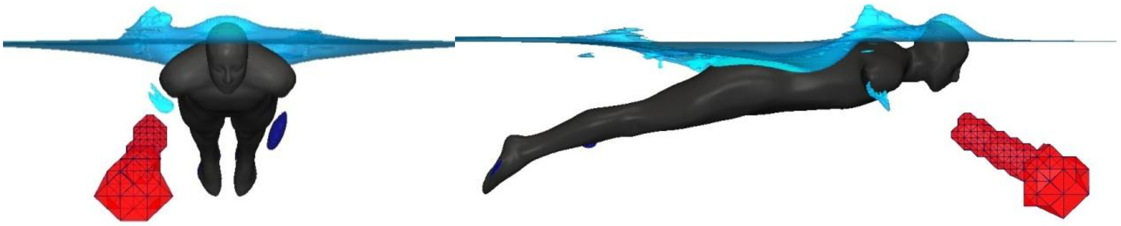

$t/T_{stroke}= 0.3$

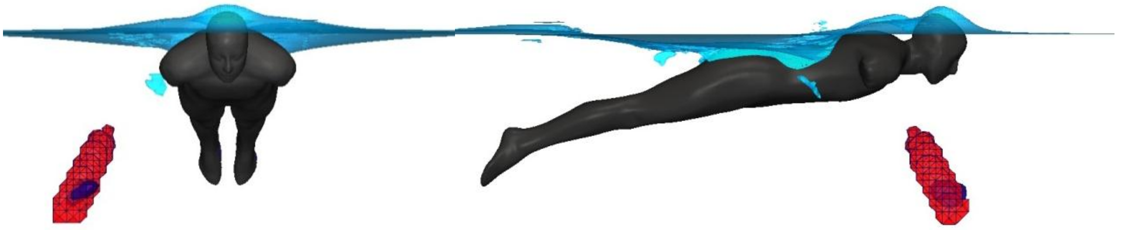

$t/T_{stroke}= 0.4$

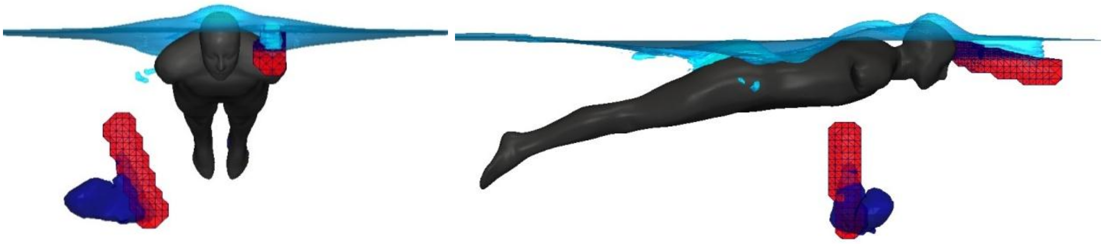

$t/T_{stroke}= 0.5$

$t/T_{stroke}= 0.6$

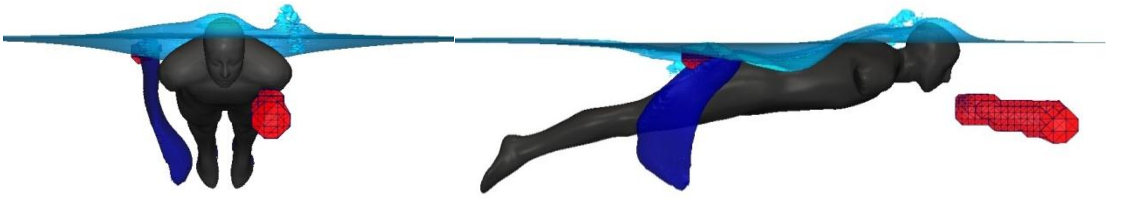

$t/T_{stroke}= 0.7$

Figure 8-11 – Position of the arms at key times throughout a stroke cycle. Cells contained within the arm propulsive domain's shown in red, accelerated axial velocity indicated by dark blue iso-surface ($u/U_0=1.4$) and local free surface position provided in light blue.

8.3.1 $t/T_{stroke} = 0.3$

At t/T_{stroke} equal to 0.3 the right arm has just started its outward sweep and the left arm has started its recovery above the water. The right arm position can be seen in figure 8-12. It should be pointed out that the increase in width of the arm's propulsive domain towards the finger tips is due to the increased cell size in this region of the mesh and not a physical change in arm width. A comparison to the side-on experimental video footage is provided in figure 8-13, along with the head-on free footage of the same. This type of comparison allows the arm kinematics to be verified at different points within the stroke, but also highlights some of the differences observed between a static athlete geometry and a dynamically rolling swimmer.

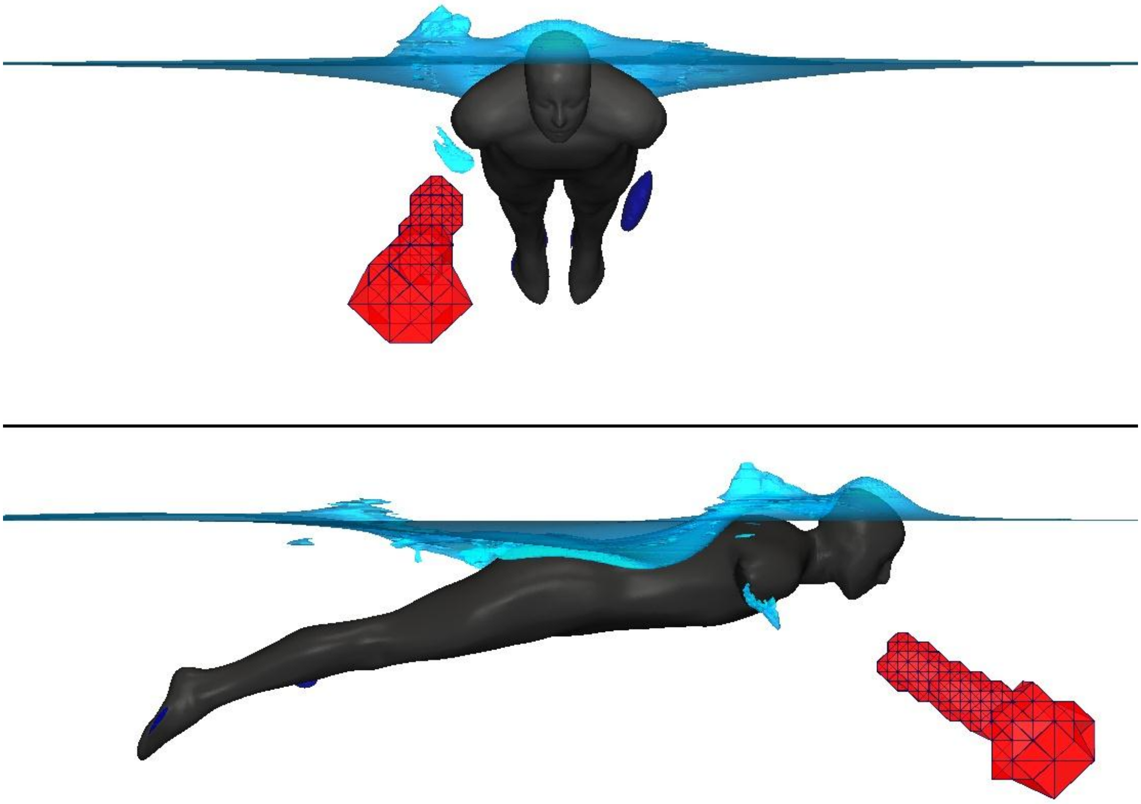

Figure 8-12 - Cells contained within the arm propulsive domain's shown in red, accelerated axial velocity indicated by dark blue iso-surface ($u/U_0=1.4$) and local free surface for $t/T_{stroke}=0.3$.

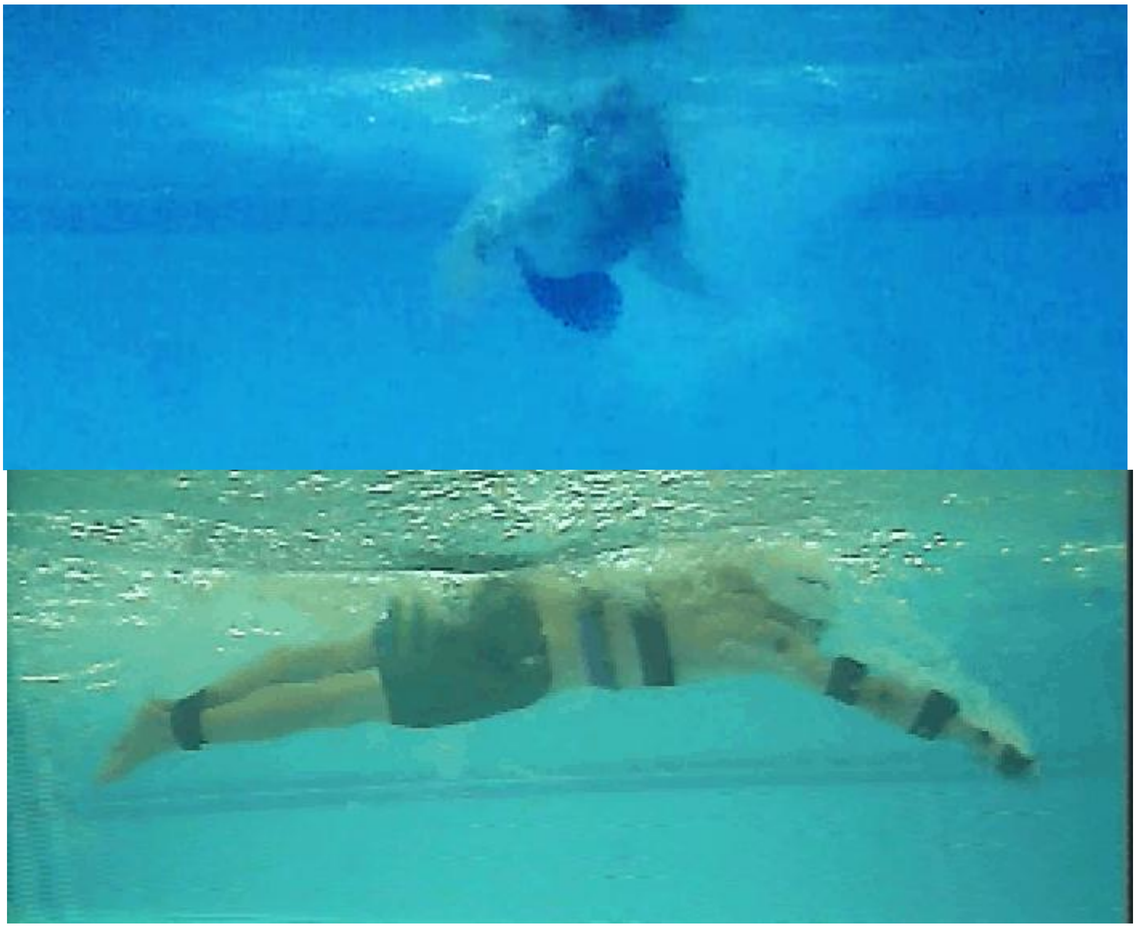

Figure 8-13 – Video footage at $t/T_{stroke} = 0.3$ for experimental case C009 (bottom) and normal freestyle technique for the same athlete (top).

The peak in free surface height that can be observed over the right shoulder in figure 8-12 is a consequence of the right arm entry at the beginning of the stroke cycle. The impact of the arm entry will be discussed in more detail as the left arm enters at t/T_{stroke} equal to 0.5). This peak in free surface height can also be seen in figure 8-14, along with the peak associated with the left arm exit seen alongside the left knee.

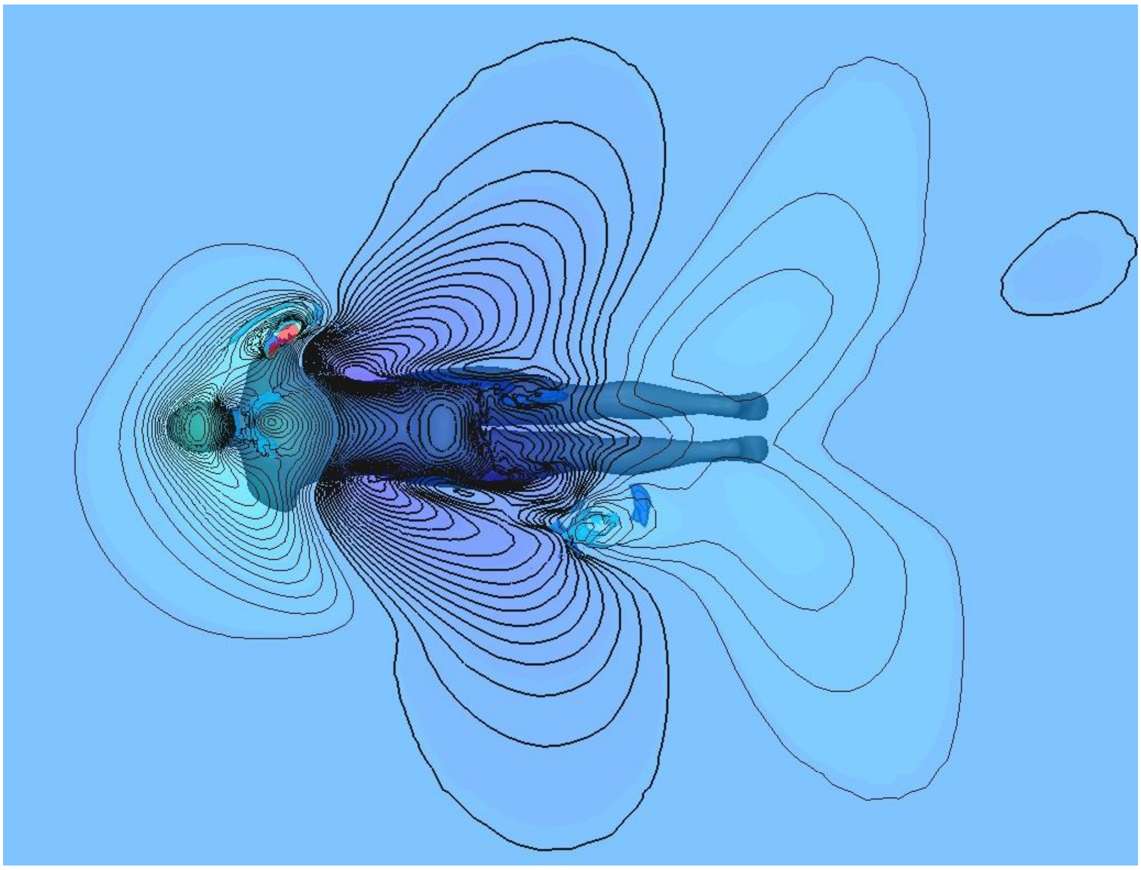

Figure 8-14 – Free surface deformation with contours +-0.005 m for t/T_{stroke}=0.3. Negative deformation indicated by bold contour lines.

Despite the obvious effect the arms are having on the free surface near the swimmer, they have little impact on the hydrodynamic forces at this stage in the stroke. In figure 8-10 we can see that for t/T_{stroke} equal to 0.3 the forces acting on the body are practically the same for the propelled simulations as in the passive case.

If we look in detail at the change in skin friction compared to the passive solution (Figure 8-15), we can see that there are some differences in the shear stress distribution over the body. The large magnitude variations seen down the back of the legs can be attributed to the unsteady turbulent flow in this separated region. This leads to significant local differences in skin friction for any given time, but has very little impact on the total skin friction. The same features can be observed in the change in pressure coefficient (Figure 8-16). It is worth mentioning that the same features would be observed if a comparison was made between two different times of the passive solution (due to the inherent instability in separated flows).

It is possible to identify small changes in the different force components due to the arms. On the right shoulder local changes associated with the free surface peak in this location can be seen. A reduction in pressure over the neck and right shoulder can also be detected. There is a small area of increased skin friction that can be observed on the side of the left leg. This coincides with a small region of accelerated flow, seen in figure 8-12, which was generated by the previous left arm pull. This process will be discussed in more detail later on with reference to the right arm. Apart from these small changes observed, the forces acting on the body are broadly the same as the passive case at this point.

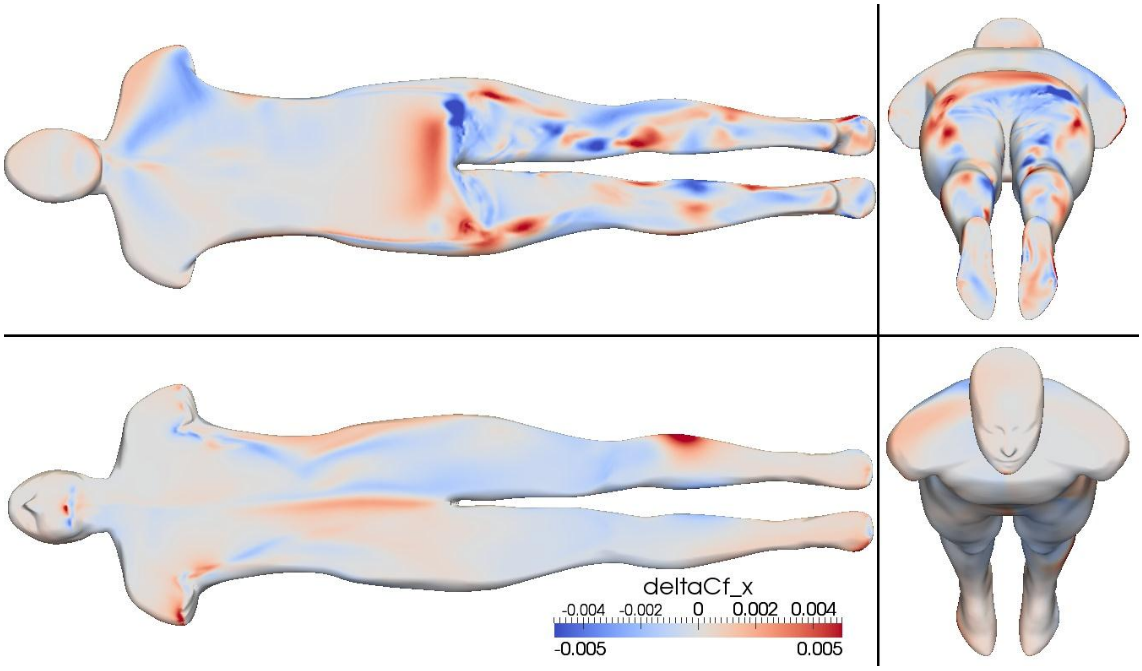

Figure 8-15 – Change in propelled skin friction coefficient ($t/T_{stroke}=0.3$) compared to the passive solution. A change in *Cf_x* of ±0.005 represents ±16% of the total variation in *Cf_x* observed over the body in the passive simulation of C009.

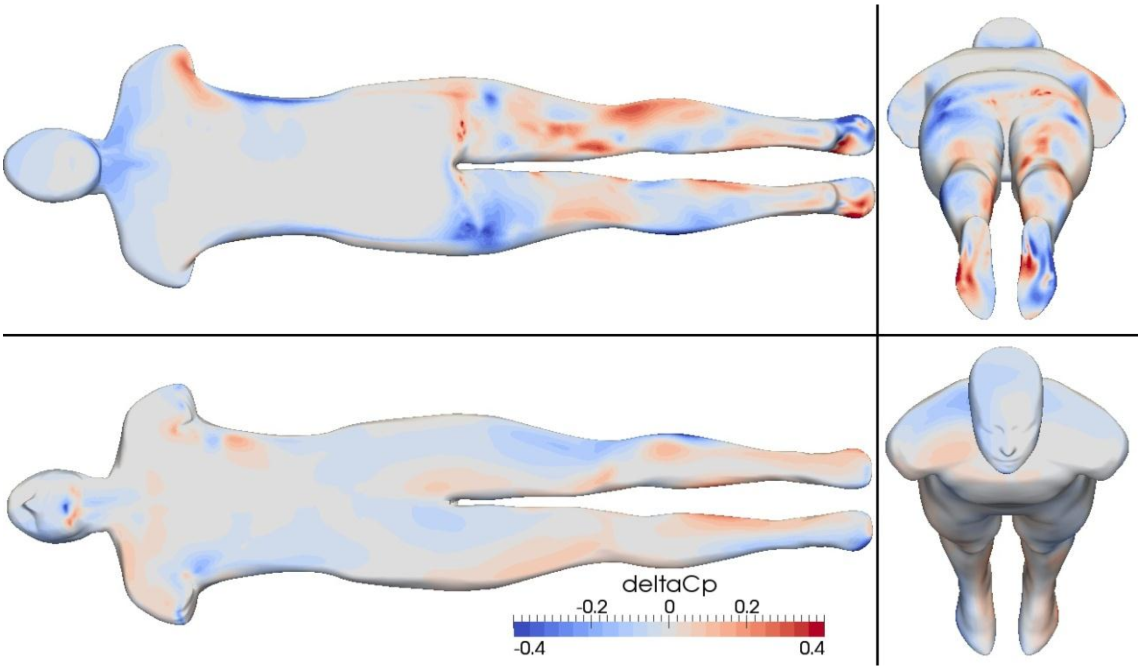

Figure 8-16 - Change in propelled pressure coefficient (*t/T*$_{stroke}$=0.3) compared to the passive solution. A change in *Cp* of ±0.4 represents ±24% of the total variation in pressure (*Cp_rgh)* observed over the body in the passive simulation of C009.

8.3.2 t/T$_{stroke}$ = 0.4

At this point in the stroke the right arm is at the end of the outward sweep before moving back inwards towards the body (see figure 8-17 for location of propulsive domain). This produces a dip in the thrust generated due to the lack of lateral motion eliminating the lift component of thrust at this point. A small region of accelerated flow can be observed from the thrust generated during the outward sweep.

A comparison of the simulated and experimental arm kinematics can be made through the use of figure 8-18. The lower right arm appears to agree well with the experimental footage although there is some discrepancy with the left arm position. In the side on video footage the left arm has already entered the water. This is due to slight differences in the kinematics between left and right arms, whereas in the simulated arm model they are assumed to be the same; but 180 degrees out of phase. It is likely however that there will be some variation from stroke to stroke when using non-elite athletes, as demonstrated by the fact that the left arm has yet to enter the water in the head-on view footage. The experimental video footage also shows that the athlete's body has now rolled back to a more neutral position.

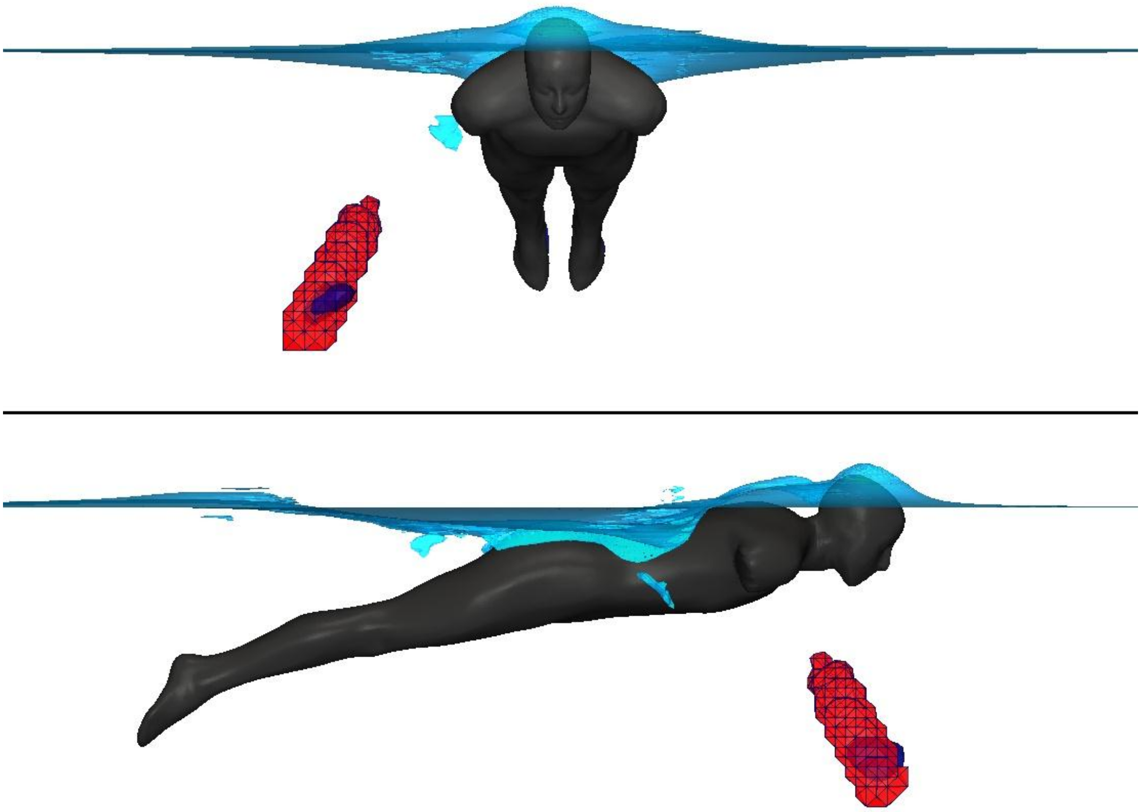

Figure 8-17 - Cells contained within the arm propulsive domain's shown in red, accelerated axial velocity indicated by dark blue iso-surface (u/U0=1.4) and local free surface for t/Tstroke=0.4.

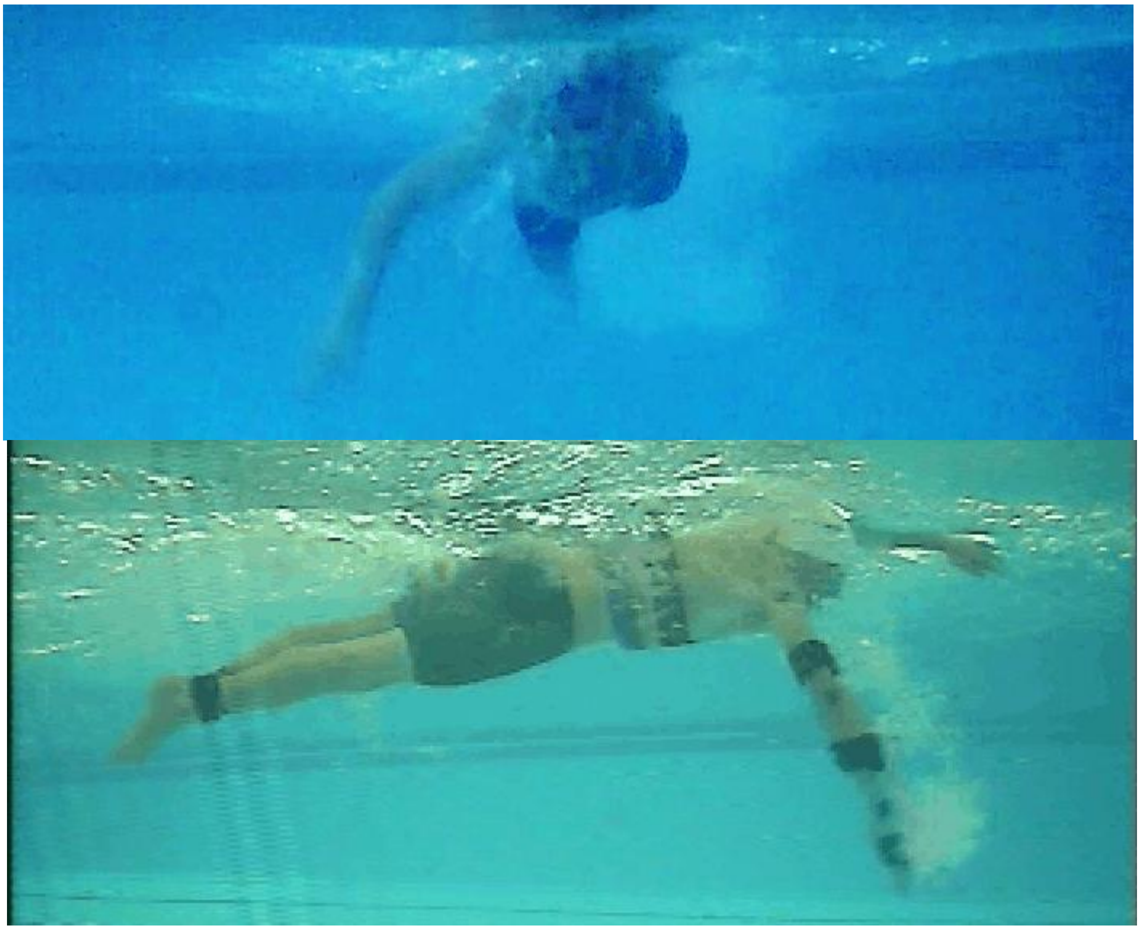

Figure 8-18 - Video footage at t/Tstroke = 0.4 for experimental case C009 (bottom) and normal freestyle technique for the same athlete (top).

The free surface deformation at this point in the stroke can be seen in figure 8-19. The disturbance caused by the right arm entry can now be seen to be modifying the shape of the wave trough positioned on the right hand side of the athlete's waist. The trough has become deeper, with what appears to be breaking wave features on either side of it. This deeper wave trough can also be observed in figure 8-17.

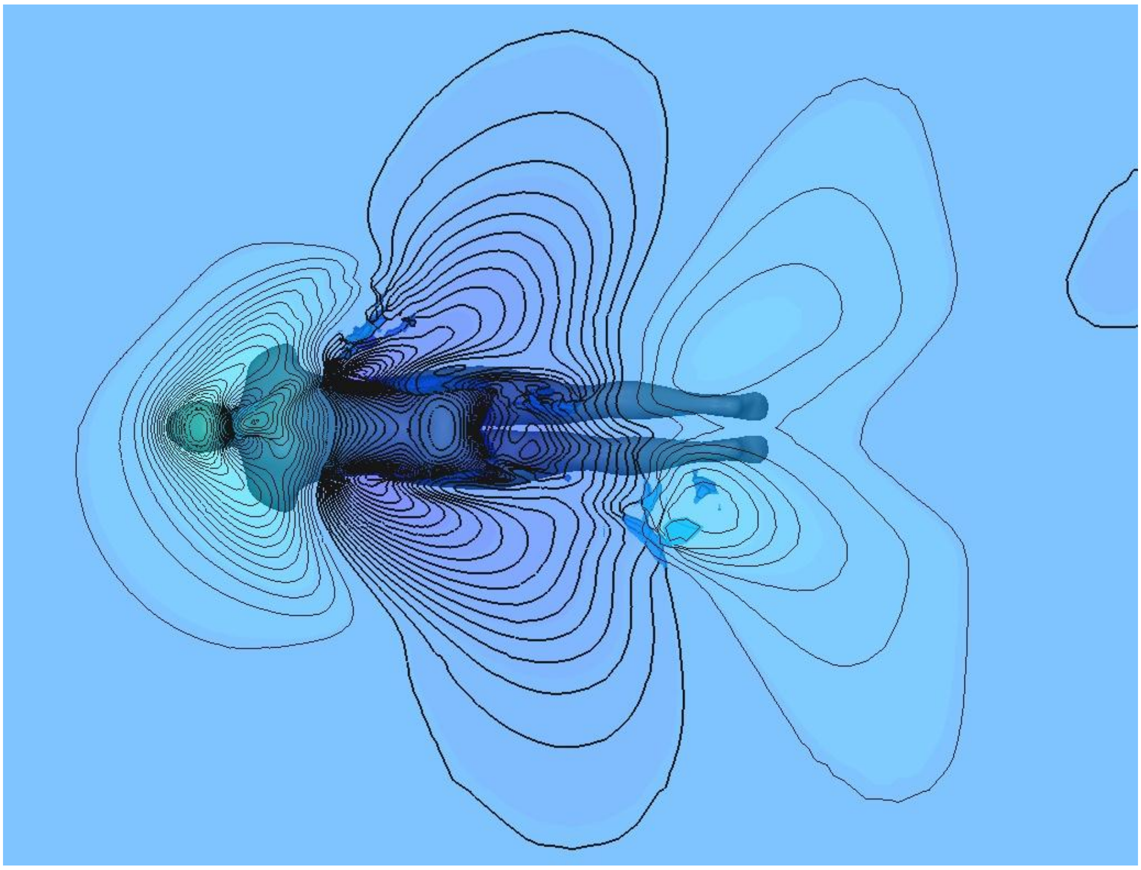

Figure 8-19 - Free surface deformation with contours +-0.0005 m for t/T_{stroke}=0.4. Negative deformation indicated by bold contour lines.

Figure 8-6 indicates that at this stage in the stroke there is little change to the skin friction (confirmed in figure 8-20), but there is a gradual rise in the pressure resistance. It would appear from figure 8-21 that this is due to the free surface interaction on the right hand side of the geometry increasing the pressure on the hips. This difference in pressure from left to right also causes a change in side force of approximately 20 N.

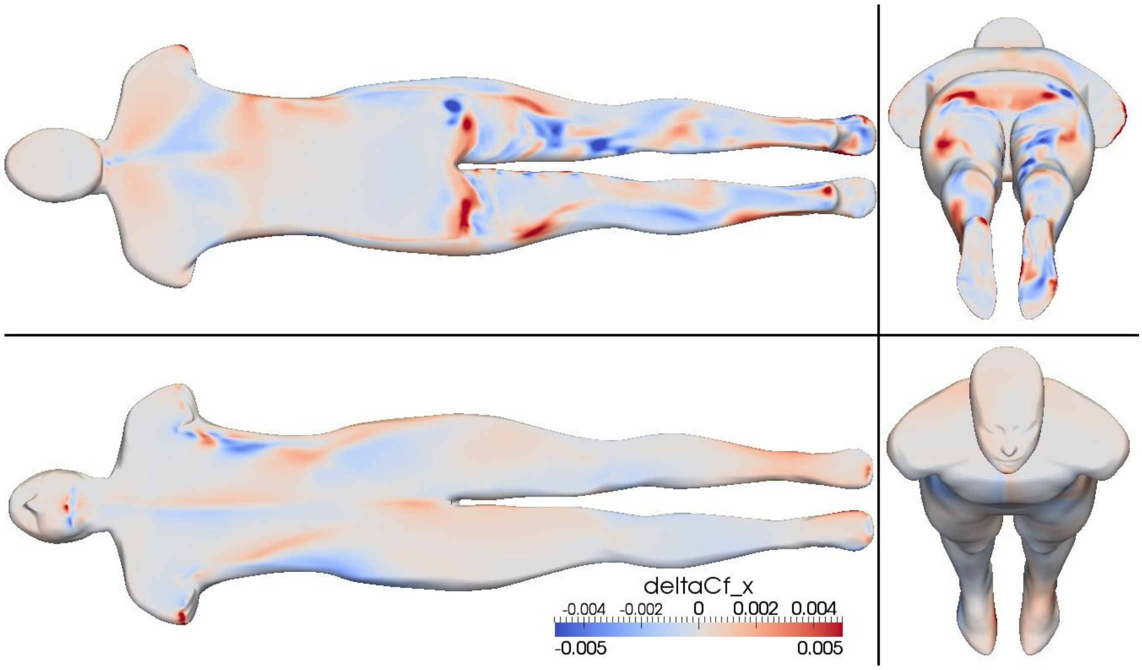

Figure 8-20 - Change in propelled skin friction coefficient (t/T_{stroke}=0.4) compared to the passive solution. A change in Cf_x of ±0.005 represents ±16% of the variation in Cf_x observed over the body in the passive simulation of C009.

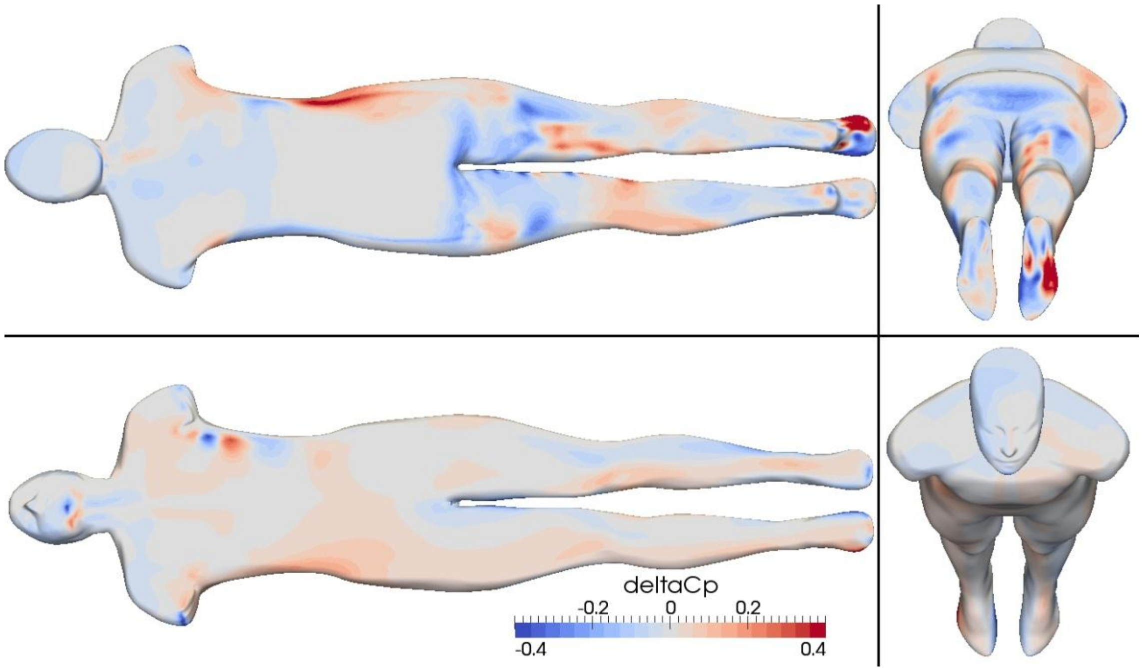

Figure 8-21 - Change in propelled pressure coefficient (t/T_{stroke}=0.4) compared to the passive solution. A change in *Cp* of ±0.4 represents ±24% of the total variation in pressure (*Cp_rgh)* observed over the body in the passive simulation of C009.

8.3.3 $t/T_{stroke} = 0.5$

Half way through the full stroke cycle the right arm is producing maximum thrust as it sweeps back in towards the body, whilst the left arm has just entered the water ahead of the swimmer. The position of the two propulsive domains can be seen in figure 8-22, along with the accelerated axial flow generated by the right arm. By comparing these to figure 8-23 it can be seen that the general position of the lower arm agrees well with the experimental footage, although it appears to be at a slightly different angle in the head-on view. This could be a slight error associated with the kinematic interpolation or, considering the high lateral velocity of the arm at this point, a slight discrepancy in the exact time of the simulated view and the video frame.

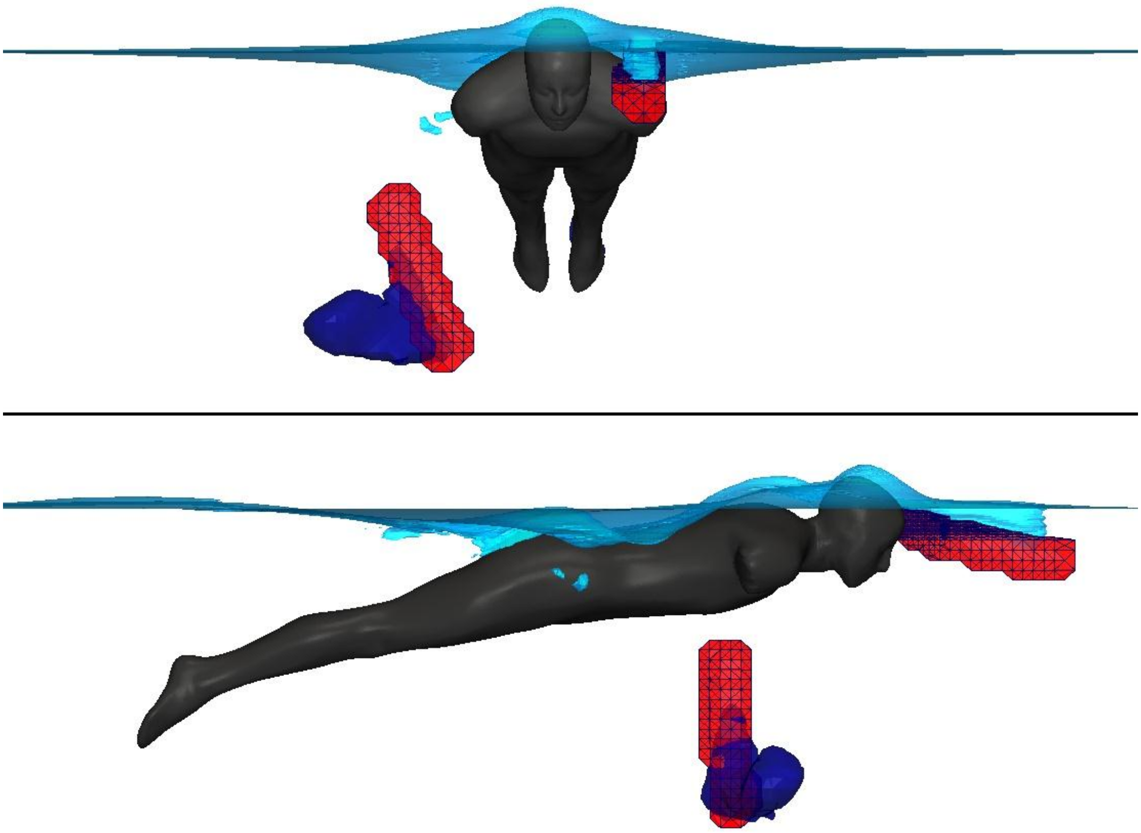

Figure 8-22 - Cells contained within the arm propulsive domain's shown in red, accelerated axial velocity indicated by dark blue iso-surface (u/U0=1.4) and local free surface for t/Tstroke=0.5.

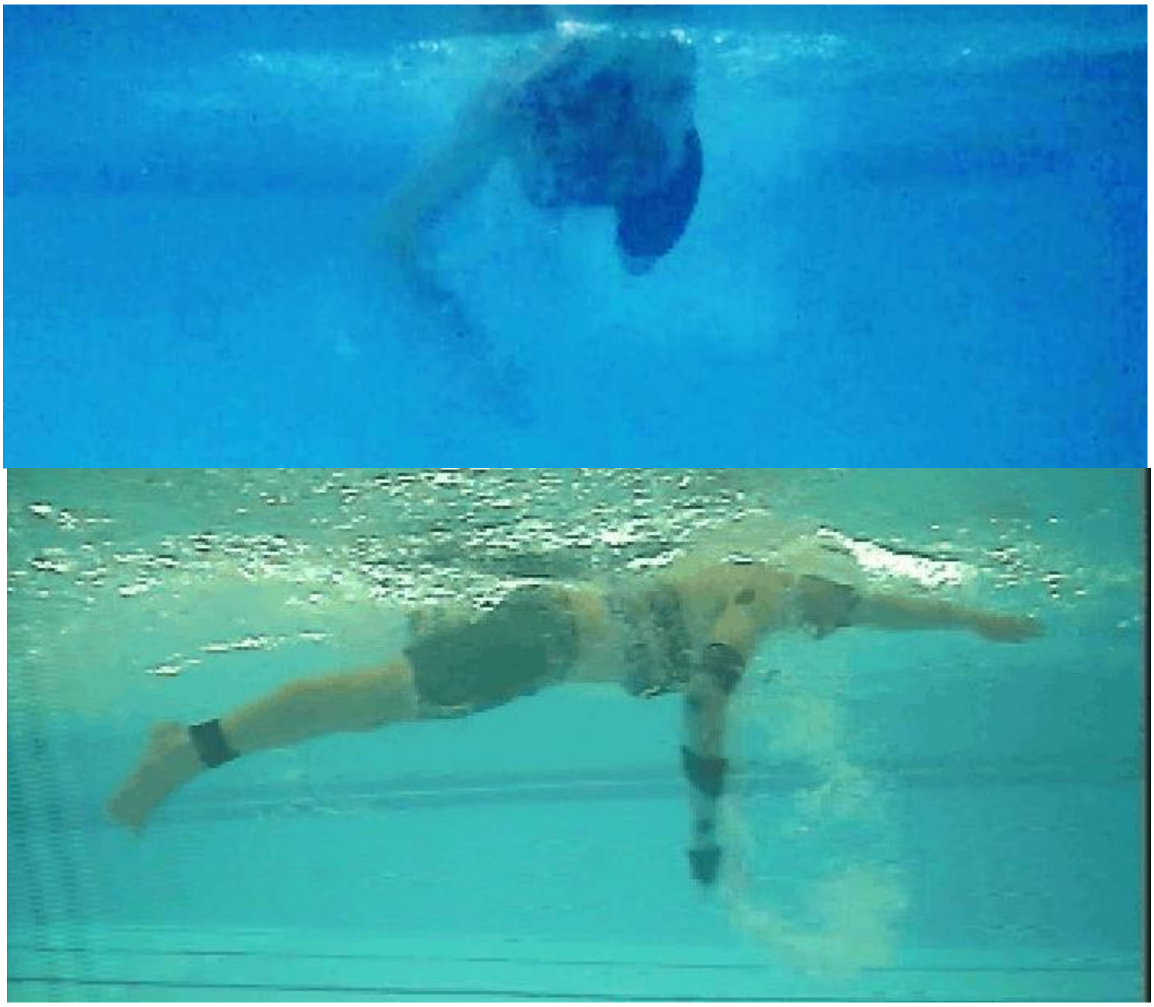

Figure 8-23 - Video footage at t/Tstroke = 0.5 for experimental case C009 (bottom) and normal freestyle technique for the same athlete (top).

There are two key free surface features observed at this point in the stroke cycle. Firstly there is a large depression in the free surface due to the left arm entering the water. This can be seen within the simulation in both figure 8-22and figure 8-24. The same feature is also captured in the video footage, but appears to be made up of more broken water and entrained air than the simulated version, showing up as a band of lighter fluid just above the left arm.

The other key difference in the free surface compared to the passive simulation is an elevated breaking wave feature over the right hip. This is obviously an evolution of the same free surface feature observed at t/T_{stroke}=0.4, originally from the right arm entry at the beginning of the stroke cycle.

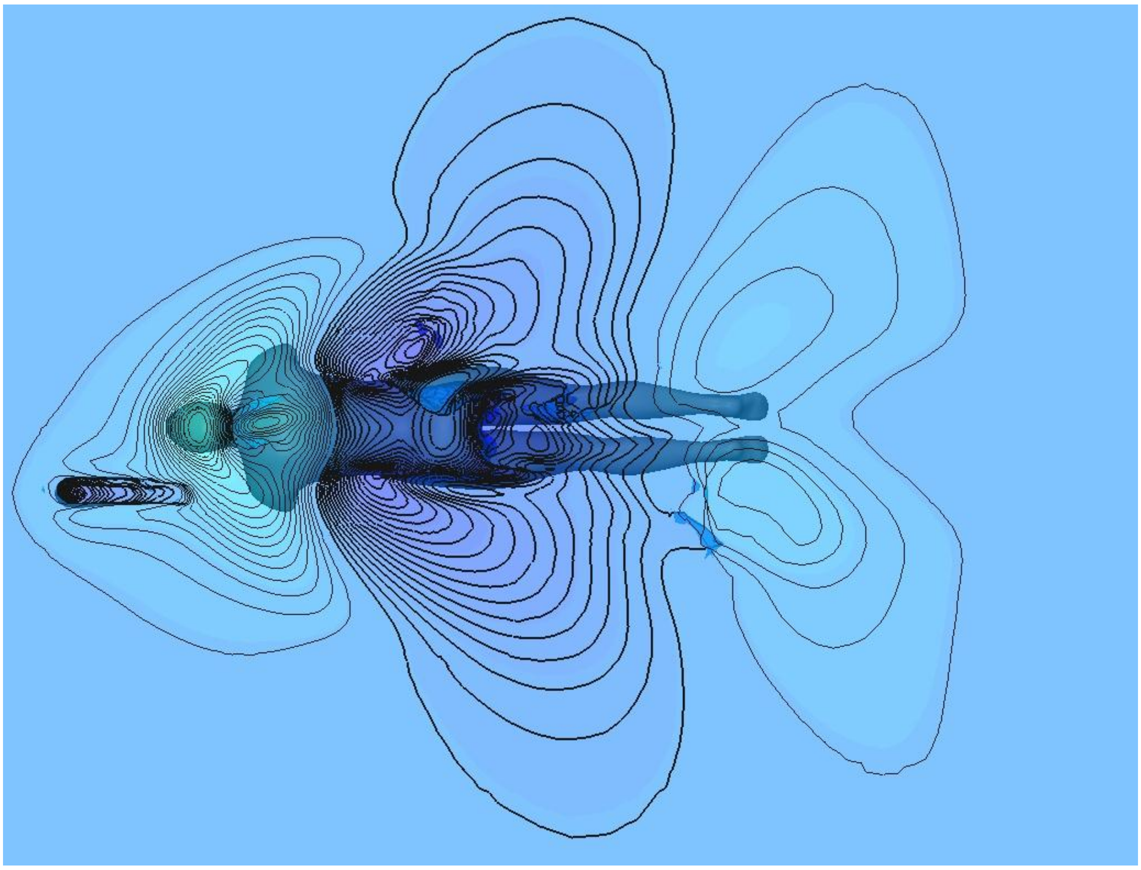

Figure 8-24 - Free surface deformation with contours +-0.0005 m for t/T_{stroke}=0.5. Negative deformation indicated by bold contour lines.

Figure 8-6 indicates that at this stage in the stroke there is an increase in both the skin friction and pressure resistance. Figure 8-25 shows that the breaking wave feature is creating a region of increased skin friction in the small of the back on the right hand side of the athlete geometry. This would appear to indicate that this local free surface feature is increasing the velocity near the body surface and therefore raising the shear stress values in this region. However the increase is less than 1 N and therefore does not feature significantly in the total resistance.

The sharp increase in pressure resistance at this point can be attributed to an increase in pressure on the head and shoulders, due to the left arm entry (observed in figure 8-26). This pressure peak is most acute on the left hand side of the head, but also affects the shoulder and chest of the athlete. This is combined with the increased pressure associated with the free surface feature on the right hand side of the torso. A further consequence of this high pressure region on the underside of the body is an increase in heave force.

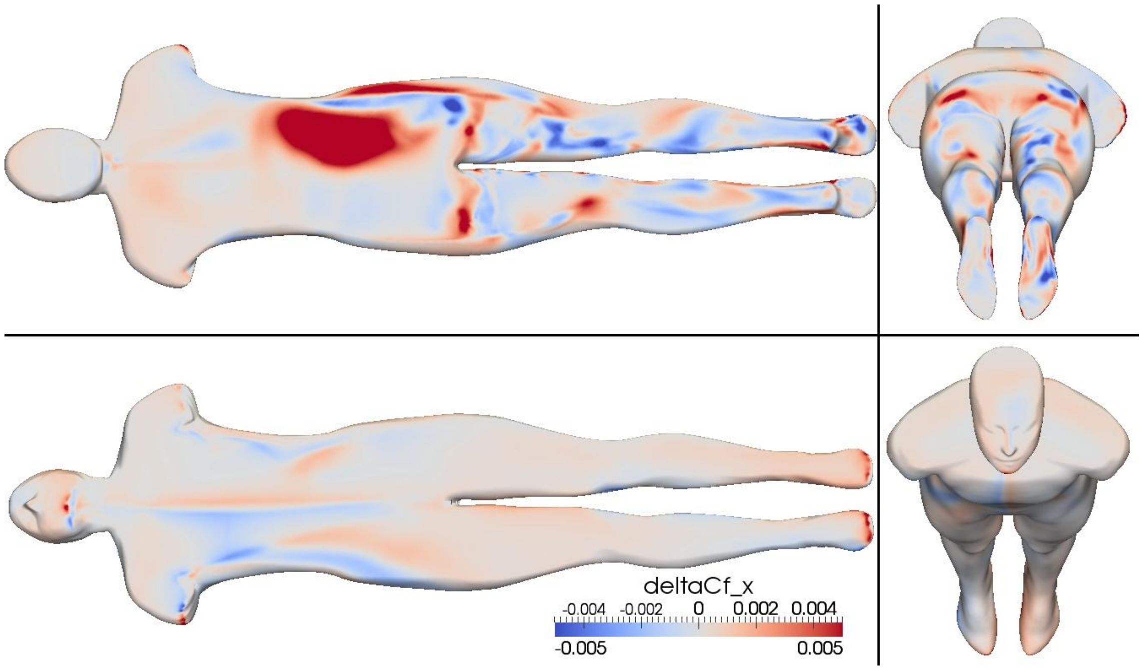

Figure 8-25 - Change in propelled skin friction coefficient (t/T_{stroke}=0.5) compared to the passive solution. A change in Cf_x of ±0.005 represents ±16% of the variation in Cf_x observed over the body in the passive simulation of C009.

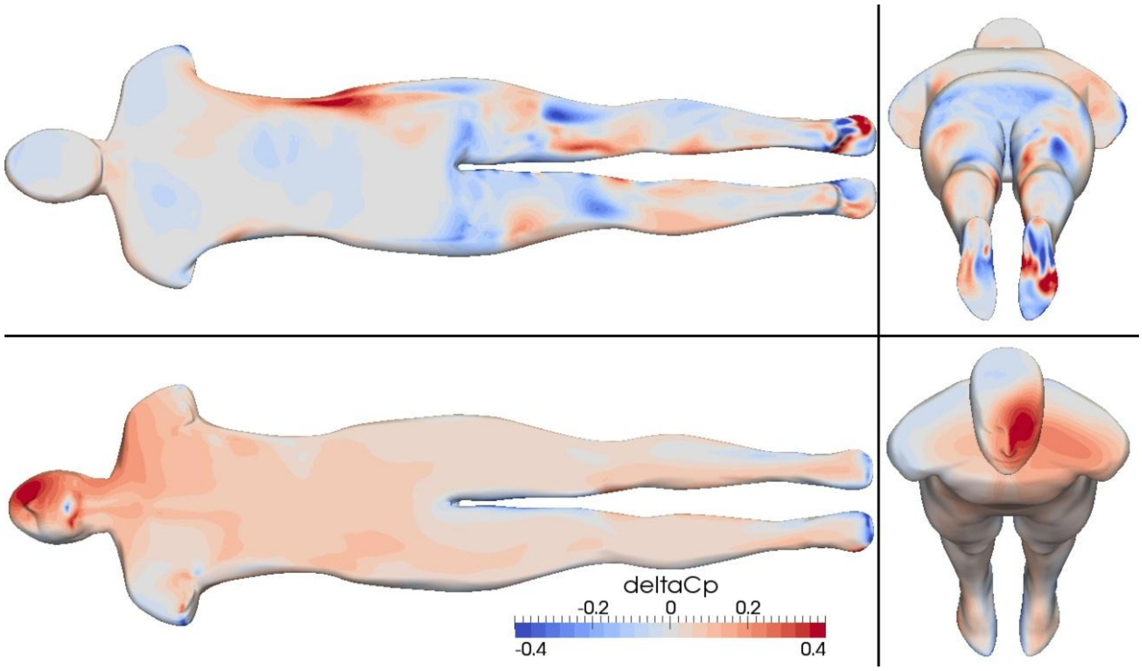

Figure 8-26 - Change in propelled pressure coefficient (t/T_{stroke}=0.5) compared to the passive solution. A change in *Cp* of ±0.4 represents ±24% of the total variation in pressure (*Cp_rgh)* observed over the body in the passive simulation of C009.

Interestingly, almost immediately after this large peak in pressure resistance, the pressure drag is reduced by almost the same magnitude compared to the passive case, see figure 8-10. The change in pressure at this point in the stroke (t/T_{stroke} = 0.55) can be seen in figure 8-27, showing how almost the entire front half of the torso now has a lower pressure than the passive case. An explanation for this can be found in the entrained air cavity, created by the left arm entry, collapsing back in on its self (see figure 8-28). This creates an artificially low static pressure as the fluid surrounding the air bubble flows back in to fill it.

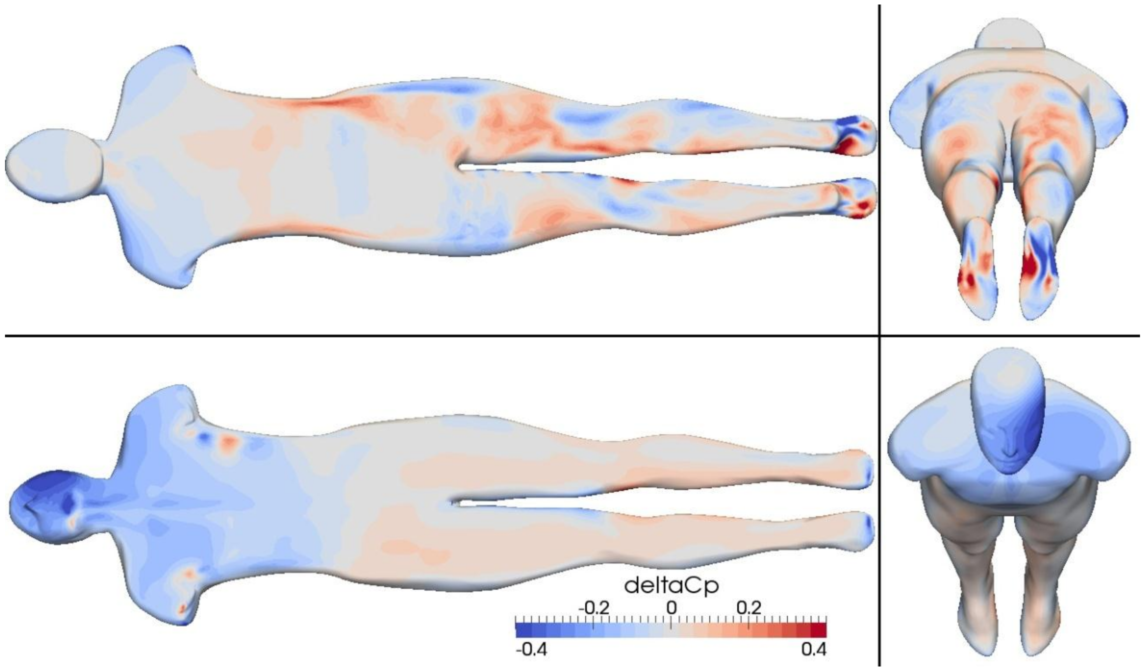

Figure 8-27 - Change in propelled pressure coefficient (t/T_{stroke}=0.55) compared to the passive solution. A change in Cp of ±0.4 represents ±24% of the total variation in pressure (Cp_rgh) observed over the body in the passive simulation of C009.

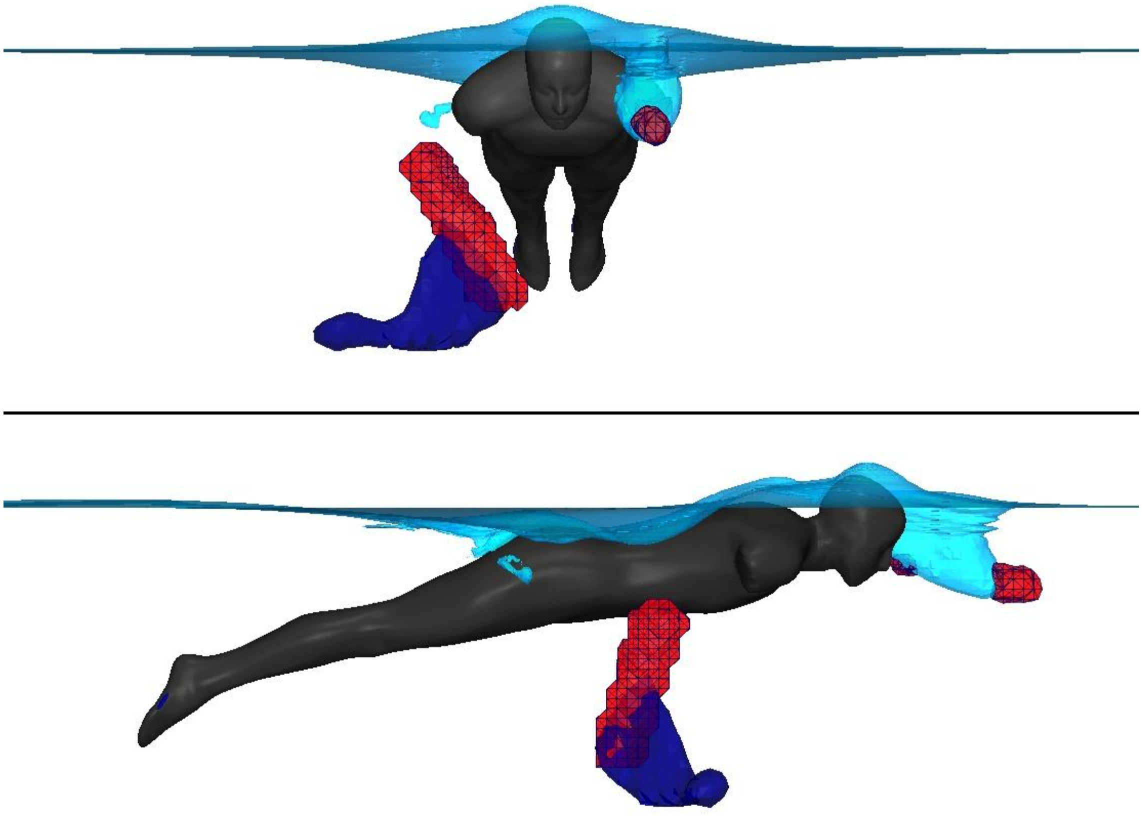

Figure 8-28 - Cells contained within the arm propulsive domain's shown in red, accelerated axial velocity indicated by dark blue iso-surface (u/U0=1.4) and local free surface for t/T_{stroke}=0.55.

8.3.4 $t/T_{stroke} = 0.6$

At this point in the stroke cycle the right arm is driving backwards in the mainly drag based propulsive phase of the stroke, close to the side of the athlete geometry. The left arm is fairly stationary as it pauses after entering the water before starting the outward sweep. The positions of the arms' propulsive domains can be seen in figure 8-29 and compared to experimental video footage in figure 8-30. Close agreement is observed between the arm kinematics at this point, however the lack of body roll in the simulation will change the relative proximity of the arm to the body.

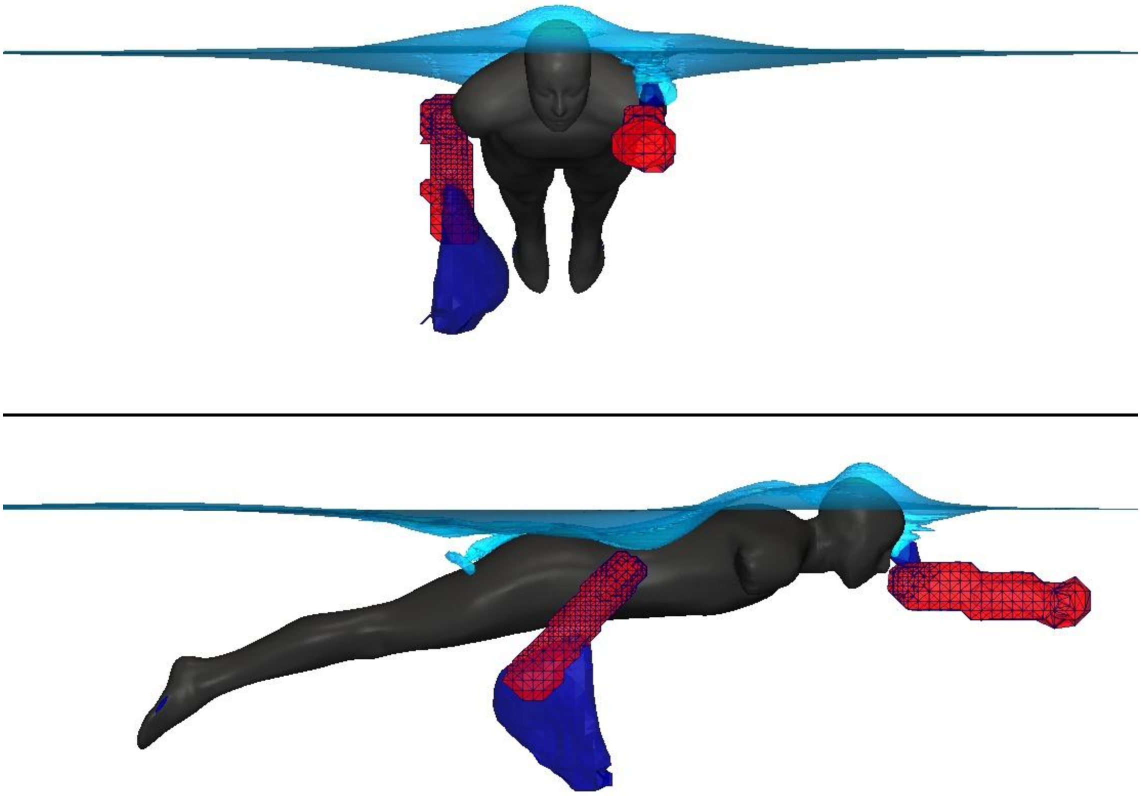

Figure 8-29 - Cells contained within the arm propulsive domains shown in red, accelerated axial velocity indicated by dark blue iso-surface (u/U0=1.4) and local free surface for t/T_{stroke}=0.6.

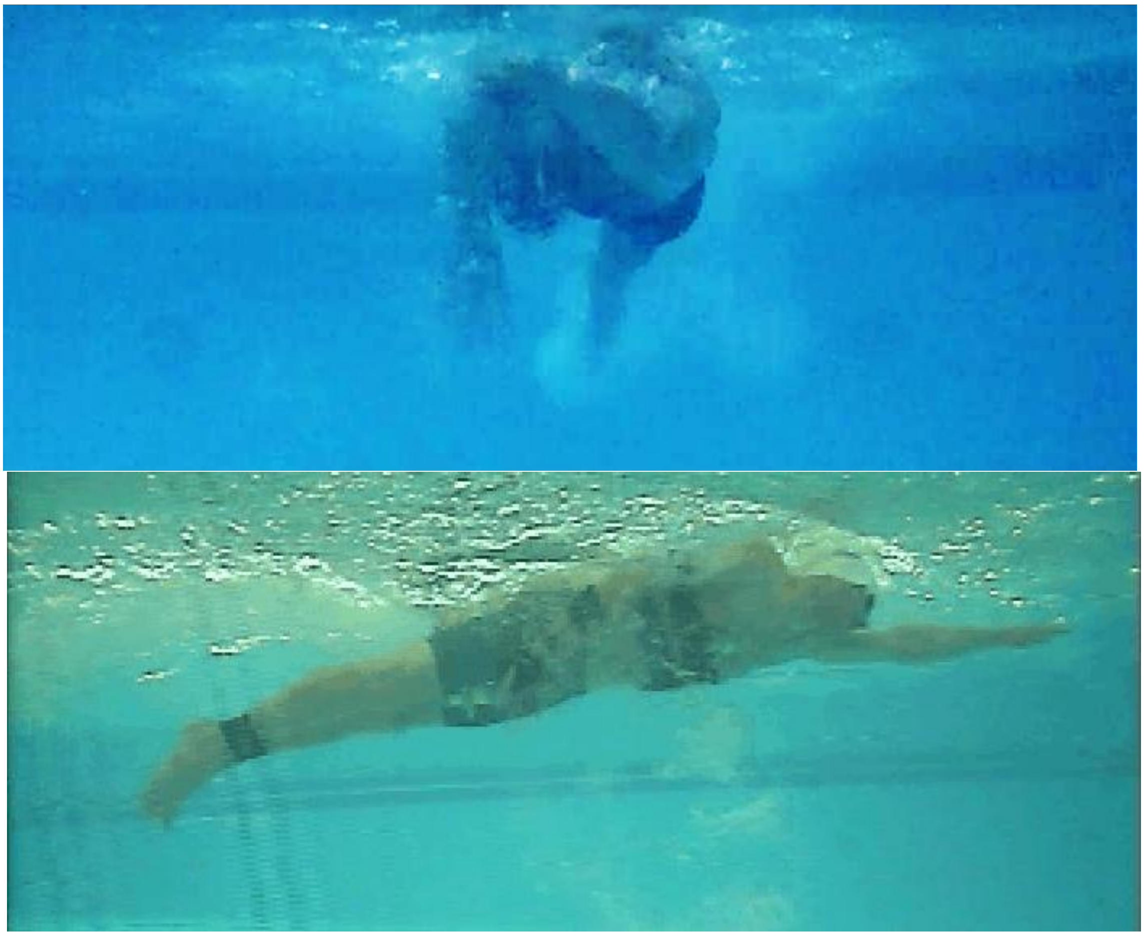

Figure 8-30 - Video footage at $t/T_{stroke} = 0.6$ for experimental case C009 (bottom) and normal freestyle technique for the same athlete (top).

The free surface flow features observed in figure 8-31 are essentially just the time evolving features previously described around the hip on the right hand side and the left arm entry feature. The deeper wave trough on the right hand side of the waist might also be a consequence of the right arm's proximity to this location.

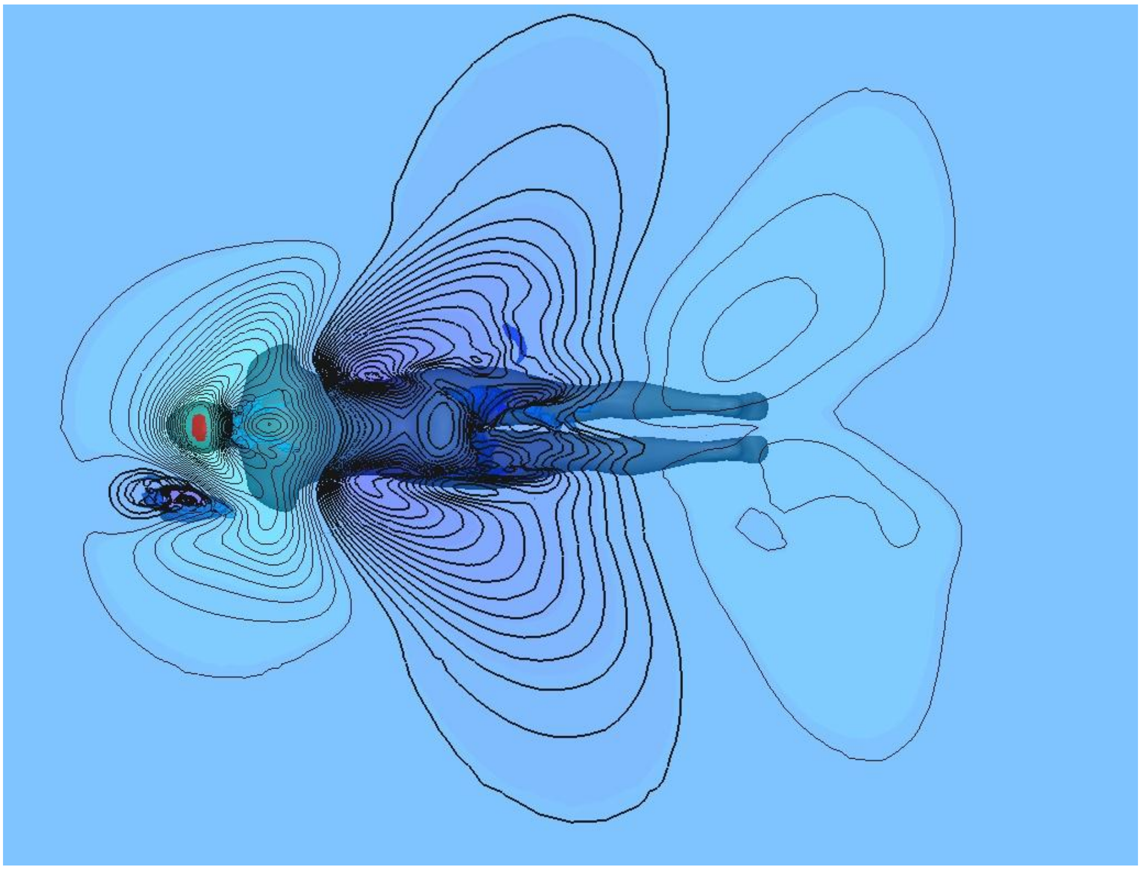

Figure 8-31 - Free surface deformation with contours +-0.0005 m for t/T_{stroke}=0.6. Negative deformation indicated by bold contour lines.

The increased skin friction region on the lower back is still clearly visible in the surface plot in figure 8-32, maintaining the increased viscous resistance observed in the hydrodynamic force traces in figure 8-10. This is despite there being no obvious free surface feature in this region to cause it.

The close proximity of the right arm can be observed in the pressure field in figure 8-33. A high pressure region can be seen ahead of the arm as it pushes water in front of it leaving a low pressure region behind it, near the athlete’s waist. However, this does not appear to be having a significant effect on the skin friction in this region.

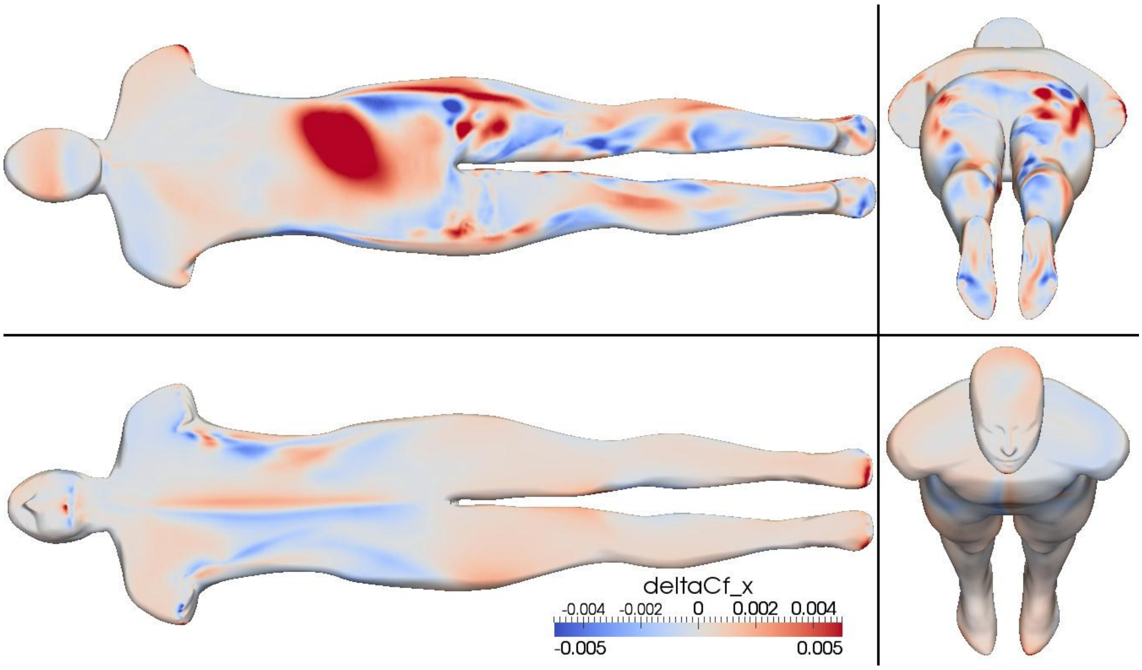

Figure 8-32 - Change in propelled skin friction coefficient (t/T_{stroke}=0.6) compared to the passive solution. A change in Cf_x of ±0.005 represents ±16% of the variation in Cf_x observed over the body in the passive simulation of C009.

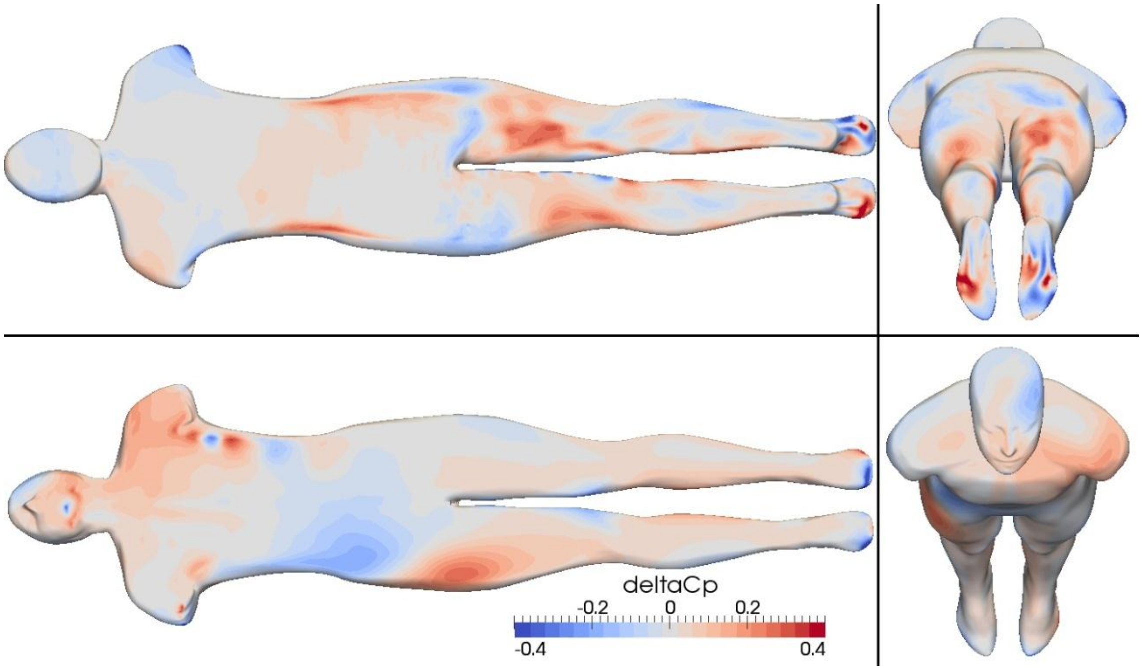

Figure 8-33 - Change in propelled pressure coefficient (t/T_{stroke}=0.6) compared to the passive solution. A change in *Cp* of ±0.4 represents ±24% of the total variation in pressure (*Cp_rgh)* observed over the body in the passive simulation of C009.

8.3.5 $t/T_{stroke} = 0.7$

The final phase of the right arm pull is as it exits the water close alongside the hips. Again the comparison between simulated position (Figure 8-34) and video footage (Figure 8-35) highlights the main difference between the two is the roll angle of the body.

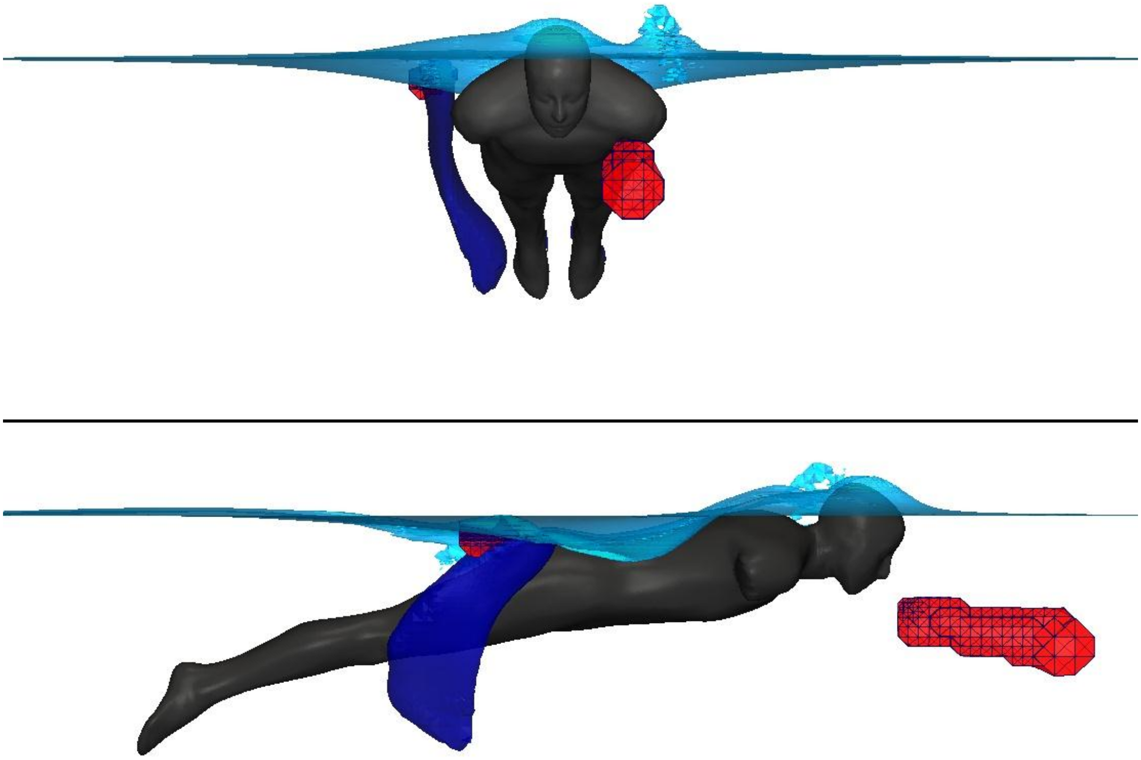

Figure 8-34 - Cells contained within the arm propulsive domain’s shown in red, accelerated axial velocity indicated by dark blue iso-surface (u/U0=1.4) and local free surface for t/T_{stroke}=0.7.

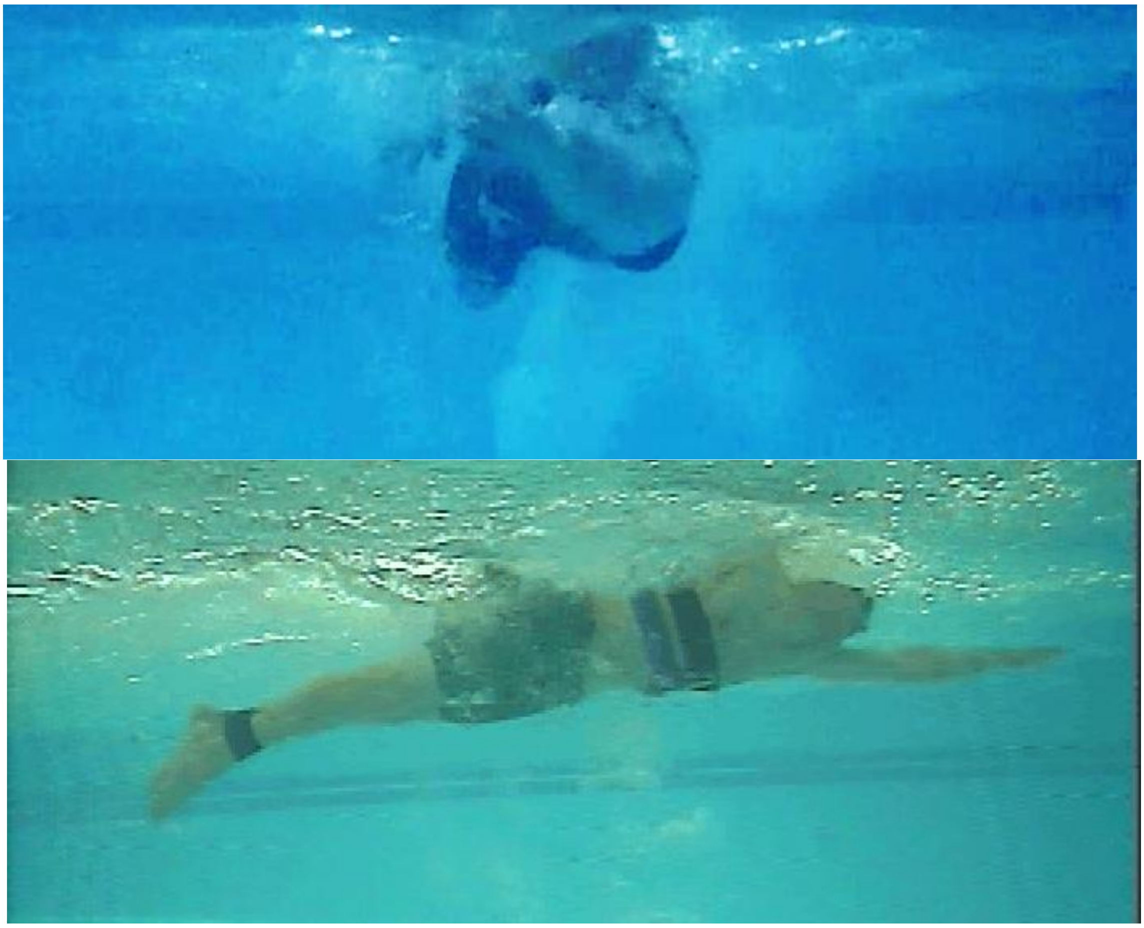

Figure 8-35 - Video footage at t/T_{stroke} = 0.7 for experimental case C009 (bottom) and normal freestyle technique for the same athlete (top).

The key free surface feature identified in figure 8-36 is the peak in surface elevation where the right arm is exiting the water. The influence of the left arm entry can now be seen to have reduced the free surface elevation over the left shoulder, resulting in a slight reduction in the pressure on the left hand side of the head and shoulders (see figure 8-38).

The impact of the right arm's accelerated axial flow (observed in figure 8-34) can now be seen to be reducing the local skin friction on the body's right hand hip and thigh. This is due to the accelerated flow creating a pressure differential in the axial direction. This has the effect of actually reducing the fluid velocity between the body and the accelerated region, causing a reduction in local skin friction. A similar effect was observed between a kayak paddle and hull using the same body force methodology in (Banks et al., 2013) see Appendix 2. The combined effect of this low skin friction region and a weakening area of high skin friction on the lower back/buttocks, reduces the total skin friction to approximatley the same value as the passive case.

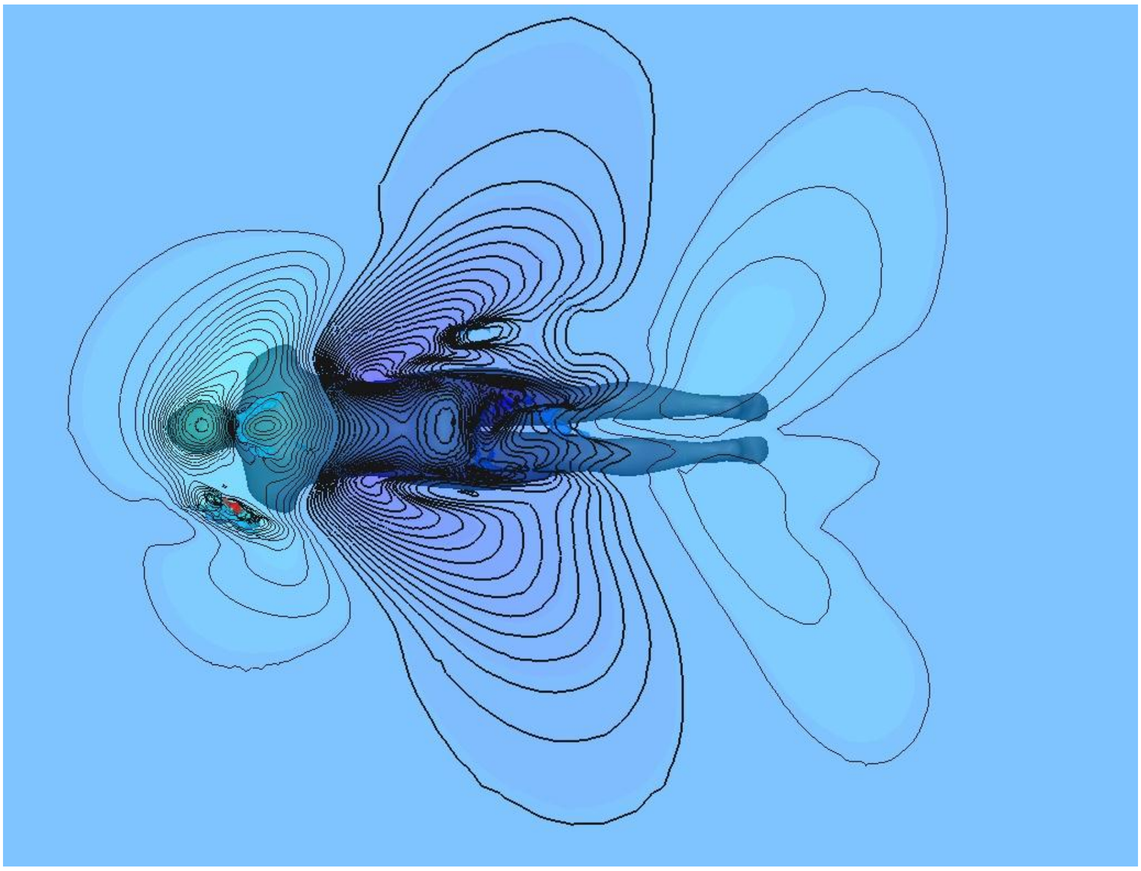

Figure 8-36 - Free surface deformation with contours +-0.0005 m for t/T_{stroke}=0.7. Negative deformation indicated by bold contour lines.

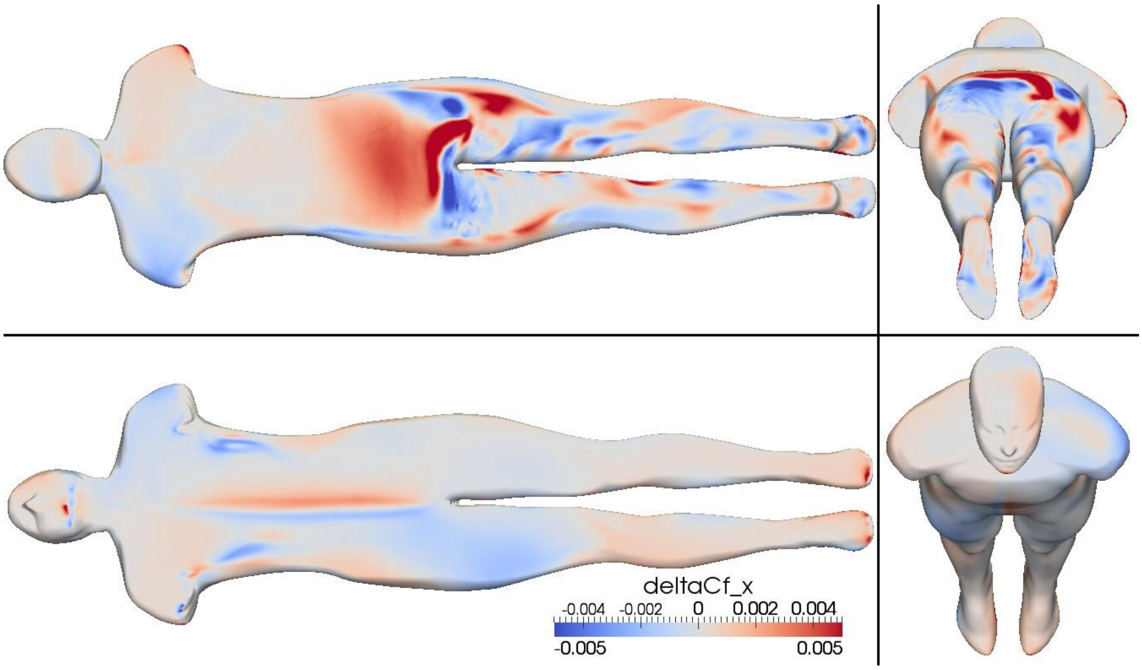

Figure 8-37 - Change in propelled skin friction coefficient (t/T_{stroke}=0.7) compared to the passive solution. A change in Cf_x of ±0.005 represents ±16% of the variation in Cf_x observed over the body in the passive simulation of C009.

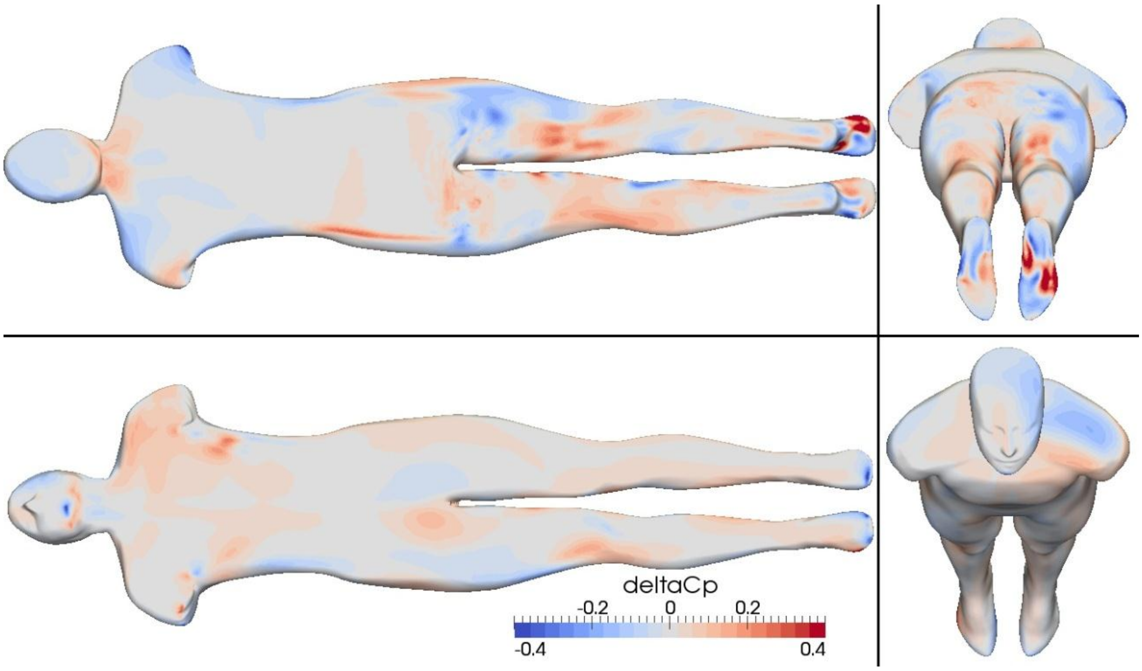

Figure 8-38 - Change in propelled pressure coefficient (t/T_{stroke}=0.7) compared to the passive solution. A change in *Cp* of ±0.4 represents ±24% of the total variation in pressure (*Cp_rgh)* observed over the body in the passive simulation of C009.

8.3.6 Summary and discussion

A summary of the key interactions identified between the arm and the body is provided in Table 8-1.

Table 8-1 – Summary of the observed interactions between the arm and the body within the propelled freestyle simulation for case C009

t/T_{stroke}	Phase of stroke	Forces on the body
0.3	Right arm has just started its outward sweep and the left arm has started its recovery above the water.	No change in forces compared to passive case.
0.4	Right arm is at the end of the outward sweep before moving back inwards towards the body.	No change in skin friction, but a gradual rise in the pressure resistance associated with free surface interaction from features propagated downstream from right arm entry. Change in side force
0.5	Right arm producing maximum thrust on in-sweep. Left arm has just entered the water	Large increase in pressure resistance on head and shoulders due to arm entry, followed by sudden decrease as the air cavity created by the arm entry collapses. Increase in skin friction on the right hip and back associated with free surface features from the right arm entry.
0.6	Right arm is driving backwards close to the side of the athlete. Left arm fairly stationary after entry.	A pressure differential observed on the surface of the swimmer due to the arm's close proximity. This creates a small variation in pressure resistance as the arm passes the body.
0.7	Right arm is about to exit the water close alongside the hips.	Region of accelerated flow from the right arm generates a pressure differential which retards the flow near the body. This is observed as a reduction in skin friction in this region

The impact of the freestyle arm model has been shown to cause a variation of approximately 24% in the total resistance acting on the athlete's body. However this variation has not caused a significant change in the average resistance over a stroke.

The most significant variation in the resistance is as a result of the free surface interactions originating from the arm entry phase of the stroke. The deformations in the free surface, created as the arm enters the water, cause significant pressure variations around the head and shoulders of the athlete.

These deformations propagate downstream, interacting with the free-surface features around the body, causing local changes to the hydrodynamic forces. This highlights the importance of the arm entry as it has the potential to affect the flow over the rest of the body. The magnitude of the arm entry's impact should be viewed with some caution, however, due to the potential error associated with the current arm model's accuracy in capturing the arm entry phase. This has been discussed in detail in chapter 7.4.6 and is due to several factors. Firstly, the arm's kinematics out of the water are unknown and therefore have been linearly interpolated. This means that the velocity of the arm as it enters the water is unknown. Secondly, there is likely to be some error in the vertical position of the arm model, due to it being determined by eye from video footage. This could also change the arm velocity as it enters the water. Thirdly, the impact of an object with the free-surface is a complex and highly non-linear problem which the steady lift and drag coefficients will not represent. Therefore it would seem likely that the free surface deformation caused by the arm entry is overestimated by the current method. This being said, visual observations of freestyle swimmers indicate that the arm entry can have a significant impact on the free surface. Several examples of this are provided in figure 8-39. Nevertheless, although the large air cavity observed in the simulation appears inaccurate, the significance of the arm entry on the free surface is very real. The fact that these free surface features are then propagated downstream over the body only increases the significance of the arm entry on the hydrodynamic forces.

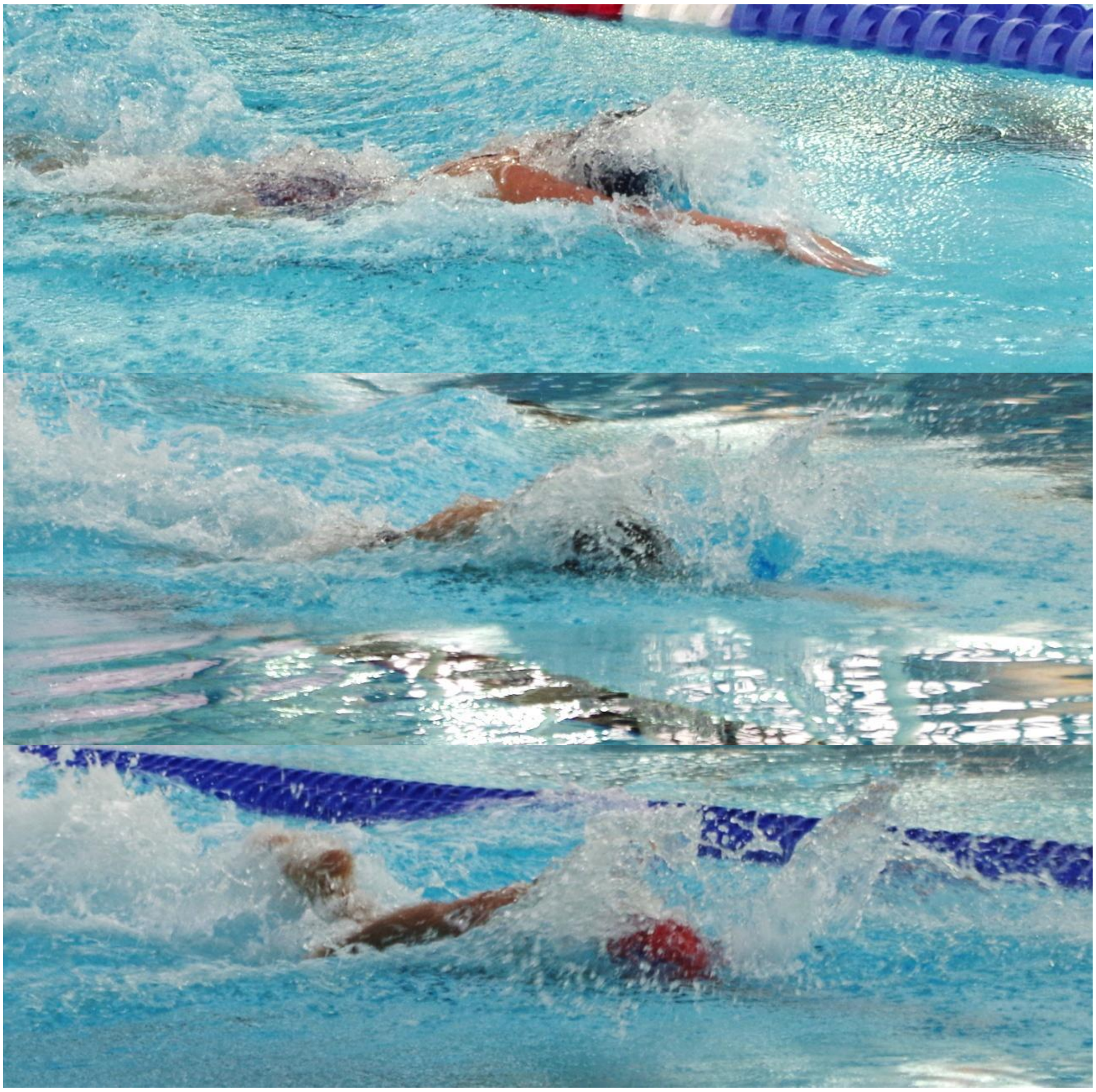

Figure 8-39 – Examples of arm entry free surface features.

If we ignore the free surface interactions associated with the arm entry the arm appears to have very little impact on the resistance. The accelerated flow created by the right arm is seen to generate a pressure differential on the body towards the end of the right arm's propulsive stroke. However, the variation in pressure resistance at this point in the stroke is less than 7% of the total resistance, and some of this can still be attributed to free surface interactions. Likewise, the impact of the arm on the skin friction at this stage of the stroke can be observed, but has almost no impact on the total resistance. Therefore for this experimental test case it would appear that the only significant impact the arms have on the hydrodynamic resistance is in the free surface interactions.

A key observation from comparing the experimental footage with the simulated geometry is the potential impact the body roll is likely to have on the resistance. The roll motion of the body will not only affect the dynamic free surface, but will also change the relative proximity of the arm to the body. This actually has the potential to increase the impact the arm has on the hydrodynamic forces; due to a greater surface area being exposed to the accelerated flow at the end of the arm pull. This relationship between arm proximity and the variation in resistance would be interesting to investigate more thoroughly in the future. This would help broaden the scope of these findings across different free style techniques. As for the impact of the roll motion itself, this was deliberately left out of this investigation so as to simplify the process and focus instead on the impact the arm has on the flow. However this would seem like the logical next stage of the analysis of active swimming resistance. The effect of just the roll motion could be investigated independently, which would provide useful insight into the breakdown of self-propelled forces. Due to the obvious relationship between the arm kinematics and roll motion, plus the interaction between roll induced and arm induced free surface features, a full assessment of the arm's impact on the fluid forces would benefit from including the roll motion of the geometry. Body roll could be included through the use of deforming meshes or a sliding cylindrical interphase. This would provide an active freestyle simulation environment that includes all the major unsteady features whilst still minimising the computational cost.

Given the dominance of the free surface features in producing variations in the hydrodynamic force, it should also be pointed out that ignoring the upper arms in these simulations will have minimised the arm's impact on the free surface. This is due to their close proximity to the surface of the water during much of the stroke. There is a strong argument for including these as separate body-force models in future research using this method.

Whilst there are many improvements that can be made to these propelled simulations, this work has generated a novel contribution and should not be understated. The impact a freestyle swimmer's arm has on the propelled resistance has been assessed for the first time. This has identified the importance that the arm entry has on the free surface flow features throughout the stroke. It has also identified that the observed variations in resistance have little impact on the mean propelled resistance. The impact of the arm's accelerated fluid on the resistance appears to be very small. It is likely that body motion throughout the stroke, including roll and heave motion, will have a greater impact on the self-propelled forces.

8.4 Experimental tow force comparison

The simulated tow force (the difference between resistance and thrust *R-T)* is presented in figure 8-40 for both simulated cases. The experimental tow force for the same period of kinematic data is also provided. The discrepancy between the simulations and the experimental data is quite extreme. The simulation with the lower thrust value of 33N (C009_SP_33N) does not provide the correct mean *R-T*. Therefore this case will be discounted. The other case with the increased thrust value of 66N does achieve the correct *R-T* value compared to the experimental data. However the variation in *R-T* is over twice that measured experimentally and becomes negative during each of the arm's main propulsive phases. One possible reason for this could be that the arm model is over predicting the peak thrust magnitude. However, the thrust peak seems plausible compared to the simulated thrust generated on just the hand (Sato & Hino, 2003) and the total thrust profile generated from the full freestyle simulation (Keys,M. et al., 2010). There is also a discrepancy in the timing of the propulsive phase, shown as a dip in the R-T curves.

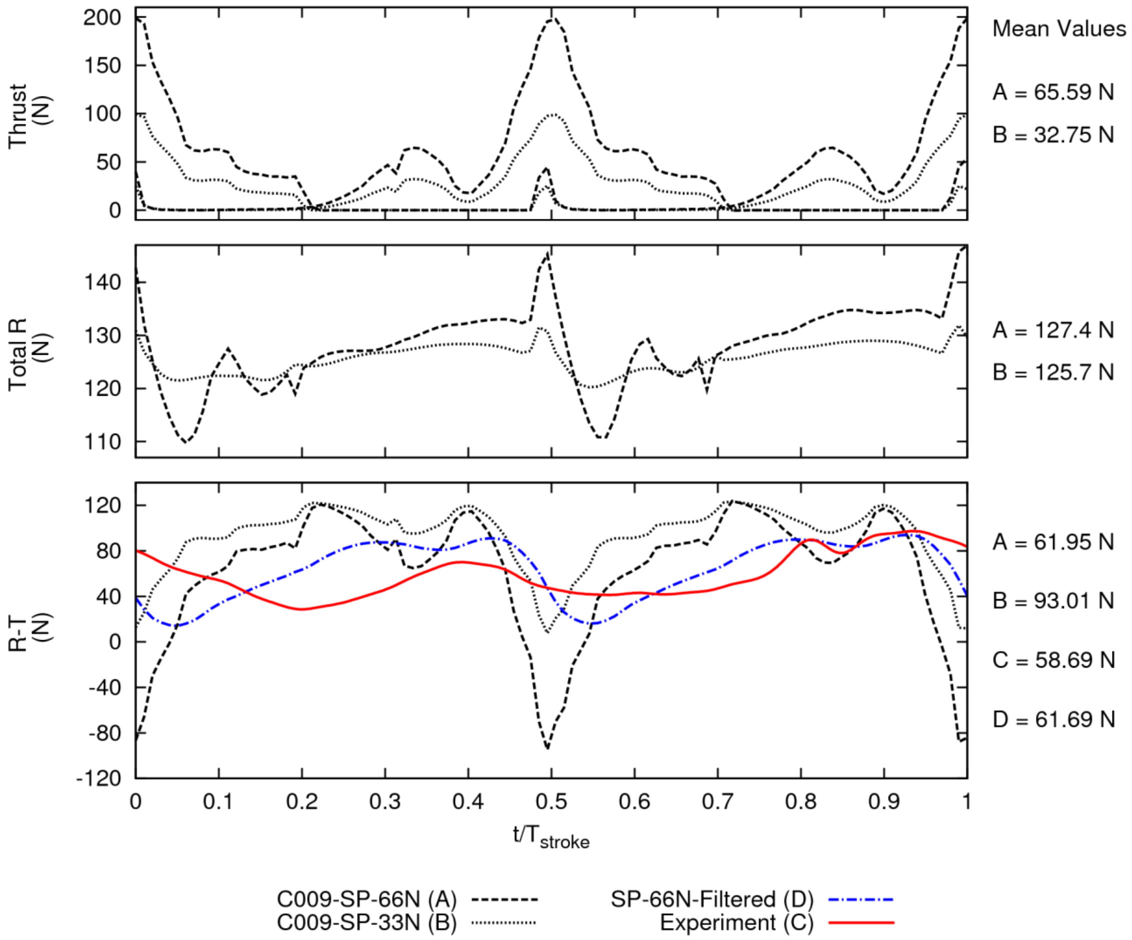

Figure 8-40 –Comparison of the simulated tow force compared to the experimental case for a single stroke. A heavily filtered version of C009_SP_66N is included to represent the potential effect of damping in the experiment.

Another hypothesis presented by (Webb, 2013) is that the experimental tow force is being smoothed before being measured at the tow system. This may be due to elastic properties in the flexible connection of the tow line to the swimmer implementing a time averaging process to the measured tow force. It is clear that the attachment of a towline to a swimmer via belt will not provide a rigid connection. There is also likely to be elastic properties associated with the towline, despite it being a high performance low stretch material. Ultimately these features could have the effect of delaying the transmission of force down the towline and smoothing out the peaks in the process. In an attempt to replicate this effect on the simulated tow force, the *R-T* data was run through a Butterworth low pas filter with a cut off frequency of 6Hz, designed to provide a similar magnitude of variation as the experimental data (see figure 8-40). This comparison is provided as a crude way of investigating the plausibility of this hypothesis. Obviously the magnitude of the filtered simulation data now matches the experimental trace. The filtered data also appears to be more in phase with the experimental data although significant differences still exist. This comparison does not confirm the hypothesis presented by (Webb, 2013) but does imply that it is a plausible explanation of the discrepancies. It should be highlighted that the proposed smoothing effect would not change the mean tow force measured.

8.5 Conclusions

A propelled simulation of a freestyle swimmer has been performed by combining a passive free surface RANS methodology with a body-force representation of the arms. This has allowed the impact of the arms on the propelled resistance of a swimmer to be quantified for the first time. The variation in the total resistance due to the arm motions was approximately 24% throughout a stroke cycle. However no significant change in the mean resistance was found.

The most significant variation in the resistance is as a result of the free surface interactions originating from the arm entry phase of the stroke. These variations are first identified as a large change in the pressure field as the arm enters the water. The resulting free surface deformations propagate downstream, interacting with the free-surface features around the body, causing local changes to the hydrodynamic forces. This highlights the importance of the arm entry as it has the potential to affect the flow over the rest of the body. The absolute magnitude of these variations should be viewed with caution, however, due to the potential error associated with the current arm model’s accuracy in capturing the arm entry phase. Nevertheless, comparison with visual observations of freestyle swimming confirms the significant impact the arms have on the free surface during arm entry.

Apart from the free surface interactions, the arm was found to have very little impact on the resistance. The pressure field associated with the arm was found to create small variations in pressure resistance, but these do not appear to have a significant effect on the mean resistance. The accelerated flow generated by the arm actually causes a slight reduction in skin friction on the surface of the body. This is due to a pressure differential in the fluid retarding the flow between the body and the accelerated region. This effect, however, is very small and does not really register in the total resistance.

It is therefore concluded that for the analysed arm technique the only significant impact the arms have on the active resistance of a freestyle swimmer is their effect on the free surface flow over the body. This would indicate that from the point of view of swim suit and equipment design, the local effects of the arm on the velocity field can be ignored.

The free surface interactions do not have a significant impact on the mean resistance of the freestyle swimmer. Therefore the effect of the arms is not required for assessing the resistance implications of equipment, body shape or body position in the water.

Based on these conclusions and visual observations it is recommended that the effects of body roll on freestyle resistance are investigated further in order to develop a better understanding of the roll induced free surface interactions and their effect on resistance.

The developed simulation methodology provides a computationally efficient approach to including the effects of the arms into a RANS simulation. The addition of the arm body force model increased the computational cost by between 8 and 28%, depending on the thrust magnitude. The majority of this additional cost is due to the increased velocities and complex free surface features rather than the actual implementation of the body force model.

9. Conclusions

The unsteady fluid flow around a freestyle swimmer has been investigated numerically through the use of a combined free surface RANS methodology, with the impact of the arms represented using a generic body force model. This provides a computationally efficient method for assessing the propelled resistance acting on a freestyle swimmer. The additional computational cost of including the impact of the arms is between 8-28 % depending of the magnitude of the induced velocities.

The variation in the total resistance due to the impact of the arms was approximately 24% throughout a stroke cycle. This variation was primarily due to the free surface interactions associated with the arm entering the water. This highlights the importance of the arm entry phase of the stroke, as it has the potential to affect the flow over the rest of the body.

The impact of the arm's propulsive stroke on the propelled resistance appears to be very small. A small variation in the pressure resistance (less than 7%) is observed as the arm passes close to the body, but this results in no observed net change in resistance. Even including the free surface interaction effects, the arms cause no significant change in the mean resistance. It is therefore concluded that for the simulated swimmer's technique, including the effect of the arms is not required in considering the resistance implications of equipment, body shape or body position in the water.

The free surface interactions were found to be very significant in both the passive and propelled simulations. Comparisons between surface and deeply submerged passive simulations of the same geometry found that the free surface could modify the entire flow field around the swimmer's body. This had the effect of changing the locations of flow separation, impacting on all the components of resistance. It is concluded, therefore, that the effect of the free surface must be taken into account when assessing the resistance implications of equipment, body shape or body position in the water.

9.1 Passive resistance of a freestyle swimmer (Objective 1)

An unsteady RANS methodology for free surface passive swimming simulations was developed. A geometry morphing process was used to match a basis athlete geometry to the body shape and position adopted by the athlete in the experimental test cases. This had key weakness associated with an inability to cope with complex joint rotations such as those of the shoulders.

A series of specific mesh development studies were conducted into the impact of boundary layer resolution and free surface mesh refinement. It was concluded that a fully resolved boundary layer mesh was required to capture the complex separation features that develop over the swimmer's body. A lack of wave propagation throughout the simulation domain was attributed to the large amplitude wave breaking features that occur around the swimmer's body. This appears to artificially dissipate the energy from the wave system and is identified as a weakness of the implemented volume of fluid methodology in the openFOAM solver InterFoam.

The final mesh structure developed from the specific investigations was subjected to a global mesh sensitivity study. Visual inspection of the variation in resistance components indicated that the simulations were converging on a grid independent solution.

This RANS methodology has been used to simulate the passive resistance components for two different experimental test cases of swimmer on the free surface. In both cases complex free surface features close to the swimmer have been well replicated. The discrepancies that were observed appear to be due to errors in the simulation geometry when compared to the experiment. In both cases the initiation of wave breaking was found to dissipate energy from the wave system, preventing it from propagating out over the simulation domain. This resulted in the simulated waves not being fully validated against experimental wave cuts, however acceptable comparisons were made with an inviscid thin-ship prediction.

The first simulated case (N003) not only captured the local free surface flow, but reproduced the total experimental resistance to within 1%. This total resistance was made up of 8.3% skin friction and 91.7% pressure (30% wave and 62% form drag). The second case (DA003) over-estimated the total resistance by 20%. However this is believed to be mainly due to the inaccuracies of the simulated geometry, causing a different free surface flow regime over the athlete's back. The total resistance was made up of 9.6% skin friction and 90.4% pressure (36% wave and 54% form drag). This case highlights the importance of using accurate geometries and the need to obtain athlete specific scan data with the correct body posture. Ultimately it should be accepted that this process will always provide some inaccuracies and therefore CFD validation data should, if possible, be acquired using a manufactured mannequin with controlled attitude and depth to ensure consistency.

These simulations provide the first presented resistance breakdown for a passive swimmer on the surface which include explicit measurements of the wave resistance.

For both experimental cases additional simulations were conducted with the same geometry at a depth of 1m. This allowed a comparison to the surface simulation to be made to assess the impact of the free surface on the different resistance components. In both cases the interaction of the free surface was found to change the boundary layer growth and points of separation on the swimmer's body entirely. In general the free surface maintained attached flow over the swimmer's back, suppressing separation. This emphasises the complex effect of the free surface on the flow around a swimmer, making it impossible to assess wave making resistance from the difference in total resistance between two different depths.

9.2 Body force model of a freestyle swimmer's arm (Objective 2)

A generic arm propulsion model has been created that uses experimental arm kinematics of a freestyle swimmer to generate the hydrodynamic forces acting on the arm. These propulsive forces are applied to the fluid domain using a body force model that varies in both time and space. The force magnitude of the propulsive model is tuned to the experimental forces measured during the test case C009. This approach has been shown to work effectively for simulating the unsteady forces generated by an unsteady rotating kayak blade. This methodology has also been implemented to perform self-propelled kayak simulations (see Appendix 2)

The basic underlying flow physics of a free style arm stroke is suitably well captured to enable the different propulsive phases of a free style arm stroke to be identified. This allows its impact on the hydrodynamic forces acting on a swimmer's body to be assessed in detail for the first time.

9.3 Propelled freestyle simulations (Objective 3)

A propelled simulation of a freestyle swimmer has been performed by combining a passive free surface RANS methodology with a body-force representation of the arms. This has allowed the impact of the arms on the propelled resistance of a swimmer to be quantified for the first time. The variation in the total resistance due to the arm motions was approximately 24% throughout a stroke cycle. However no significant change in the mean resistance was found.

The most significant variation in the resistance is as a result of the free surface interactions originating from the arm entry phase of the stroke. These variations are first identified as a large change in the pressure field as the arm enters the water. The resulting free surface deformations propagate downstream, interacting with the free-surface features around the body, causing local changes to the hydrodynamic forces. This highlights the importance of the arm entry as it has the potential to affect the flow over the rest of the body. The absolute magnitude of these variations should be viewed with caution however, due to the potential error associated with the current arm model's accuracy in capturing the arm entry phase. Nevertheless, comparison with visual observations of freestyle swimming confirms the significant impact the arms have on the free surface during arm entry.

Apart from the free surface interactions the arm was found to have very little impact on the resistance. The pressure field associated with the arm was found to create small variations in pressure resistance, but these do not appear to have a significant effect on the mean resistance. The accelerated flow generated by the arm actually creates flow in the opposite direction near the surface of the body, producing a slight reduction in skin friction. However this effect is very small and does not really register in the total resistance measured.

It is therefore concluded that for the analysed arm technique, the only significant impact the arms have on the active resistance of a freestyle swimmer, is their effect on the free surface flow over the body. This would indicate that from the point of view of swim suit and equipment design the local effects of the arm on the velocity field can be ignored.

The developed simulation methodology provides a computationally efficient approach to including the effects of the arms into a RANS simulation. The addition of the arm body force model increased the computational cost by between 8 and 28%, depending on the thrust magnitude. The majority of this additional cost is due to the increased velocities and complex free surface features rather than the actual implementation of the body force model.

9.4 Implications of this research

One key finding for the sport of swimming is the impact that free surface interactions can have on the resistance of a swimmer. Therefore any effort that can be made to minimise the swimmer’s disturbance of the free surface is likely to be beneficial to performance.

The same key finding has an implication for the evaluation of new sporting equipment in swimming. Assessments of potential changes in resistance need to take account of the effect of the free surface. However it appears the impact of the arms on the unsteady flow do not need to be included.

Another outcome of this research is to provide British Swimming and UKSport with a developed methodology for passive free surface simulations. This can now be used to answer questions they might have on body shape and attitude of athletes in the water, which can often be difficult to investigate experimentally.

The development of a generic moving body force model has been used to simulate the self-propelled flow around both a swimmer and a kayak, however there are potentially many more applications for this type of efficient representation of different propulsion mechanisms.

9.5 Recommendations for further work

Based on the conclusions of this work and the visual observation of freestyle swimming, the next unsteady feature that should be assessed is the impact of the body roll. This is likely to have a significant impact on the free surface flow around the body and therefore cause significant interaction within the resistance components. This could include the use of the developed body-force methodology in order to provide a more complete active simulation if required.

There are many improvements that could be made to the body-force arm model to improve its fidelity in estimating the thrust produced. These would include: more accurate arm kinematics; representing the arm as a series of body force models for the different arm sections and; adding unsteady effects into the force prediction. However, based on the current study the most relevant improvement that could be made would be regarding the representation of the arm's entry into the water. If a few of these key modifications were included the mathematical representation of the fluid forces on the arm could provide an efficient method for investigating different stroke techniques. This could be performed in isolation or within a self-propelled swimmer environment.

When considering improvements to the passive CFD methodology, a series of strictly controlled validation cases, including free surface data, would be of great benefit. Further investigation into the free surface implementation within the simulation would seem sensible. An analysis of the increased fidelity provided by fully unsteady LES or DES methodologies would help to inform the debate about the cost / benefits for such complex cases.

Appendices

Appendix 1 – Paper submitted to Gothenburg 2010: A workshop on Numerical Ship Hydrodynamics

RANS SIMULATIONS OF THE MULTIPHASE FLOW AROUND THE KCS HULLFORM

J Banks (University of Southampton, UK)
A B Phillips (University of Southampton, UK)
P W Bull (QinetiQ Ltd, UK)
S R Turnock (University of Southampton, UK)

1. SUMMARY

A commercial RANS code is used to investigate the multiphase flow field surrounding the KCS hull form. Results are presented for the associated wave pattern (case 2.1), dynamic sinkage and trim (case 2.2b) and self propulsion parameters for the hull using a body force propeller model (case 2.3a). Simulated results showed good correlation with experimental wave pattern and sinkage and trim data. However greater accuracy in the simulated nominal wake is required to accurately match experimental self propulsion data.

2. INTRODUCTION

Traditionally the resistance of ships has been determined using towing tank experiments. Over the past two decades increased computational power has allowed numerical approaches to replicate and potentially start to replace towing tank experiments. This work investigates the quality of results that can be achieved using a commercial Reynolds Averaged Navier Stokes (RANS) flow solver, ANSYS CFX Version 12 (ANSYS, 2009). This work is a contribution to the Gothenburg 2010 workshop on CFD in ship hydrodynamics and compares the results from CFD based methods with model tests performed by participating towing tanks on the KRISO Container Ship (KCS).

3. THEORETICAL APPROACH

A finite volume method, using a Volume of Fluid (VOF) approach was used. This method is derived from the surface integration of the conservative form of Navier Stokes' equations over a control volume. Equations (1) and (2) are the incompressible Reynolds averaged Navier-Stokes (RANS) equations in tensor form and Equation (3) is the volume fraction transport equation (Peric and Ferziger, 2002).

$$\frac{\partial(\rho U_i)}{\partial t}+\frac{\partial(\rho U_i U_j)}{\partial x_j}=-\frac{\partial P}{\partial x_i}+\frac{\partial}{\partial x_j}\left[\mu\left(\frac{\partial U_i}{\partial x_j}+\frac{\partial U_j}{\partial x_j}\right)\right]-\frac{\partial}{\partial x_j}\left(\rho\overline{u'_i u'_j}\right)+f_i \quad (1)$$

$$\frac{\partial U_i}{\partial x_i}=0 \quad (2) \qquad \frac{\partial c}{\partial t}+\frac{\partial(cU_j)}{\partial x_j}=0 \quad (3)$$

The volume fraction c is defined as (V_{air}/V_{total}) and the fluid density, ρ, and viscosity, μ, are calculated as $\rho=\rho_{air}c+\rho_{water}(1-c)$ and $\mu=\mu_{air}c+\mu_{water}(1-c)$. External forces applied to the fluid are represented as f_i, which include buoyancy forces and momentum sources representing the influence of a propeller. The effect of turbulence is represented in (2) by the Reynolds stress tensor $\rho\overline{u'_i u'_j}$ and is modelled using a turbulence model.

3.1 Turbulence modelling

Both a Shear Stress Transport (SST) eddy viscosity model and a Baseline (BSL) Reynolds stress model (ANSYS, 2009) were used to evaluate the Reynolds stress tensor.

Case	Description	Turbulence model
2.1	Wave pattern	SST & BSL
2.2b	Sinkage and trim	SST
2.3a	Self propelled	SST

The SST model blends a variant of the k-ω model in the inner boundary layer and a transformed version of the k-ε model in the outer boundary layer and the free stream (Menter, 1994). This has been shown to be better at replicating the flow around the stern of a ship, than simpler models such as k-ε, single and zero equation models (Larsson *et al*, 2000, Hino, 2005). The BSL Reynolds stress model includes transport equations for each component of the Reynolds stress tensor. This allows anisotropic turbulence effects to be modelled helping to model complex flow features such as separation off curved surfaces (Peric and Ferziger, 2002). The BSL model is blend of a Reynolds stress-ω model for the inner boundary layer and ε based in the outer and free stream (Bull, 2005).

3.2 Sinkage and Trim

To capture the sinkage and trim experienced by a vessel travelling at a forward speed, the surface mesh representing the hull was displaced based on the total heave force and pitching moment acting on the vessel and the vessels water plane area and moment to change trim. This was achieved using CFXs in built "mesh morphing" model which is used to calculate the new node locations throughout the fluid domain at each time step, while maintaining mesh topology. The resulting vessel orientation has no net heave force or pitching moment.

3.3 Propeller models

To reduce the computational cost associated with self propulsion simulations a body force propeller model was used. This represents the impact of the propeller on the fluid as a series of axial and tangential momentum source terms, fb_x and fb_θ respectively. These are calculated using the Hough and Ordway Thrust and Torque distribution (Hough, 1965), as was implemented by (Stern *et* al, 1988). A detailed description of the methodology adopted here is presented in (Phillips et al, 2009, Phillips *et al*, 2010).

The momentum source terms were calculated based on the propeller rps (n), the open water propeller characteristics and the inflow velocity field providing the mean wake fraction $\bar{w}_t$, which is assumed to be equal to the Taylor wake fraction w_t.

Initially no momentum sources were applied, by setting n=0, providing the initial flow field entering the propeller domain. Once the convergence criteria were met the velocity components entering the propeller disk are sampled providing the wake fraction. This is then used along with an initial estimate of n=9 to calculate the thrust and torque generated by the propeller, which are represented by axial and tangential momentum source terms. The rps is then iteratively varied using a Secant method (each time convergence is achieved) until;

$$|\text{Thrust} - \text{Drag} + \text{SFC}| < 1 \text{ N} .$$

4. NUMERICAL MODEL

Table 1 Numerical simulation properties.

Property	**SOTON**	**QINETIQ**
Half mesh No. of elements	~ 10M	~9M
y+ on the hull	~ 1 (max value 1.2)	< 10
Domain Physics	Homogeneous Water/Air multiphase, SST or BSL turbulence model, Automatic wall function, Buoyancy model –density difference, Standard free surface model	
Boundary physics:		
Inlet	Defined volume fraction and flow speed	
	Turb. Intensity= 0.05	Zero gradient
Outlet	Opening with entrainment with relative pressure = hydrostatic pressure	
Bottom/side wall	Wall with free slip condition	Outlets with hydrostatic pressure
Top	Opening with entrainment with relative pressure 0 Pa	
Hull	Wall with no slip condition	
Symmetry plane	Along centreline of the hull	
Solver settings:		
Advection scheme	High Resolution (ANSYS, 2009)	
Timescale control	Physical timescale function: 0.01[s] + 0.09[s]*step(atstep-20)+ 0.1[s]*step(atstep-200)	$0.03\left(\frac{L_{pp}}{Fn\sqrt{gL_{pp}}}\right)$
Convergence criteria	Residuary type: RMS	
	Target: 1e-5	Target: 1e-6
Multiphase control	Volume fraction coupling	
Processing Parameters:		
Computing System	Iridis 3 Linux Cluster (University of Southampton)	Linux cluster (QinetiQ Haslar)
Run type	Parallel (24 Partitions run on 3x8 core nodes each with 23 Gb RAM)	Parallel(up to 64 Partitions run on 8x8 core nodes each with 8 Gb RAM)

Simulations are performed using ANSYS CFX V12 (ANSYS, 2009). This is a commercial finite volume code, which uses collocated (nonstaggered) grids for all transport equations, coupling pressure and velocity using an interpolation scheme. The physical parameters and solver settings used to define the numerical solution are provided in Table 1, along with details of the computing resources used for the largest mesh.

5. MESHING TECHNIQUE

Wave Pattern (Case 2.1) - Southampton

A structured mesh was built using ANSYS ICEM around the full scale KCS hull geometry. The domain width and depth matched the dimensions of one half of the KRISO towing tank. The length was selected to allow one ship length in front of the hull and two behind. This was then converted to model scale dimensions each time a mesh was generated.

A blocking structure was developed that allowed a good quality surface mesh to be created over the hull (see Figure 1). It was found that collapsing the blocks under the stern down to a point provided the best overall mesh structure in this region. This approach allowed extra mesh density to be added in this localised area where large surface curvatures needed to be captured. Elements were also clustered within the region of the free surface to allow a sharp interface to be captured.

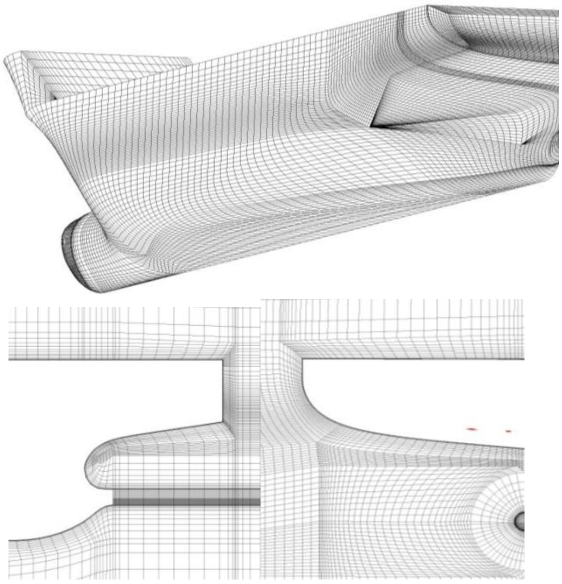

Fig. 1 SOTON: Hull surface mesh structure (top), O-grid structure at stern from the side (left) and from the stern (right), for the initial mesh containing 0.8M elements.

Once satisfied with the surface mesh structure an O-grid blocking structure was grown out from the surface of the hull. The depth of the inner O-grid was matched to approximately that of the maximum expected boundary layer. Another outer O-grid was then created so as to provide a smooth transition between the near wall radial mesh and the far field Cartesian structure. Another key feature is the continuation of the O-grids about the propeller axis, towards the outlet of the domain. The outer O-grid was expanded to match the propeller diameter allowing a propeller model to be easily added later. Two splits were also placed within the outer domain blocking structure, one behind the hull and one offset from the hull centreline. This allowed the regions of high mesh density to be forced onto the free surface both on the hull surface and in the outer domain.

A half body mesh of 10M elements was produced with two $\sqrt{2}$ global mesh reductions, providing 4M and 1.5M element meshes, each with a y^+ of 1 over the hull. More details of this process can be found in (Banks et al, 2010).

5,2 Wave Pattern (Case 2.1) QinetiQ

In a similar manner, a structured mesh was built using ANSYS ICEM around the full scale KCS hull geometry. The domain length, width and depth were chosen based on the ship length with one ship length in front of the hull and two behind. The top and bottom of the domain were defined as one ship length below and a half ship length above the keel line, whilst the width was 1.3 ship lengths (see Fig 2).

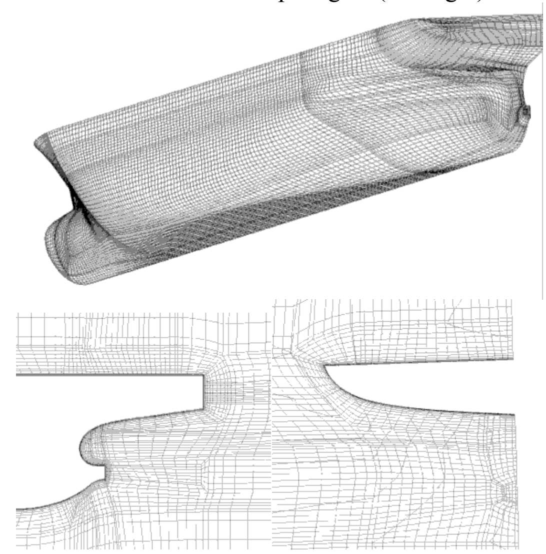

Fig 2 QINETIQ: Hull surface mesh structure (top), O-grid structure at stern from the side (left) and from the stern (right), for the coarsest mesh containing 1M elements.

The topological structure of the O-grids on the hull was defined to give a near uniform, quadrilateral surface grid on the hull surface for the baseline grids but with some control within the free-surface region. A small O-grid was also placed downstream of the propulsor hub which extended to just aft of the transom. The first cell height for the O-grid around the hull was chosen to give $y^+ < 10$ for the model scale flow Reynolds number.

Two sequences of grids were generated based on grid topologies with 4M and 5M cells. Finer and coarser grids were produced using global element refinement factors of 1.25 and 0.8 respectively to give a series of grids with 1M, 2M, 2.5M, 4M, 5M, 6.8M and 9M computation cells. Each of the grid spacings perpendicular to the outer boundaries of the domain were adjusted for the coarsest grids to provide smooth expansion rates.

5.3 Sinkage and Trim (Case 2.2b) – QinetiQ

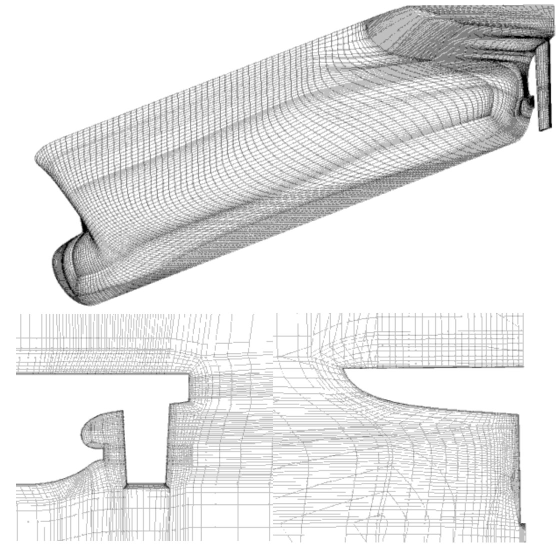

Fig 3. QINETIQ: Hull with rudder surface mesh structure (top), O-grid structure at stern from the side (left) and from the stern (right), for the coarse mesh containing 1M elements.

The rudder was included in the geometry definition for the ANSYS ICEM mesh generation process. Additional vertical splits were created in the overall topology for the 4M cell baseline grid which corresponded to the leading and trailing edge of the rudder and additional O-grid topologies were placed around the rudder. Additional grid points were required in the overall topology to resolve the rudder geometry, and its boundary layer, increasing the baseline grid from 4M cells to 5M cells.

Finer and coarser grids were produced using global element refinement factors of 1.25 and 0.8 respectively to give a series of grids with 680K, 1M, 1.7M, 3M, 5M and 9M computation cells.

5.4 Self propelled (Case 2.3a)

To incorporate a propeller model a separate cylindrical mesh was inserted into the Southampton mesh in the position of the propeller. The mesh density in the outer O-grid was increased to provide a higher mesh resolution entering and leaving the propeller domain. Due to the intrinsic asymmetry in self propelled simulations the entire domain had to be modelled by mirroring the half body mesh. As this doubles the total mesh density a further $\sqrt{2}$ mesh reduction was conducted to minimize computing requirements. This resulted in three half body meshes of 0.75M, 1.7M and 4.5M elements.

6. MESH SENSITIVITY STUDY

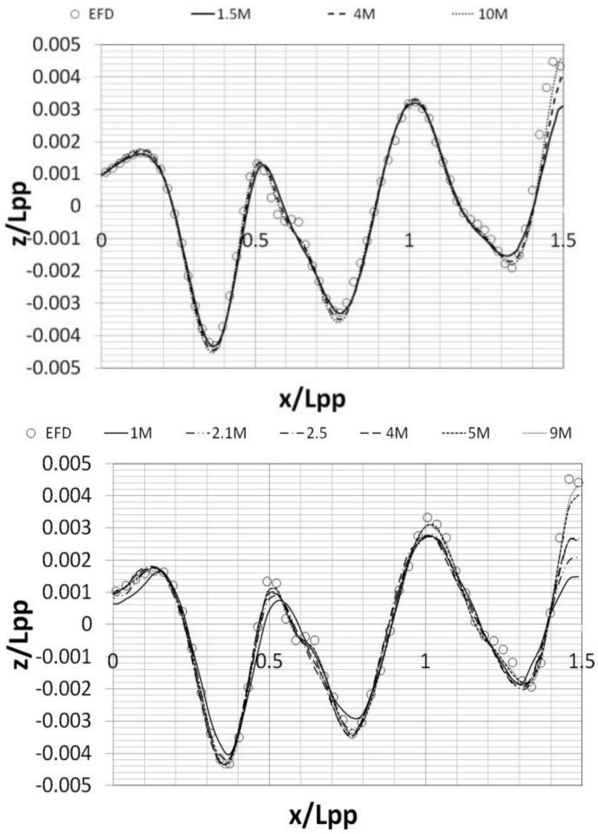

Fig 4 Comparison between experimental (EFD) and CFD wave elevation at a distance of y/Lpp=0.15 from the ship centreline at Fn=0.26. Southampton results (top), QinetiQ results (bottom). The Forward perpendicular is positioned at x/Lpp=0.

To observe the impact of mesh density on the different mesh structures (Southampton Vs QinetiQ) a wave cut profile, using the BSL turbulence model, was compared with EFD data for each of the different mesh densities (Fig 4). It can be seen that both of the mesh structures display significant sensitivity to mesh density astern of the hull, particularly at the next wave peak (x/Lpp = 1.5). However, over the rest of the observed wave cut we see good convergence between the highest mesh densities as well as with EFD data.

7. COMPARISON OF BSL WAVE PATTERN DATA (CASE 2.1)

To assess the influence of different meshes and numerical models a comparison of the wave pattern data obtained using the BSL Reynolds stress turbulence model from case 2.1 was made. In Fig 5 (located at the end) it can be seen that in both cases the global wave pattern shows good correlation to the EFD surface plot. Some variation is observed in the size of the stern wave leaving the transom and magnitude of the stern wave pattern further down stream of the hull. These can be directly compared in the wave cut profile.

In Fig 6 (located at the end) we can see that in both cases the free surface along the hull appears irregular with the Southampton results showing large gapes and drops in the free surface caused by air pockets on the hull surface near the bow and stern. This ventilation problem was also observed by QinetiQ whilst using a y^+ of 1 but was improved by increasing it to 5-10. It can be seen that this resulted in a more continuous free surface along the hull but with increased smaller undulations along its length.

The components of resistance obtained by both the Southampton and QinetiQ simulations for case 2.1 are also compared to the experimental data provided in (Kim *et al*, 2001) in 0. The static wetted surface area used in the calculation of force components was 9.5121 m^2. It can be seen that both turbulence models used by QinetiQ provided total resistances that agree closely with the experimental data, with the BSL model providing a slightly better match with the frictional and pressure components. The Southampton results, however, appear to over estimate all components of resistance, despite significant improvement being made to the pressure component using the BSL turbulence model. One of the factors contributing to this could be the increased air resistance due to the Southampton mesh containing the full topside geometry of the hull, see Fig 1 and Fig 2. Although air resistance is normally assumed small enough to neglect, it appears to be making up 2 – 5% of the total resistance and therefore potentially needs to be accurately modelled so as to match the experimental procedure. This topic is discussed in more detail in (Banks et al, 2010), where aerodynamic and hydrodynamic components of drag are presented. It should be noted that the ventilation problems seen in Fig 6 caused some of the hydrodynamic drag to be misrepresented as aerodynamic drag for the 10M element BSL case.

Table 2 Comparison of Resistance Components.

Mesh	Turbulence model	CT (x10^3)	CF (x10^3)	CP (x10^3)
Soton	SST	3.96	3.04	0.92
Soton	BSL	3.79	3.01	0.78
QinetiQ	SST	3.61	2.95	0.67
QinetiQ	BSL	3.60	2.87	0.73
Experimental		3.56		
Calculated from ITTC Procedure			2.83	0.73

8. SINKAGE AND TRIM - CASE 2.2B

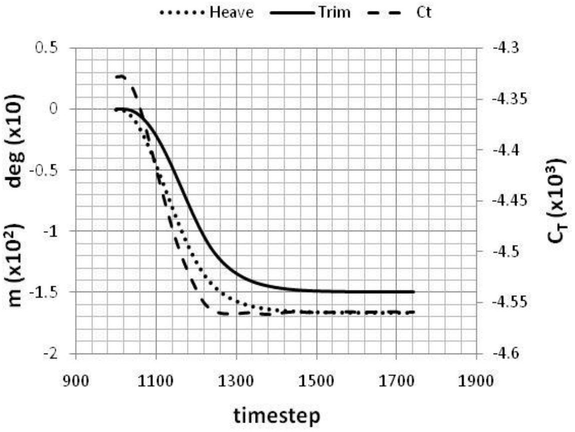

Fig 7 Example time history of a sinkage and trim simulation for Fn = 0.2816 using the finest mesh (9M).

In each simulation the hull geometry was fixed in position for the first 1000 timesteps to allow the fluid forces and moments to converge. From this point the hull is free to heave and trim for another 1000 timesteps or until convergence is reached. An example time history of this process is given in Fig 7, whereas the close correlation with the EFD data over the Froude number range can be seen in Fig 8.

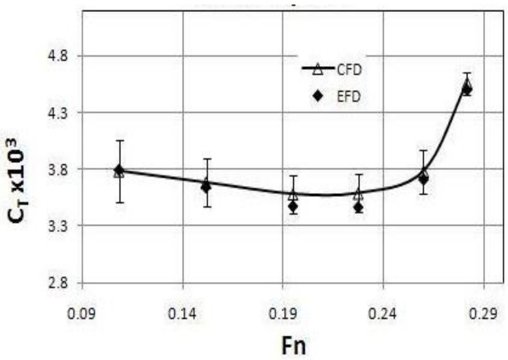

Fig 8 Comparison of EFD and CFD variation of total resistance with Froude number, with numerical uncertainty error bars.

8.1 Uncertainty analysis

The procedure adopted is presented in (Eca &Hoeksra, 2008). The experimental values for each mesh density were determined as the mean value over the last 200 iterations, with the standard deviation providing the iterative uncertainty U_I. The least squares fit to the data was conducted using the software environment Matlab, assuming a grid ratio of 1.2.

9. SELF PROPELED – CASE 2.3A

Table 3 Resistance propeller parameters for self propulsion at ship point.

Parameters	EFD	Coarse	Medium	Fine
		(1.5M)	(3.4M)	(9M)
$CT\times10^3$	4.162	4.344	4.321	4.287
$CF\times10^3$		2.903	2.959	2.988
$CP\times10^3$		1.441	1.362	1.300
K_T	0.170	0.200	0.199	0.202
K_Q	0.0288	0.034	0.033	0.034
w_T	0.208	0.281	0.279	0.296
n (rps) (for given SFC*)*	9.5	9.463	9.464	9.358

The results presented in table 3 show noticeable discrepancies between the numerical and experimental results. The reason for this is two fold. The wake into the propeller plane has not been accurately captured, (see w_T values in table 3) this has reduced the propeller advance coefficient value and thus increased the K_T and K_Q predicted from the open water curves. However, since the drag is also over predicted the required thrust is increased which causes the predicted rps to be nearly correct. However, while the results presented are less than ideal the methodology appears to work and provides a simple method of replicating the propeller forces and calculating the self propulsion parameters. However, further effort is required to ensure that the vessel drag and wake fraction are correctly predicted.

Fig 9 illustrates the velocity components downstream of the propeller. Variation in the axial component can be attributed to not replicating the hub geometry and the over prediction of thrust. The asymmetry is not captured due to the non-uniform inflow into the propeller plane not being included in the body force model.

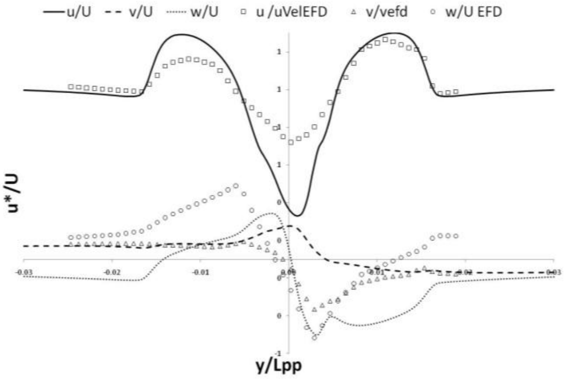

Fig 9 Velocity components down stream of propeller (x/Lpp=0.911, z/Lpp = -0.03)

10. DISSCUSION

10.1 Differences in Mesh structure

The main difference appears to be the surface mesh structure created on the hull. To accommodate the complex geometry of the KCS stern sections the QinetiQ mesh uses multiple O-grids to create a complex mesh structure localised to the hull surface. This leaves a relatively simple mesh structure in the outer domain. In contrast, the surface structure created in the SOTON mesh is maintained throughout the rest of the domain.

Apart from comparing the fundamental mesh structure it is important to assess how the elements are distributed in the two different meshes. Tabel 4 provides details of how the elements are distributed over different regions in the mesh. It should be noted that although both meshes leave 1xLpp ahead and 2xLpp astern of the hull the width and depth of the domains vary leading to different volumes.

An immediate observation is that the QinetiQ mesh places more cells ahead and along the waterline of the hull. Whereas the Southampton mesh, despite having a smaller free surface area, places more cells here, especially astern of the hull. Another important observation is the increase in hull surface and waterline nodes in case 2.2b due to the addition of the rudder.

Table 4 Comparison of mesh distribution.

Number of grid nodes in location:	Case 2.1		Case 2.2b
	Soton	QinetiQ	QinetiQ
Total in half hull domain	10312611	8791499	9251577
In hull O-grid	1694265	1354698	1354698
On static Free Surface	71504	66710	56056
Distribution ahead of hull	40	62	62
Distribution behind hull	101	67	67
Distribution to side of hull	80	76	76
Hull surface	64237	52827	77313
Along Static Waterline	366	396	434
Along hull midgirth (BWL)	97	74	118
Along hull midgirth (AWL)	40	26	27

10.2 Turbulence modelling

Both groups found that the BSL Reynolds stress model provided noticeably superior results for both the free surface deformation and components of resistance for case 2.1. Ideally this would also have been used in both cases 2.2b and 2.3a, however, reduced numerical stability made this impractical.

11. CONCLUSION

Numerical simulations of the KCS hull form are presented as part of the work jointly submitted by the University of Southampton and QinetiQ Ltd to the Gothenburg 2010 workshop. Despite the differences in meshing technique and numerical setup the wave pattern data obtained shows good correlation to each other and the experimental data. Simple and effective methods for modelling both the dynamic sinkage and trim, and the propeller behind a ship, have been implemented. However a greater level of detail is needed in the propeller inflow to achieve accurate self propelled results.

Both parties experienced problems with air ventilation on the wetted surface of the hull. It was found that this could be significantly reduced by increasing the y^+ from 1 to 5-10.

Another interesting finding was that when the entire topside hull geometry was modelled the air drag equated to 2-5% of the total hull drag, raising into question the common assumption that the air phase can be neglected in CFD simulations. Additional information about the experimental procedure regarding the air drag and the above water structure would enable validation of this component.

REFERENCES

ANSYS. (2009) ANSYS CFX, Release 12.0. ANSYS.

Banks, J., Phillips, A. B., Turnock, S. R., (2010) Free-surface CFD Prediction of Components of Ship Resistance for KCS, 13th Numerical Towing Tank Symposium, Duisburg, Germany.

Bull, P.W., (2005) Verification and Validation of KVLCC2M Tanker Flow, CFD Workshop Tokyo 2005.

Eca, L., Hoekstra, M., (2008) Testing Uncertainty Estimation and Validation Procedures in the Flow Around a Backward Facing Step, 3rd Workshop on CFD Uncertainty Analysis, Lisbon.

Hino T. (2005) CFD Workshop Tokyo 2005. In: The Proceedings of CFD Workshop Tokyo.

Hough, G..R., Ordway, D.E., The generalised actuator disc, Developments in Theoretical and Applied Mechanics, Vol 2, pp 317–336.

Kim, W.J., Van, D.H. and Kim, D.H., (2001) Measurement of flows around modern commercial ship models, Exp. in Fluids, Vol. 31, pp 567-578

Larsson L, Stern F, Bertram V. (2003) Benchmarking of Computational Fluid Dynamics for Ship Flows: The Gothenburg 2000 Workshop. Journal of Ship Research 2003, Vol47, pp 63–81.

Menter, F.R., (1994) Two-equation eddy-viscosity turbulence models for engineering applications. AIAA Journal, Vol 32, pp 1598 –605.

Peric, M., Ferziger, J.H., (2002) Computational Methods for Fluid Dynamics, Springer, 3rd edition.

Phillips, A.B., Turnock, S.R. and Furlong, M.E. (2009) Evaluation of manoeuvring coefficients of a self-propelled ship using a blade element momentum propeller model coupled to a Reynolds averaged Navier Stokes flow solver. Ocean Engineering, Vol 36, Issues 15-16, pp1217-1225.

Phillips, A.B., Turnock, S.R. and Furlong, M.E. (2010) Accurate capture of rudder-propeller interaction using a coupled blade element momentum-RANS approach. *Ship Technology Research (Schiffstechnik)*, Vol 57, pp 128-139.

Stern, F., Kim, H.T., Patel, N.M., Chen, H.C., (1988) A Viscous-Flow Approach to the Computation of Propeller-Hull Interaction. Journal of Ship Research , Vol 32, pp 246–262.

(Please see Figures 5 and 6 over the page)

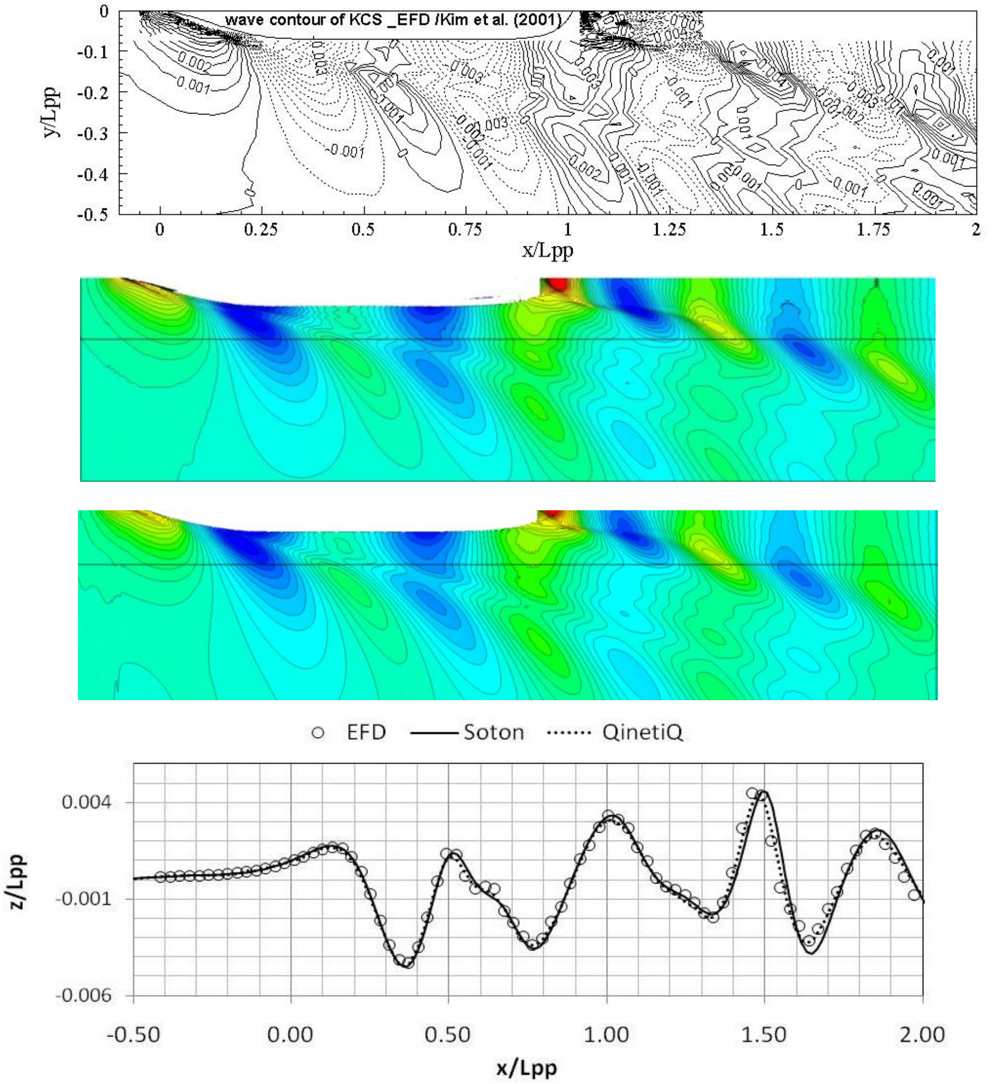

Fig 5 Free surface elevation, z/Lpp, of global wave pattern, at Fn=0.26, for (Top Down) Experimental data, SOTON CFD results and QinetiQ CFD results. Contours range from z/Lpp = -0.005 to 0.010 in steps of 0.0005. The straight lines represent the positions of the wave cut at y/Lpp= 0.15 which are plotted against EFD data for both meshes (Bottom).

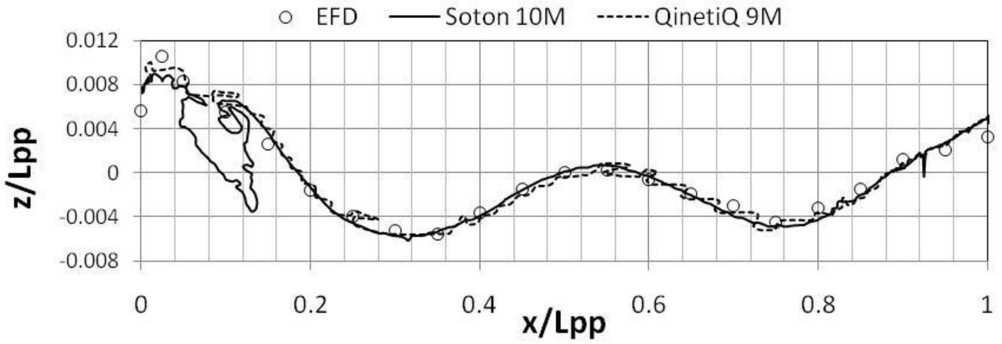

Fig 6 Comparison of free surface elevation along the surface of the hull plotted agaings EFD data at Fn=0.26

Appendix 2 - Required mesh density for simulating a hand

To enable an estimate of the y^+ on both the hand and the swimmers body to be made, the friction velocity, defined as

$$u_\tau = \sqrt{\frac{\tau_w}{\rho}} \quad 9\text{-}1,$$

with w_τ as the wall shear stress, needed to be calculated. This was done by calculating the coefficient of frictional resistance (C_F) for each based on their Reynolds numbers, using the ITTC skin friction correlation line (ITTC, 2007). The length and velocity used for each were taken from swimmer B in (Sato and Hino, 2003). The wall shear stress could then be determined as

$$\tau_w = C_F \frac{1}{2} \rho U^2 \quad 9\text{-}2.$$

The calculated values are provided in Table 9-1. It can be seen that the friction velocity on the hand is approximately twice that of the body.

Table 9-1 calculated values for determining the friction velocity for hand and body

	Body	Hand
Length	1.8 m	0.1 m
Expected fluid velocity	1.75 ms^{-1}	2.5 ms^{-1}
Reynolds number	3.15×10^6	0.25×10^6
Coefficient of Frictional resistance (C_F)	3.706×10^{-3}	6.496×10^{-3}
Wall shear stress w_τ	5.675 Nm^{-2}	20.29 Nm^{-2}
Frictional velocity u_*	0.0753	0.1424

Appendix 3 – AdaptFlexi Joint Manipulation

Initial scripting of the joint manipulation process and the writing of this summary report was conducted by a UK Sport intern student Mike Ellis.

Abstract

A summary of how the scriptwriter.m, multibend1.txt, and joint.txt files can be used with AdaptFlexi to manipulate the geometry of a person in an .stl file is presented. The limitations of the code are explained.

Input file

The input file, joint.txt, contains information about each joint. The only column the user needs to change is the one labelled angle. This is the rotation required of each joint in degrees. It should not be necessary to change the other columns. The file is read in by number of bytes so the current format should be preserved. Columns 2 to 10 control the position and axis of the joints and which end of the joint is held in place and which is rotated. The last 3 columns control the range over which the .stl file is distorted by Adaptlexi at each joint.

The rotations are all done about the y-axis, taking anticlockwise as positive.

At the bottom of the file is a list of limits which the joints should not be rotated beyond. These limits are illustrated in figures 1-8. The limits prevent the .stl turning inside out, or ensure the body maintains a realistic shape.

The middle section of the file contains inputs for scaling the body to height and weight which is not yet functional as the AdaptFlexi functions for this do not work. The 3rd line of this section contains an angle in degrees to rotate the entire body by, to enable an angle of attack to be applied. Currently this is converted from degrees to radians by Matlab because this is the only input required to be in radians for AdaptFlexi.

Entering a new joint

The quickest way to create a script for a new joint will be to copy one of the other joint files. Below is the script for the ankle.

```
0 0 -1 10 1 !
1 1 -1 10 0 !
2 0 -1 10 11 !

3 1 -1 10 13 ! Choose CODE DEVELOPMENT menu option
4 1 0 40
C:\panel\mike\swimmer_for_joe\unitswim2_MOD_MOD_MOD.stl
5 1 -1 10 9 ! Choose STL transform option
6 1 0 50 0 ! ###CHANGE JOINT POSITION###
7 1 1 30 00.385 00.000 -0.011!  Enter new value
8 1 2 50 0 ! ###CHANGE JOINT AXIS###
9 1 3 30 00.000 01.000 00.000 !  Enter new value
10 1 4 50 0 ! ###CHANGE GENERATOR###
11 1 5 30 01.000 00.000 00.000 !  Enter new value
12 1 6 50 1 !  ###CHANGE ANGLE OF ROTATION###
13 1 7 20 027.0 !  Enter new value :
14 1 8 50 1 !  Current  ###CHANGE MINIMUM ANGLE###
15 1 9 20 -110.00 !  Enter new value :
16 1 10 50 1 !  Current  ###CHANGE MAXIMUM ANGLE###
17 1 11 20 135.00 !  Enter new value :
18 1 12 50 1 !  ###CHANGE STRETCH/SQUASH REGION###
19 1 13 20 0090.0  Enter new value :

20 1 -1 10 0 !
21 0 -1 10 0 !
22 0 0 50 1 !
```

Line 7 contains the Cartesian coordinates of the joint. Line 11 controls the direction of the generator, this determines which end of the body rotates and which is fixed. The angle of rotation is determined by line 13. The maximum and minimum angles in lines 17 and 15 respectively control where the stl is morphed from. The angle is measured from the generator. The stetch/squash region in line 19 determines how much of the stl from the maximum and minimum back towards the generator is morphed. This

A new joint has to be entered into the script in the correct place. If it is put in before a joint which is closer to the extremities of the body than itself the centre of rotation for the second joint will be in the wrong place.

Matlab script

The Matlab script opens the adapt_flexi, joint, and multibend1 text files. It then updates the adapt_flexi.txt file to cause AdaptFlexi to read from a script, the location and name of this script need to be specified on the 3rd and 4th lines of this file.

Matlab reads data from joint.txt and prints it to multibend1.txt so this can be read by AdaptFlexi. The position to read and write text from and to are specified by a number of bytes from the start of the file for this reason the format of joint.txt and multibend1.txt must be preserved.

AdaptFlexi Script

This script is in multibend1.txt and is separated into sections for each joint rotation. The order of the rotations is set so that the joints nearer the extremities are rotated first, to maintain the position of the position of the other joints. The neck is rotated first, then the hips, followed by the ankles and finally the knees. The final section rotates the entire .stl file as a rigid body. Each rotation creates a new .stl file which is opened by the subsequent section of code. These files are distinguished by the addition of "_MOD" to the name.

Currently the .stl file which is modified is called unitswim.stl. This name can be changed in each section of the script. The correct number of "_MOD" suffixes should already be in place.

Problems have been experienced with running script all in one go, however if each section is copied into another file, with the first four and last three lines copied in as they are, and the lines numbered correctly the script can be run in sections without any problems. The necessary files for this operation are the neck, back, hip, ankle, knee and rigbod text files. They should be run in the order they are listed above.

Output

Each rotation creates a new .stl file with the same name as the previous one but with "_MOD" as a suffix on the filename. The file with the largest number of these suffixes will contain the final output.

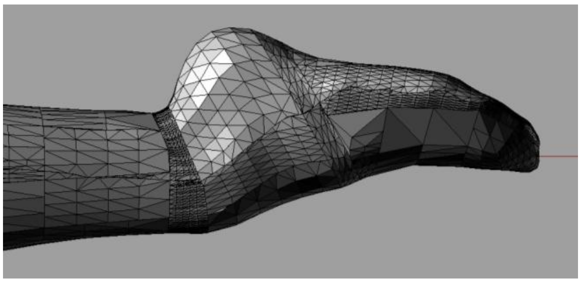

Maximum positive ankle rotation.

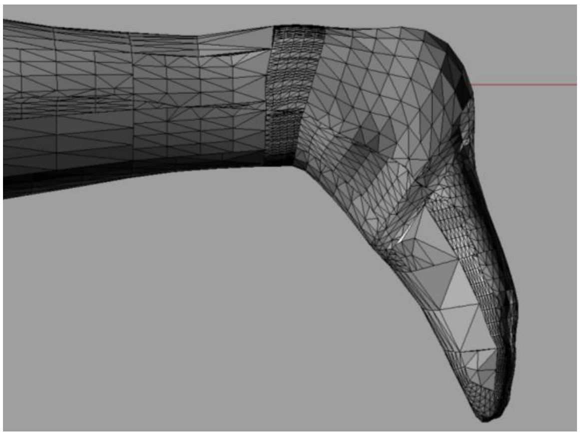

Maximum negative ankle rotation.

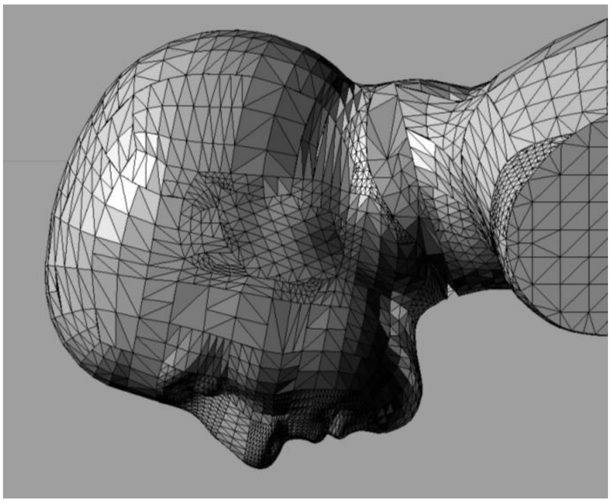

Maximum positive neck rotation.

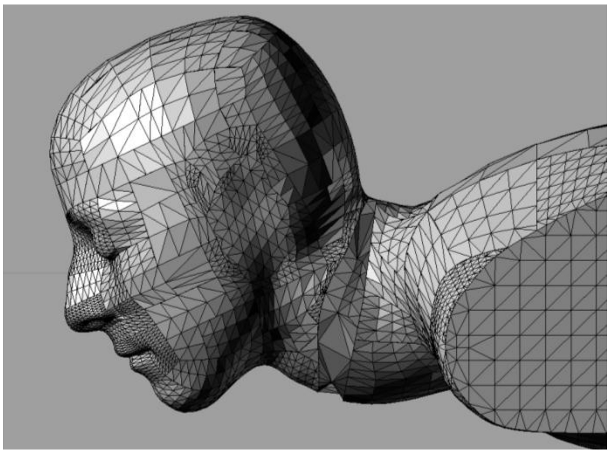

Maximum negative neck rotation.

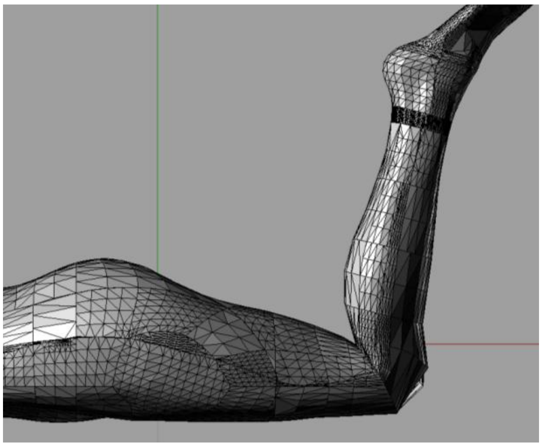

Maximum positive knee rotation.

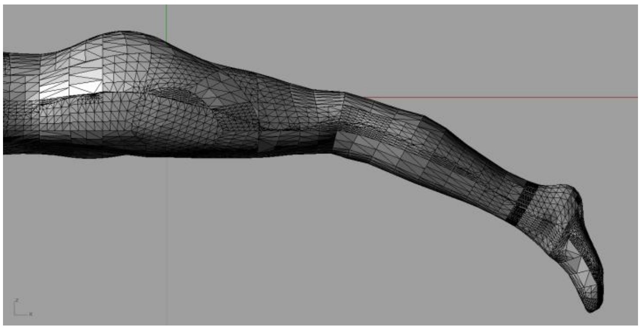

Maximum negative knee rotation.

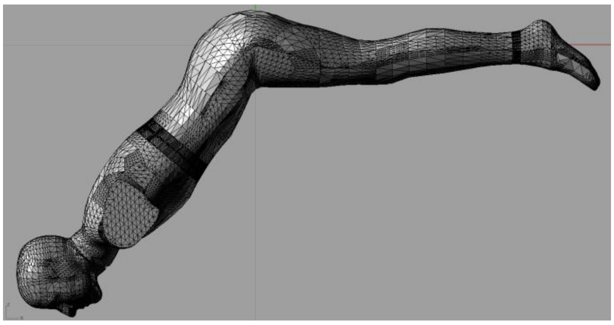

Maximum positive hip rotation.

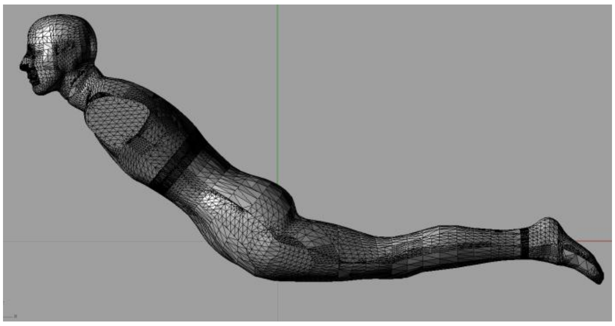

Maximum negative hip rotation.

Appendix 4 – Inner Boundary layer study

A previous study was conducted, using a different athlete geometry, to investigate the impact of mesh density within the inner boundary layer of the double layer structure. In this case the geometry was submerged to a depth of 1m to remove any impact of the free-surface.

For the double-layer structure, three different inner layer meshes were created over the same distance by varying the expansion ratio and number of cells grown. This allowed the effect of the expansion ratio within the inner boundary layer to be investigated. Inner expansion ratios of 1.2, 1.1 and 1.05 provided layer meshes that placed 9, 12 and 14 cells within a y^+ of 20 respectively.

The impact of these different boundary layer meshes on the resistive force acting on the body can be observed in the figures below (along with a comparison to a wall function mesh). Very little difference was observed in the viscous resistance between the different wall resolved meshes, however there was a small change in the pressure resistance (less than two percent of the total resistance). It also appears that increasing the refinement level in the inner layer produces an oscillatory convergence as the finest mesh (expansion ratio of 1.05) resulted in a pressure resistance similar to that of the coarsest mesh. It was therefore decided that significant improvements were not achieved by increasing the mesh refinement in the inner boundary layer region beyond an expiation ratio of 1.2. This appears to broadly agree with the recommendations made in (WS Atkins Consultants, 2003) for at least 10 cells within a y^+ of 20 for a fully resolved boundary layer.

Total Resistance:

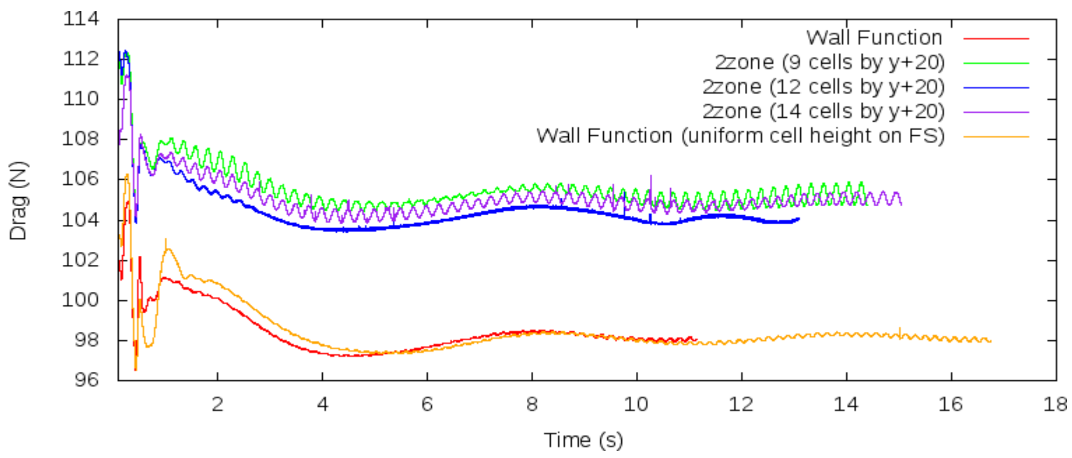

Skin Friction:

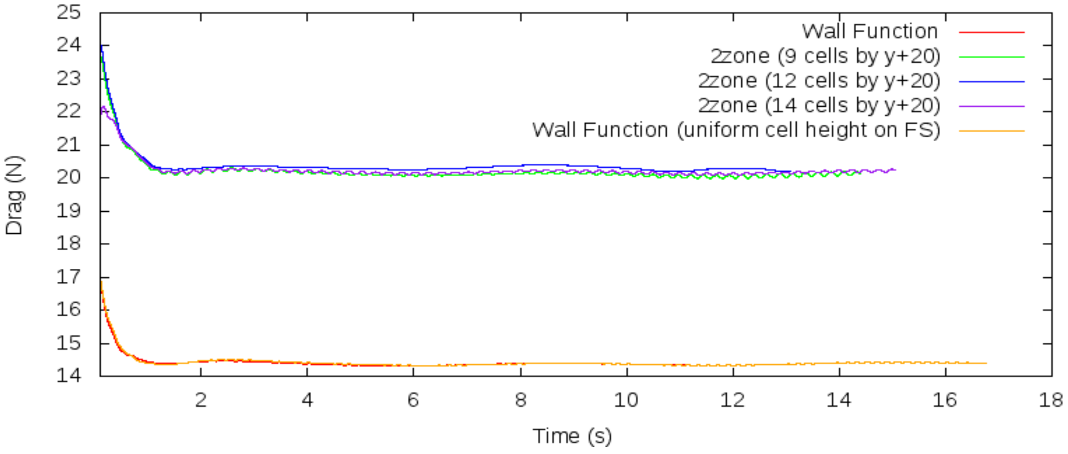

Pressure Resistance:

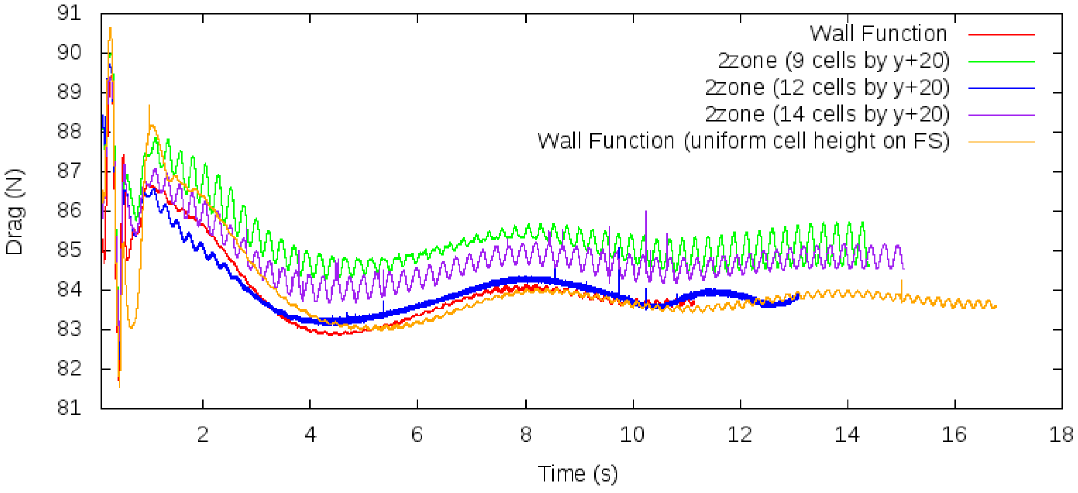

References

Banks, J., Phillips, A. B., Bull, P. W., & Turnock, S. R. (2010). RANS simulations of the flow around the KCS hullform. In L. Larsson, F. Stern, & M. Visonneau (Eds.), *Gothenburg 2010; A Workshop on Numerical Ship Hydrodynamics* (pp. 601-607). Gothenburg.

Banks, J., Phillips, A. B., Turnock, S. R., & Hudson, D. A. (2011). Performing self propelled simulations of a kayak , using a Body-force paddle model. In D. A. Turnock, S.R., Bertram, V., Hudson (Ed.), *Proceedings of the 14th Numerical Towing Tank Symposium* (pp. 71-76). Poole, UK.

Banks, J., Phillips, A. B., Turnock, S. R., Hudson, D. A., & Taunton, D. J. (2013). Kayak blade-hull interactions: A Body-Force approach for self-propelled simulations. *Proceedings of the Institution of Mechanical Engineers, Part P, Journal of Sports Engineering and Technology. (Under review).*

Barber, S., Chin, S. B., & Carré, M. J. (2009). Sports ball aerodynamics: A numerical study of the erratic motion of soccer balls. *Computers & Fluids*, *38*(6), 1091-1100. doi:10.1016/j.compfluid.2008.11.001

Bixler, B., Pease, D., & Fairhurst, F. (2007). The accuracy of computational fluid dynamics analysis of the passive drag of a male swimmer. *Sports biomechanics / International Society of Biomechanics in Sports*, *6*(1), 81-98. doi:10.1080/14763140601058581

Bixler, B., & Riewald, S. (2002). Analysis of a swimmer's hand and arm in steady flow conditions using computational fluid dynamics. *Journal of biomechanics*, *35*(5), 713-7. Retrieved from http://www.ncbi.nlm.nih.gov/pubmed/11955512

Bixler, B., & Schloder, M. (1996). Computational fluid dynamics: an analytical tool for the 21st century swimming scientist. *Journal of Swimming Research*, *11*, 4-22.

Bjorn, W., Turnock, S. R., & Hudson, D. (2012). Validating Force Calculations using OpenFOAM c on a Fixed Wigley Hull in Waves. *Proceedings of the 15th Numerical Towing Tank Symposium* (pp. 1-6). Cortona, Italy.

Bugalski, T. J. (2009). Development of the New Line of Sprint Canoes for the Olympic Games. *In Proceedings of the 10th International Conference on Fast Sea Transportation (FAST 2009)* (pp. 1039-1049). Athens: FAST Organizing Committee.

Cohen, R. C. Z., Cleary, P. W., & Mason, B. R. (2012). Simulations of dolphin kick swimming using smoothed particle hydrodynamics. *Human movement science*, *31*(3), 604-19. doi:10.1016/j.humov.2011.06.008

Comstock, J. P. (1976). *Principles of Naval Architecture*. New York: The Society of Naval Architects and Marine Engineers.

D. C. Wilcox. (1998). Reassessment of the scale-determining equation for advanced turbulence models. *AIAA journal*, *26*(11), 1299–1310.

Day, A., Campbell, I., Clelland, D., & Cichowicz, J. (2011). An experimental study of unsteady hydrodynamics of a single scull. *Proceedings of the Institution of Mechanical Engineers, Part M: Journal of Engineering for the Maritime Environment*, *225*(3), 282–294. doi:10.1177/1475090211406775

Day, Alexander, Campbell, I., Clelland, D., Doctors, L. J., & Cichowicz, J. (2011). Realistic evaluation of hull performance for rowing shells, canoes, and kayaks in unsteady flow. *Journal of sports sciences*, *29*(10), 1059–69. doi:10.1080/02640414.2011.576691

Defraeye, T., Blocken, B., Koninckx, E., Hespel, P., & Carmeliet, J. (2010). Aerodynamic study of different cyclist positions : CFD analysis and full-scale wind-tunnel tests. *Journal of Biomechanics*, *43*(7), 1262–1268. doi:10.1016/j.jbiomech.2010.01.025

Deshpande, S. S., Anumolu, L., & Trujillo, M. F. (2012). Evaluating the performance of the two-phase flow solver interFoam. *Computational Science & Discovery*, *5*(1), 014016. doi:10.1088/1749-4699/5/1/014016

Ellison, W., & Turnock, S. S. (2010). *Investigation into the effect of the kayak paddle stroke on elite kayak performance (3rd year Research Project)*. Southampton.

Hoerner, S. F. (1965). *Fluid-Dynamic Drag* (3rd–16th ed.). Midland Park, NJ: Published by the author, Midland Park, NJ.

Honda, K., Keys, M., Lyttle, A., Alderson, J., Bennamoun, M., & El-sallam, A. (2012). FREESTYLE SWIMMING : AN INSIGHT INTO PROPULSIVE AND RESISTIVE MECHANISMS. *30th Annual Conference of Biomechanics in Sports* (pp. 96–99). Melbourne.

Insel, M. (1990). *An investigation into the resistance components of high speed displacement catamarans.* PhD Thesis, University of Southampton.

Insel, M., Molland, A. F., & Wellicome, J. F. (1994). Wave resistance prediction of a catamaran by linearised theory. *Fifth International Conference on Computer Aided Design, Manufacture and Operation. CADMO'94.*

International Canoe Federation. (2011). Results from ICF Canoe Sprint World Championships. Retrieved July 18, 2012, from http://results.sportline.hu/competition/16777217/race/515

Jackson, P. S. (1995). Performance prediction for Olympic kayaks. *Journal of Sports Sciences*, *13*(3), 239–245.

Kendal, S., & Ross, H. (1992). The Technique of Elite Flatwater Kayak Paddlers Using the Wing Paddle. *International Journal Of Sport Biomechanics*, *8*, 233–250.

Keys,M., Lyttle, A., Blanksby, B. A., & Cheng, L. (2010). A Full Body Computational Fluid Dynamic Analysis of the Freestyle Stroke of a Previous Sprint Freestyle World Record Holder. *11th International symposium of Biomechanics and Medicine in Swimming* (pp. 105–107). Oslo, Norway.

Larsson, L., Stern, F., & Bertram, V. (2003). Benchmarking of computational fluid dynamics for ship flows: The Gothenburg 2000 workshop. *Journal of Ship Research*, *47*(19), 63–81.

Larsson, L., Stern, F., & Visonneau, M. (2010). A Workshop on Numerical Ship Hydrodynamics. *Gothenburg 2010 Proceedings, Volume II*. Gothenburg.

Larsson, L., Stern, F., & Bertram, V. (2003). Benchmarking of Computational Fluid Dynamics for Ship Flows: The Gothenburg 2000 Workshop. *Journal of Ship Research*.

Lazauskas, L, & Tuck, E. (1996). *Low drag racing kayaks*. *Adelaide: The University of Adelaide, Department of* …. Adelaide. Retrieved from http://www.cyberiad.net/library/ kayaks/racing/racing.htm

Lazauskas, Leo, & Winters, J. (1997). *Hydrodynamic Drag of Some Small Sprint Kayaks John Winters ' Sprint Kayak*. Adelaide. Retrieved from http://www.cyberiad.net/library/ kayaks/racing/racing.htm

Leroyer, A., Barré, S., Kobus, J.-M., & Visonneau, M. (2010). Influence of free surface, unsteadiness and viscous effects on oar blade hydrodynamic loads. *Journal of sports sciences*, *28*(12), 1287–98. doi:10.1080/02640414.2010.485646

London2012. (2012). Canoe Sprint Results from London 2012 Olympic Games. Retrieved August 10, 2012, from http://www.london2012.com/canoe-sprint/schedule-and-results

Lyttle, A., & Keys, M. (2004). The use of computational fluid dynamics to optimise underwater kicking performance. *22nd Internatiantinal Syposium on Biomechanics in Sport* (pp. 438–441). Ottawa, Canada.

Lyttle, A. & Keys, M. (2006). The application of computational fluid dynamics for technique prescription in underwater kicking. *Portuguese Journal of Sport Sciences*, *6*(2), 233–235.

Marinho, D. A. (2009). *The study of swimming propulsion using computational fluid dynamics: A three-dimensional analysis of the swimmer ' s hand and forearm*. PhD Thesis, UNIVERSIDADE DE TRÁS-OS-MONTES E ALTO DOURO.

Marinho, D. A., Barbosa, T. M., Kjendlie, P. L., Mantripragada, N., Vilas-boas, J. P., & Machado, L. (2012). Modelling Hydrodynamic Drag in Swimming using Computational Fluid Dynamics. In H. L. Juarez (Ed.), *Fluid Dynamics, Computational Modeling and Applications* (pp. 393–438). InTech.

Marinho, D. A., Barbosa, T. M., Mantha, V. R., Rouboa, A. I., & Silva, A. J. (2012). Modelling Propelling Force in Swimming Using Numerical

Simulations. In H. L. Juarez (Ed.), *Fluid Dynamics, Computational Modeling and Applications* (pp. 439–448). InTech.

Marinho, D. A., Barbosa, T. M., Reis, V. M., Kjendlie, P. L., Alves, F. B., Vilas-Boas, J. P., Machado, L., et al. (2010). Swimming propulsion forces are enhanced by a small finger spread. *Journal of applied biomechanics*, *26*(1), 87–92. Retrieved from http://www.ncbi.nlm.nih.gov/pubmed/20147761

Marinho, D. A., Reis, V. M., Alves, F. B., Vilas-Boas, J. P., Machado, L., Silva, A. J., & Rouboa, A. I. (2009). Hydrodynamic drag during gliding in swimming. *Journal of applied biomechanics*, *25*(3), 253–7. Retrieved from http://www.ncbi.nlm.nih.gov/pubmed/19827475

Menter, F. R. (1994). Two-equation eddy-viscosity turbulence models for engineering applications. *AIAA-Journal*, *32*(8), 269–289.

Minetti, A. E., Machtsiras, G., & Masters, J. C. (2009). The optimum finger spacing in human swimming. *Journal of biomechanics*, *42*(13), 2188–90. doi:10.1016/j.jbiomech.2009.06.012

Miwa, T., Matsuuchi, K., Shintani, H., Kamata, E., & Nomura, T. (2006). Unsteady flow measurement of dolphin kicking wake in sagittal plane using 2C-PIV. In P. Vilas-Boas, F. Alves, & A. Marques (Eds.), *Biomechanics and medicine in swimming X: Portuguese Journal of Sport Sciences.*

Molland, A. F., Turnock, S. R., & Hudson, D. A. (2011). *Ship resistance and propulsion: practical estimation of ship propulsive power*. Cambridge Univ Press.

Morgoch, D., & Tullis, S. (2011). Force analysis of a sprint canoe blade. *Proceedings of the Institution of Mechanical Engineers, Part P: Journal of Sports Engineering and Technology*, *225*(4), 253–258. doi:10.1177/1754337111407793

Nakashima, M., Satou, K., & Miura, Y. (2007). Development of Swimming Human Simulation Model Considering Rigid Body Dynamics and Unsteady Fluid Force for Whole Body. *Journal of Fluid Science and Technology*, *2*(1), 56–67. doi:10.1299/jfst.2.56

Novais, M. L., Silva, A. J., Mantha, V. R., Ramos, R. J., Rouboa, A. I., Vilas-Boas, J. P., Luís, S. R., et al. (2012). The Effect of Depth on Drag During the Streamlined Glide: A Three-Dimensional CFD Analysis. *Journal of human kinetics*, *33*(June), 55–62. doi:10.2478/v10078-012-0044-2

OpenFOAM®. (2009). *OpenFOAM – The Open Source CFD Toolbox- User Gide, Version 1.6x.*

OpenFOAM®. (2011). *OpenFOAM – The Open Source CFD Toolbox- User Gide, Version 2.01.*

Peric, M., & Ferziger, J. H. (2002). *Computational Methods for Fluid Dynamics* (3rd ed.). Springer.

Phillips, A. B. (2009). *Cost Effective Hydrodynamic Concept Design of Autonomous Underwater Vehicles*. PhD Thesis, University of Southampton.

Phillips, A., Furlong, M., & Turnock, S. (2010). Accurate capture of rudder-propeller interaction using a coupled blade element momentum-RANS approach. *Ship Technology Research (Schiffstechnik),*, *57*(2), 128–139.

Phillips, C. (2013). *Musculoskeletal Modelling of Human Swimming for Technique and Performance Evaluation*. PhD Thesis, University of Southampton.

Phillips, A. B., Turnock, S. R., & Furlong, M. E. (2009). Evaluation of manoeuvring coefficients of a self-propelled ship using a blade element momentum propeller model coupled to a Reynolds averaged Navier Stokes flow solver. *Ocean Engineering*, *36*(15-16), 1217–1225.

Ritchie, A. C., Faizal, M., & Selamat, B. (2010). Comparison of blade designs in paddle sports Comparison of blade designs in paddle sports. *Journal of Sports Technology*, *3*(2), 141–149.

Rouboa, A., Silva, A., Leal, L., Rocha, J., & Alves, F. (2006). The effect of swimmer's hand/forearm acceleration on propulsive forces generation using computational fluid dynamics. *Journal of biomechanics*, *39*(7), 1239–48. doi:10.1016/j.jbiomech.2005.03.012

Sato, Y., & Hino, T. (2003). Estimation of Thrust of Swimmer' s Hand Using CFD. *Second International Symposium on Aqua Bio-Mechanisms*, 71–75.

Sato, Y., & Hino, T. (2010). CFD simulation of flows around a swimmer in a prone glide position. *Suiei Suichu Undo Kagaku*, *13*(1), 1–9. doi:10.2479/swex.13.1

Silva, A. J., Rouboa, A., Moreira, A., Reis, V. M., & Alves, F. (2008). Analysis of drafting effects in swimming using computational fluid dynamics, (September 2007), 60–66.

Sliasas, a, & Tullis, S. (2010). The dynamic flow behaviour of an oar blade in motion using a hydrodynamics-based shell-velocity-coupled model of a rowing stroke. *Proceedings of the Institution of Mechanical Engineers, Part P: Journal of Sports Engineering and Technology*, *224*(1), 9–24. doi:10.1243/17543371JSET57

Sumner, D., Sprigings, E. J., Bugg, J. D., & Heseltine, J. L. (2003). Fluid forces on kayak paddle blades of different design. *Sports Engineering*, (6), 11–19.

Toussaint, H., & Truijens, M. (2005). Biomechanical aspects of peak performance in human swimming. *Animal Biology*, *55*(1), 17–40. doi:10.1163/1570756053276907

Turnock, S R., Phillips, A. B., Banks, J., & Nicholls-Lee, R. (2011). Modelling tidal current turbine wakes using a coupled RANS-BEMT approach as a tool for analysing power capture of arrays of turbines. *Ocean Engineering*, *38*(11-12), 1300–1307. doi:10.1016/j.oceaneng.2011.05.018

Turnock, S.R. (2004). *Parametric definition of complex multi-appended bodies for marine and aerospace application: a user guide to Adaptflexi.* Southampton. Retrieved from http://eprints.soton.ac.uk/179377/1/Adaptflexi_UG_ssr136_050131.doc

Vennell, R., Pease, D., & Wilson, B. (2006). Wave drag on human swimmers. *Journal of biomechanics*, *39*(4), 664–71. doi:10.1016/j.jbiomech.2005.01.023

Versteeg, H. K., & Malalasekera, W. (2007). *An introduction to computational fluid dynamics: the finite volume method*. (W. Malalasekera, Ed.)*World Wide Web Internet And Web Information Systems* (Vol. M, p. 503). Pearson Education. Retrieved from http://books.google.nl/books?id=RvBZ-UMpGzIC&hl=nl&source=gbs_navlinks_s

Von Loebbecke, A., Mittal, R., Mark, R., & Hahn, J. (2009). A computational method for analysis of underwater dolphin kick hydrodynamics in human swimming. *Sports biomechanics / International Society of Biomechanics in Sports*, *8*(1), 60–77. doi:10.1080/14763140802629982

Wackers, J., Koren, B., Raven, H. C., Ploeg, a., Starke, a. R., Deng, G. B., Queutey, P., et al. (2011). Free-Surface Viscous Flow Solution Methods for Ship Hydrodynamics. *Archives of Computational Methods in Engineering*, *18*(1), 1–41. doi:10.1007/s11831-011-9059-4

Webb, A. (2013). *Identifying race time benefits of best practice in freestyle using simulation*. PhD Thesis, University of Southampton.

Webb, A., Banks, J., Phillips, C., Hudson, D., Taunton, D., & Turnock, S. (2011). Procedia Engineering Prediction of Passive and Active Drag in Swimming, *00*, 1–7.

Weymouth, G. D., & Yue, D. K.-P. (2010). Conservative Volume-of-Fluid method for free-surface simulations on Cartesian-grids. *Journal of Computational Physics*, *229*(8), 2853–2865. doi:10.1016/j.jcp.2009.12.018

Wolfson Unit for Marine Technology and Industrial Aerodynamics (WUMTIA). (n.d.). *Confidential experimental test data*. Southampton.

WS Atkins Consultants. (2003). *Best Practice Guidelines for Marine Applications of Computational Fluid Dynamics*.

Yang, J., & Stern, F. (2007). Large-Eddy Simulation of Breaking Waves Using Embedded-Boundary/Level-Set Method. *Proc. 45th AIAA Aerospace Sciences Meeting and Exhibit* (pp. AIAA–2007–1455). Reno, Nevada.

Zaïdi, H., Taïar, R., Fohanno, S., & Polidori, G. (2008). Analysis of the effect of swimmer's head position on swimming performance using computational fluid dynamics. *Journal of biomechanics*, *41*(6), 1350–8. doi:10.1016/j.jbiomech.2008.02.005